UNIVERSITÀ DEGLI STUDI DI BOLOGNA
Dottorato in Modellistica fisica per la protezione dell'ambiente
XX ciclo

PhD Thesis

NUMERICAL SIMULATIONS OF MAGMA CHAMBER DYNAMICS AT CAMPI FLEGREI, AND ASSOCIATED SEISMICITY, DEFORMATION AND GRAVITY CHANGES

Candidate: **Melissa Vassalli**

Supervisor
Prof. Stefano Tinti

PhD Coordinator
Prof. EzioTodini

Assistant supervisors
Dott. Paolo Papale

Dott.ssa Antonella Longo

Dott. Gilberto Saccorotti

Lo scienziato non è l'uomo che fornisce le vere risposte;
è quello che pone le vere domande.
(Claude Lévi-Strauss)

Acknowledgements

I wish to thank my supervisors Prof. Stefano Tinti, Dott. Paolo Papale, Dott.ssa Antonella Longo and Dott. Gilberto Saccorotti for their help, support and advice.

I also wish to thank Prof. Chris Bean and Dott. Gareth O'Brien for the opportunity to work with them, and to discover Dublin.

Maky thanks to Prof. Aldo Zollo and his co-workers for their collaboration and help.

Molte sono le persone da ringraziare per l'aiuto scientifico e morale che ho ricevuto durante questi anni di dottorato. Per primi i miei compagni di ufficio, che mi hanno ascoltato, consolato, spronato e, soprattutto, sopportato. Grazie anche a tutti coloro con cui ho discusso di quel che facevo nella tesi e che mi hanno dato aiuto e spunti di riflessione interessanti.

Ringrazio il Cyrcolo, e singolarmente i vari componenti, per l'amicizia e il calore che mi danno, per le risate, i film, le chiacchiere e le accese discussioni.

Ringrazio Silva per avermi sempre detto "va tutto bene". Ringrazio Massimo, Federico e Matilde. Ringrazio Antonio per le discussioni e i consigli cinefili.

Ringrazio Vieri.

Se dovessi aver dimenticato qualcuno, non ve ne abbiate a male, vi ho dimenticato soltanto sulla carta (ho finito la tesi stanotte alle 3).

Abstract

Understanding the complex relationships between quantities measured by volcanic monitoring network and shallow magma processes is a crucial headway for the comprehension of volcanic processes and a more realistic evaluation of the associated hazard. This question is very relevant at Campi Flegrei, a volcanic quiescent caldera immediately north-west of Napoli (Italy). The system activity shows a high fumarole release and periodic ground slow movement (bradyseism) with high seismicity. This activity, with the high people density and the presence of military and industrial buildings, makes Campi Flegrei one of the areas with higher volcanic hazard in the world.

In such a context my thesis has been focused on magma dynamics due to the refilling of shallow magma chambers, and on the geophysical signals detectable by seismic, deformative and gravimetric monitoring networks that are associated with this phenomenologies. Indeed, the refilling of magma chambers is a process frequently occurring just before a volcanic eruption; therefore, the faculty of identifying this dynamics by means of recorded signal analysis is important to evaluate the short term volcanic hazard.

The space-time evolution of dynamics due to injection of new magma in the magma chamber has been studied performing numerical simulations with, and implementing additional features in, the code `GALES` (Longo et al., 2006), recently developed and still on the upgrade at the Istituto Nazionale di Geofisica e Vulcanologia in Pisa (Italy). `GALES` is a finite element code based on a physico-mathematical two dimensional, transient model able to treat fluids as multiphase homogeneous mixtures, compressible to incompressible. The fundamental equations of mass, momentum and energy balance are discretised both in time and space using the Galerkin Least-Squares and discontinuity-capturing stabilisation technique. The physical properties of the mixture are computed as a function

of local conditions of magma composition, pressure and temperature.The model features enable to study a broad range of phenomenologies characterizing pre and sin-eruptive magma dynamics in a wide domain from the volcanic crater to deep magma feeding zones.

The study of displacement field associated with the simulated fluid dynamics has been carried out with a numerical code developed by the Geophysical group at the University College Dublin (O'Brien and Bean, 2004b), with whom we started a very profitable collaboration. In this code, the seismic wave propagation in heterogeneous media with free surface (e.g. the Earth's surface) is simulated using a discrete elastic lattice where particle interactions are controlled by the Hooke's law. This method allows to consider medium heterogeneities and complex topography.

The initial and boundary conditions for the simulations have been defined within a coordinate project (INGV-DPC 2004-06 V3_2 "Research on active volcanoes, precursors, scenarios, hazard and risk - Campi Flegrei"), to which this thesis contributes, and many researchers experienced on Campi Flegrei in volcanological, seismic, petrological, geochemical fields, etc. collaborate. Numerical simulations of magma and rock dynamis have been coupled as described in the thesis.

The first part of the thesis consists of a parametric study aimed at understanding the effect of the presence in magma of carbon dioxide in magma in the convection dynamics. Indeed, the presence of this volatile was relevant in many Campi Flegrei eruptions, including some eruptions commonly considered as reference for a future activity of this volcano. A set of simulations considering an elliptical magma chamber, compositionally uniform, refilled from below by a magma with volatile content equal or different from that of the resident magma has been performed. To do this, a multicomponent non-ideal magma saturation model (Papale et al., 2006) that considers the simultaneous presence of CO_2 and H_2O, has been implemented in `GALES`. Results show that the presence of CO_2 in the incoming magma increases its buoyancy force promoting convection ad mixing. The simulated dynamics produce pressure transients with frequency and amplitude in the sensitivity range of modern geophysical monitoring networks such as the one installed at Campi Flegrei .

In the second part, simulations more related with the Campi Flegrei volcanic

system have been performed. The simulated system has been defined on the basis of conditions consistent with the bulk of knowledge of Campi Flegrei and in particular of the Agnano-Monte Spina eruption (4100 B.P.), commonly considered as reference for a future high intensity eruption in this area. The magmatic system has been modelled as a long dyke refilling a small shallow magma chamber; magmas with trachytic and phonolitic composition and variable volatile content of H_2O and CO_2 have been considered. The simulations have been carried out changing the condition of magma injection, the system configuration (magma chamber geometry, dyke size) and the resident and refilling magma composition and volatile content, in order to study the influence of these factors on the simulated dynamics. Simulation results allow to follow each step of the gas-rich magma ascent in the denser magma, highlighting the details of magma convection and mixing. In particular, the presence of more CO_2 in the deep magma results in more efficient and faster dynamics. Through this simulations the variation of the gravimetric field has been determined.

Afterward, the space-time distribution of stress resulting from numerical simulations have been used as boundary conditions for the simulations of the displacement field imposed by the magmatic dynamics on rocks. The properties of the simulated domain (rock density, P and S wave velocities) have been based on data from literature on active and passive tomographic experiments, obtained through a collaboration with A. Zollo at the Dept. of Physics of the Federici II Univeristy in Napoli. The elasto-dynamics simulations allow to determine the variations of the space-time distribution of deformation and the seismic signal associated with the studied magmatic dynamics. In particular, results show that these dynamics induce deformations similar to those measured at Campi Flegrei and seismic signals with energies concentrated on the typical frequency bands observed in volcanic areas.

The present work shows that an approach based on the solution of equations describing the physics of processes within a magmatic fluid and the surrounding rock system is able to recognise and describe the relationships between geophysical signals detectable on the surface and deep magma dynamics. Therefore, the results suggest that the combined study of geophysical data and informations from numerical simulations can allow in a near future a more efficient evaluation of the short term volcanic hazard.

Contents

Chapter 1

Introduction

Volcanic eruptions can bring devastation to lands and civilisations, and in the past have been responsible for creating volcanic winters on the Earth (Rampino et al., 1987; Courtillot, 1990). The historical record indicates that about 1 million people have been killed by volcanic eruptions in the past 2000 years and that most of the deaths occurred in a few eruptions. In the twentieth century, the 1902 eruption of Mt. Pelée (Martinique) killed about 29,000 people, whereas in 1985 Nevado del Ruiz (Colombia) killed another 25,000. In the nineteenth century, the two eruptions in Indonesia, Tambora in 1815 and Krakatau in 1883, killed about 130,000 people (Decker and Decker, 1991). In 1792 the eruption of Unzen volcano (Japan) killed about 15,000 people (Yanagi et al., 1992). The eruption of Vesuvius in 1631 killed another 10,000 people, whereas its A. D. 79 eruption that destroyed Pompei and Ercolano produced at least 3,000 deaths (Sigurdsson et al., 1985). The city of San Salvador (El Salvador) lies close to a lake originated from a massive eruption in around A.D. 300 that was estimated to displace or kill thousands to hundreds of thousands of people and changed the course of local civilisations.

Today, the countries and regions more exposed to volcanic risk by explosive volcanoes are Italy, Indonesia, New Zealand, Papua New Guinea, the Philippines, Japan, the Western United States, Mexico, Central America, Colombia, Ecuador, Peru and Chile. Milions of people live too close to some of the most dangerous volcanoes in the world, which could erupt and produce a catastrophe even in the near future. Such a critical situation requires that the volcanic risk be mitigated so that people could cohabit with volcanoes in security. For this reason, eruption forecasting and volcanic risk assessment are mandatory for many modern societies.

Nevertheless, they are a very difficult task to deal with because of the necessity of combining socio-economic data with engineering and urban-planning.

Current volcanic eruption forecasting is a human endeavour where the best forecasts range from hours to a few days in advance, as in the situations of the Mt. ST. Helens eruption in 1980 and Mt. Pinatubo eruption in 1991. In 1993 six volcanologists studying the Galeras volcano (Colombia) lost their lives when the volcano exploded with lava, ash and incandescent boulders (Fisher et al., 1997). In 1995 the small volcanic island of Montserrat in central America began to come alive and most of 11,000 residents of Plymouth were evacuated, and in 1997 an eruption occurred without warning and killing some people.

Volcanologists base eruption forecasts on the information or data from eruption history, useful to learn about volcano behaviour and features, and volcano monitoring (seismicity, ground deformation, gas emission, hydrological regimes, and magnetic, electric and gravity fields). A change of the seismicity or earthquake activity of a volcano may be associated with the rearrangement or rise of molten rock material within the volcano, since this kind of activity produces rock fracturing and pressure variations which in turn are transformed into ground motions. However, seismicity does not always lead to the conclusion that a volcano has become restless since a seismic signal can also be produced by the tectonic motions of the volcanic region that may have nothing to do with the volcano itself. Nevertheless, a volcano in the process of erupting produces seismic signals that are sufficiently representative of an "eruption in progress" and can serve as precursory signals that some sort of external activity will take place. Similarly, the ground movements are good indications that something is happening within the volcano, especially when these movements become large relative to the background noise or instrumental error. Changes in the electrical conductivity, magnetic and gravity fields can trace molten rock movements inside a volcano and may be detected even when a volcano is not preparing for an eruption. Changes in the composition of the emitted gas from fractures may be related to the rearrangement of the molten rock within the volcano or gas escape routes through fractured medium. Moreover, changes of ground water temperature, water level in wells or lakes, and others can also be considered useful signals for eruption forecasts. Eruption forecasting is improved by appropriate scientific studies, such as physical modeling of volcanic processes or laboratory experiments, that allow to better

understand the relationship between these signals and the volcanic processes and to more realistically evaluate the volcanic hazard.

Nowadays, eruption forecasts are based on very narrow windows of hours or several days and can lead to catastrophic consequence in a densely populated area, since it is very difficult to evacuate hundreds of thousands of people on a very short notice and possibly in a state of panic. The politicians who must issue an evacuation order are thus given no alternative but to wait until the last minute in order to avoid a false alarm and become responsible for the expenditure of very large national resources. The end result of this dilemma between the uncertainty in eruption forecasting and the desire to avoid false alarm can produce a tragedy for those living close to volcanoes; examples are the tragedies of St. Pierre in 1902 and Armero in 1985 where the city administrators failed to give evacuation orders (Dobran, 2001).

As pointed out before, Italy is a country characterised by a very high volcanic risk because of the presence of densely populated active volcanic areas; examples of such areas are Campi Flegrei, Vesuvio, Stromboli, Etna, Colli Albani and Vulcano. In such a contest the Dipartimento di Protezione Civile together with the Istituto Nazionale di Geofisica e Vulcanologia funded the 2-years coordinate project "Research on active volcanoes, precursors, scenarios, hazard and risk" with the main objective of improving the definition of hazard and risk in all the active or potentially active volcanic areas in Italy.

This thesis contributed to the subproject focused on the study of the Campi Flegrei caldera. The volcanic hazard of this area is extremely high because of its explosive character and the occurrence in the past of large scale eruptions. Close to 1.5 million people live within the caldera, with about 350,000 people living in its active portion. Due to the high volcanic hazard and the intense urbanisation of both the active portion of the caldera and its surroundings, the volcanic risk at Campi Flegrei is very high. The project results leave open the possibility that the on-going unrest occurring at Campi Flegrei could culminate in a new eruption in a short-medium time range.

The research performed in this thesis focused on the numerical simulation of convection processes in magma chambers and associated seismicity, deformation and gravity changes in order to establish links between deep, potentially hazardous magmatic processes and measurable quantities at the surface. Many

recent volcanic eruptions at Campi Flegrei have been shortly preceded, in fact, by efficient mixing of different magmas, which was likely due to the onset of convection in magma chamber. Magma chamber refilling, convection and mixing of different magmas are well-known processes widely recognised from the analysis of volcanic products (Snyder, 1997). Such processes are often hypothesized to have occurred repetitively in magma chambers, and to have triggered volcanic eruptions over a tile scale of days to hours (Sparks et al., 1977; Pallister et al., 1992; Venetzky and Rutherford, 1997; Coombs et al., 2000; Mashima, 2004). Typically, the new magma entering a chamber is chemically less evolved and carries less water and more crystals. Although it is commonly hotter, its capability to induce buoyancy-driven convection can be scarce or null (Phillips and Woods, 2002). Nevertheless, convection in magma chambers may arise from compositional variations caused by fractional crystallization, partial melting of reservoir boundaries and internal crystal matrix, injection of fresh magma into the chamber, or volatile exsolution. The bulk of knowledge on the past history at Campi Flegrei suggests that at least in some cases a shallow magma chamber was invaded, hours to tens of hours before the onset of the eruption, by a CO_2-rich magma of deep provenance. For this reason, convection and mixing dynamics induced by the arrival of new CO_2-rich magma into a hypothetical shallow magma chamber at Campi Flegrei , and the associated rock elasto-dynamics, have been the subject of my studies.

Part I

Methods

Chapter 2

State of the Art

The elaboration of a comprehensive theory of seismic sources associated with magma dynamics is critical to a more realistic evaluation of the behaviour of volcanoes and, hence, of the hazard in volcanic areas. The modelling of magma dynamics and associated wave propagation in rocks is an important tool for understanding the nature and dynamics of seismic sources associated with movement of magma and/or hydrothermal fluids. Many efforts have been aimed on modelling the fluid-dynamics of magma and the elasto-dynamics of the surrounding solid in either separate or coupled schemes. However, the nonlinearity of fluid-dynamics equations and the complexity of volcanic fluids and the highly heterogeneous materials and rough topography of volcanoes, force models to make many simplifying assumptions on fluid behaviour and rock properties.

2.1 Modelling of fluid dynamics

Magma is a multicomponent, multi-phase mixture constituted of silicate liquid, crystals and gas. The silicate liquid composition is adequately represented by the elements O, Si, Al, Fe, Mg, Ca, Na and K since the remaining elements usually occur in minor amounts. Crystals come either from magma cooling or from surrounding rocks as xenocrystals; volatile components are H_2O and CO_2 , and, subordinately, H_2S, SO_2, HCl, HF, CO, N_2, H_2 and HBr. Volatiles can be in liquid or gaseous phase depending on whether the system pressure is below or above their saturation pressure. If volatiles are totally dissolved in the liquid phase, magma behaves essentially as an incompressible fluid; when volatiles

exsolve and a gas phase forms, the mixture becomes compressible. All relevant magma properties depend significantly on pressure, temperature and magma composition.

The modelling of subsurface magma dynamics has to take into account the complex magma behaviour due to many microscopic and macroscopic physical and chemical processes such as melt segregation, mixing or mingling of different magmas, magma differentiation due to crystal fractionation, changes in flow regime (bubbly flow, slug flow, annular flow and gas flow with dispersed particles), magma fragmentation, heat and mass transfer between solid, liquid and gas phases, momentum and energy transfer between phases and between magma and surrounding rocks, diffusion of heat, momentum and chemical species, changes from subsonic to supersonic velocities.

The quantitative study of magma dynamics is complicated by often large uncertainty about most of the potentially critical factors. These include, for instance, the transport properties of the mixing magmas (e.g. viscosity, chemical diffusivities), the role of chemical and thermal buoyancy and the configuration of the system. Moreover, magma dynamics are made more complex by gas loss through system walls, refilling or withdrawal of magma, melting and assimilation of surrounding rocks, thermo-mechanical deformation of volcanic system, interaction between magma and water reservoir and collapse of chamber walls or roof.

Regarding magma chamber modelling, a further complication is due to the fact that the chamber walls are not clearly defined as a rigid and impermeable-to-mass partition; the chamber walls, in fact, extend in length as a porous structure where crystals deposit and through which the exsolved gas and hypercritical fluids can escape. Three regions distinguished by a different fraction of solid and liquid, hence with different mechanical behaviour, can be recognised in the magma chamber even though the transition between these zones is gradual. The inner part of reservoirs is a liquid-dominated region where mixture behaves as a liquid with dispersed solid particles and gas bubbles. The outer zone of chamber is a solid-dominated region and the intermediate part (mushy or cumulitic region) is a crystal network through which the silicate liquid flows.

The physico-mathematical models try to reproduce the processes occurring within the magmatic system through the three fundamental conservation equations for continua (Bird et al., 1960):

- mass conservation (or continuity equation):

$$\frac{\partial \rho}{\partial t} + \nabla \cdot \rho \mathbf{u} = 0 \tag{2.1}$$

where ρ is density, t is time and $\mathbf{u}$ is the velocity vector;

- momentum balance (or fundamental Newton's law):

$$\frac{\partial (\rho \mathbf{u})}{\partial t} + \nabla \cdot (\rho \mathbf{u}\mathbf{u}) = \rho \mathbf{g} - \nabla p + \nabla \cdot \tau \tag{2.2}$$

where $\mathbf{g}$ is the gravity acceleration, p the pressure and τ the stress tensor. In the left-hand side, the first term is the so-called *unsteady term* (which vanishes for steady conditions) and expresses the variation with time of the velocity through a fluid volume, while the second is the *convective term*, giving the variation of velocity through a fluid volume due to its transport by the velocity field through a gradient of velocity. In the right-hand side, all terms are force per unit mass acting on the particle: the first one corresponds to body force (gravity), and the remaining ones to surface forces, divided in two terms corresponding to pressure and to viscous stress;

- energy balance (or first principle of thermodynamics)

$$\frac{\partial \rho \left(U + \frac{1}{2}\mathbf{u}^2\right)}{\partial t} + \nabla \cdot \left(\rho \mathbf{u} \left(U + \frac{1}{2}\mathbf{u}^2\right)\right) = -\nabla \cdot \mathbf{q} + \rho \mathbf{u} \cdot \mathbf{g} - \nabla (p\mathbf{u}) - \nabla \cdot [\tau \cdot \mathbf{u}] \tag{2.3}$$

where U is the internal energy per unit mass and $\mathbf{q}$ the energy flux per unit volume. The left-hand side terms are the time variation and the accumulation rate of energy due to the overall flow through a fluid volume. The first term of the right-hand side is the energy transport due to conduction while the other terms are the rate of work done by the gravitational, pressure and viscous forces, respectively.

If the mixture is treated as multi-phase and multi-component, the mass needs to be conserved for each component in each phase:

$$\frac{\partial \rho_{k,i}}{\partial t} + \nabla \cdot \rho_{k,i} \mathbf{u}_{k,i} = \mathbf{S}_{k,i} \tag{2.4}$$

where the subscript k,i indicates component k in phase i, and $\mathbf{S}_{k,i}$ is the source-sink term of component $k$in phase i. If the mixture is not in mechanical and/or

thermal equilibrium, the momentum and/or energy conservation equations have also to be solved for each phase.

The definition of appropriate constitutive equations (i.e., equations of state, stress tensor, heat flux, and fluid properties like density, viscosity (entering into the stress tensor), specific heats, etc.) allows the description of the physico-chemical properties of magma. Phase changes need also to be modeled through appropriate sets of equations.

Due to the nonlinearity of the balance equations and the complexity of the magmatic mixture, all models consider simplifying assumptions depending on what aspects of the investigated processes the model wants to focus on, and what are the major factors controlling the processes under investigation. The more common simplifications are the steady state, the reduction of domain dimensions (from 3D to 2D or 1D), the mechanical and/or chemical and/or thermal equilibrium, the fluid incompressibility, the low-Reynolds flow regime (or neglect of turbulence) and the Boussinesq approximation (or neglect of compressible effects).

The system dynamics can be modeled using either lumped or non-lumped methods. The lumped approach reduces the problem dimensions from 3D to 0D and considers an overall description of the fluid dynamics, treating the system with the aid of globally-averaged quantities. Usually, lumped models allow solution of the conservation equations analytically or semi-analytically. The non-lumped approach solves the equations for each point into the system allowing a description of the internal dynamics of the fluid; usually this approach adopts numerical methods to solve the system of conservation equations.

2.1.1 Lumped models

Examples of lumped models applied to magma chamber dynamics are those defined by Blake (1981), Bower and Woods (1997) and Snyder (2000).

Blake (1981)

Blake (1981) modeled a magma chamber open to an inflow of material from below. He calculated the volume of liquid magma required to increase the chamber pressure, through elastic deformation of the magma, to a value sufficient to trigger an eruption in a rigid homogeneous chamber with uniform pressure. He derived a relationship giving the critical volume of added magma required to

cause an eruption as a function of magma compressibility and the volume by which the chamber expands.

Bower and Woods (1997)

Bower and Woods (1997) developed a steady-state model for the mass erupted from a magma chamber for a given decrease in chamber pressure, as a function of compressibility of the mixture in the chamber. The magma chamber is assumed one-dimensional (that is, pressure, volatile content and mixture density vary only with depth) and isothermal. The model considers homogeneous mixture of liquid, crystals and gas bubbles, accounting for the effect of crystallization and gas exsolution on mixture density and, hence, on reservoir pressure and volume. The crystal and bubble content is modeled as a function of pressure, temperature and mixture composition. Thermal, chemical and mechanical equilibrium between the different phases is assumed.

Snyder (2000)

Snyder (2000) modeled the thermal and compositional effects due to an intrusion of basaltic magma into a more silicic magma chamber. This model takes into account crystal growth and re-absorption and their fractionation from the melt. It considers a two-phase mixture, neglecting the presence of gas bubbles. The phase equilibria and the thermodynamic and rheological effects of crystallization, such as density and viscosity changes, are computed through the `MELTS` algorithm (Ghiorso, 1994). The assumption of chamber geometry much more extended in the horizontal direction than in the vertical one allows neglecting the heat flux due to sidewall crystallization and the heat loss through the country rocks.

2.1.2 Non-lumped models

The most common methods employed to solve the system of equations (2.1)-(2.3) together with the constitutive equations describing the magma properties are based on finite element, finite difference and, subordinately, finite volume approach. The numerical models allow treating the interdependency between small scale (i.e., evolution of magma composition and properties) and large scale (i.e., convection, thermal or chemical zonation) processes through the solution of conservation equations in terms of the intensive variables (P, T, composition). Examples of models of magma chamber dynamics are those defined by Oldenburg

et al. (1989), Spera et al. (1995), Trial et al. (1992), Folch et al. (1999) and Simakin and Botcharnikov (2001).

Oldenburg et al. (1989)

Oldenburg et al. (1989) developed one of the first numerical models for magma mixing in magma chambers. They implemented a two-dimensional model that considers mixing between incompressible homogeneous magmas induced mainly by diffusion and thermal-compositional convection. The main assumptions are that magma behaves as a Newtonian fluid and crystallization and assimilation are not allowed. Magma chamber walls are considered rigid and insulating.

The mass, momentum and energy conservation equations are solved using a Galerkin finite element method.

Bergantz (2000) improved the model by Oldenburg et al. (1989) explicitly taking into account the multiphase fluid-dynamics of the magmatic mixture. This model allows the study of the convection and mixing following the intrusion of a crystal-bearing magma in a chamber hosting a crystal-free magma.

Spera et al. (1995)

Spera et al. (1995) developed a two-dimensional model to study the thermal and compositional evolution of a compositionally zoned magma chamber where convection occurs. The model computes the local phase and composition variations in a cooling magma, initially homogeneous and slightly superheated.

The model accounts for solidified, mushy and all-liquid regions including latent heat effects, percolative flow of melt through the mush and the variation of system enthalpy with composition, temperature and solid fraction. Relative motion between crystals and melt is not allowed in the melt-dominated regions, whereas in the solid-dominated region melt percolates through a crystal network assumed static and undeformable. Thermal and chemical equilibrium is assumed everywhere. The phase relations are determined by the equilibrium phase diagram and only binary component systems are considered. The magma is treated as an incompressible, Newtonian fluid. The gas phase is not accounted for and the Boussinesq approximation is adopted.

The model equations are solved using a finite difference method.

As an improvement of this model, Kuritani (2004) modeled the magmatic differentiation processes in a cooling magma reservoir using a numerical model that computes crystallization by means of multicomponent thermodynamic models.

The model assumes that the solid phases are stationary except for olivine and plagioclase that are the earliest crystallization phases in basaltic magmas and, hence, are considered as fractionating phases.

Trial et al. (1992) modeled the two-dimensional magma withdrawal from a compositionally zoned chamber driven by pressure forces associated with chamber replenishment. This model is an improvement of the model from Spera et al. (1986). The magma is treated as an incompressible, single-phase Newtonian fluid with variable properties, such as density and viscosity; the effect of temperature on viscosity is neglected. The equations of conservation of mass and momentum are solved using the Galerkin finite element formulation.

Folch et al. (1999)

Folch et al. (1999) developed a numerical model for the simulation of the dynamics of incompressible/compressible homogeneous bubbly magma driven by exsolution of water and/or caldera subsidence in non-replenished shallow magma chambers (Folch et al., 1998).

The model considers the magma as an homogeneous, incompressible, Newtonian fluid below the exsolution level and as a compressible, homogeneous two-phase mixture of liquid and gas bubbles above that level. The compressible behaviour is accounted for through a barometric state law.

The system of equations is solved using a finite element method with a fractional step approach; time is discretized through a finite difference scheme, whereas a Galerkin finite element scheme is used for the space discretization. The implemented algorithm is able to treat simultaneously compressible and incompressible flow and allows simulating the temporal evolution of quantities like pressure and velocity, eruption rate and position of the exsolution level. The model employs cylindrical coordinates with axisymmetrical geometry.

Regarding the mixture properties, the main assumptions are chemically homogeneous composition of magma, presence of water as the only volatile, and perfect behaviour of gas. Further assumptions are constant temperature, fixed geometry of the system and rigid and erosion-free domain walls.

Folch et al. (2001) developed a fluid-structure interaction model for eruptions from caldera collapse, to overcome the assumption of fixed system geometry. In this model, the flow and structure equations are alternately integrated in time by using separate solvers and accounting for fluid-structure mechanical interaction

by means of changes in the boundary conditions. The structure is treated as a rigid body that slides along the caldera vertical fractures.

Simakin and Botcharnikov (2001)

Simakin and Botcharnikov (2001) modeled the passive degassing of a 2D stratified magma chamber and the compositional convection driven by vesiculation. The magmatic mixture is treated as multi-phase non-homogeneous allowing crystal settling and gas bubble rise and escape through magma chamber roof. A small bubble content is assumed in order to consider a simplified set of equations describing convection with bubble formation and dissolution. Elastic deformation of solid rock bounding the chamber due to pressure changes, and viscoelastic behaviour of the aureole of heated rocks, are accounted for.

2.2 Modelling of rock deformation

Seismic waves originate from the forced motion of a portion of a deformable medium. As some of the elements of the medium are deformed, the disturbance progresses through the medium as a wave. In this process the resistance offered to deformation by the consistency of the medium, as well as the resistance to motion offered by inertia, must be overcome. As the disturbance propagates through the medium it carries along amounts of kinetic and potential energies. Energy can be transmitted over considerable distances by wave motions. The transmission of energy is possible because motion is passed on from one particle to the next, without sustained bulk motion of the entire medium. Mechanical waves are characterized by the transport of energy through motion of particles around an equilibrium position.

A model of seismic wave propagation and seismic motion should allow for anisotropy and heterogeneity of the medium (i.e., presence of fluids, material discontinuities and property gradients), realistic wave attenuation, complex free-surface topography, and resolve a broad frequency range. The majority of rock-dynamics models compute the energy propagation and rock deformation within solid materials by solving the equations of continuum mechanics (Malvern, 1969). The displacement is computed through the equation of motion (Newton's law):

$$\rho \frac{\partial^2 \mathbf{u}}{\partial t^2} = \mathbf{f} + (\lambda + 2\mu) \nabla (\nabla \cdot \mathbf{u}) - \mu \nabla \times (\nabla \times \mathbf{u}) \tag{2.5}$$

where λ and μ are the so-called Lamé coefficients describing the elastic properties of the medium and corresponding to the incompressibility and shear modulus respectively, ρ is density, $\mathbf{f}$ the source function and $\mathbf{u}$ the displacement vector. This equation, together with constitutive relationships linking stresses to displacement, fully describe the propagation of seismic wave. If linearity is assumed and if the medium is homogeneous and isotropic, the stress tensor σ is computed using the Hooke's law:

$$\sigma_{ij} = \lambda \delta_{ij} \varepsilon_{kk} + 2\mu \varepsilon_{ij} \tag{2.6}$$

where δ_{ij} is Kronecker delta, ε strain expressed through the following equation:

$$\varepsilon_{ij} = \frac{1}{2}\left(\frac{\partial u_j}{\partial x_i} + \frac{\partial u_i}{\partial x_j}\right) \tag{2.7}$$

Since the continuum theory assumes that matter fills the whole available volume, equations 2.5-2.7 cannot be used to model rock discontinuities at either macroscopic (such as fractures, cavities, rock pores) or microscopic (molecular and atomic structure of material) scale.

These limitations have been overcome by using the discrete lattice scheme, whose utilisation is becoming widespread thanks to recent advances in computational power. These models do not solve continuum equations directly, but try to replicate the underlying physics at a "microscopic scale" allowing to easily consider complex boundary conditions and heterogeneous materials (see section 3.2 for a more detailed description).

For homogeneous or flat-layered structures, the ground displacement and the seismic signal can be calculated through analytical methods, such as the reflectivity method (Muller, 1985) and the discrete wavenumber method (Bouchon, 1981; Chouet, 1982), or by using propagator matrices (Dunkin, 1965; Kennett and Kerry, 1979; Chouet, 1987). Some models include anelastic effects by using the dispersive complex velocities for P- and S-waves (O'Neill and Hill, 1979; Aki and Richardson, 1980). However, analytical methods do not provide solutions of the equation of motion (elastodynamic equation) for complex or sufficiently realistic models of the Earth's interior. Therefore, approximate numerical methods are usually adopted. The more common method used to solve the non-linear system of equations is the finite difference method. Secondarily, finite elements, hybrid finite difference-finite elements and spectral methods are employed. A

detailed description of the different numerical methods for simulating seismic wave propagation is reported in Moczo et al. (2007).

2.3 Modelling of magma-rock dynamics

Volcano seismology investigates the mechanism of seismic sources associated with the dynamical interaction between magmatic and/or hydrothermal fluids and their hosting rocks. A detailed study of the excitation mechanisms of long-period events and tremor requires a rigorous formulation of both macro- and microphysics in multiphase compressible fluids under a variety of dynamical conditions. However, because of the nonlinearity of fluid-dynamics equations and the complexity of fluid mixtures usually encountered in volcanoes, most of the efforts aimed at developing elastic radiation models have focused on the understanding of the resonance properties of fluid-filled systems under simplifying assumptions, in order to avoid the complexities of fluid behaviour.

Examples of these models are those of Chouet (1986), Julian (1994), Neuberg et al. (2000) and Nishimura and Chouet (2003).

Chouet (1986)

Using a stress-velocity finite difference method, Chouet (1986) modeled the resonance of a three-dimensional fluid-filled crack excited by the instantaneous failure of a small barrier on the crack surface. The method treats the elasto-dynamics equations in terms of velocity and stress, and the fluid-dynamics in terms of flow velocity and pressure. The fluid motion is computed solving the mass and momentum conservation equations; convective terms are neglected under the assumption that they are small compared to the time-derivatives of pressure and flow velocity. The fluid is assumed homogeneous and inviscid with constant density but finite compressibility. The crack walls are allowed to deform. The solid is modeled as an uniform elastic medium. The fluid and solid are coupled by applying the continuity of wall velocities and normal and shear stresses across the crack boundaries. Mass transfer between fluid and solid system is not allowed.

Julian (1994)

Julian (1994) modeled the tremor-generating process in terms of a flow-induced oscillation in channels transporting a magmatic fluid. In particular,

he proposed that tremor oscillations are excited by a nonlinear instability that arises when the fluid flows through a constricted channel with deformable walls. The model schematises the channel walls as masses connected by a spring and a dashpot; the spring represents the effect of the elastic stiffness of the surrounding rocks, while the dashpot represents the viscous attenuation of the wave propagation. The acoustic resonance effects in the channels are omitted. The magma flow model treats the masses and other parameters as lumped in order to solve ordinary equations instead of partial differential equations in the description of the fluid flow along the channel length. The mixture is assumed incompressible and Newtonian. The equations of motion are numerically integrated using a step-size extrapolation method.

Neuberg et al. (2000)

Neuberg et al. (2000) used a staggered-grid finite difference scheme to solve the 2D elastic equations of motion in order to model the tremor and low-frequency earthquake induced by a seismic source in a fluid-filled conduit. Rock properties (such as density and wave velocities) are assumed homogeneous and anelastic wave attenuation is neglected. The free-surface is modeled as a stress-free surface boundary condition. Magma is treated as an elastic solid with null rigidity, constant density, and acoustic velocity either constant or changing with depth because of the presence of gas bubbles.

Nishimura and Chouet (2003)

The model of Nishimura and Chouet (2003) used the finite difference method to compute the magma dynamics and the seismic radiation and crustal deformation associated with an eruption. The volcanic system consists of a cylindrical fluid-filled reservoir connected to the surface by a narrow cylindrical conduit with a lid capping its exit; the conduit inlet may be blocked by a plug. The system is pressurised by the addition of new magma and an eruption is triggered by the instantaneous removal of the lid or the plug. The magmatic mixture is modeled as an homogeneous, multiphase (liquid + gas), compressible and inviscid fluid and its volume changes are taken into account. The rock properties are assumed perfectly elastic and homogeneous, and the free surface is accounted for through the stress-free condition. The fluid and solid are dynamically coupled by applying the continuity of wall velocities and of normal stresses across the conduit and reservoir boundaries.

Chapter 3

Numerical codes

Two different numerical codes have been used to simulate the fluid-dynamics in magma and the associated elasto-dynamics induced in rocks. The numerical code for magma dynamics (named `GALES`; Longo et al. (2006)) has been implemented at Istituto Nazionale di Geofisica e Vulcanologia (INGV) in Pisa (Italy) in the last six years and it is under continous improvement; the code for rock deformation (named `ELM`; O'Brien and Bean (2004b)) has been developed at the Geophysical group of the University College Dublin (Ireland).

3.1 Numerical code for fluid dynamics (`GALES`)

The numerical code for the simulation of fluid dynamics describes the time-dependent 2D dynamics of a compressible-to-incompressible homogeneous multicomponent mixture made of liquid in equilibrium with an H_2O + CO_2 gas phase at the local conditions of pressure, temperature and composition.

The numerical algorithm used in the solution of equations of conservation is based on the finite element formulation by Hauke and Hughes (1998). This consists in a space-time discretization with Galerkin least-squares and discontinuity capturing terms that is third order in time and space. This method allows to study both compressible and incompressible flows (Shakib et al., 1991; Chalot and Hughes, 1994; Hauke and Hughes, 1998) and it is effective in the stabilisation of the numerical solution without introducing excessive overdiffusion. With respect to the original formulation, the numerical model has been extended to include a general formulation for multicomponent fluids (Longo et al., 2006), making it

particularly suitable for the investigation of processes involving chemical changes and phase transitions.

The governing equations are mass conservation of each component and momentum and energy conservation of the mixture as a whole:

$$(\rho y_k)_{,t} + (\rho u_i y_k)_{,i} = -J^k_{i,i} \quad \text{for } k = 1, \ldots, n \tag{3.1}$$

$$\left(\rho u_j\right)_{,t} + \left(\rho u_i u_j + p\delta_{ij}\right)_{,i} = \left(\tau_{ji}\right)_{,i} + \rho b_j \quad \text{for } j = 1, \ldots, d \tag{3.2}$$

$$(\rho e_t)_{,t} + (\rho u_i e_t + p u_i)_{,i} = \left(\tau_{ij} u_j - q_i - \sum_{k=1}^{n} J^k_i h_k\right)_{,i} + \rho \left(b_i u_i + r\right) \tag{3.3}$$

where ρ is mixture density, y_k mixture mass fraction of component k , t time, u_i velocity in i-th direction, J^k_i mass diffusion flux of component k in i-th direction, n number of components, p pressure, δ_{ij} Kronecker delta, τ_{ij} the ij component of viscous stress tensor, b_j body force vector per unit mass in j-th direction, d = 1,2 or 3 number of spatial dimensions, e_t specific total energy mixture, q_i diffusive heat flux in i-th direction, h_k specific enthalpy of component k and r heat source per unit mass. Indexes after an inferior comma represent variables with respect to which partial differentiation is computed; the summation convention on repeated indexes is applied throughout. The conservation equations (3.1)-(3.3), togheter with the gas-liquid equilibrium model and the constitutive equations for mixture properties, are discretized and solved for the primitive variables pressure, velocity, temperature, and concentration of components. Numerical solutions of these equations are obtained through the appositely developed finite element C++ code `GALES`, which makes use of `OFELI` (Touzani, 2004), Diffpack (Numerical Objects, 1997) and TRILINOS (Sandia National Laboratories, 2007) libraries. The numerical code was verified and validated with laboratory experiments, exact solutions and numerical results from literature. As the test cases show, the features of this method allow the solution of a large number of problems such as shock wave interaction with contact discontinuities, evolution of internal interface in incompressible or compressible flows, bubbly flows with evaporation or gas dissolution (see http://www.pi.ingv.it/ longo/gales/gales).

The physical model considers a single fluid compressible-incompressible multicomponent mixture at mechanical, thermal and chemical local equilibrium; the mixture is ideal, constituted of n components that may be either in the liquid or

gaseous state and instantaneous phase change is assumed. Gas bubbles are assumed to be undeformable. Solid phase is not considered as a separate phase but it is taken into account for computing the mixture properties. Chemical reactions resulting in component production or consumption are not allowed to occur.

The composition of the mixture is described by $n-1$ independent mass fractions of components (y_k) and by the partition coefficients of components in their phases, which depend on pressure and temperature (see Appendix A). Different components are miscible, that is, interdiffusion is allowed. The diffusive fluxes of mass of components (J_i^k) are expressed by the Curtiss and Hirschfelder law for multi-component fluids (A.18) (Hirschfelder et al., 1969; Bird et al., 1960). The stress tensor (τ_{ij}) (A.16) assumes Newtonian rheology. The energy flux (first term at the right-hand side of energy equation (eq. 3.3)) is due to viscous dissipation ($\tau_{ij}u_j$), heat conduction (q_i) expressed by Fourier's law (A.17), and interdiffusion of components carrying a specific enthalpy (h_k). The heat source per unit mass (r) includes the latent heat due to phase change. Mass diffusion due to pressure gradients, Soret and Dufour effects, and surface tension, are neglected.

The capability of dissolved water in affecting major liquid properties like density and viscosity is accounted for as explained below, while the effects of small amounts of dissolved CO_2 are neglected.

The equation of state for mixture density is based on the ideal solution assumption (Modell and Reid, 1983), which implies that mixture density is calculated as:

$$\frac{1}{\rho} = \sum_{k,\pi} \frac{y_k^\pi}{\rho_k^\pi} = \sum_k \frac{y_k}{\rho_k} \tag{3.4}$$

where subscripts k and superscripts π indicate mixture component and phase, respectively.

The density of the dense (liquid + crystals) phase (ρ^D) is computed correcting the liquid density (ρ^L) to consider the presence of crystals. The influence of crystals is taken into account by the equation:

$$\rho^D = (1-\alpha^C)\rho^L + \sum \alpha^{C_i}\rho^{C_i} \tag{3.5}$$

where $\alpha^C = \sum_i \alpha^{C_i}$ is total volume fraction of crystals, α^{C_i} and ρ^{C_i} are respectively volume fraction and density of i-th crystal species.

The liquid density is calculated using the Lange equation of state (Lange, 1994) that considers partial molar volume of oxides and their thermal expansivity;

the partial molar volume of water in the silicate liquid is calculated using the calibration from Burnham and Davis (1974).

Mixture viscosity (μ) is calculated under the assumption of Newtonian rheology, the viscosity μ is calculated with the standard rules of mixing (Reid et al., 1977) for one phase mixtures and with a semi-empirical relation (Ishii, 1977) for bubbly mixtures:

$$\mu = \exp\left(\sum_k x_k \ln \mu_k\right) \qquad \text{for one phase mixture} \tag{3.6}$$

$$\mu = \mu^c \left(1 - \frac{\alpha^d}{\alpha^{dm}}\right)^{-2.5\alpha^{dm}\frac{\mu^d+0.4\mu^c}{\mu^d+\mu^c}} \qquad \text{for bubbly mixture} \tag{3.7}$$

where μ^c and μ^d are viscosities of the continuous and dispersed phases, respectively, α^d is the volume fractions of the dispersed phase and $\alpha^{dm} = 0.75$ is the volume fractions of the dispersed phase at its maximum package.

The viscosity of the dense phase is obtained from the liquid viscosity (μ_L) using the extension by Marsh (1981) of the equation of Einstein-Roscoe to take into account the effect of crystals.

Since no models are available to take into account the compositional variation of magma, the liquid viscosity is computed using parameterizations that derive from experiments on natural melts (Hess and Dingwell, 1996; Giordano et al., 2000; Giordano and Dingwell, 2003; Romano et al., 2003) and appropriate for magma with specific compositions (e.g. Etna Basalt, Agna-Monte Spina trachyte, Campanian Ignimbrite, phonolite of Vesuvius 1631 eruption, etc . . .).

3.2 Numerical code for wave propagation (`ELM`)

The numerical code for rock deformation describes the static and dynamic deformation in a 2D or 3D elastic medium using an elastic lattice method (Ladd and Kinney, 1997). The discrete particle method do not solves the continuum equations directly (i.e. the wave equation) but it tries to replicate the underlying physics at a "microscopic scale" employing discrete micro-mechanical interaction rules between the material particles. This scheme represents the elastic solid by a series of particles arranged on a regular lattice and interconnected by springs

(fig. 3.1). The interconnected particles represent block of intact rock interacting through local radial and shear forces. The force F_{ij} on an individual node i from

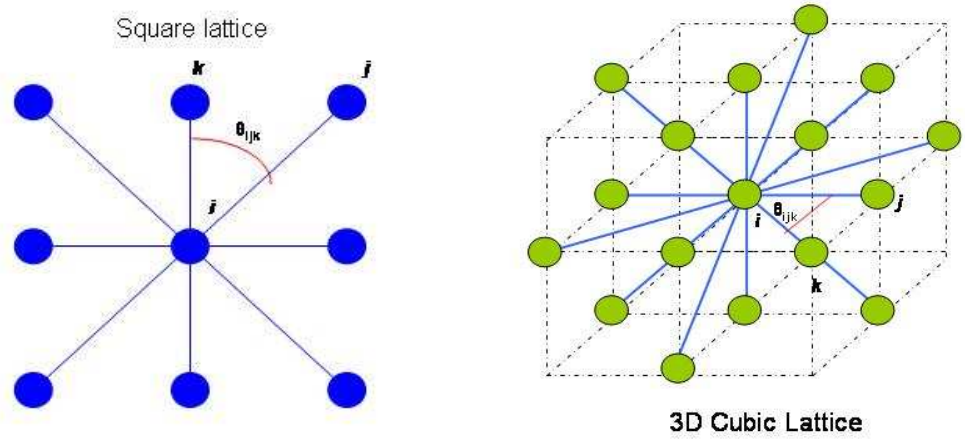

(a) (b)

Figure 3.1: Representation of the 2D (a) and 3D (b) elastic lattice; nodes are connected by springs that allow each node interacting with its eight neighbours.

node j is given by

$$\mathbf{F}_{ij} = -Kg_{ij}\left[\left(\mathbf{u}_i - \mathbf{u}_j\right)\cdot \mathbf{x}_{ij}\right] + \frac{c}{|\mathbf{x}_{ij}|^2}\left(\mathbf{u}_i - \mathbf{u}_j\right) \tag{3.8}$$

where K is the elastic spring constant, $\mathbf{u}_i$ the displacement at node i, x_{ij} the vector connecting nodes $\mathbf{x}_i$ and $\mathbf{x}_j$ in the undistorted lattice and c the bond-bending constant. The constants g_{ij} remove the lattice anisotropy by weighting each of the lattice links (Monette and Anderson (1994),O'Brien and Bean (2004a)). The first term in the right-hand side of equation (3.8) is the central force term described by the Hooke's law, while the second term represents the bond-bending force. Without the inclusion of this bond-bending term the Poisson's ratio in the model is restricted to 0.25, (see equations 3.9 and 3.9).

The Lamé constants are expressed in terms of the spring and bond-bending constants.

$$\begin{aligned} \lambda &= K - \frac{c}{a^2} \\ \mu &= K + \frac{c}{a^2} \end{aligned} \qquad \textit{2D Square lattice} \tag{3.9a}$$

$$\lambda = \frac{K}{a} - \frac{2c}{a^3}$$
$$\mu = \frac{K}{a} + \frac{2c}{a^3} \qquad \textit{3D Cubic lattice} \tag{3.9b}$$

where a is the spacing between off diagonal nodes. Thus, the elastic lattice method behaves as an elastic continuum where the elastic wave speeds are easily calculated from the Lamé constants:

$$\mathrm{v}_p^2 = \frac{1}{\rho}\left(3K + \frac{c}{a^2}\right)$$
$$\mathrm{v}_s^2 = \frac{1}{\rho}\left(K + \frac{c}{a^2}\right) \qquad \textit{2D Square lattice} \tag{3.10a}$$

$$\mathrm{v}_p^2 = \frac{1}{\rho}\left(\frac{3K}{a} + \frac{2c}{a^3}\right)$$
$$\mathrm{v}_s^2 = \frac{1}{\rho}\left(\frac{K}{a} + \frac{2c}{a^3}\right) \qquad \textit{3D Cubic lattice} \tag{3.10b}$$

The force acting on each spring is calculated at each time step and the new position of the lattice nodes and node velocities are updated using the velocity-Verlet numerical integration scheme (Allen and Tildesley (1987)). This scheme is a second-order in time and fourth order in space finite difference solution to the elastic wave propagation, including free surface boundary conditions.

The elastic energy E_i for node i on a cubic lattice is expressed as (Arbabi and Sahimi, 1988):

$$E_i = \frac{K}{2}\sum_{j=1}^{N}\left(\left[\mathbf{u}_i - \mathbf{u}_j\right]\cdot\mathbf{n}_{ij}\right)^2 + \frac{c}{2}\sum_{jik}\left(cos\theta_{jik} - \frac{1}{\sqrt{2}}\right)^2 \tag{3.11}$$

where θ_{jik} is the angle between particles jik with node i as the apex of the angle, N is the number of nearest neighbours and n_{ij} is $x_{ij}/|x_{ij}|$. The energy density Φ is the total energy stored in each spring divided by the total volume and can be written as

$$\Phi^{square\,lattice} = \frac{1}{2a^2}\sum_{ij=1}^{4} K\left(\frac{\mathbf{u}_{ij}\cdot\mathbf{x}_{ij}}{|\mathbf{x}_{ij}|^2}\right)^2 + \frac{1}{4a^2}\sum_{ij=1}^{8} c\left(\frac{\mathbf{u}_{ij}\otimes\mathbf{x}_{ij}}{|\mathbf{x}_{ij}|^2} - \frac{\mathbf{u}_{ik}\otimes\mathbf{x}_{ik}}{|\mathbf{x}_{ik}|^2}\right)^2 \tag{3.12a}$$

$$\Phi^{cubic\,lattice} = \frac{1}{2a^3}\sum_{ij=1}^{8} K\left(\frac{\mathbf{u}_{ij}\cdot\mathbf{x}_{ij}}{|\mathbf{x}_{ij}|^2}\right)^2 + \frac{1}{4a^3}\sum_{ij=1}^{1} 6c\left(\frac{\mathbf{u}_{ij}\otimes\mathbf{x}_{ij}}{|\mathbf{x}_{ij}|^2} - \frac{\mathbf{u}_{ik}\otimes\mathbf{x}_{ik}}{|\mathbf{x}_{ik}|^2}\right)^2 \tag{3.12b}$$

where $\mathbf{u}_{ij}$ is the displacement vector $\left(\mathbf{u}_i - \mathbf{u}_j\right)$.

Since the elastic lattice method solely rely on particle-particle interactions, complex boundary conditions can be accounted for. This model allows to consider free surface with complex and strong topography and subsurface heterogeneity as fractures or pore fluids. A vacuum free-surface boundary condition is implicit in the method and topography is introduced by removing any particle above the required free surface. The material heterogeneities can be incorporated into the model by changing the elastic spring constants on each spring.

The model is able to compute the effects of attenuation in the Earth's crust (O'Brien, 2008). However, in the present work these effects have been not taken into account in order to reduce the complexity of the result interpretation since at the moment we are just interested in the first order effects of the simulated dynamics.

The rock properties are defined specifying density, P-wave and S-wave velocity for each grid node. The grid spacing and time step must be chosen to satisfy the following criteria:

$$\begin{aligned} \mathrm{d}t &< \frac{\mathrm{d}x}{2 \cdot v_{max}} \\ \mathrm{d}x &< \frac{\lambda_{min}}{10} \end{aligned} \tag{3.13}$$

where v_{max} is the maximum compressional wave velocity and λ_{min} the minimum wave length. The first condition ensures numerical stability while the second one avoids numerical dispersion.

3.3 Coupling between GALES and ELM

The coupling between the two codes is accomplished with a "one way" procedure. This means that the fluid dynamics simulated by GALES triggers and drives the energy propagation in rocks simulated by ELM but not vice versa. This approximation is a significant simplification, because in reality the energy waves would affect also fluids movement, influencing and modifying the flow dynamics; consequently, the changes in dynamics would cause a rocks deformation different from that due to the undisturbed fluid movement. Hence, the seismic wave field generated can be highly scattered and attenuated by the presence of heterogeneous fluid reservoirs through complex interactions at the solid-liquid boundaries, including

diffractions, reflections, refracted waves, wave conversion and interface waves. A fully two-way coupled fluid-rock model is presently under developement at the INGV in Pisa. In details, the coupling has been achieved considering all nodes of the fluid-dynamics grid located along the system walls as point source in the elasto-dynamics simulations. The time-space distribution of stresses computed by `GALES` in these nodes have been used as boundary conditions for the simulation of rock elasto-dynamics. Before being imposed as boundary conditions, these stresses have been filtered to avoid the numerical noise and re-sampled to the time step adopted in the `ELM` simulation. While the frequency of integration in time for the fluid calculation is 100 Hz, the filter used is a low pass filter with cut frequency of 10 Hz. Since the fluid simulations have been performed only on half a magmatic domain, the source points have been reconstructed considering the symmetry with respect to the chamber middle plan to obtain the complete source.

Chapter 4

Saturation model

The present research includes the investigation of the mixing dynamics between CO_2 -rich magmas in a refilled magma chamber as one of its major goals. Mixing between magmas with different composition and volatile contents involves changes in composition and physico-chemical properties of the resulting magmatic liquid. It is worth noting that the composition of the melt in which volatile components are dissolved plays a crucial role in the definition of the shape and position of the volatile saturation surface. Furthermore,the coexistence of water and carbon dioxide enhances the complexity of saturation surface because of the mutual influence of a species on the solubility of the other.

At the beginning of my PhD, the saturation model implemented in `GALES` assumed that volatiles behave as an Henrian gas; it did not take into account the dependence of the gas-liquid equilibrium conditions on the local magma composition and it considered only one volatile species at a time. For these reasons, the saturation model was not suitable to compute the volatile solubility in the studied system. The choice and the implementation in the numerical code of a new saturation model able to follow the effects of compositional difference and compositional changes accompanying the evolution and dynamics of natural magmas and to take into account the contemporaneous presence of water and carbon dioxide in the system was then required.

4.1 Thermodynamic model

The adopted saturation model (Papale et al., 2006) computes the volatile saturation surface in H_2O-CO_2-silicate melt systems by applying thermodynamic equilibrium between gaseous and liquid volatile components. The model parameters are calibrated on > 1000 existing saturation data in the C-O-H-silicate liquid system over a broad spectrum of silicate melt compositions.

The model is based on the computation of the Gibbs free energy of mixing and then, it is able to provide component activities through the Gibbs-Duhem rule. It is fully non-ideal, assuming only that the excess Gibbs free energy of the silicate mixture can be represented by an expansion of first-order symmetric interaction terms. The thermodynamic properties of the liquid mixture are modeled through binary interaction coefficients expressing the attractive-repulsive behaviour of each pair of component molecules in magma. No a-priori assumption is made on the P-T dependence of the volatile-oxide interaction terms, meaning that no assumption is made on the partial molar volume and enthalpy of the dissolved volatiles. Deriving from calibration and statistical evaluation, the interaction coefficients involving water are taken as constant, while those involving carbon dioxide are pressure-dependent:

$$\begin{aligned} w_{\mathrm{H_2Oi}} &= w^{(0)}_{\mathrm{H_2Oi}} \\ w_{\mathrm{CO_2i}} &= w^{(0)}_{\mathrm{CO_2i}} + w^{(1)}_{\mathrm{CO_2i}} \ln\frac{P}{P^0} \end{aligned} \tag{4.1}$$

where $P^0 = 0.1$ MPa is the reference pressure. The mixed volatile interaction term ($w_{\mathrm{H_2OCO_2}}$) is neglected since its inclusion does not result in appreciable improvement of model predictions.

The basic mechanical, thermal and chemical equilibrium equations are the followings:

$$\begin{aligned} &P^G = P^L = P \\ &T^G = T^L = T \\ &f^G_{H_2O} = f^L_{H_2O} \Longrightarrow \phi_{H_2O} y_{H_2O} P = \gamma_{H_2O} x_{H_2O} f^{oL}_{H_2O} \\ &f^G_{CO_2} = f^L_{CO_2} \Longrightarrow \phi_{CO_2} y_{CO_2} P = \gamma_{CO_2} x_{CO_2} f^{oL}_{CO_2} \end{aligned} \tag{4.2}$$

where f is the fugacity, ϕ the fugacity coefficient in the gas phase, γ the activity coefficient in the liquid phase, y and x the mole fractions in gas and liquid phase, respectively, the superscripts G and L refer to the gas and liquid phase,

respectively and the superscript oL refers to the reference state in the liquid phase. These equations are closed by the mass balance equations:

$$\begin{aligned} & y_{H_2O} + y_{CO_2} = 1 \\ & \frac{x^T_{H_2O} - y_{H_2O}}{y_{H_2O} - x_{H_2O}} = \frac{x^T_{CO_2} - y_{CO_2}}{y_{CO_2} - x_{CO_2}} \end{aligned} \tag{4.3}$$

where the superscript T refers to mole fractions with respect to the gas-liquid mixture.

The fugacity coefficient in the gas phase is calculated by means of the equation of state by Kerrick and Jacobs (1981) for H_2O , CO_2 and H_2O - CO_2 mixtures while the reference state for volatiles dissolved in the liquid phase is obtained by standard thermodynamic relationships as

$$\ln f_i^{oL}(P,T) = \ln f_i^{oL}(P^o,T^o) + \int_{P^o}^{P} \frac{v_i^o}{RT} \mathrm{d}P - \int_{T^o}^{T} \frac{1}{RT^2} \int_{P^o}^{P} \left[v_i^o - T\left(\frac{\partial v_i^o}{\partial T}\right)_P \right] \mathrm{d}P \mathrm{d}T \tag{4.4}$$

where v is molar volume, R is the universal gas constant and the superscript o refers to a standard state defined at P^o and T^o. The activity coefficient of dissolved volatiles is calculated from the excess Gibbs free energy that is computed as function of mole fraction of components and interaction coefficients between pairs of component; the interaction coefficient not involving volatiles are taken from Ghiorso et al. (1983). The resulting expressions for the activity coefficients of dissolved H_2O and CO_2 are the following:

$$\begin{aligned} RT\ln\gamma_{H_2O} &= (1 - x_{H_2O})\, x_{CO_2} w_{H_2OCO_2} \\ &+ (1 - x_{H_2O})(1 - x_{H_2O} - x_{CO_2}) \sum_{i \neq CO_2 = 1}^{n} x'_i w^{(0)}_{H_2Oi} - x_{CO_2} \\ &\times (1 - x_{H_2O} - x_{CO_2}) \left[\sum_{i \neq H_2O = 1}^{n} x'_i w^{(0)}_{CO_2 i} + \ln\frac{P}{P^0} \sum_{i \neq H_2O = 1}^{n} x'_i w^{(1)}_{CO_2 i} \right] \\ &- (1 - x_{H_2O} - x_{CO_2})^2 \sum_{i \neq H_2O, CO_2 = 1}^{n} \sum_{j \neq H_2O, CO_2 = i+1}^{n} x'_i x'_j w_{ij} \end{aligned} \tag{4.5}$$

$$\begin{aligned} RT\ln\gamma_{CO_2} &= (1 - x_{CO_2})\, x_{H_2O} w_{H_2OCO_2} \\ &- x_{H_2O}(1 - x_{H_2O} - x_{CO_2}) \sum_{i \neq CO_2 = 1}^{n} x'_i w^{(0)}_{H_2Oi} + (1 - x_{CO_2}) \\ &\times (1 - x_{H_2O} - x_{CO_2}) \left[\sum_{i \neq H_2O = 1}^{n} x'_i w^{(0)}_{CO_2 i} + \ln\frac{P}{P^0} \sum_{i \neq H_2O = 1}^{n} x'_i w^{(1)}_{CO_2 i} \right] \\ &- (1 - x_{H_2O} - x_{CO_2})^2 \sum_{i \neq H_2O, CO_2 = 1}^{n} \sum_{j \neq H_2O, CO_2 = i+1}^{n} x'_i x'_j w_{ij} \end{aligned} \tag{4.6}$$

where x' is the concentration of non-volatile components in the volatile-free liquid:

$$x'_{i \neq H_2O, CO_2} = \frac{x_i}{1 - x_{H_2O} - x_{CO_2}} \tag{4.7}$$

4.2 Implementation

The saturation model has been implemented in a new C++ library able to deal with `GALES` but also to work independently. The implementation is based on a previous FORTRAN code developed at the Istituto Nazionale di Geofisica e Vulcanologia in Pisa (Italy).

The library consists of a main class where the thermodynamic model has been implemented and a class with methods required to solve the numerical system of equations. The non-linear system of the saturation model is solved using the secant method or the globally convergent Newton method depending on the presence of one or both volatiles. In addition to these methods, accessory methods for the usage of the Newton algorithm have been implemented (e.g. LU decomposition, forward approximation of jacobian). All the implementations are derived from Numerical Recipes in C++ (Press et al., 1992).

Furthermore, on the basis of the design pattern "strategy" (Gamma et al., 1994), a class and a few derived classes have been implemented to allow an optimised usage of the mathematical methods to solve any equation or system of equations. The pattern "strategy" defines a family of algorithms, encapsulates each one and makes them interchangeable. Its structure, indeed, lets the algorithm vary independently from clients that use it; in particular, the methods in which equations are defined have no conditions on structure or interface to be used with these mathematical methods.

Part II

Preliminary study on magma chamber refilling dynamics

Chapter 5

Introduction

The simulations related to the Campi Flegrei system have been preceded by the investigation of the capability of CO_2 to induce buoyant-driven convection in a refilled magma chamber. The presence of CO_2 in a magma, in fact, is expected to produce significant buoyancy forces, since even small amounts of this largely insoluble component produce a decrease of the H_2O and liquid saturation content, increasing the gas volume in magma (Holloway and Blanck, 1994) (fig. 5.1). The consequent increase of the gas volume may produce the density decrease necessary for triggering efficient buoyancy of the refilling magma. Due to the much lower solubility of carbon dioxide with respect to water, open system degassing invariably results in a decrease of the total CO_2/H_2O ratio in the multiphase magma (Papale, 2005). As a consequence, deeper magmas which have undergone lower degrees of open system degassing can carry significant amounts of CO_2 with respect to magmas which have resided at shallow chamber levels.

The efficiency of CO_2 in inducing buoyant-driven convection has been investigated by numerically simulating the 2D transient dynamics inside magma chambers due to the entrance from below of new magma. By parameterizing the CO_2 content in the feeding magma, CO_2 efficiency in producing buoyant plumes and large scale convection has been evaluated. Moreover, the effects of different magma viscosities and chamber depths have been studied.

It is useful to stress once again that tis first set of simulations does not represent any expected real situation at Campi Flegrei . Rather, its scope is that of studying the capability of CO_2 to induce convection and mixing within a chamber hosting magma with composition similar to that commonly erupted at Campi Flegrei .

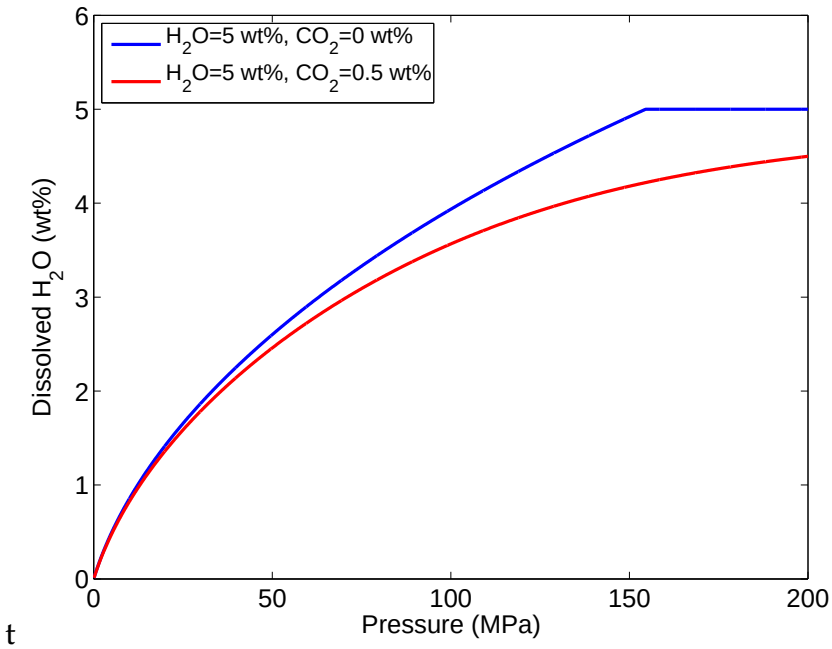

Figure 5.1: Weight fraction of dissolved water in function of pressure for a trachytic magma with different content of total water and carbon dioxide. The phase distribution has been computed using the multi-component non-ideal model from Papale et al. (2006) implemented in GALES.

Chapter 6

Numerical simulations

6.1 Initial and boundary conditions

The simulated system consists of an elliptic chamber 4 km wide and 2 km high, with its top at 3 or 4 km depth (fig. 6.1), hosting trachytic magma with composition corresponding to the composition of the B1 eruptive phase of the Agnano-Monte Spina eruption (see table 6.1, Romano et al. (2003)). The magma initially present in the chamber contains 5 wt% total H_2O, distributed among the liquid and gas phases according to the local magmastatic pressure, and no carbon dioxide. The viscosity is described as a function of dissolved water and temperatures through a VTF-like parameterization recently developed by Misiti et al. (2006). Although crystals can be accounted for in the present homogeneous formulation, they have not been considered here for simplicity. However, in order to investigate a large spectrum of possible conditions embracing high crystal concentrations, viscosities calculated as described above have been arbitrarily increased by up to three orders of magnitude in some simulations. Resident and refilling magmas have same temperature and composition (apart from CO_2) to avoid thermal exchange (therefore, no use of eq. 3.3), and consider relatively simple conditions with only gas-liquid reaction. Although real cases are expected to involve more complex chemical reactions including the formation of solid components, the present simplification allows focusing on the role of CO_2 in inducing buoyant plume rise and convection.

At t = 0 s new magma having the same temperature, composition, and total H_2O content of the resident magma, but different total CO_2 content, enters the

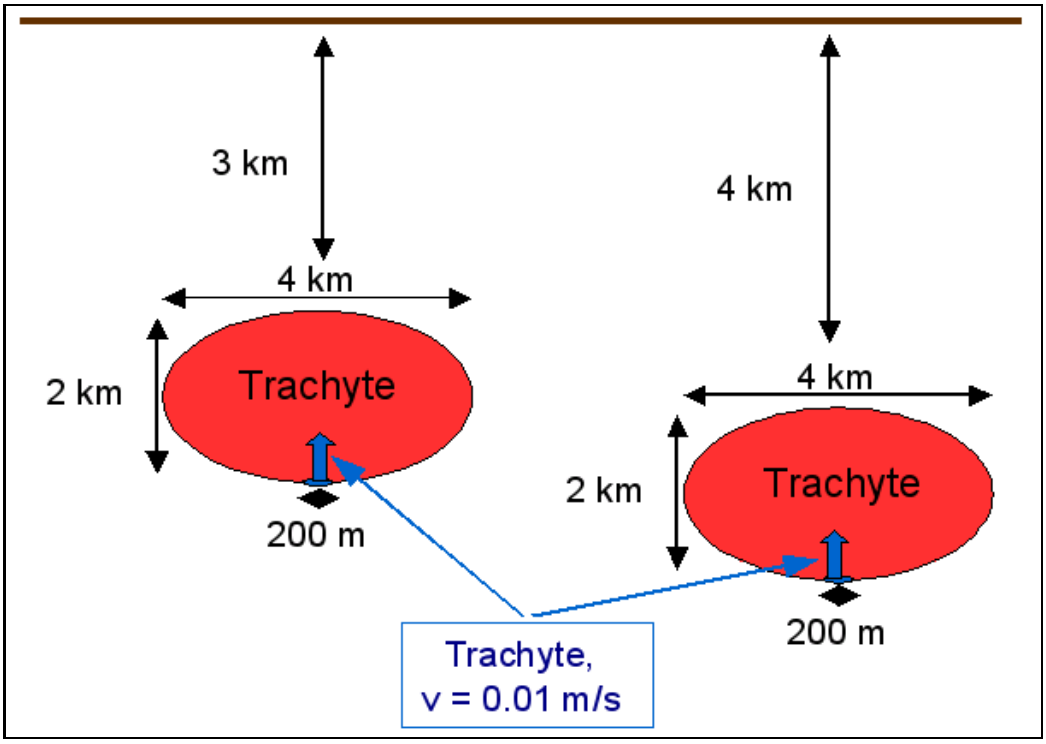

Figure 6.1: Scheme of the simulated system

SiO_2	TiO_2	Al_2O_3	Fe_2O_3	FeO	MnO	MgO	CaO	Na_2O	K_2O
61.26	0.38	18.38	1.17	2.33	0.14	0.74	2.97	4.58	8.04

Table 6.1: Composition (wt %) of trachyte in the eruptive phase B1 of the Agnano-Monte Spina eruption (from Romano et al. (2003))

chamber from a bottom centered inlet 200 m wide (fig. 6.1), at the constant velocity of 1 cm/s. Three cases are considered: (A) the refilling magma has a zero CO_2 content as the resident one; (B) refilling magma has a 0.5 wt% total CO_2 content; (C) the refilling magma has a large 3.5 wt% total CO_2 content. Comparison between the numerical results pertaining to the three cases above allows therefore an evaluation of the role of CO_2 in inducing buoyancy, convection and mixing in a magma chamber. In a fourth reported simulation (case D) the same conditions as in case C are employed, but with lower magma viscosity and lower chamber depth (therefore lower chamber pressure). It is shown that such changes concur to produce more efficient dynamics of plume rise and magma convection, thus representing an end-member in the range of the simulated conditions. The parameters used in the simulations are summarized in table 6.2.

	Resident/ Refilling	Total H_2O[a] (wt%)	Total CO_2 (wt%)	Depth[b] (km)	Viscosity[c]	Inlet vel (m/s)
Case A	resident	5	0	4	10^3	
	refilling	5	0		10^3	0.01
Case B	resident	5	0	4	10^3	
	refilling	4.97	0.5		10^3	0.01
Case C	resident	5	0	4	10^3	
	refilling	4.82	3.5		10^3	0.01
Case D	resident	5	0	3	1	
	refilling	4.82	3.5		1	0.01

[a] Progressive decrease of H_2O content in case B-D with respect to case A reflects dilution due to the presence of CO_2.

[b] Depth of magma chamber top.

[c] Factor multiplying viscosity as calculated from Misiti et al. (2006).

Table 6.2: Parameters for the performed simulations. Resident and refilling magma are trachyte with 1220 K of temperature. Different total H_2O contents in the refilling magma reflect dilution due to the presence of CO_2.

The numerical simulations are executed on a 2D Cartesian system of coordinates, assuming translational symmetry along the third direction. The computational domain represents one half of the chamber, under the assumption of symmetry with respect to its vertical median plane. The discretization grid is non-uniform, being progressively denser when approaching the symmetry plane and the inlet area. A total of 1,500 nodes from 5 to 140 m apart constitutes the computational grid. Note that the present grid resolution implies that mixing processes described here refer to a macroscopic scale, with no reference to processes occurring at the molecular scale where chemical mixing actually occurs.

The time step is also non-uniform, starting with 10^{-4} s and progressively increasing to 10^{-1} s according to local residuals of the solution and speed of convergence.

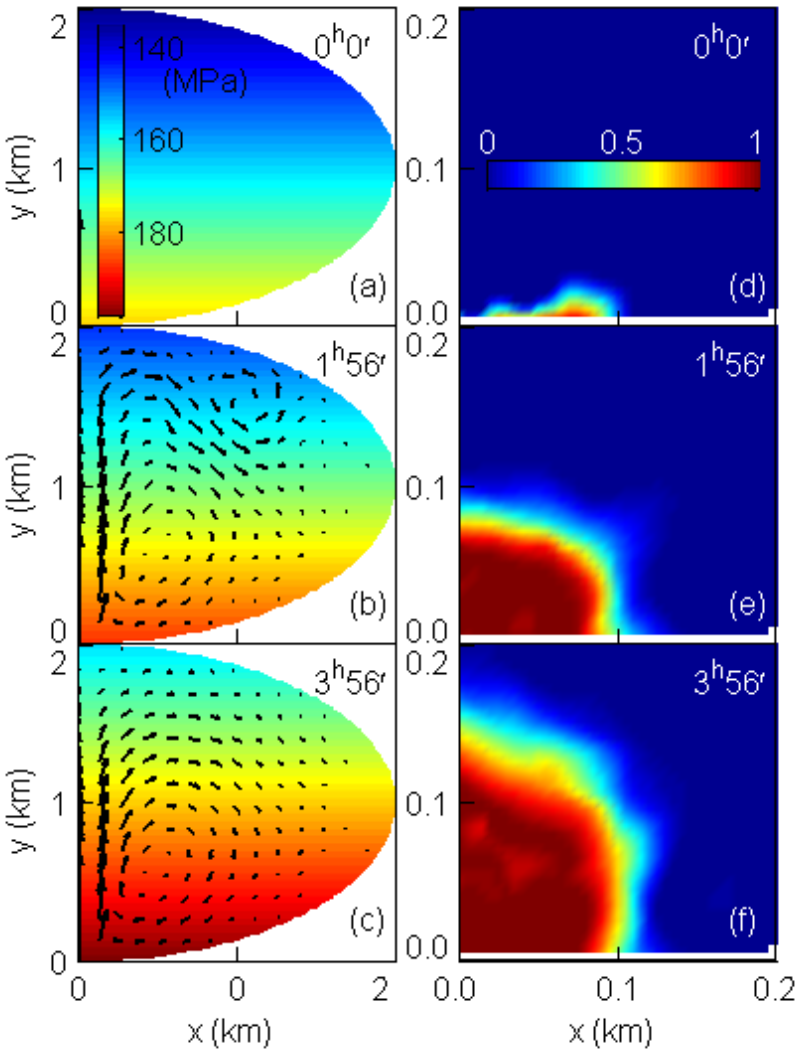

Figure 6.2: a-c: distribution of pressure (colours) and velocity field (arrows); d-f: distribution of mass fraction of resident and refilling magma. All panels refer to the case with no CO_2 in the refilling magma (case A) at three times after the beginning of magma injection

6.2 Results

Results for case A with refilling magma equal to the resident one (no CO_2 in the system), are shown in figure 6.2. The different panels show the evolution of pressure and velocity field (a-c), and the distribution of resident and refilling magmas (d-f) at different times up to nearly 4 hours after the beginning of new

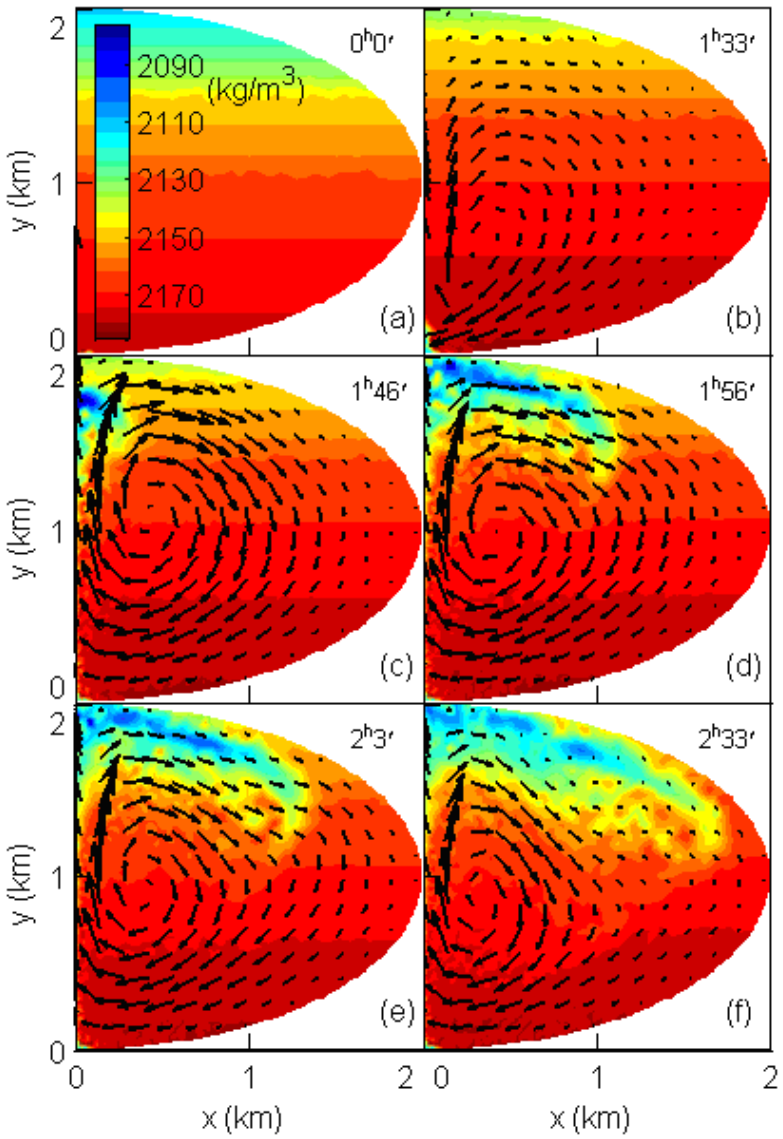

Figure 6.3: Distribution of density (colours) and velocity field (arrows) for case C (0.5 wt% CO_2 in the refilling magma) at six times after the beginning of magma injection

magma entrance into the chamber. In this case no buoyancy acts on the refilling magma, since its characteristics and properties are the same as those of the surrounding magma. After about 4 hours a bulge of new magma representing 3.7% of the total mass in the chamber has accumulated above the chamber inlet, reaching the height of about 150 m.

Slow convective dynamics inside the chamber are induced by the formation of

the bulge in fig. 6.2 d-f, with maximum velocities of the order of the assumed inlet velocity (1 cm/s). However, the magmatic pressure (fig. 6.2 a-c), and therefore the distribution of the gas volume fraction, changes at the scale of the whole chamber, reflecting the increase of the mass hosted within it. After about 4 hours the pressure has grown nearly homogeneously in the chamber by about 20 MPa, an amount larger than the tensile strength of most natural rocks (Chau and Wong, 1996; Roche and Druitt, 2001; Zhang, 2002) and likely to produce wall rock fracturing and dyke injection. Meanwhile, the gas volume, which was initially about 3% close to the chamber top and zero at its bottom, has become zero everywhere.

Figure 6.3 shows the case where the refilling magma carries 0.5 wt% total CO_2. The pressure corresponding to chamber bottom is such that the resident magma is initially undersaturated, with 5 wt% dissolved H_2O . This content decreases to 4.4 wt% in the refilling magma, with the addition of 200 ppm dissolved CO_2. Accordingly, the gas volume at chamber bottom is zero in the resident magma, and 5.7% in the refilling magma. The associated density difference between the resident (2180 kg/m^3) and refilling (2100 kg/m^3) magmas induces buoyancy of the latter. After about 1h30' a buoyant plume starts rising above the chamber inlet. At this time the entrance of new magma has produced a pressure increase in the chamber of about 6 MPa, reducing the gas volume at the chamber top from 3.3% to 2.2%. Once formed, the plume rapidly accelerates, since its rise is accompanied by pressure decrease, further volatile exsolution and gas expansion, decrease of density and finally enhanced buoyancy. In the case of fig. 6.3 the plume takes only about 15' to reach the chamber top, then it spreads laterally. This induces the formation of a vortex centered at about half chamber height, 3-400 m horizontally displaced from the chamber axis. After about 2h30' the magmatic pressure inside the chamber has grown by about 9.3 MPa, and the mass of new magma represents 2.3% of total mass. Nonetheless, the injection of CO_2 -rich magma has resulted in a net increase of the gas volume and decrease of bulk density at the chamber top.

Figure 6.4 shows case C in which the refilling magma carries 3.5 wt% total CO_2. The amounts of dissolved H_2O and CO_2 in the refilling magma at time zero are in this case 3.4 wt% and 330 ppm, respectively; the gas volume is as large as nearly 19%, and the bulk density is 250 kg/m^3 less than that of the surrounding resident magma. The larger density contrast of case C with respect to case B in fig.

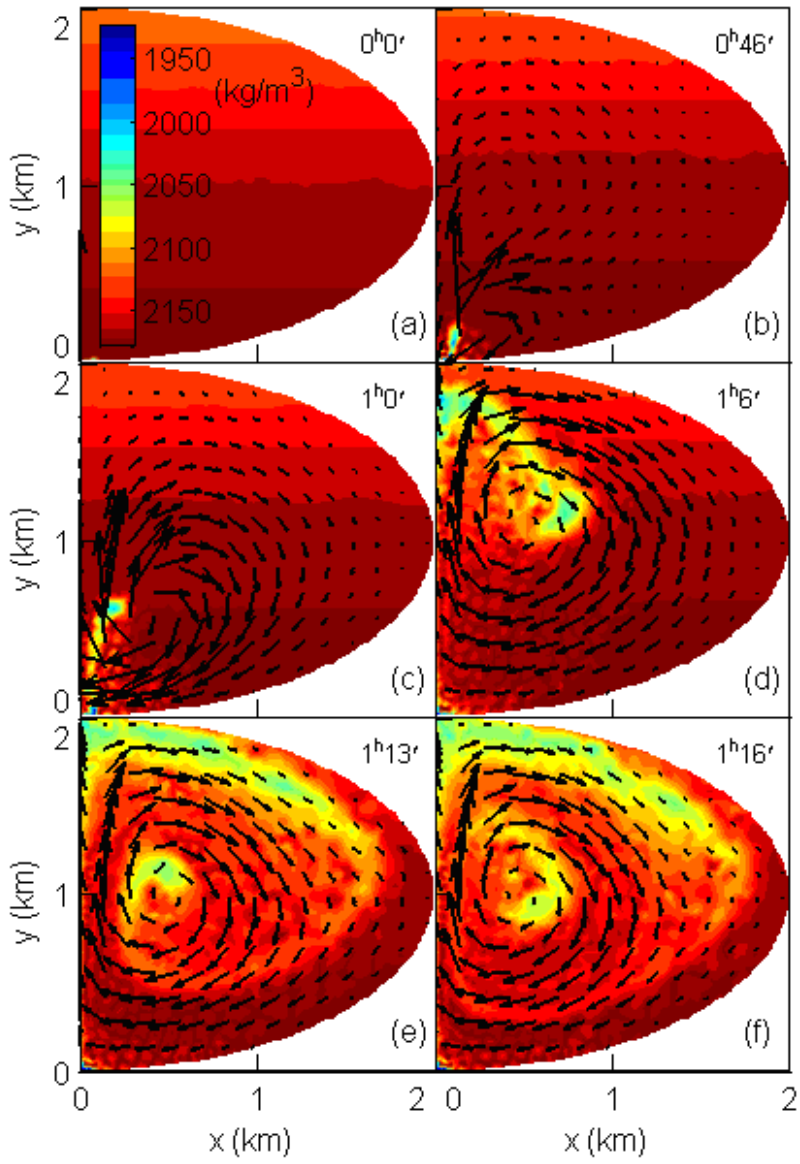

Figure 6.4: Distribution of density (colours) and velocity field (arrows) for case C (3.5 wt% CO_2 in the refilling magma) at six times after the beginning of magma injection

6.3 induces more efficient buoyancy, so that a rising plume starts forming after only about 45′. The plume in this case is initially displaced from the chamber axis of about 100 m, and it soon starts forming a vortex due to its large ascent velocity. After about 1h the vortex is centered at about 500 m above the chamber bottom, 3-400 m from the chamber axis, and it moves up as long as the plume continues to

rise. The generation of the vortex contributes to keep the rising plume close to the chamber axis. The plume reaches the chamber top after 1h5′ from the beginning of magma injection, implying an average ascent velocity during plume rise of about 1.7 m/s. The progressive displacement of the vortex towards the chamber top and the rapid acceleration of the rising magma cause the detachment of a CO_2-rich region which remains trapped within the vortex, being re-circulated at about half chamber height around the vortex center. Additional CO_2-rich magma rising with the buoyant plume is instead mostly transported towards the chamber top, afterwards it moves laterally forming a large vortex at the scale of the whole magma chamber. After 1h16′ the pressure and total mass in the chamber have grown by about 5 MPa and 0.12%, respectively.

Cases A, B and C reported in figures 6.2-6.4 involve high-viscosity magma (corresponding to that of the trachyte in Misiti et al. (2006) increased by three orders of magnitude) and chamber top at 4 km depth. In fig. 6.5 the same conditions as in case C (large CO_2 content of the refilling magma) are considered, but in this case the viscosity is that from Misiti et al. (2006), and the chamber top is at 3 km depth. The combination of lower pressure that enhances volatile exsolution and lower viscosity results in an increased efficiency of buoyancy forces, producing much more rapid dynamics inside the chamber. In this case, only after 3′40″ from the beginning of new magma injection a buoyant plume has reached the height of about 250 m above the chamber bottom (fig. 6.5b). The value of Re along the rising plume (based on local plume width and average properties and velocity) is of order $10^2 - 10^3$, compared with values ≤ 1 in cases B and C. Such a relatively high Re (still in the range of dominantly laminar motion (Bergantz, 2000)) rapidly induces the formation of a well developed vortex only a few hundred metres above the chamber inlet (fig. 6.5c). This vortex results in turn in more efficient mixing of the new magma with the deep magma in the chamber, with respect to cases B and C above, and develops instabilities which fragment the plume into separated batches of rising magma. After 6′40″ a main plume reaches the top of the chamber (fig. 6.5d). At this time two vortexes are visible. The largest one is associated with the main plume and is centered at about 1.25 km height, 300 m from the chamber axis. The second vortex is centered at about 650 m from the bottom, 500 m from the chamber axis, and partly re-circulates magma which descends from the chamber top. The bulk density in the plume top

resulting from the injection of volatile-rich light magma and associated increase of chamber pressure is about 1650 kg/m^3, about 7% less than the initial density at the same level. After 8'20" the large vortex has moved away from the chamber axis, being centered at more than 1 km from it (fig. 6.5e). The second vortex has been adsorbed into the main rising plume close to the chamber axis. The magma is re-circulated from the vortex into the rising plume, then again in the vortex, and magma circulation involves the whole chamber. After 11'40" the total mass in the chamber has grown only by about 0.02%. The main vortex has moved down along the chamber border and a number of smaller vortexes have formed around it, producing complex patterns of magma flow and re-circulation (fig. 6.5f).

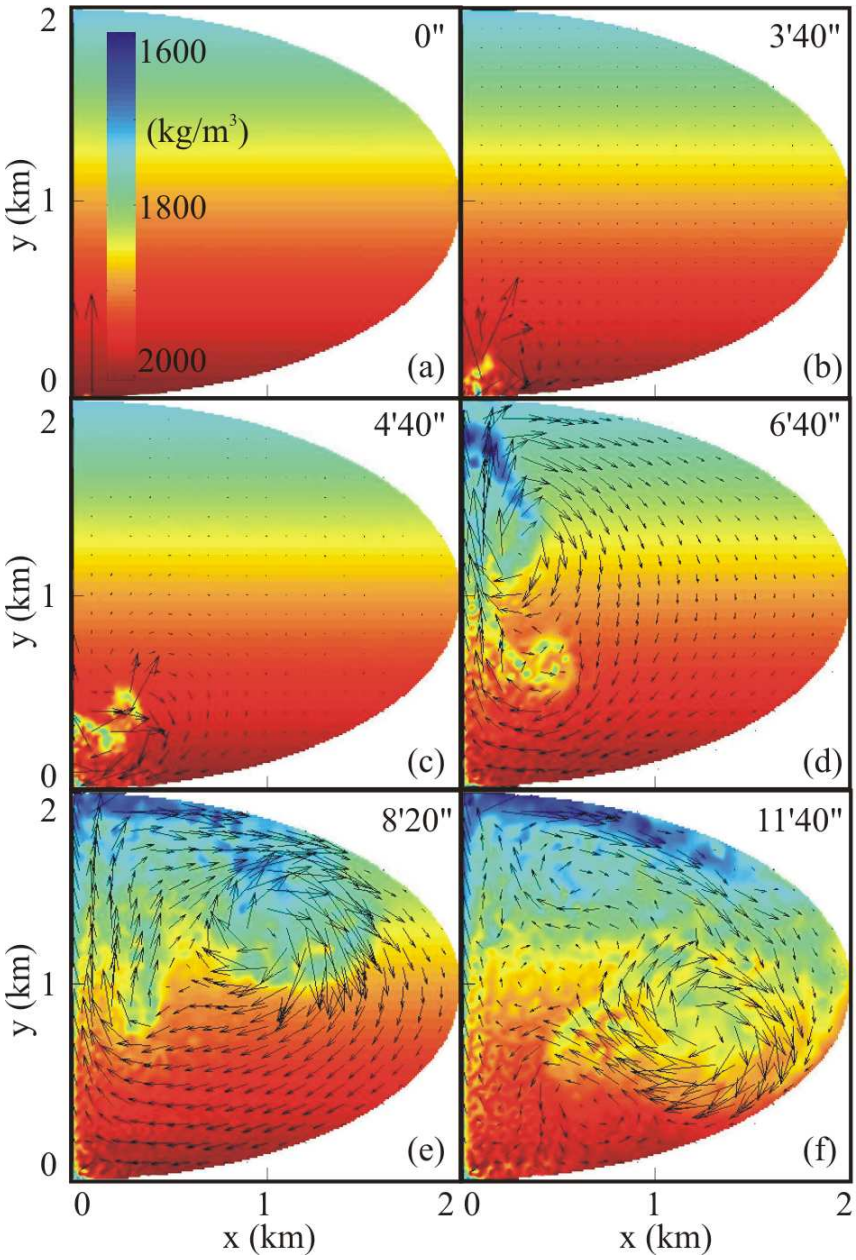

Figure 6.5: Distribution of density (colours) and velocity field (arrows) for case D (3.5 wt% CO_2 in the refilling magma, lower viscosity and chamber depth with respect to cases A-C) at six times after the beginning of magma injection

Chapter 7

Discussion

7.1 Conditions of buoyancy of the refilling magma

For simplicity, in this work conditions where the refilling magma has the same total H_2O content as the resident magma have been considered . This allows a simpler numerical treatment and more stable numerical solutions. However, the efficiency of carbon dioxide in decreasing density and inducing buoyancy of magma is not limited to such cases. Figure 7.1 shows the results of thermodynamic calculations which allow such an evaluation. The two lines refer to the magma composition in table 6.1, conditions at magma chamber bottom for the two considered cases of 3 (plain line) and 4 km (dotted line) deep chamber. Each line represents pairs of total H_2O and CO_2 content in the refilling magma resulting in a magma density equal to that of resident magma at chamber bottom. Therefore, the lines divide the total H_2O -total CO_2 field in two regions of buoyant or sinking conditions for the refilling magma. As an example, a magma having the same characteristics of those considered in the present simulations but total H_2O and CO_2 contents of 3 and 1.3 wt%, respectively, will be buoyant if entering a chamber localised as in cases A-C, while it will be sinking if entering the shallower chamber of case D. Note that buoyant conditions can involve a refilling magma having a total volatile content lower than that of the resident magma. This is due to the much lower solubility of CO_2 with respect to H_2O and to its strong effect in reducing the H_2O saturation content, therefore resulting in a larger volume occupied by the gas phase.

During the evolution of magma bodies, two main processes concur to mod-

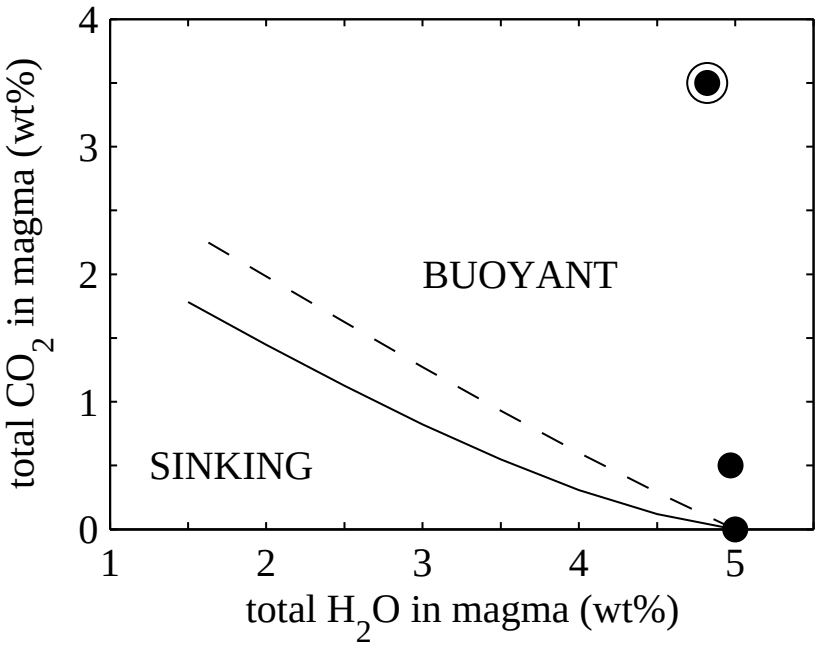

Figure 7.1: Fields of sinking and buoyant conditions for the refilling magma with respect to the resident magma, in terms of total H_2O and CO_2 content in the refilling magma for the composition in table 6.1, H_2O + CO_2 saturation from the model in Papale et al. (2006), liquid density model from Lange (1994). The lines connect pairs of total H_2O and CO_2 content in the refilling magma resulting in a magma density equal to that of resident magma at chamber bottom for a chamber 3 (plain line) and 4 (dotted line) km depth. The symbols indicate the conditions pertaining to the simulations A-C (black circles) and D (open circle) in table 6.2. Note that the total H_2O content for the simulated cases is slightly different, reflecting dilution due to the presence of CO_2.

ify the total volatile content. These are crystallization of magma, which implies volatile concentration with respect to the liquid phase, and open system degassing, which instead results in volatile depletion. While crystallization does not produce a change of the total CO_2 /H_2O ratio in magma (except in cases where a volatile enters the crystal lattice), open system degassing invariably results in a remarkable depletion of the less soluble CO_2 component (Papale, 2005). As a consequence, deep magmas which have suffered gas loss to a lower extent easily contain less H_2O and more CO_2 than shallow magmas which have lost a significant fraction of their original volatile content. This excess CO_2 content

may in turn be sufficient to trigger buoyancy of magmas coming from depth, as illustrated in fig. 7.1.

7.2 Conclusions

This preliminary study shows that the presence of carbon dioxide in magma refilling pre-existing chambers is a very efficient mean of producing buoyant plume rise and large-scale convection, likely to create the conditions for the eruption of magmas mixed to various extents; the convection patterns are complex showing multiple vortexes, either stable in position or migrating with time. Larger amounts of carbon dioxide translate into higher average velocities and decreased time scales of mixing and convection; larger CO_2 contents, lower magma viscosities and lower chamber depths increase the Reynolds number (Re) in the rising plume, producing a shift from simple plume rise and spreading at the chamber top, to early vortex formation and efficient mixing all along the rising plume.

As long as CO_2 is present in appreciable quantities in the feeding magma, and magma chamber evolution is accompanied by open system degassing, convection and mixing are expected to be common occurrences following the injection of deep magma into a magma chamber. Since the efficiency of convection and mixing increases with increasing difference in CO_2 content between the refilling and resident magmas, and since this difference increases with increasing amount of volatiles lost from the magma chamber, it is also expected that more efficient chamber degassing or longer periods with no chamber refilling be followed by more efficient dynamics of convection and mixing with the next episode of magma ingression into the chamber.

One of the major limits of this preliminary study, which is removed in the followuing investigation, is that the inlet velocity is assumed not to vary with time. This choice prevents the formation of vortexes immediately above the chamber inlet, avoiding mass outflows and favouring numerical convergence. On the other hand, it implies that the confidence in the numerical results decreases as long as the pressure inside the magma chamber increases, since this is expected to produce a parallel decrease of the inlet velocity. A second important limit is that mechanical separation between gas and liquid phases is not allowed. As noted before (Phillips and Woods, 2002), gas-liquid decoupling can reduce the ef-

ficiency of convection, since the degassing magma would progressively increase its density and reduce its buoyancy. The present results are therefore more appropriate in cases where inertia is small and the Archimedes number (Ar), with the average gas bubble diameter, or where inertia dominates over gas bubble buoyancy, i.e., $\mathrm{Ar}/\mathrm{Re}^2 < 1$. In the present case, efficient separation of gas bubbles would require bubble diameters of the order of 10^{-1} m. Finally, one other limit is that the only chemical reactions allowed to occur are those related to multicomponent gas-liquid equilibrium. In real cases it should be expected that resident and refilling magmas have different composition, temperature, and crystal content besides having different volatile content. Therefore, mixing and convection would be accompanied by heat exchange, complex patterns of chemical diffusion, and chemical reactions involving gas-liquid-solid equilibria. The effects of these complex patterns should form the object of future investigation with more sophisticated modeling.

Part III

Application to Campi Flegrei (Italy)

Chapter 8

Introduction

Campi Flegrei are a complex volcanic area about 1.5 km north-west of Napoli (Italy) characterized by a resurgent nested caldera with many eruptive centers (fig. 8.1). Its structure formed during two major caldera collapses related to the eruptions of the Campanian Ignimbrite (CI, 39 ka, 200 km^3 DRE: Barberi et al. (1978); Fisher et al. (1993); Rosi et al. (1996); Civetta et al. (1997); Fedele et al. (2002); Pappalardo et al. (2002)) and the Neapolitan Yellow Tuff (NYT, 15 ka, 50 km^3 DRE: Orsi et al. (1992, 1995); Scarpati et al. (1993); Wohletz et al. (1995); Deino et al. (2004); Orsi et al. (1996)). After each caldera collapse, volcanism was restricted within the collapsed area. The NYT eruption and associated caldera collapse (which covered an area of 90 km^2, nested within the CI caldera) was the more recent cataclysmic event in the history of the caldera, and its pyroclastic flow deposits cover an area of more than 1,000 km^2. After the NYT eruption, both volcanism and deformation were very intense within the caldera, with at least 72 eruptions (the last of which is the Monte Nuovo eruption, occurred in A.D. 1538) grouped in 3 epochs of activities separated by long periods of quiescence (fig. 8.2). The eruptions were mainly explosive and with low and medium magnitude except two events, one in the I epoch and the other in the III epoch.

The I epoch lasted from 15 to 9.5 ka and it was mainly characterized by a pyroclastic activity, among which only the Pomici Principali eruption (10.3 ka; Lirer et al. (1987); Di Vito et al. (1999)) was a high magnitude eruption. After a quiescence of about 1 ka, the II epoch began and lasted from 8.6 to 8.2 ka, giving rise to low magnitude eruptions, occurring along parts of the NYT caldera borders (fig. 8.1). The III epoch lasted from 4.8 to 3.8 ka after a 3.5 ka quiescence period

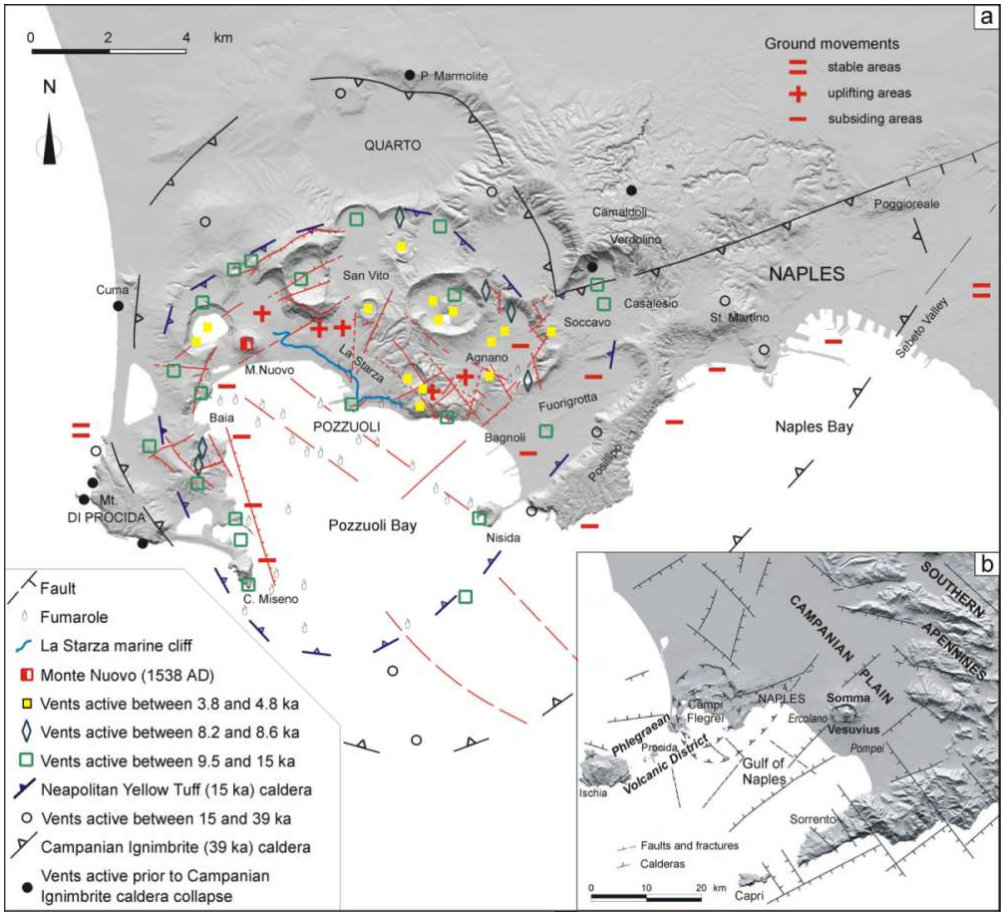

Figure 8.1: Structural sketch map of the Campi Flegrei caldera (from Orsi et al. (2004))

and characterized by the La Starza block uplift (Orsi et al., 1996; Di Vito et al., 1999). During this epoch, vents migrated toward the inner part of the caldera and eruption activity was explosive and effusive and less intense than the past one; the only high-magnitude eruption was the Agnano-Monte Spina eruption (4.1 ka; de Vita et al. (1999); Dellino et al. (2001, 2004)) accompanied by a volcano-tectonic collapse. The last period of quiescence was interrupted in 1538 A.D. by the Monte Nuovo eruption, one of the lower magnitude events in the Campi Flegrei history (Di Vito et al., 1987; D'Oriano et al., 2005).

The volcanic system is still active, as it is proven by intense degassing mainly from fumaroles (Chiodini et al., 2001), ground deformation (Caputo, 1979), seismic activity (De Natale et al., 1991) and thermal anomalies (de Lorenzo et al., 2001a,b) which define a period of unrest lasting from decades.

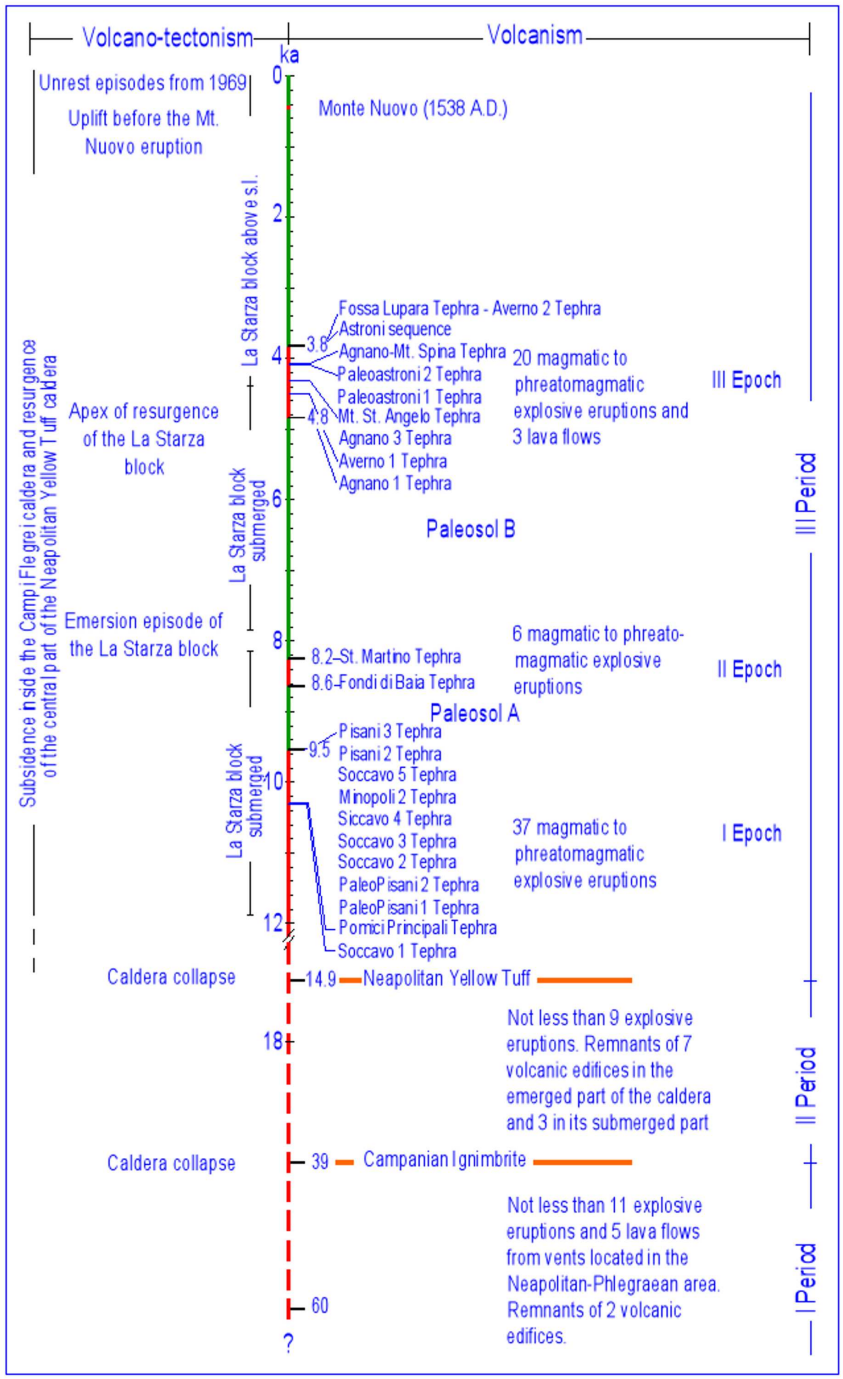

Figure 8.2: Chronostratigraphy of the volcanic and deformational history of the Campi Flegrei caldera (from Orsi et al. (2004))

Ground deformation affected the Campi Flegrei caldera over the past 2 ka (Parascandola, 1947; Dvorak and Gasparini, 1991). The whole structure is subsiding, while the central part of the NYT caldera is affected by resurgence. Two major unrest episodes (bradyseismic events) occurred between 1969-1972, and 1982-1984 (Barberi et al., 1984, 1989; Berrino et al., 1984; De Natale and Pingue, 1993; Bonafede and Mazzanti, 1998; Orsi et al., 1999). The maximum ground uplift was about 170 cm during the first, and about 180 cm during the second episode. Since 1984 the ground has been generally affected by subsidence, which has been interrupted by small episodes of inflation in 1989 (7 cm), 1994 (<1 cm), in 2000 (4 cm) (Avallone et al., 1999; De Natale et al., 2001; Chiodini et al., 2003), and in 2005-2006 (4 cm) Troise et al. (2007).

The volcanic hazard in the Campi Flegrei caldera is extremely high because of the intense activity described above, its explosive character and the frequent occurrence of high-magnitude and high-intensity eruptions in the past. Moreover, the presence of about 1.5 million people who live within the caldera combined with the high hazard, makes the volcanic risk in this area extremely high.

Chapter 9

Definition of the simulated system

The system configuration and initial and boundary conditions for both magma fluid-dynamics and rock elasto-dynamics simulations have been defined according to the past knowledge about Campi Flegrei and results coming from the project INGV-DPC 2004-06 V3_2 "Research on active volcanoes,precursors, scenarios, hazard and risk - Campi Flegrei" to which this thesis contributed.

The reconstruction of the Campi Flegrei magmatic system is mostly based on the last epoch of activity (5 ka) because it is considered as reference for the future behaviour of this volcano, as a consequence of major structural changes occurred within the caldera determining the present stress regime.

The caldera structure has been mainly reconstructed by seismic tomography (Judenherc and Zollo, 2004; Vanorio et al., 2005). The top of the carbonate basement is placed at about 3 km depth; three main horizons have been recognised by seismic reflection studies: the first one, at 5-700 m of depth, identifies a region above it with incoherent, water saturated volcanics and marine sediments that filled the bay of Pozzuoli during the post-caldera activity. The second one, 3 km deep, is associated with the presence of a supercritical gas-bearing rock layer. The third at 7.5 km depth, possibly could identify the top of a region with partially molten rocks (figure 9.1). Moreover, no evidence of the presence of magma reservoirs with size >1 km^3 has been found at shallow depth (< 4 km).

The re-interpretation of seismic lines obtained in the 1970's (Finetti and Morelli, 1974) off-shore the bay of Pozzuoli, shows several solidified magma bodies with size less than 1 km^3 and depth ranging between < 1 km and about 6 km (figure 9.2). It is worth noting that magmatic reservoirs of such a small size are below

the detection limit of seismic tomography.

Processing of volatile contents in melt inclusions of crystals from the products of past eruptions suggests a distribution of the magma storage regions between < 1 and about 9 km of depth and predominance of CO_2 in the gas phase coexisting with magmas which fed some of the reference eruptions including the largest 4100 B.P. Agnano Monte Spina eruption. In particular, the analysis of volatile contents in melt inclusions in minerals from the most differentiated trachytic to phonolitic eruption products (Agnano Monte Spina, Astroni, Senga, Averno eruptions) highlights levels of crystallization between 8 and < 1 km depth, and possible additional crystallization levels at depth > 12 km (figure 9.3).

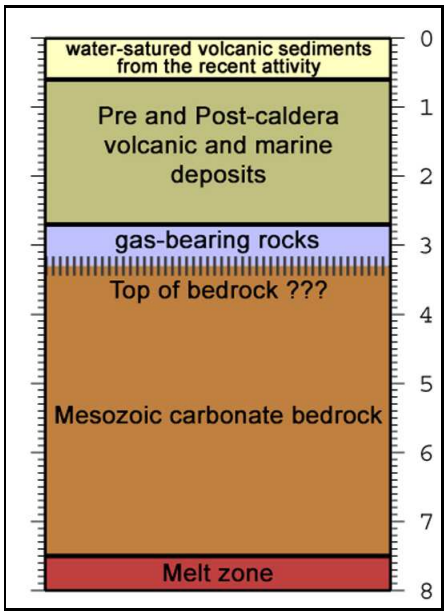

Figure 9.1: Sketch model deduced from joint interpretation of V_p and V_p/V_s ratio profiles (from Zollo et al., INGV-DPC Project V3_2 Campi Flegrei: Final report)

These results supports the existence in the past of magmatic reservoirs at variable depth. The presence of a shallow magmatic reservoir feeding the Agnano-Monte Spina eruption and large abundance of CO_2 is confirmed by experimental petrology.

On the basis of their isotopic signature, magmas of trachytic to phonolitic composition erupted during single eruption in last 5 ka are found to mostly represent residual magma of the Neapolitan Yellow Tuff system, suggesting that the large Neapolitan Yellow Tuff eruption left abundant molten magma within the crust as previously did the Campanian Ignimbrite eruption. Geochemical and isotopic studies on minerals and host glasses suggest a variety of processes including magma recharge, intra-chamber mixing, entrapment of phenocrysts left by previous eruptions, and late stage crustal assimilation. In several cases, residual magma batches were recharged by deeper trachytic magmas. In the case of the Agnano-Monte Spina eruption, the arrival of new magma probably preceded the eruption by no more than a few tens of hours (figure 9.4).

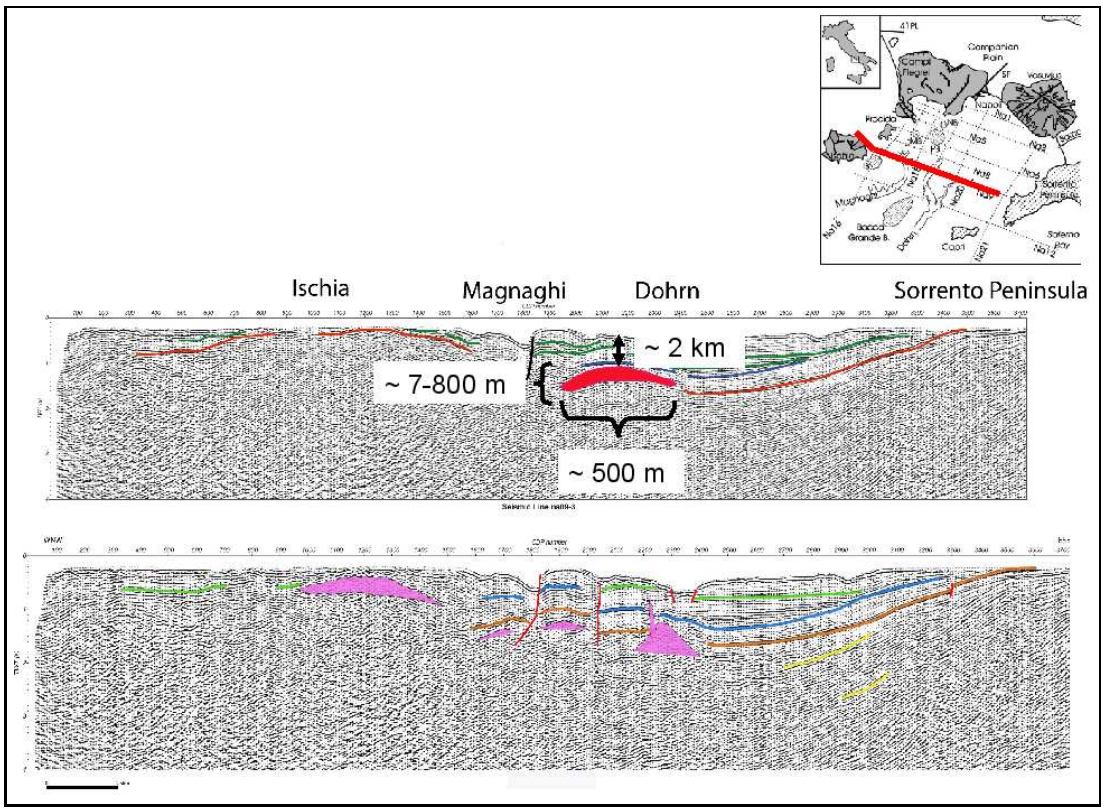

Figure 9.2: Seismic line through Ischia and Sorrento peninsula. Magmatic bodies (red and rose bodies, the geometry is only representative) intruded in a deformed sedimentary marine sequence (from Faccenna et al., INGV-DPC Project V3_2 Campi Flegrei: Final report).

The volumes erupted during last 5 ka at Campi Flegrei are less or much less than 1 km^3, and display a power law distribution (figure 9.5).

This knowledge, together with other information from this project and from literature suggests a comprehensive model of the Campi Flegrei system, summarized in the scheme in figure 9.6: a deep, possibly large reservoir with roof 7.5-9 km deep emerges from both seismic reflection and melt inclusion studies, therefore it appears to have existed during a long portion of Campi Flegrei history up to now. This reservoir is likely to be compositionally heterogeneous, mostly hosting latitic and shoshonitic magma with variable CO_2 content. The shoshonites came to the surface 10-8 ka ago along NE regional faults bordering the caldera and reactivated during the caldera collapse allowing rapid ascent and little chemical differentiation. Trachytes instead, at least during last 5 ka, preferentially rose in the eastern and subordinately western sectors of the caldera, mostly along faults

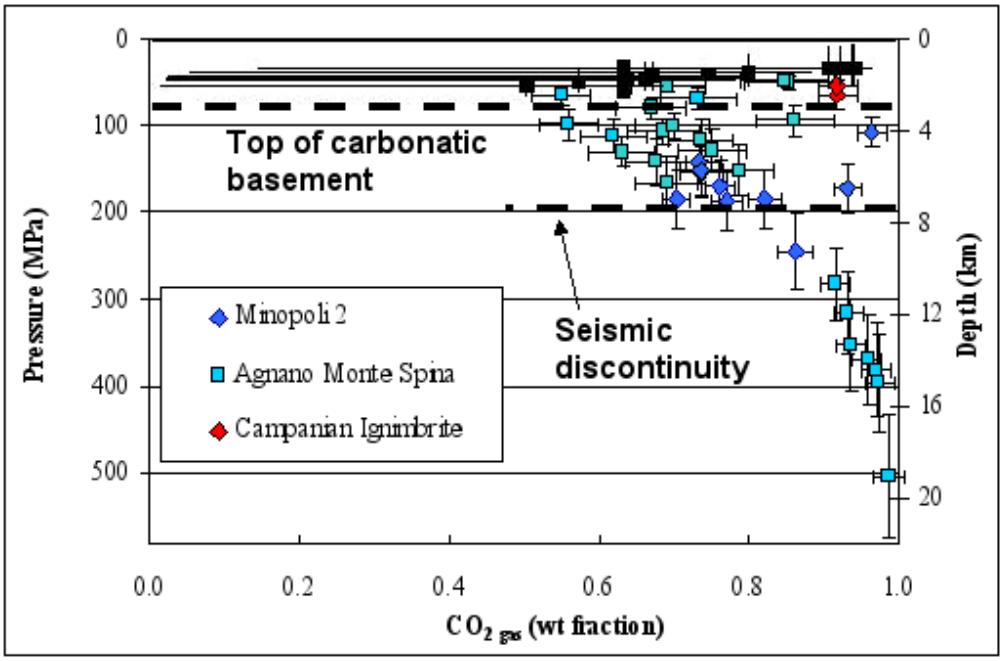

Figure 9.3: CO_2 content in the gas phase of melt inclusions for Minopoli 2 (blue diamonds), Agnano-Monte Spina (cyan squares) and Campanian Ignimbrite (red diamonds) eruptions (from Civetta et al., INGV-DPC Project V3_2 Campi Flegrei: Final report).

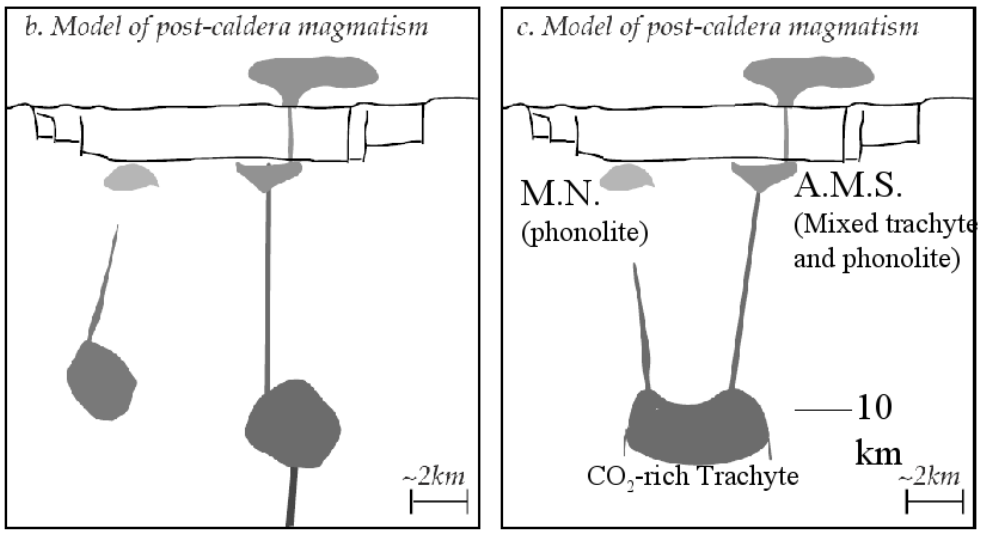

Figure 9.4: Qualitative scheme of the Monte Nuovo (M.N.) and Agnano-Monte Spina (A.M.S.) eruptions (from Rutherford et al., INGV-DPC Project V3_2 Campi Flegrei: Final report)

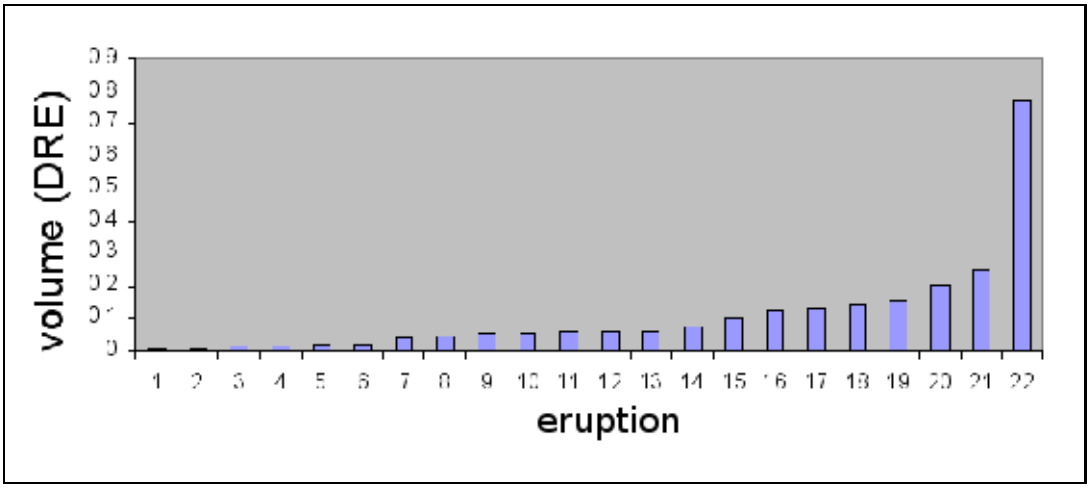

Figure 9.5: Distribution of volumes (Dense Rock Equivalent, DRE) for the eruption younger than 5 ka at Campi Flegrei

and fractures bordering the resurgent block. Repeated arrivals of dominantly trachytic magmas mixed mostly with residuals of the Neapolitan Yellow Tuff magma, possibly still discontinuously present below Campi Flegrei , at depths between 4 and < 2 km, and fed a complex system of small volume (< or << 1 km^3) reservoirs, where open-system degassing occurred and crystallization and contamination resulted in more alkaline-rich, phonolitic terms. A new eruption often occurred in conjunction with new magma arrival in a shallow reservoir.

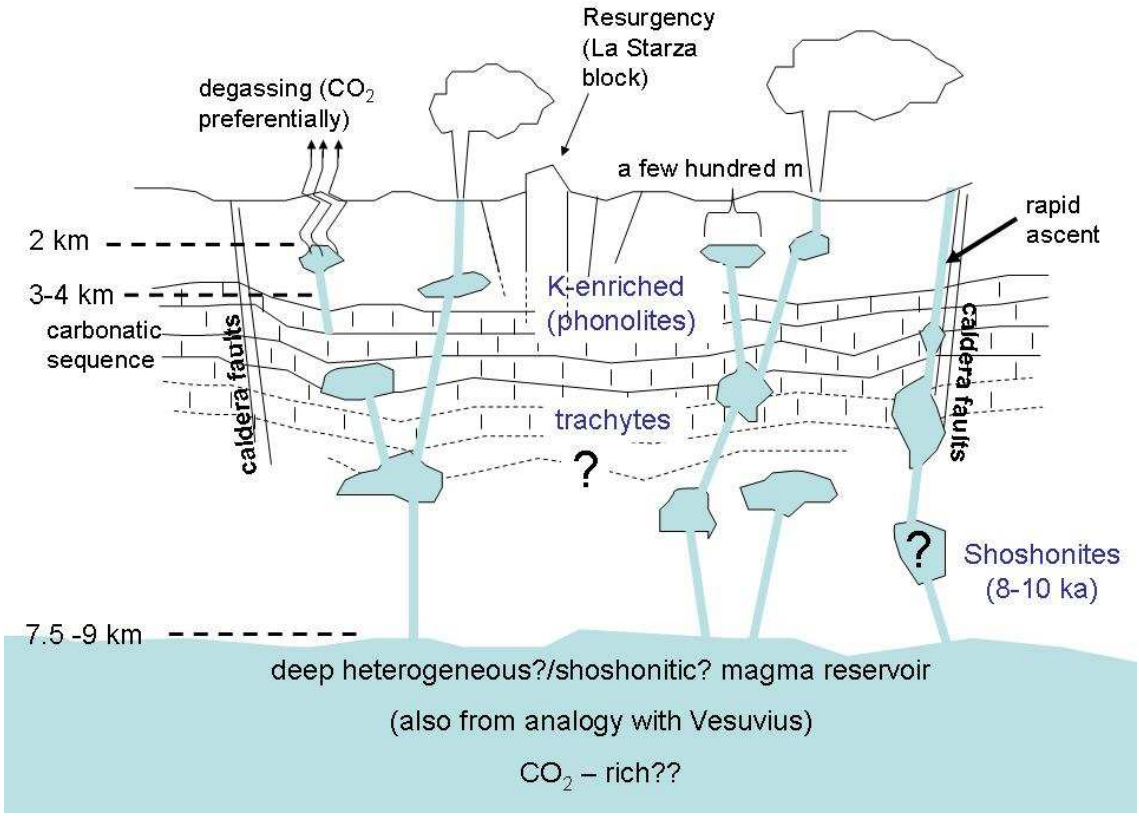

Figure 9.6: Schematic view of Campi Flegrei system in the last 5 ka (from Papale and Civetta, INGV-DPC Project V3_2 Campi Flegrei: Final report)

Chapter 10

Simulations of fluid dynamics

10.1 Initial and boundary conditions

The above reconstruction of the Campi Flegrei system allowed the definition of a simplified set of system, initial and boundary conditions for the simulation of magma dynamics at Campi Flegrei. The simulated system consists in a shallow magma chamber refilled by a deep magmatic storage zone as shown in figure 10.1. The chamber is elliptical prolate or oblate, with semi-axes of 400 and 200 m and hosting magma with phonolitic composition; the chamber top is 3 km depth. The feeding system is a 7 km long and 6 to 60 m wide dyke carring a CO_2 -rich trachytic magma. The choice of defining a very long feeding dyke, while not affecting the results significantly, guarantees a higher numerical stability and more confident calculation of the complex convection dynamics within the magma chamber.

As pointed out before, seismic tomographies carried out at Campi Flegrei do not identify any shallow magma chamber. However, a chamber as small as the one assumed in this work would not be revealed by present day tomographies (Zollo et al., 2003). The chamber size is consistent with a reservoir volume < 1 km^3, similar to those which likely fed several Campi Flegrei eruptions in the past, as well as to the small solidified magma bodies identified off-shore the bay of Pozzuoli.

The composition of the anhydrous magmas adopted in the simulations is reported in table 10.1. The phonolite is assumed carry 3 wt% total water and 0 or 0.5 wt% total CO_2 ; the trachyte bears variable H_2O and CO_2 contents ranging from 3 to 4 wt% and from 0.1 to 1 wt%, respectively. The temperature of the

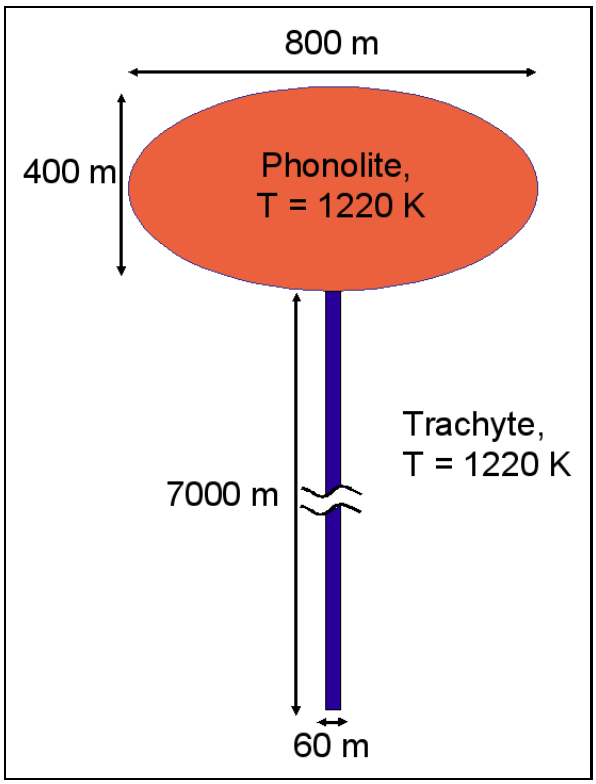

Figure 10.1: Scheme of the simulated system. Magma chamber and dyke are not in the same scale

two magma is taken constant and equal to 1220 K (corresponding to 950 °C). Although temperature differences of a few tens of degrees probably characterized the trachytic and phonolitic magmas erupted during the Agnano-Monte Spina eruption (Rutherford and coll., 2004), such a simplifying choice allows neglecting thermal exchange, resulting in more stable numerical results.

The liquid viscosity is represented as a function of magma composition, dissolved water content and temperature (fig. 10.2(a)); it is calculated using the

	SiO_2	TiO_2	Al_2O_3	Fe_2O_3	FeO	MnO	MgO	CaO	Na_2O	K_2O
TR	61.26	0.38	18.38	1.17	2.33	0.14	0.74	2.97	4.58	8.04
PH	53.52	0.60	19.84	1.60	3.20	0.14	1.76	6.76	4.66	7.91

Table 10.1: Composition (wt %) of anhydrous trachytic and phonolitic liquid phase assumed in simulations (from Romano et al. (2003)). TR and PH mean trachyte and phonolite, respectively

parametric equation:

$$\log\mu = a_1 + a_2 \ln w_{H_2O} + \frac{b_1 + b_2 w_{H_2O}}{T - (c_1 + c_2 \ln w_{H_2O})} \tag{10.1}$$

where w_{H_2O} is the dissolved water content (in wt%) and a_1, a_2, b_1, b_2, c_1 and c_2 are fit parameters depending on magma composition . The fit parameters used in simulations have been taken from Misiti et al. (2006) for trachyte and Romano et al. (2003) for phonolite and they are reported in table 10.2.

	a_1	a_2	b_1	b_2	c_1	c_2
Trachyte	-4.73153	-0.0047295	10786.2	-585.492	173.44	-26.8303
Phonolite	-6.7898	-0.02653	12143.2	-541.20	145.14	-33.342

Table 10.2: Fit parameters to compute liquid viscosity for trachyte (from Misiti et al. (2006)) and phonolite (Romano et al. (2003)).

The system configuration described above is gravitationally unstable since the overlying phonolitic magma is denser than the underlying trachyte. Figure 10.2(b) shows that the phonolite is denser than the trachyte even without taking into account the large volatile content of the latter; moreover the studied cases consider that the trachytic magma brings more CO_2 , therefore a larger amount of exsolved gas, increasing further the density difference between the two magma types. This gravitationally unstable situation induces natural buoyancy. In order to study the more realistic case where new magma entrance is due to a force from below, in most simulations we have assumed an initial overpressure at dyke base, varying from 1 to 20 MPa. This condition leads to take into account mixing dynamics in the magma chamber originating from a combination of natural and forced convection. The 20 MPa overpressure is likely to represent an overestimate of possible overpressure in the real case, and it is adopted her as an end-member condition of forced convection. The opposite end-member condition is given by purely natural convection induced by buoyancy only, when the initial overpressure at dyke base is fixed at zero.

In order to perform the fluid-dynamics simulations, the system domain has been mapped with a grid of about 2000 quadrangular elements. The elements have different size with side ranging from 2 to 30 m (fig. 10.3); the grid density has been increased where the more complex dynamics are waited, i.e. at the

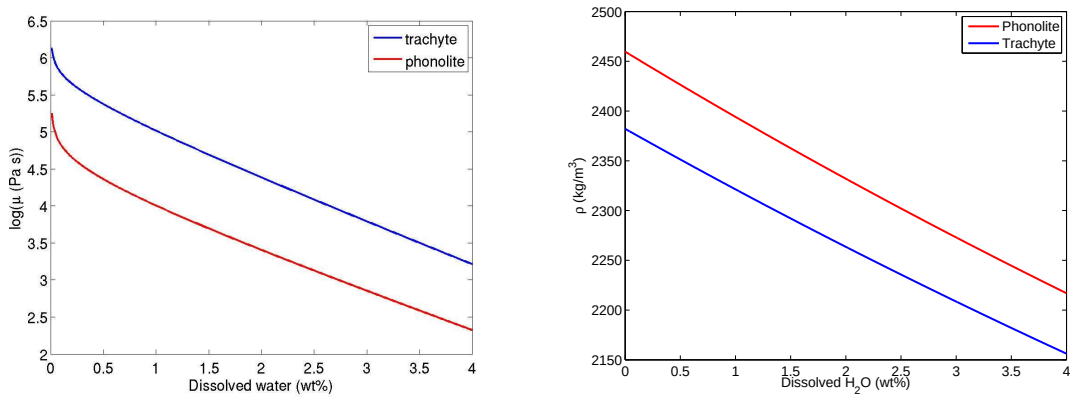

(a) (b)

Figure 10.2: (a) Viscosity and (b) density of anhydrous liquid phase for trachyte (blue line) and phonolite red line). Viscosity is plotted as a function of the dissolved water content, bulk density as a function of pressure

chamber inlet. The time step has been fixed equal to 10^{-3} s for the first 0.4 s, then it is increased to 10^{-2} s. The smaller initial time step is taken to avoid possible initial convergency problems, because the initial conditions of zero velocity make the linear system ill-conditioned. With such a grid spacing and time interval the Courant number (Co=$\frac{c\Delta t}{\Delta x}$, where c is the sound velocity) is less then 1, assuring that the sound waves are well propagated and the information is advectively transported in the fluid at subsonic regime.

The simulations have been performed with the aim of understanding the effects of parameters such as driving overpressure, volatile content and system configuration (chamber orientation and dyke width) on the dynamics of mixing and convection in the refilled magma chamber. The simulated cases are reported in table 10.3. The influence of the overpressure applied at dyke inlet has been studied comparing cases CF-1 to CF-3: in these simulations, a volatile-rich trachyte with 4 and 1 wt% total water and carbon dioxide, respectively, refills a magma chamber containing phonolite with 3 and 0.5 wt% of total water and carbon dioxide. In case CF-1 (chosen as reference case for additional parametric studies) an overpressure of 1 MPa has been assumed; such a value is relatively large, but not enough to trigger rock fracturing and, possibly, an eruption (Chau and Wong, 1996; Roche and Druitt, 2001; Zhang, 2002). In case CF-2 no overpressure has been applied with the purpose to study purely natural convection

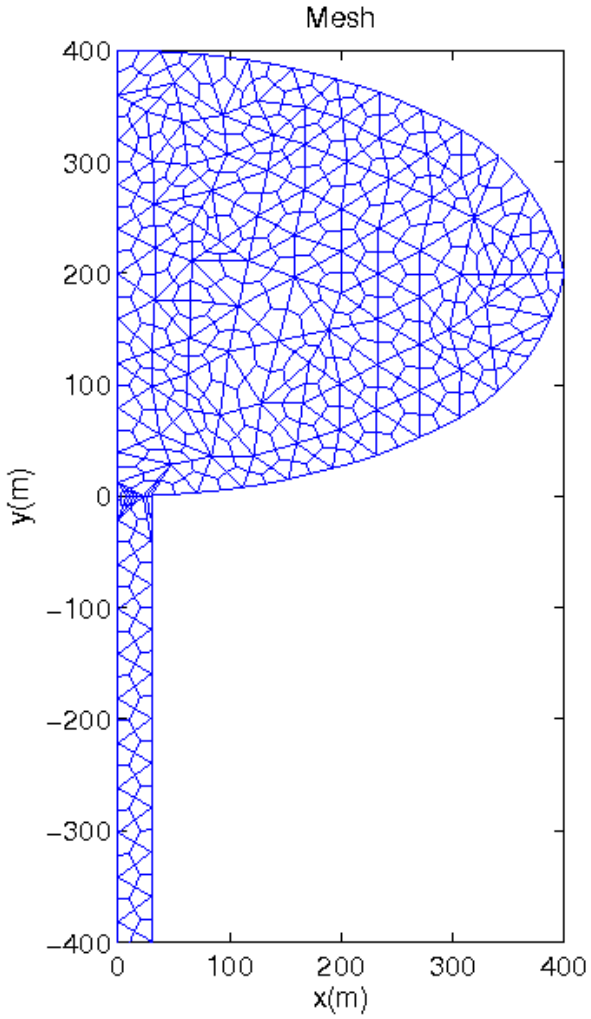

Figure 10.3: Mesh grid used for the fluid-dynamics simulations; the grid was computed by the free software BAMG (Hecht, 1998).

dynamics. In case CF-3 a very high overpressure (20 MPa) has been considered. Such a large overpressure is expected to produce large rock deformation and cracking, therefore, simulation CF-3 and CF-4 (which assumes the same value) should not be considered realistic cases. Rather, they are included in the present study as end-member conditions for forced convection, as explained above.

The effect of chamber orientation has been studied by comparing simulations CF-3 and CF-4. In order to understand the extent to which the efficiency and patterns of mixing and convection are influenced by magma volatile content, one simulation (CF-5) equal to the reference case CF-1 but with the feeding trachyte carrying lower volatile content has been run. Case CF-6 considers a system con-

figuration where the refilling and resident magmas are exchanged; this simulation has been performed to understand what happens when applying an overpressure in a gravitationally stable system. All cases described above assume a dyke width of 60 m, whereas the last three simulations (CF-7 to CF-9) have been carried out considering a dyke width decreased by an order of magnitude (6 m width) with the intent of studying the influence on the refilling dynamics. CF-7 and CF-8 are equal to the reference case CF-1 and case CF-5, respectively, except for dyke size; finally, case CF-9 considers magmas with very low volatile content: the phonolite carries 3 wt% of total water and no carbon dioxide; the trachyte bears 3 wt% of total H_2O and 0.1 wt% of total CO_2 .

All the simulations have been run in a half domain since the system is assumed to be symmetrical with respect to the middle plan. Preliminary simulations of convection dynamics in a refilled container made by simulating the entire domain have shown that the GALES code correctly predicts symmetric flow patterns.

The computed initial conditions of pressure, gas phase distribution, mixture density and viscosity for all the simulations are show in figures 10.4-10.7. The initial pressure at chamber top is equal to 70 MPa, corresponding to a depth of about 3 km. From this pressure, the initial magmastatic profile has been calculated; afterwards, the pressure within dyke has been increased to take into account the initial driving pressure (fig. 10.4). The added overpressure is assumed equal to the driving pressure at dyke base, and linearly decreased to zero along all the dyke length. No initial overpressure is assumed within the magma chamber.

The calculated initial gas phase content in the trachyte carrying 4 wt% total H_2O and 1 wt% total CO_2 ranges from 5 to 20 volume % when this magma fills the dyke (cases CF-1 to CF-4, CF-7; fig. 10.4 (a)-(d) and (g)) and from 20 to 25 volume % when it fills the chamber (case CF-6, fig. 10.4 (f)); when the CO_2 content is 0.6 wt% (cases CF-5 and CF-8; fig. 10.4 (e), (h)), the gas volume varies from 2 to 10 %. The CO_2 -poor trachyte (case CF-9; fig. 10.4 (i)) shows a gas volume < 5 %. Phonolite bears 8-10 volume % of gas in all simulations, apart from simulation CF-6 in which the phonolite fills the dyke and carries 2 to 8 volume % gas phase, and from case CF-9 where there is no gas phase because of the lack of CO_2 and consequent increase of the water saturation content. The different initial gas phase distribution depending on the total CO_2 content reflects the mutual effect of the two volatile species on their saturation content. The density distribution

	Resident/ Refilling	Comp.	H_2O (wt%)	CO_2 (wt%)	ΔP (MPa)	Dyke (m)	Chamber
CF-1	resident	phonolite	3	0.5	1	60	horizontal
	refilling	trachyte	4	1			
CF-2	resident	phonolite	3	0.5	0	60	horizontal
	refilling	trachyte	4	1			
CF-3	resident	phonolite	3	0.5	20	60	vertical
	refilling	trachyte	4	1			
CF-4	resident	phonolite	3	0.5	20	60	horizontal
	refilling	trachyte	4	1			
CF-5	resident	phonolite	3	0.5	1	60	horizontal
	refilling	trachyte	3	0.6			
CF-6	resident	trachyte	4	1	1	60	horizontal
	refilling	phonolite	3	0.5			
CF-7	resident	phonolite	3	0.5	1	6	horizontal
	refilling	trachyte	4	1			
CF-8	resident	phonolite	3	0.5	1	6	horizontal
	refilling	trachyte	3	0.6			
CF-9	resident	phonolite	3	0	1	6	horizontal
	refilling	trachyte	3	0.1			

Table 10.3: Simulations performed with GALES. For each case, composition and total volatile content of resident and refilling magma, overpressure assigned at dyke base, dyke width and chamber orientation are reported

(fig. 10.6) confirms that all of the simulations apart from case CF-6 (fig. 10.6 (f)) are gravitationally unstable, since the trachyte turns out to be lighter than the phonolite. Cases CF-5 and CF-6 show a lower density contrast due to the lower gas content of the trachyte. The viscosity of trachyte (fig. 10.7) ranges from $10^3 - 10^4 \mathrm{Pa} \cdot \mathrm{s}$, depending on pressure and water content; phonolite viscosity is less than that of trachyte by about an order of magnitude.

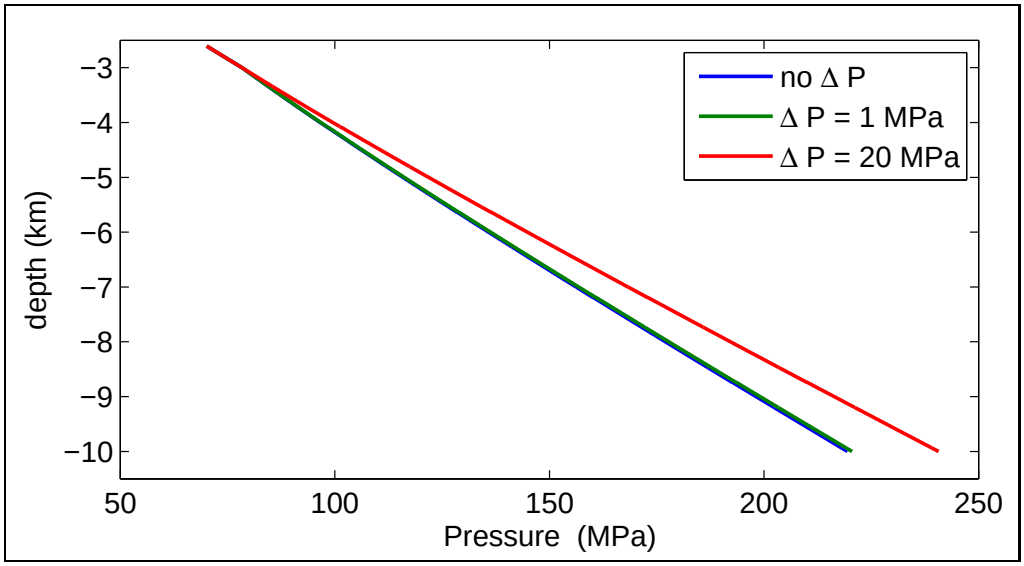

Figure 10.4: Initial pressure profile in the case of no overpressure (green line), overpressure of 1 MPa (blue line) or 20 MPa (red line).

10.2 Results

The employed code GALES allows the investigation of many features of the simulated dynamics, including the time-step evolution of magma composition, density, viscosity, gas volume and composition, dissolved volatile fraction, mass, velocity and pressure.

Table 10.4 shows the simulated times for all cases in table 10.3. Simulations CF-1, CF-3, CF-4 last less than the others because they have been performed with the first version of GALES, not yet parallelized therefore much less performing; the parallelization of the code has been completed during the second year of my PhD.

Unfortunately, simulations with narrow feeding dyke (CF-7 to CF-9) have shown remarkable convergency problems that are yet under study. Therefore, the results from these simulations are not discussed in this thesis.

Simulation	Time (s)
CF-1	380
CF-2	735
CF-3	295
CF-4	365
CF-5	1405
CF-6	1650
CF-7	1280
CF-8	1855
CF-9	2260

Table 10.4: Simulated time

Movies showing the simulated dynamics for all of the cases can be found in the cd attached to this thesis.

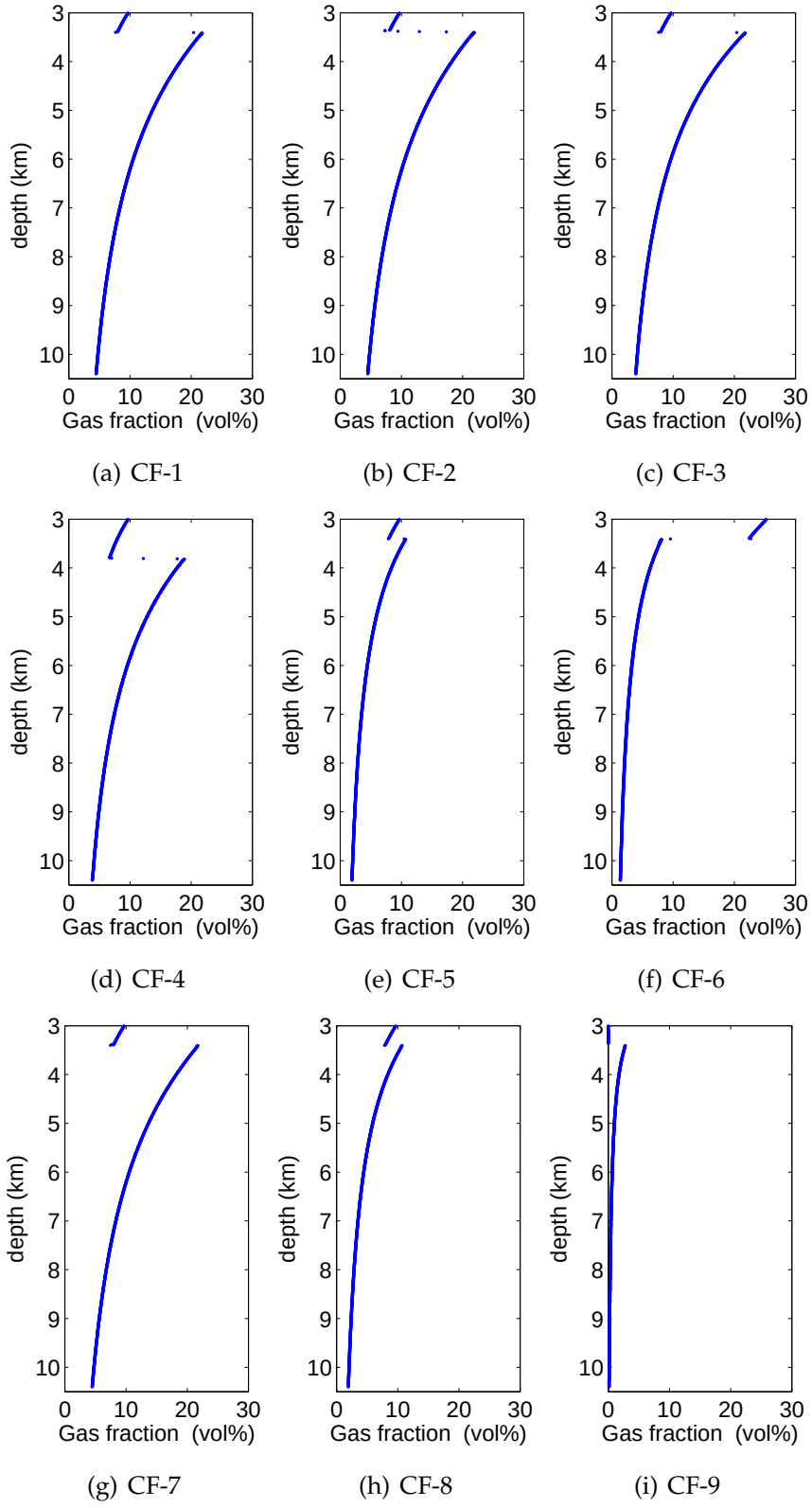

(a) CF-1 (b) CF-2 (c) CF-3

(d) CF-4 (e) CF-5 (f) CF-6

(g) CF-7 (h) CF-8 (i) CF-9

Figure 10.5: Initial gas fraction distribution with respect to depth for all the simulations reported in table 10.3.

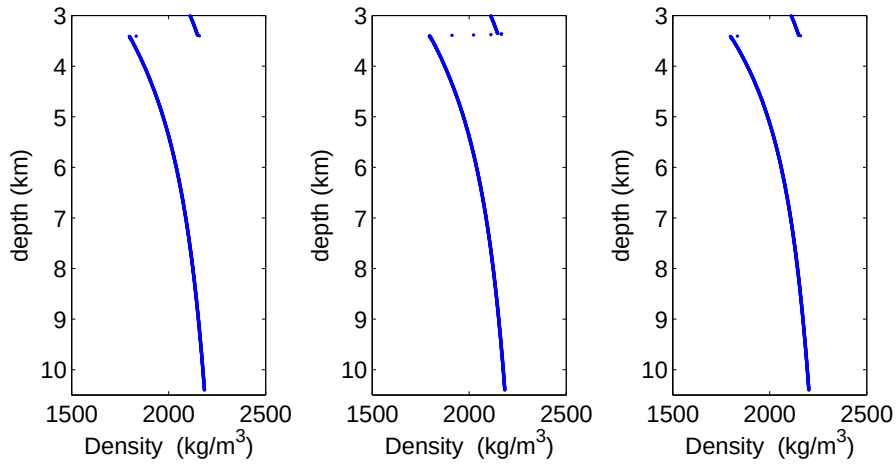

(a) CF-1 (b) CF-2 (c) CF-3

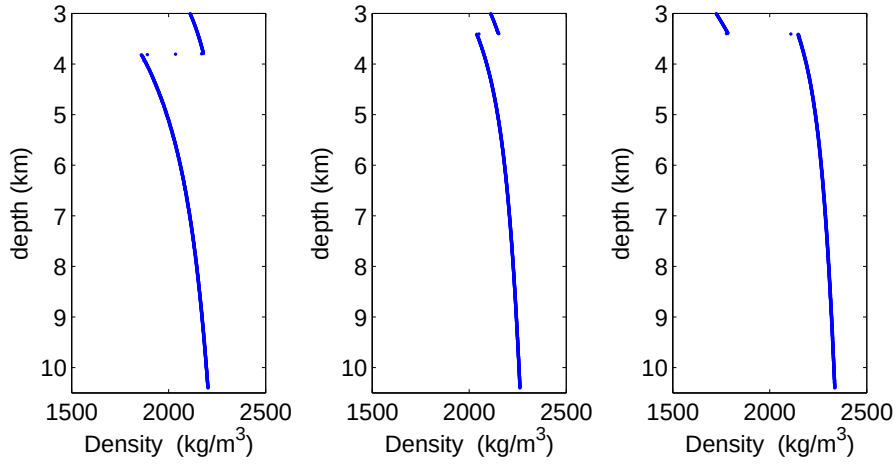

(d) CF-4 (e) CF-5 (f) CF-6

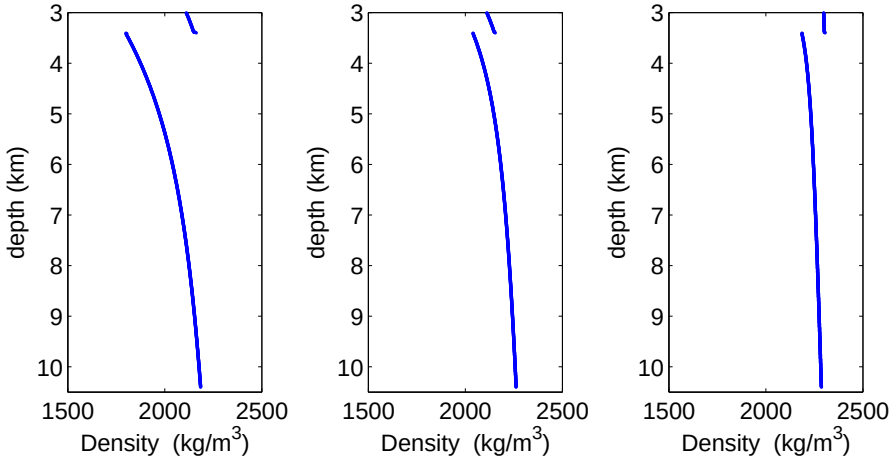

(g) CF-7 (h) CF-8 (i) CF-9

Figure 10.6: Density profile with depth at time = 0 s for all the simulations reported in table 10.3.

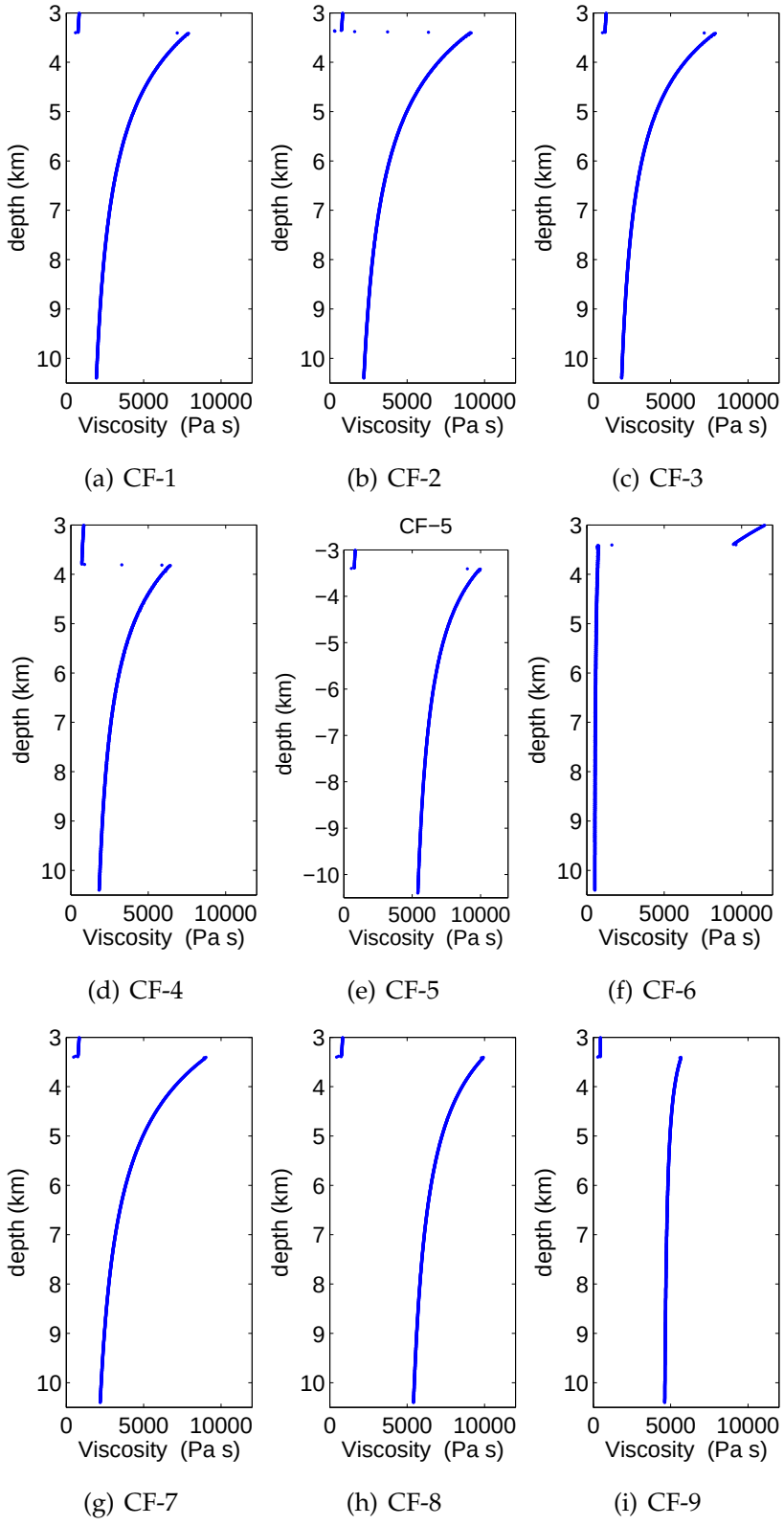

(a) CF-1 (b) CF-2 (c) CF-3

(d) CF-4 (e) CF-5 (f) CF-6

(g) CF-7 (h) CF-8 (i) CF-9

Figure 10.7: Initial viscosity profile with depth for all the simulations reported in table 10.3.

Simulations CF-1

Results for simulation with volatile-rich magmas, initial overpressure of 1 MPa, horizontal chamber and dyke width of 60 m (CF-1) are shown in figures 10.8-10.15. Figure 10.8 illustrates the evolution of magma composition and the velocity field at different times up to 380 s; deep red is equivalent to 100% phonolite, deep blue to 100% trachyte. The overpressure applied at dyke base and the buoyancy force (due to the negative density contrast) imply the formation of a plume after about 30-40 s (fig. 10.8(b)). The plume rises along the chamber axis and reaches the chamber roof after about 120 s (10.8(c) and (d)). During its ascent, the plume grows because pressure decreases with depth and, therefore, volatile exsolution and gas expansion cause plume volume expansion. Later, the plume spreads close to the chamber top (fig. 10.8(e)). As a consequence of new magma entrance, mixing and convection at global scale are triggered. Two main vortexes develop, one in the lower part of the chamber, the other in the upper one (best visible in fig. 10.8(f)); the latter shows an oscillatory behaviour with direction reversals due to the balance between inertial and buoyancy forces: the inertial force, due to the ascent thrust, induces a clockwise rotation with the new entered magma moving from the chamber top to its middle along the chamber wall; the buoyancy force due to lower density of the injected magma counteracts this movement and induces an anticlockwise rotation moving the light magma up again (fig. 10.8(f) and (g)). The maximum velocity within magma chamber is about 15 m/s, achieved after 2 minutes, when the plume is approaching the chamber roof. After an initial injection of trachyte, at about 60 s the resident phonolite is forced to enter the feeding dyke (fig 10.8(c)) being displaced down for about 500 m within it. The whole dynamics result in the rapid disappearance of the phonolitic end-member component, whereas the upper portion of the chamber is occupied by magma with nearly pure trachytic composition (fig. 10.8(h)). At dyke base the initial overpressure involves an initial small injection of new trachyte, followed by a downwards magma flow with maximum velocity of about 20 m/s computed after 140 s. Figure 10.9(a) shows that the mass flow rate at chamber and dyke inlet shows oscillations of decreasing amplitude and period of about 100 s; the maximum mass flow rate per unit length is about $3 \cdot 10^5$ kg/m s at chamber inlet and $3.5 \cdot 10^5$ kg/m s at dyke base (fig. 10.9(a)). As a result, while the trachyte progressively replaces the phonolite in the chamber, the total mass within the

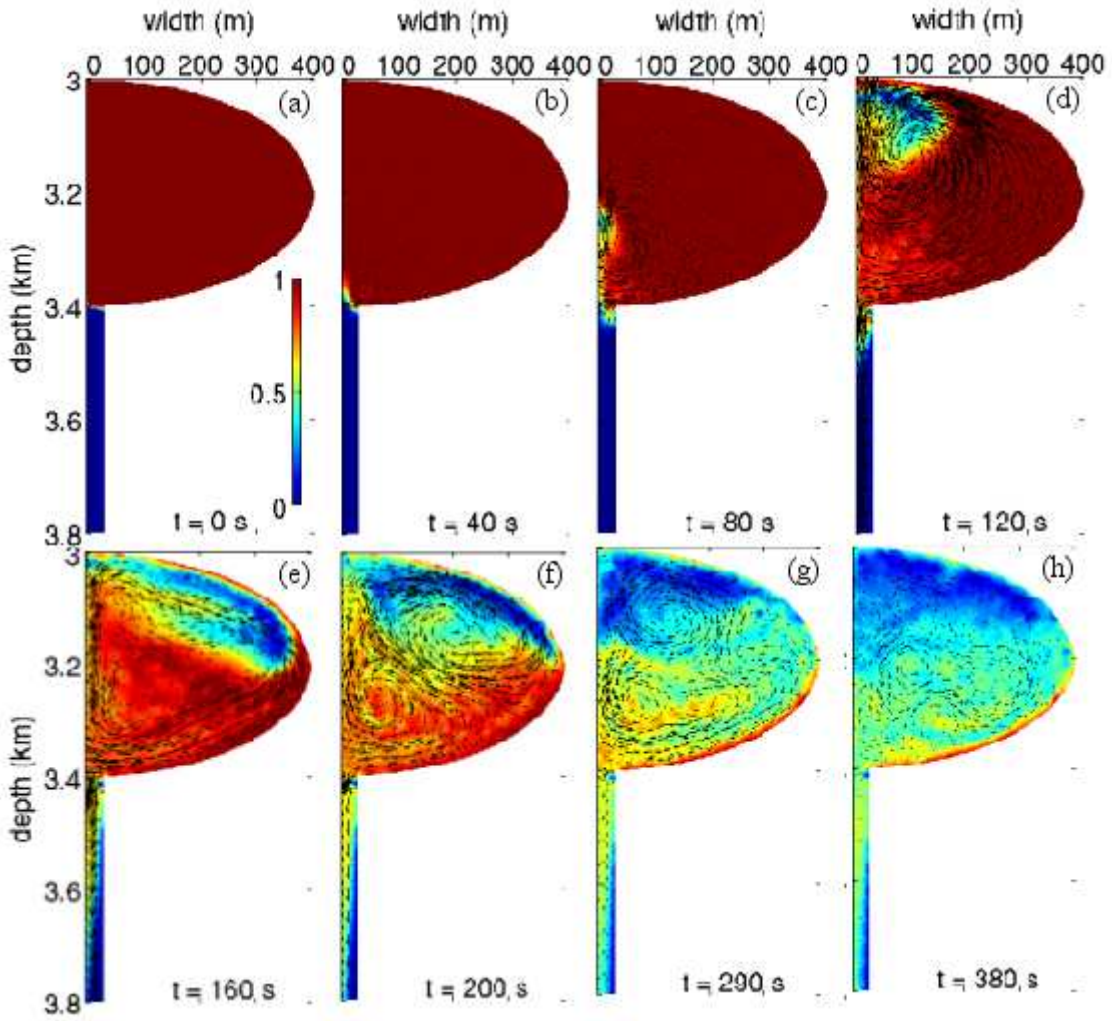

Figure 10.8: Evolution of magma composition for simulation with volatile-rich magmas, ΔP = 1 MPa, horizontal chamber and wide dyke (CF-1). Each panel shows the phonolite fraction and velocity vector within magma chamber and the first 400 m of dyke at different times.

chamber slightly increases in the initial stage, then decreases with time while dense phonolite exits the chamber (fig. 10.9(b)); the total decrease of mass per unit length within the chamber is about $3 \cdot 10^7$kg/m, or 10% of the initial mass.

Figures 10.10 and 10.11 show time evolution of mixture density and gas phase distribution for the same simulation CF-1 reported in figures 10.8 and 10.9. During its rise along the chamber axis, the plume becomes less and less dense and it expands (figs. 10.10, 10.11 (c) and (d)); the plume is, in fact, volatile rich and the pressure drop with depth triggers volatile exsolution and expansion, hence,

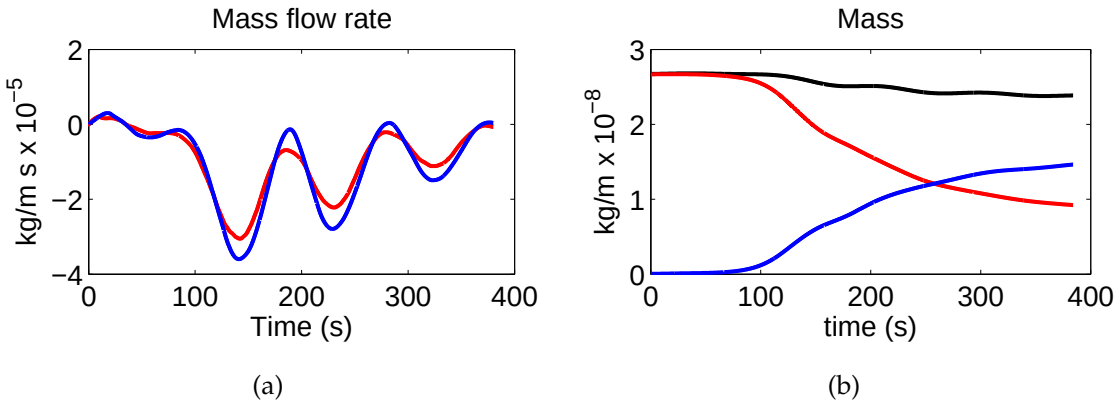

(a) (b)

Figure 10.9: (a) Mass flow rate computed at dyke base (blue) and chamber inlet (red) for case CF-1; (b) mass change in the chamber with time for mixture (black), trachytic (blue) and phonolitic (red) component in the chamber for simulation CF-1.

density decrease. The average density in the chamber decreases and the gas fraction increases with time as a consequence of the increasing content of the light trachytic magma (figs. 10.10, 10.11 (f), (g) and (h)). The pressure variation along chamber and dyke walls (fig 10.12, left) shows oscillations which tend to stabilise at an overpressure of 1 MPa equal to the driving pressure; the oscillating period is of order of 100 s in agreement with that of the mass flow rate (fig 10.9(a)). The pressure peak occurs after about 120 s, corresponding to the plume arrival to the chamber top and it is 4-5 times greater than the initial overpressure. The pressure changes have been filtered with a band-pass filter with cut-off frequencies of 0.025 and 10 Hz (corresponding to a period of 40 and 0.1 s, respectively) in order to highlight high frequency pressure changes computed by the model. These oscillations (right in fig. 10.12) have an amplitude of tens of kPa.

By integrating the contribution to the gravity field of each mass parcel during the simulated dynamics, the gravity change at the Earth surface has been calculated. This quantity corresponds to the residual of the gravity change after correction for ground deformation (free-air corrected gravity change). The gravity changes have been computed assuming a third dimension of the magma chamber equal to 2 km; this length allows to preserve the assumption of two-dimensional dynamics since it is 5-10 times greater than the chamber dimensions over which the dynamics are calculated. The consequent chamber volume of 0.5

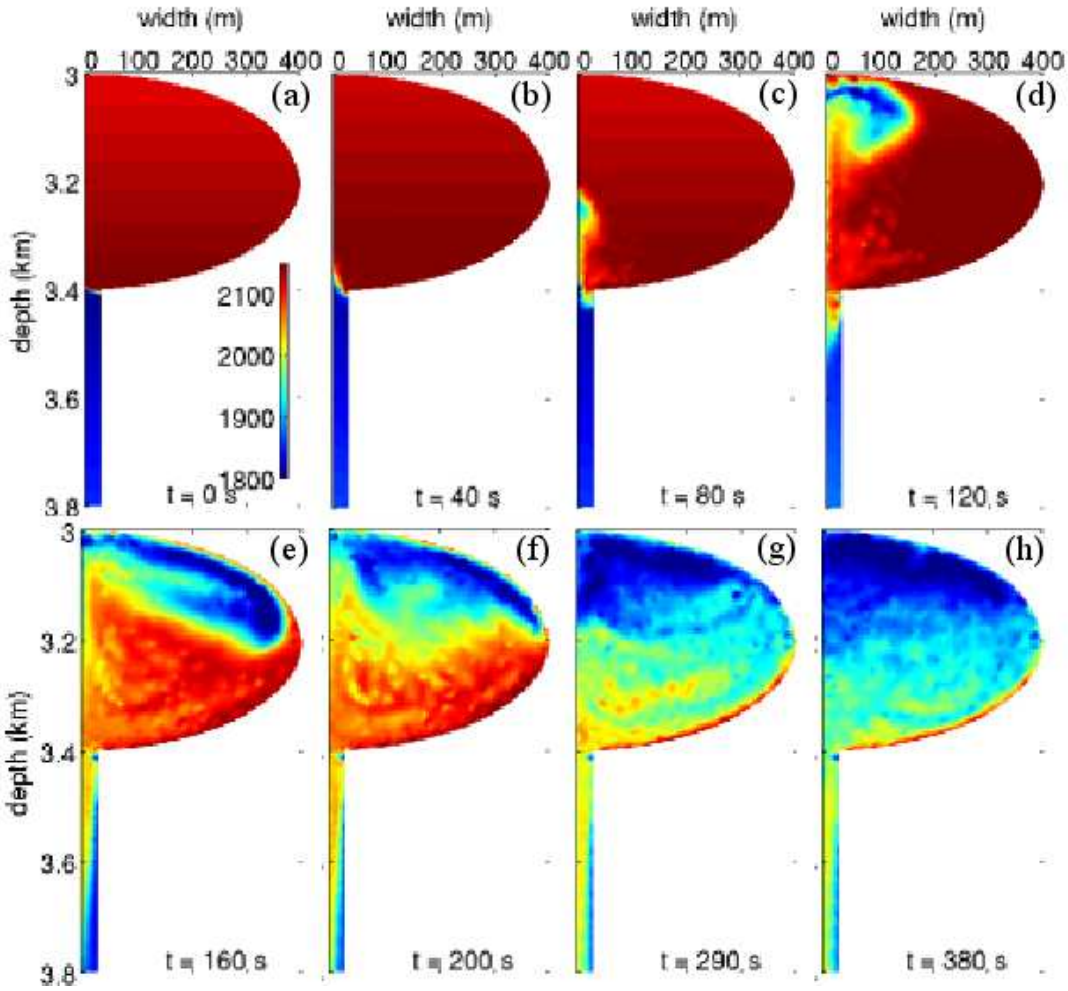

Figure 10.10: Evolution of mixture density (expressed in kg/m^3) for simulation CF-1. Each panel displays results for magma chamber and the first 400 m of dyke at different times.

km^3 is sufficiently small to ensure that such a chamber would not be imaged by today seismic tomographies (see chapter 9), and it is in agreement with small ($<$ to $\ll 1\,km^3$) erupted volumes during last epoch of Campi Flegrei activity (see chapter 9). Figure 10.14 shows the vertical and horizontal components of the gravity changes at three distances from the chamber axis corresponding to 140 m (black line), 1500 m (red line) and 3200 m (blue line); figure 10.15 shows the gravity changes at given times as a function of the distance from chamber axis, computed along a direction perpendicular to the 2 km long main chamber axis and cutting the chamber along its middle (fig. 10.13).

As expected, the maximum vertical gravity change occurs above the cham-

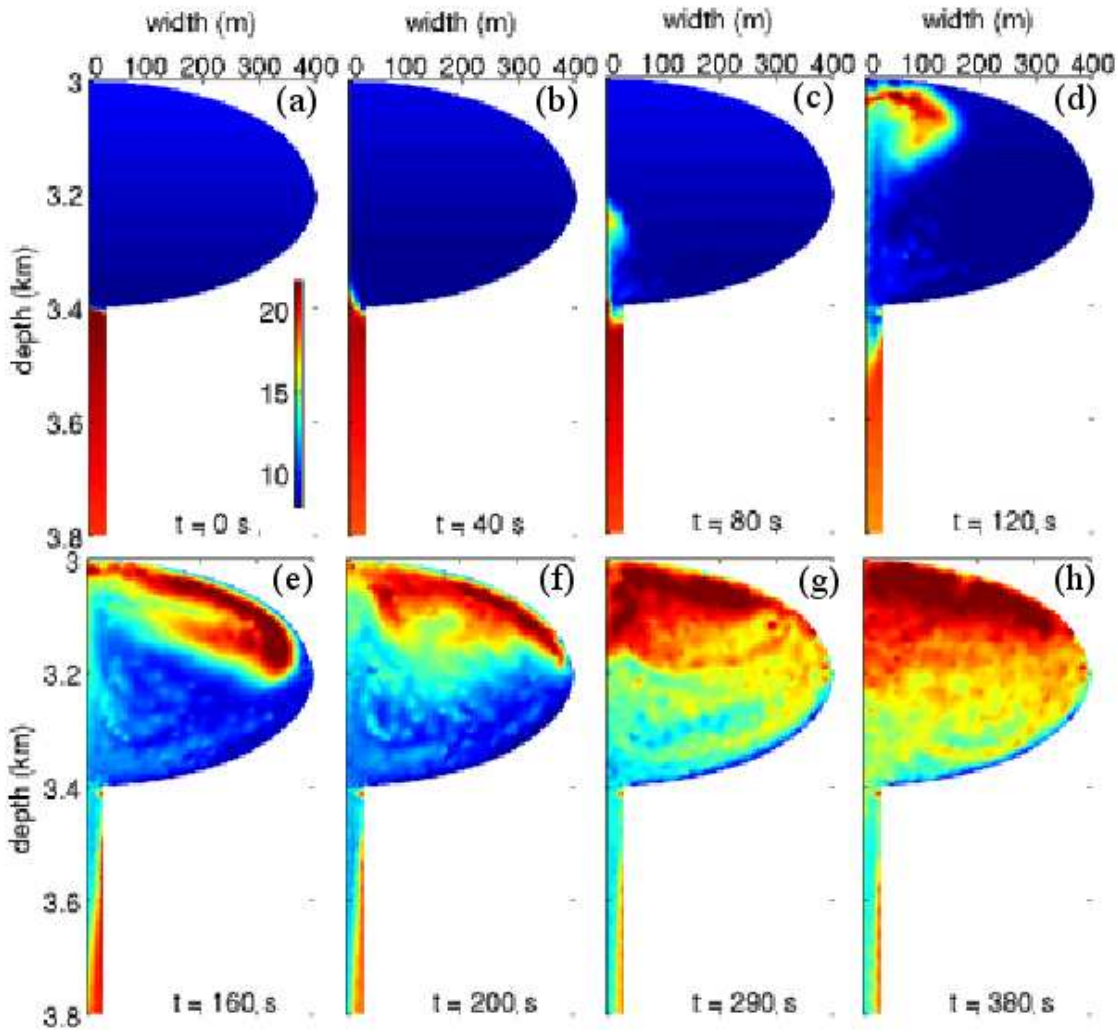

Figure 10.11: Evolution of gas phase distribution (expressed in volume %) for simulation CF-1. Each panel displays results for magma chamber and the first 400 m of dyke at different times.

ber axis where, instead, the horizontal gravity change is zero. The maximum variation of the horizontal component is achieved about 2 km away from the chamber axis. The gravity changes display an oscillating trend correlated to the mass and pressure changes (fig. 10.14). The vertical anomaly is initially slightly positive, then it becomes markedly negative achieving values as large as -70 μGal (fig. 10.14(b)). The negative values are due to progressive replacement of dense phonolite by light trachyte as shown in figures 10.8 and 10.11. The maximum horizontal gravity change has a peak value of 25 μGal. The change in the sign of the gravity change occurs when the plume reaches the chamber top. It is worth

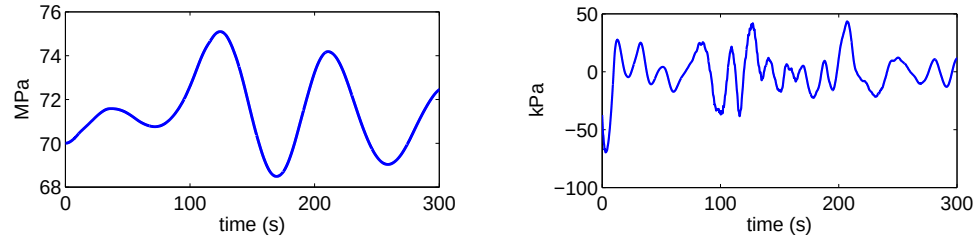

(a) chamber top, depth = 3 km

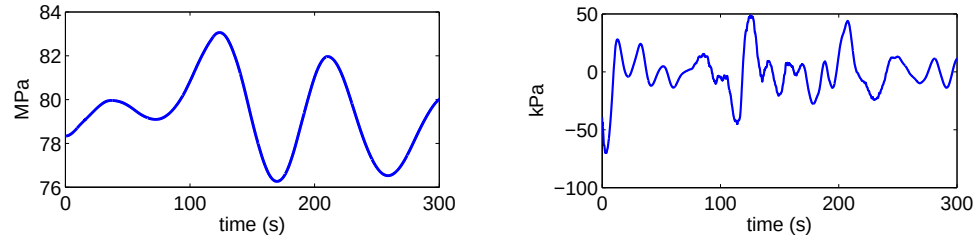

(b) chamber inlet, depth = 3.4 km

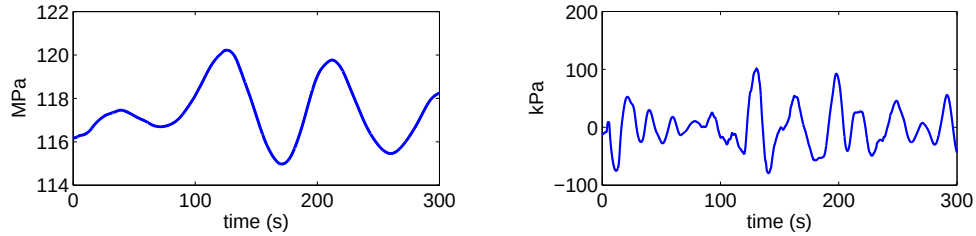

(c) dyke wall, depth = 5.4 km

Figure 10.12: Total pressure changes (left) and filtered pressure changes (right) computed at (a) chamber top, (b) chamber inlet and (c) along the dyke wall, at 3.4 km depth for simulation CF-1. Pressure has been filtered with a band-pass filter with cut-off frequencies of 0.025 and 10 Hz (corresponding to a period of 40 and 0.1 s, respectively)

noting that both the horizontal and vertical anomalies are well above the detection limit of monitoring instruments.

Simulations CF-2

Results for simulation CF-2 with volatile-rich magmas, no overpressure, horizontal chamber and wide dike, are show in figures 10.16 - 10.21; the simulation conditions are equal to those of the reference case CF-1 illustrated above, except for the initial condition of no overpressure. Therefore, comparison between sim-

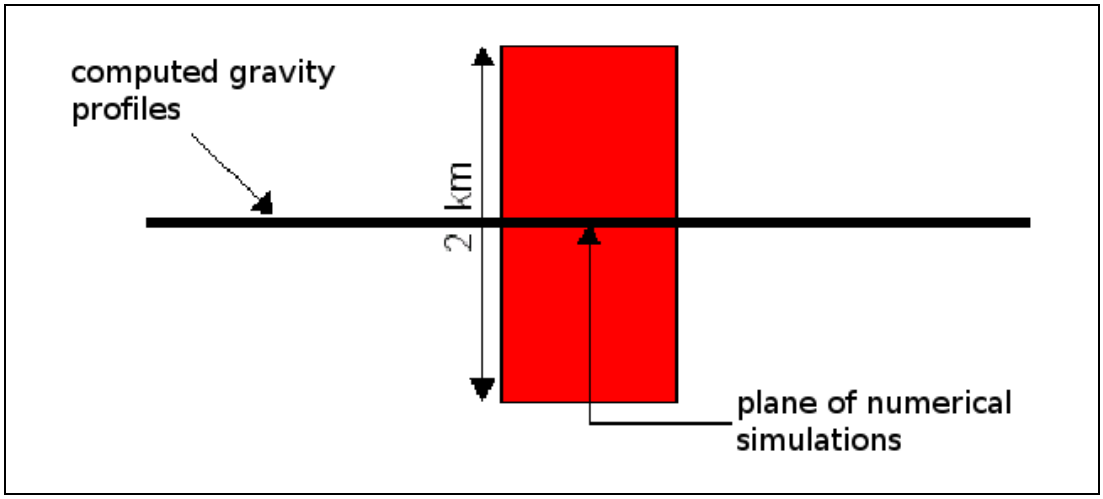

Figure 10.13: Planar view of the section along which gravity profiles are computed.

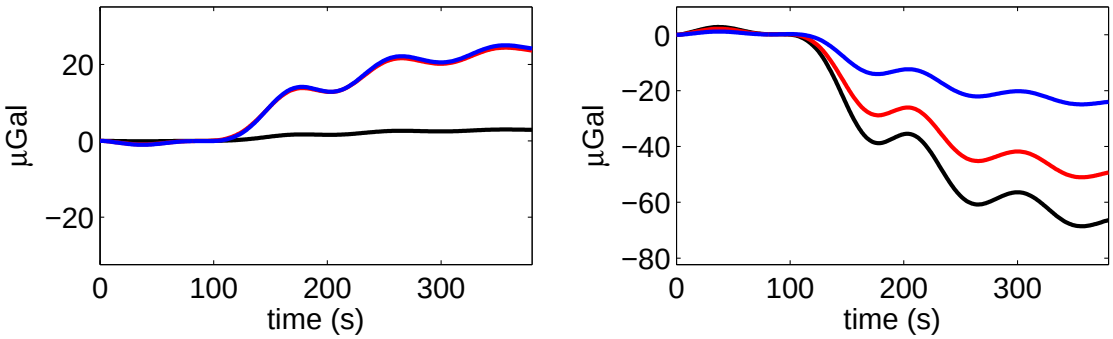

(a) Δg_x (b) Δg_z

Figure 10.14: Horizontal (a) and vertical (b) component of free-air corrected gravity changes vs. time for simulation CF-1. Profiles have been calculated for three distances from the chamber axis on the earth surface: 140 m (black), 1500 m (red), 3200 m (blue)

ulation CF-2 and CF-1 allows addressing the respective relevance of buoyancy and overpressure, or natural vs. forced convection, in the simulated dynamics.

Convection and mixing dynamics due to pure buoyancy are very similar to those induced when an additional overpressure of 1 MPa is also applied. In this case, however, the dynamics have been studied up to a much longer time of 735 s, more than twice that of case CF-1. The trachyte-rich plume starts growing and rising along the chamber axis at about 30-40 s (fig. 10.16(b) and (c)). It reaches the chamber roof after about 120 s (fig. 10.16(d)) and spreads laterally triggering

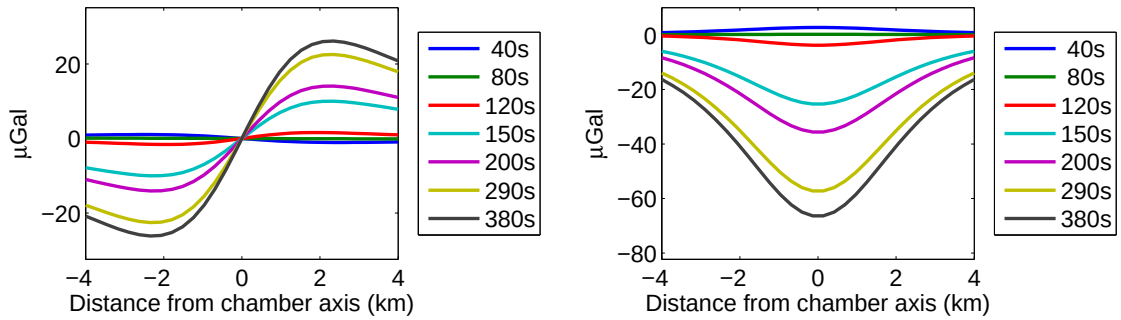

(a) Δg_x (b) Δg_z

Figure 10.15: Horizontal (a) and vertical (b) component of free-air corrected gravity changes with respect to distance from the chamber axis at fixed times, computed for simulation CF-1.

convection and mixing at global scale (fig. 10.16(e) and (f)). Meanwhile, part of the resident phonolite is pushed out of the chamber into the dyke. As in the previous case, after about 150 s the inertial force of the light injected magma is balanced by the buoyancy force due to density lower than that of resident magma (fig. 10.17) and the new light magma begins to go back upwards. Two vortexes form: one, in the upper part of chamber spins anticlockwise whereas in the lower half of chamber, a more efficient vortex rotates clockwise (fig. 10.16 (e) and (f)). From about 400 s the vortexes break out in a few convective cells; afterwards, convection tends to run out. After 700 s (fig. 10.16 (h)) the phonolitic end-member component has totally disappeared from the chamber, and the magma is approaching compositional homogeneity, at around 70-80% trachyte. With respect to the reference simulation, the dynamics induced by pure buoyancy produces a more regular convection pattern. Density and gas phase distribution for the two simulations (figs. 10.10-10.11 for case CF-1 and figs. 10.17-10.18 for case CF-2) match; the maximum achieved velocities also correspond. At simulation end, the chamber is gravitationally layered, with density from 1800 to 1900 kg/m^3 and a gas fraction ranging from 18 to 23 vol% .

Mass changes with time and mass flow rate at chamber inlet and dyke base are shown in figure 10.19. As for the reference case, the mass flows are mainly negative and tend to run out oscillating with a period of about 100 s. The mass flow rate through the chamber inlet shows a small positive initial peak related to the plume formation, as for case CF-1; smaller plume corresponds to smaller mass

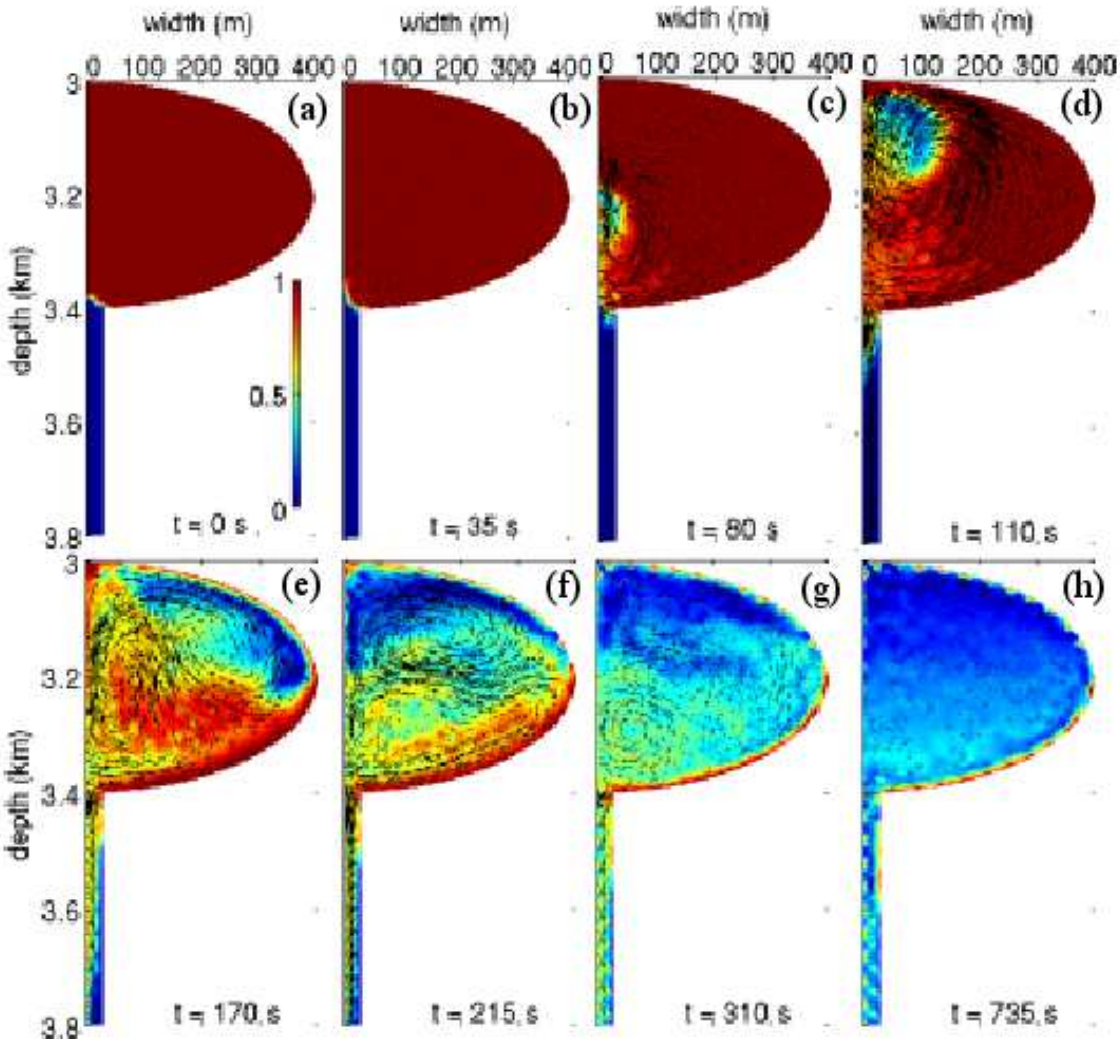

Figure 10.16: Evolution of magmas distribution for simulation of pure buoyancy (CF-2). Each panel shows the phonolite fraction and velocity vector within magma chamber and the first 400 m of dyke at different times.

flow rate peak. The mass flow at dyke base is greater then that at chamber inlet with maximum mass flow rate per unit length of $4 \cdot 10^5$ kg/m s and $3.5 \cdot 10^5$ kg/m s respectively, corresponding to downwards flows. This values are slightly bigger than that computed for the reference case because of the absence of overpressure that opposes magma outflow. Even in this simulation, a massive replacement of phonolite in favour of trachyte occurs within the chamber, causing the chamber mass to decrease with time (black line in figure 10.19(b)). Figures 10.20 and 10.21 show the vertical and horizontal components of gravity changes, respectively, at

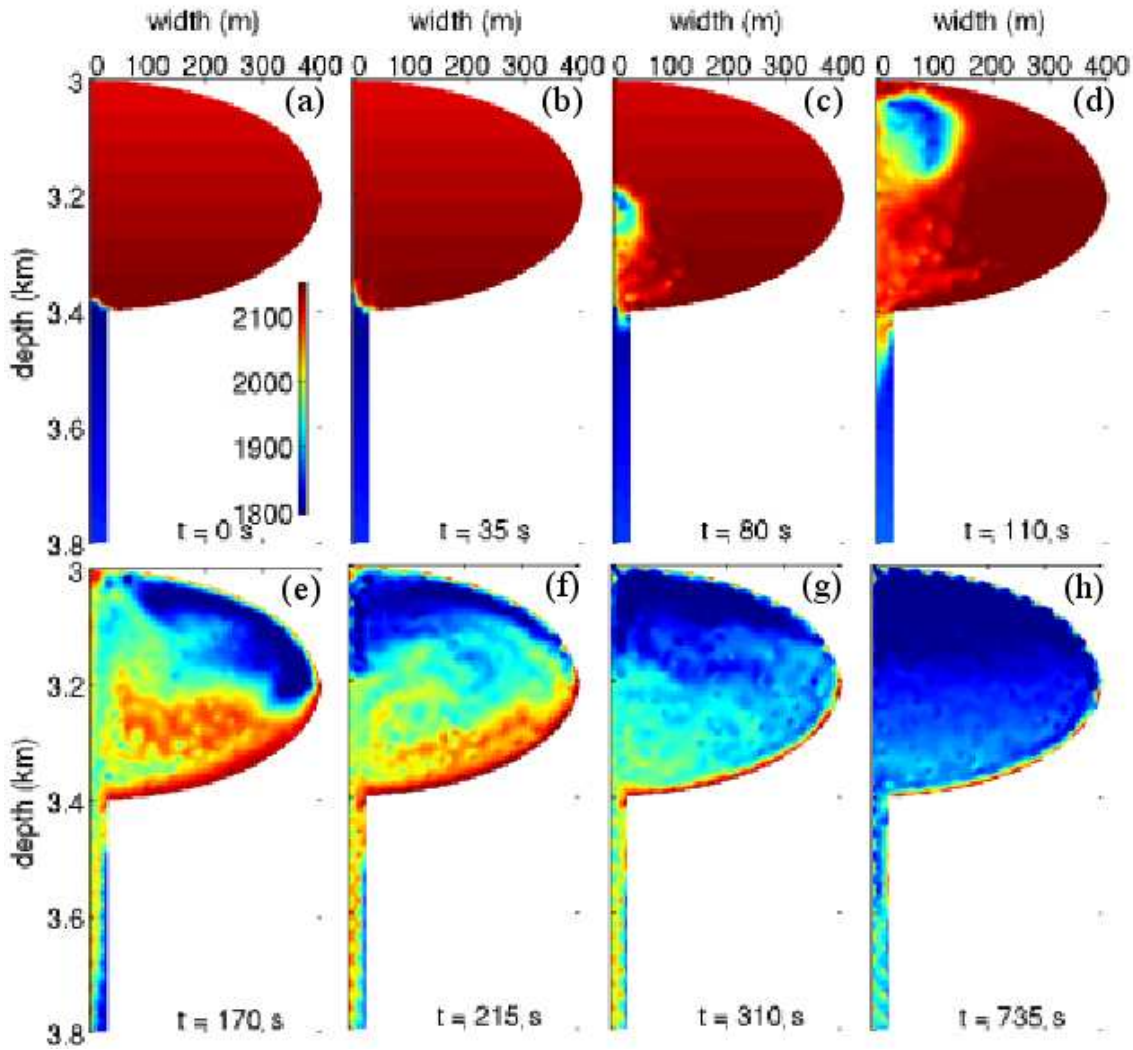

Figure 10.17: Evolution of mixture density (expressed in kg/m^3) for simulation CF-2. Each panel displays results for magma chamber and the first 400 m of dyke at different times.

the same three distances as for figure 10.14 above and at different times. The gravity starts to appreciably change after 70 s, with a trend strictly correlated with mass variation. The horizontal component varies up to about 30 μGal; the peak values occur 2 km away from the chamber axis, as for the previous case. The maximum vertical anomaly is about -85 μGal, and it tends to stabilise after 400-600 s, depending on distance (fig. 10.21).

Figure 10.22 shows the pressure variation with time before (left) and after (right) applying the band-pass filter. The pressure behaviour is similar to that

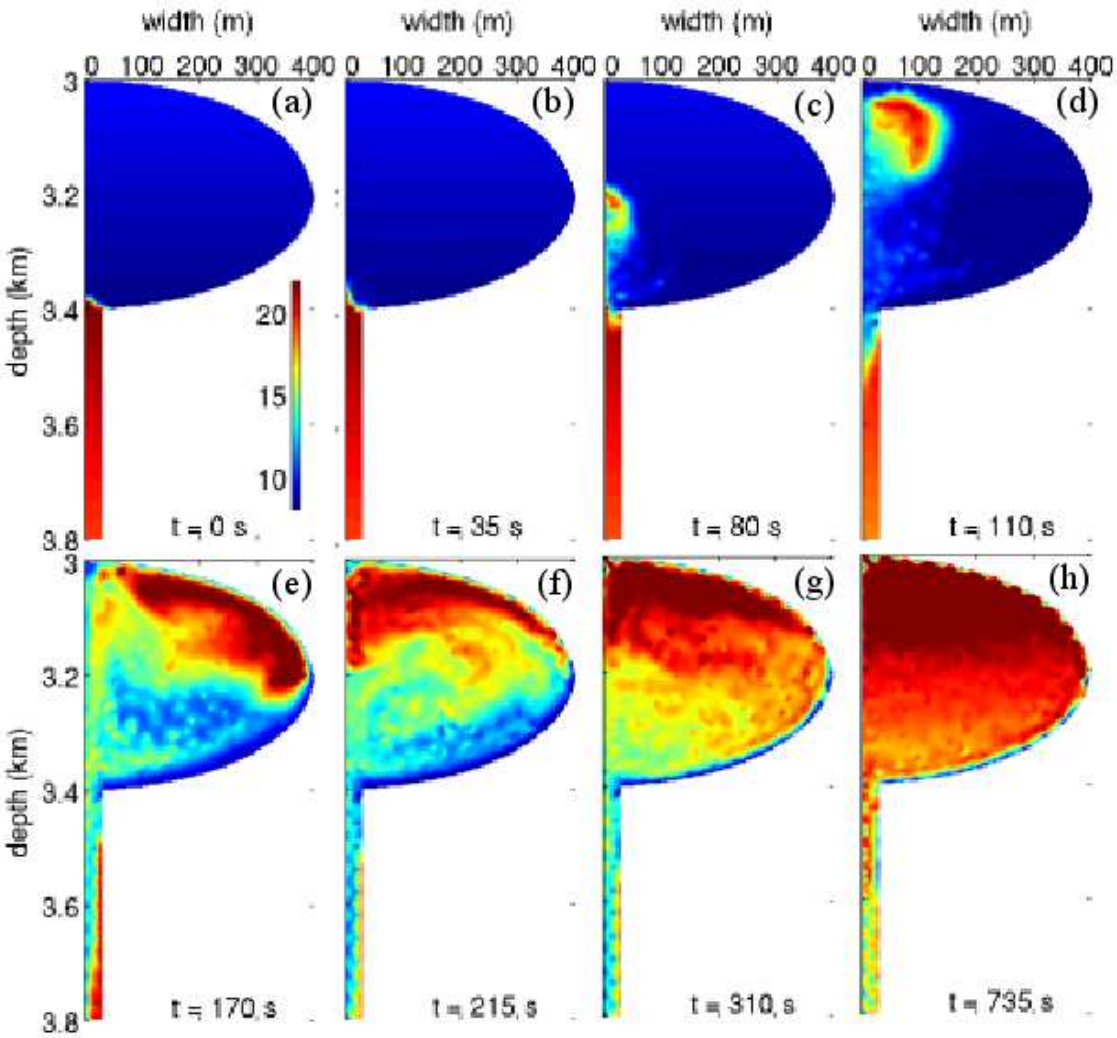

Figure 10.18: Evolution of gas phase distribution (expressed in volume %) for simulation CF-2. Each panel displays results for magma chamber and the first 400 m of dyke at different times.

of the previous simulation. Pressure diplays oscillations with a period of about 100 s which tends to grow faintly with time. Differently from CF-1, there is no initial small peak in pressure (see fig. 10.12 left); the maximum overpressure achieved is 4 MPa at 120 s, corresponding to the arrival of plume at chamber top; moreover, there is not any residual overpressure at long times, according to the no-overpressure initial condition. The filtered pressure shows high frequency oscillations with peak amplitudes similar to those for case CF-1, reported in figure 10.12 right, but significantly lower average amplitude.

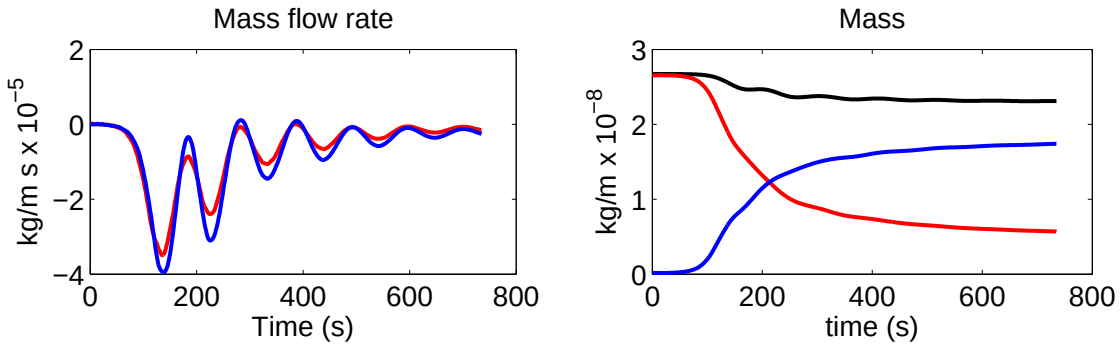

(a) (b)

Figure 10.19: Mass flow rate and mass change with time for simulation CF-2.(a) Mass flow rate computed at dyke base (blue) and chamber inlet (red); (b) mass of mixture (black), trachytic (blue) and phonolitic (red) component in the chamber.

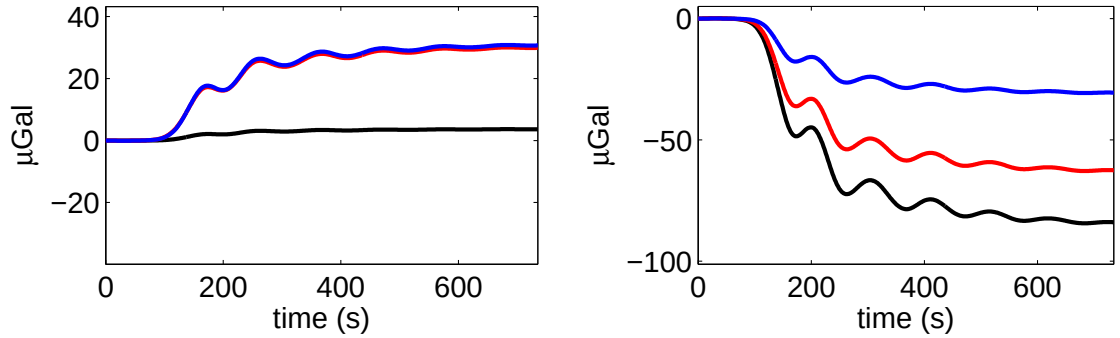

(a) Δg_x (b) Δg_z

Figure 10.20: Horizontal (a) and vertical (b) component of free-air corrected gravity changes vs. time for simulation CF-2. Profiles have been calculated for three distances from the chamber axis on the earth surface: 140 m (black), 1500 m (red), 3200 m (blue)

Simulations CF-3

Results for simulation with an applied overpressure of 20 MPa and an horizontal chamber (CF-3) are shown in figures 10.23 - 10.28. In this case the conditions are the same as for the reference case CF-1, except for the very high overpressure at dyke base. Therefore, comparison between cases CF-3 and CF-1 allows an investigation of the effects of largely different overpressure on the simulated dynamics.

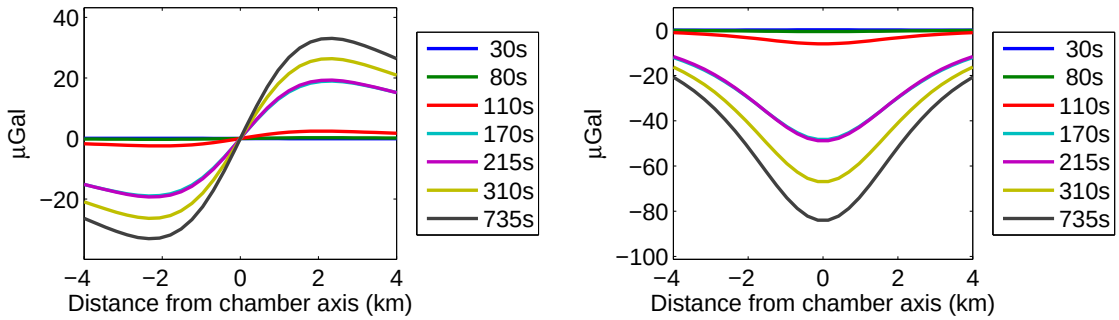

(a) Δg_x (b) Δg_z

Figure 10.21: Horizontal (a) and vertical (b) component of free-air corrected gravity changes with respect to distance from the chamber axis at fixed times, computed for simulation CF-2.

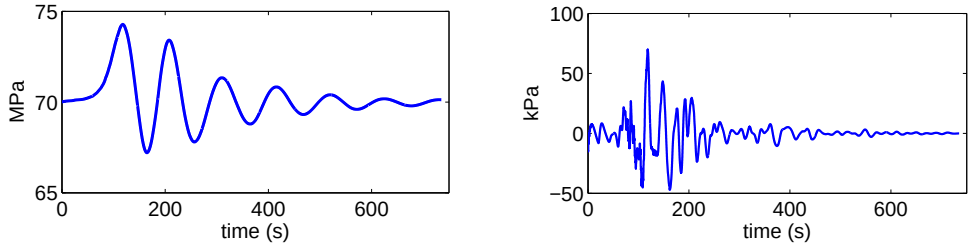

(a) chamber top, depth = 3 km

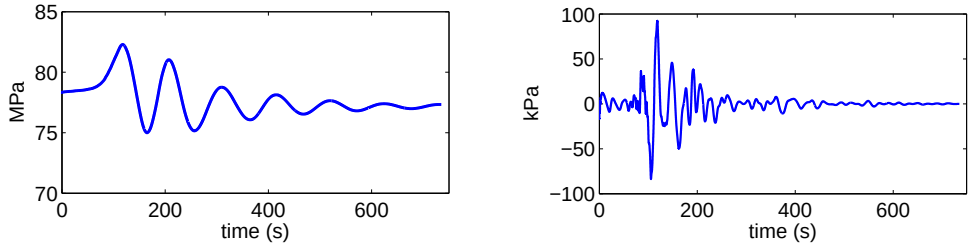

(b) chamber inlet, depth = 3.4 km

Figure 10.22: Pressure changes and filtered oscillations computed at (a) chamber top and (b) chamber inlet for simulation CF-2. Pressure has been filtered with a band-pass filter with cut-off frequencies of 0.025 and 10 Hz (corresponding to a period of 40 and 0.1 s)

The simulated dynamics are similar to the previous ones, but they are accelerated as a consequence of the larger overpressure. The plume starts growing after only 10 s (fig. 10.23(b)) and reaches the chamber top in one minute (fig. 10.23(d)). As observed above, while the lighter trachytic magma enters the chamber, part of

the denser phonolitic magma is pushed down in the dyke. Efficient convection and mixing are triggered at the whole chamber scale; a main central vortex drives the new entered mass from the chamber top towards the middle of the chamber (fig. 10.23(e)). After about 2 minutes, the buoyancy force on the light trachytic magma prevails, and begins to push the plume back to the chamber top. At this time, two main vortexes form (fig. 10.23(f)): the bigger one takes up the upper part of the chamber and it rotates anticlockwise; the other, near the chamber inlet, has a clockwise rotation. After 200 s, the convection pattern begins to be more irregular (fig. 10.23(g)). At the last simulated time (fig. 10.23(h)), the composition is mainly trachytic in the upper part of the chamber and half-half trachytic and phonolitic in the lower one. The maximum velocity is about 15 m/s and it is achieved when the plume reaches the chamber top.

Figure 10.24(a) shows that the mass flow through the chamber inlet is mainly downwards except in the first 40 s when the plume develops; the mass flow at dyke base displays the same behaviour but larger values. The maximum flow rate per unit length is $5.5 \cdot 10^5$ kg/m $\cdot$ s and $3.5 \cdot 10^5$ kg/m $\cdot$ s at dyke and chamber entrance, respectively. The mass flow rate oscillates with a period of about 70 s, shorter than for the previous simulations. After an initial increase due to the injection of trachyte, the mass within the chamber decreases with time (fig. 10.24(b)); the final mass is about 8% less than the initial one. As for CF-1 and CF-2, this decrease is due to the replacement of the resident phonolite by the light trachyte, which after 165 s becomes the major component within the chamber.
The initial high overpressure causes a global increase of pressure, with a peak in overpressure of 30-40 MPa, up to twice the applied overpressure (fig. 10.25, left). This peak is larger then the tensile strength of most natural rocks (Chau and Wong, 1996; Roche and Druitt, 2001; Zhang, 2002) and it probably would produce wall rock fracturing and, maybe, trigger an eruption. Differently from the reference case (fig. 10.12), the maximum of pressure occurs after 30 s, when the plume is only halfway along the axis and it is not preceded by a first smaller peak. The pressure oscillations along the system walls tend to smooth down with time and stabilise to a value corresponding to the driving pressure of 20 MPa (fig. 10.25, left). Applying a band-pass filter, pressure oscillations are spotlighted as in the previous cases. Except for the first large peak of the order of thousands kPa, the oscillation amplitude is of tens to a few hundreds of kPa (fig. 10.25, right). The

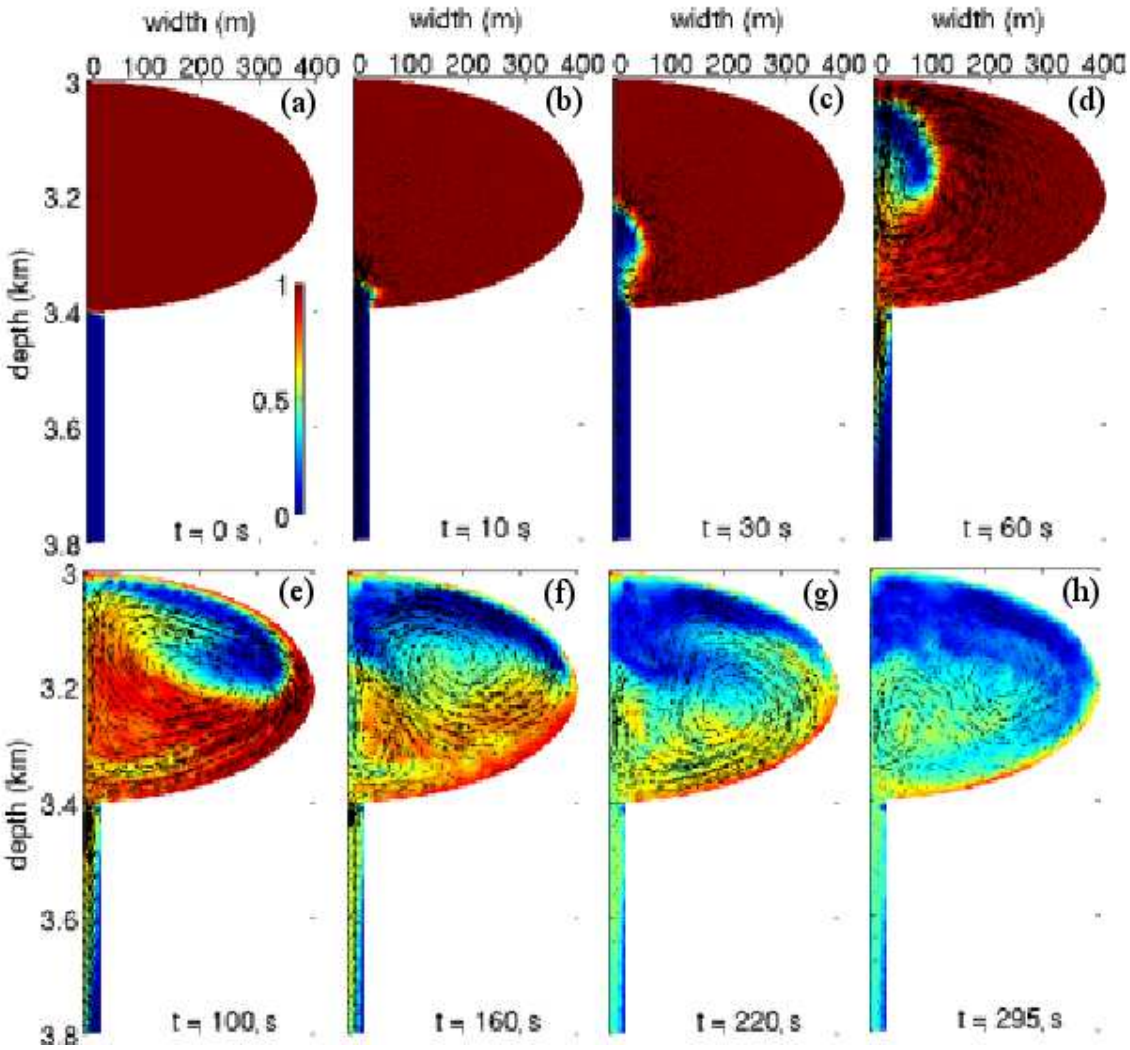

Figure 10.23: Evolution of magma composition for simulation with an applied overpressure of 20 MPa and an horizontal chamber (CF-3). Each panel shows the phonolite fraction and velocity vector within magma chamber and the first 400 m of dyke at different times.

mixture density variations with time are shown in figure 10.26. The initial global pressure increase involves an initial density increase (fig. 10.26(c)); afterward, because of pressure decrease and dominant presence of light trachytic magma, magma density decreases below the initial values.

The computed vertical and horizontal components of gravity anomaly are shown in figures 10.27 and 10.28. An initial negative peak of the horizontal component and contemporaneous positive peak of the vertical one occur after

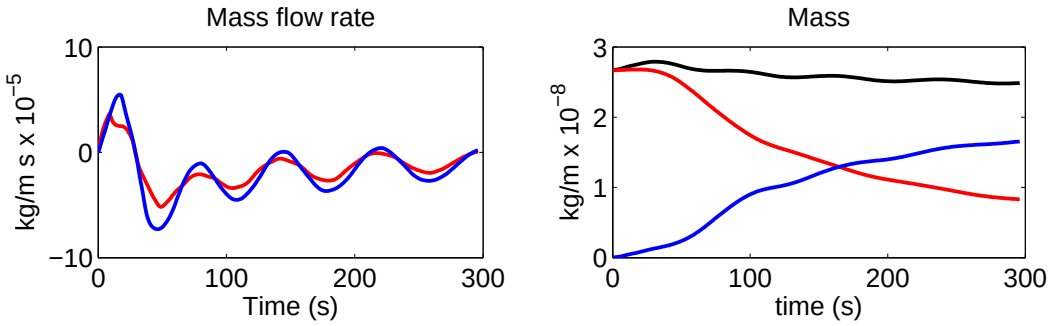

(a) (b)

Figure 10.24: Mass flow rate and mass change with time for simulation CF-3.(a) Mass flow rate computed at dyke base (blue) and chamber inlet (red); (b) mass of mixture (black), trachytic (blue) and phonolitic (red) component in the chamber.

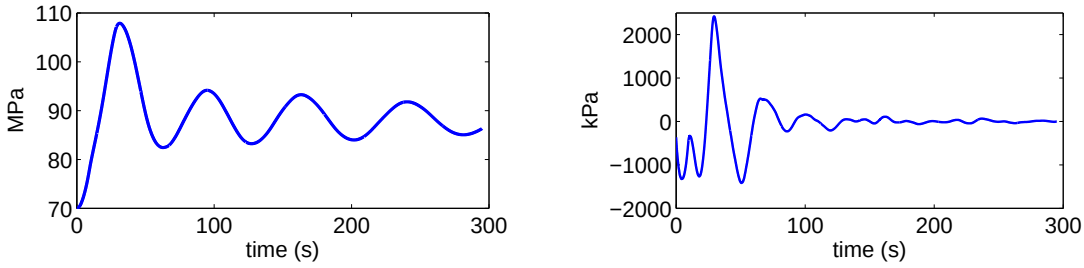

(a) chamber top, depth = 3 km

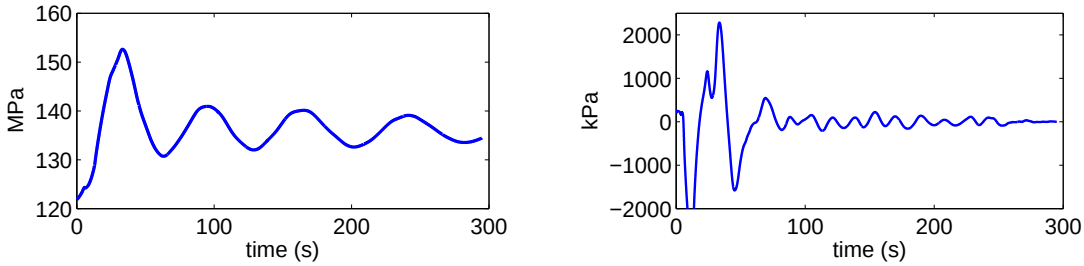

(b) dyke wall, depth = 5.4 km

Figure 10.25: Pressure changes (left) and filtered oscillations (right) computed at (a) chamber top and (b) along the dyke wall for simulation CF-3. Pressure has been filtered with a band-pass filter with cut-off frequencies of 0.025 and 10 Hz (corresponding to a period of 40 and 0.1 s). The right plots have y limits that cut the maximum oscillation but enable to observe the other oscillations

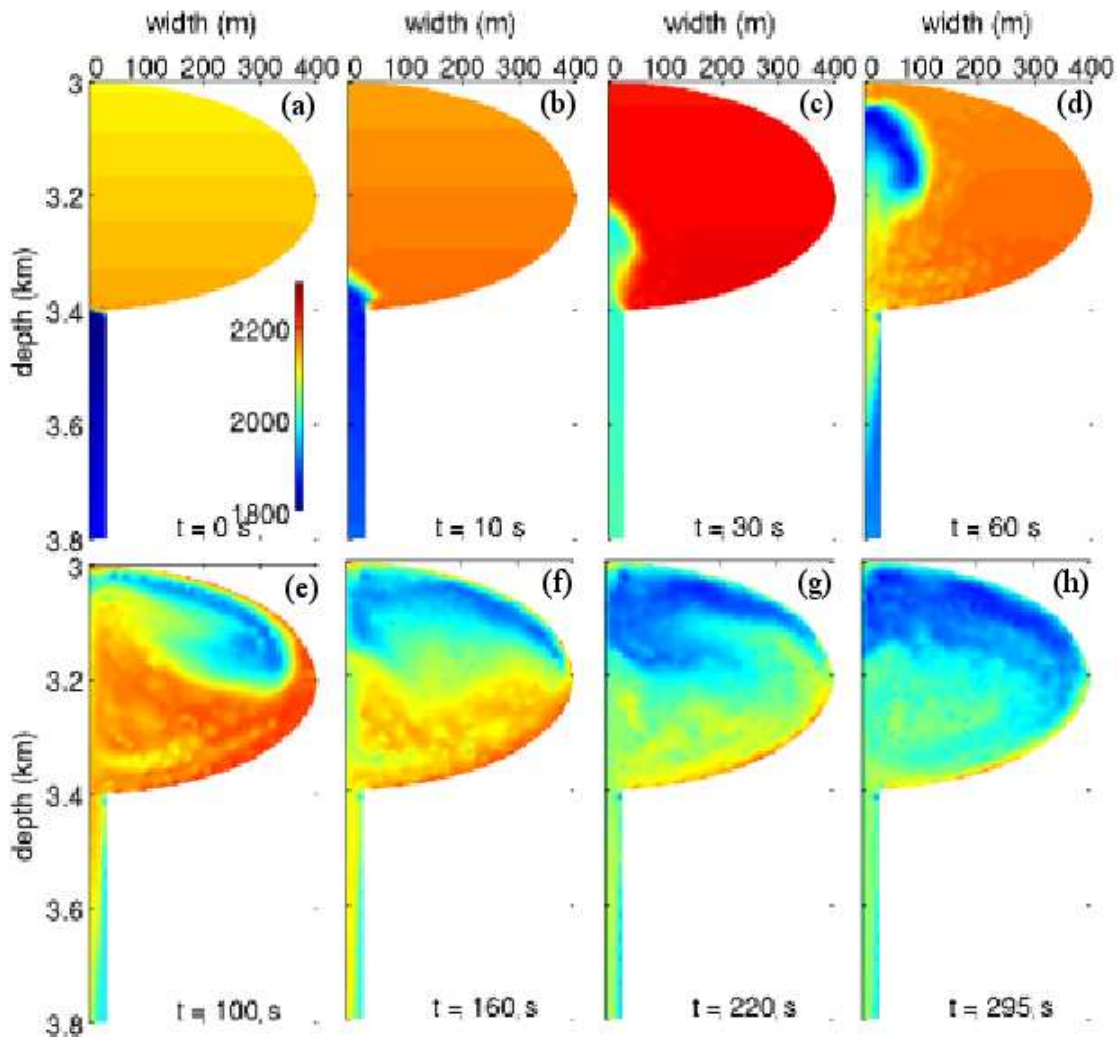

Figure 10.26: Evolution of mixture density (expressed in kg/m^3) for simulation CF-3. Each panel displays results for magma chamber and the first 400 m of dyke at different times.

about 30 s, in correspondence of the maximum pressurisation of the chamber (green lines in figure 10.28). From this time, the vertical anomaly decreases and becomes negative reaching a maximum value of -35 μGal. The horizontal component increases up to 15 μGal.

Simulations CF-4

Results for case CF-4 are shown in figures 10.29 - 10.34. The initial conditions are the same of case CF-3, except for the chamber orientation which is taken

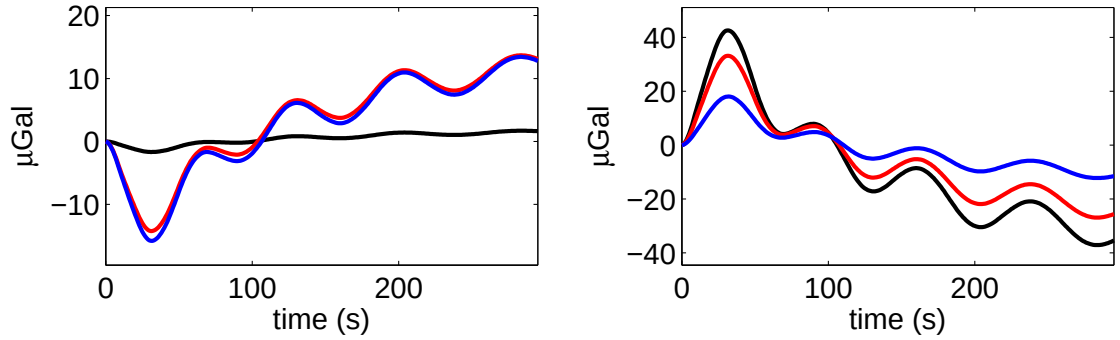

(a) Δg_x (b) Δg_z

Figure 10.27: Horizontal (a) and vertical (b) component of free-air corrected gravity changes vs. time for simulation CF-3. Profiles have been calculated for three distances from the chamber axis on the earth surface: 140 m (black), 1500 m (red), 3200 m (blue)

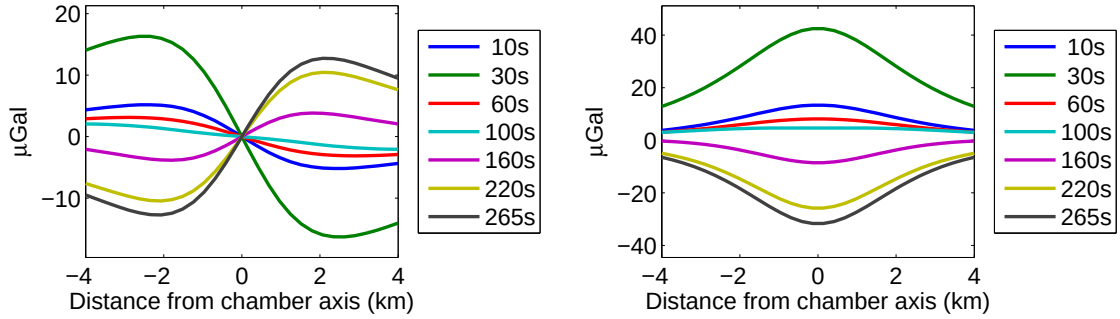

(a) Δg_x (b) Δg_z

Figure 10.28: Horizontal (a) and vertical (b) component of free-air corrected gravity changes with respect to distance from the chamber axis at fixed times, computed for simulation CF-3.

vertical in this case. Comparison between cases CF-4 and CF-3 allows therefore an evaluation of the effects of different prolate vs. oblate chamber geometry.

The plume starts growing after 10 s and reaches the chamber top after 190 s (fig. 10.29(b) and (f)). In this case, closeness of the chamber walls to the rising plume causes plume ramification and break; as a consequence, mixing between resident and new magma is very efficient during plume rise. The elongated geometry prevents the formation of large vortexes and enhances a more complex convection pattern. Panels (f)-(g) in figure 10.29 and 10.23 show that the dynamics within

the vertical chamber are more efficient in removing the resident phonolite than for the horizontal chamber. Initially, when the plume forms, the mass flow (fig.

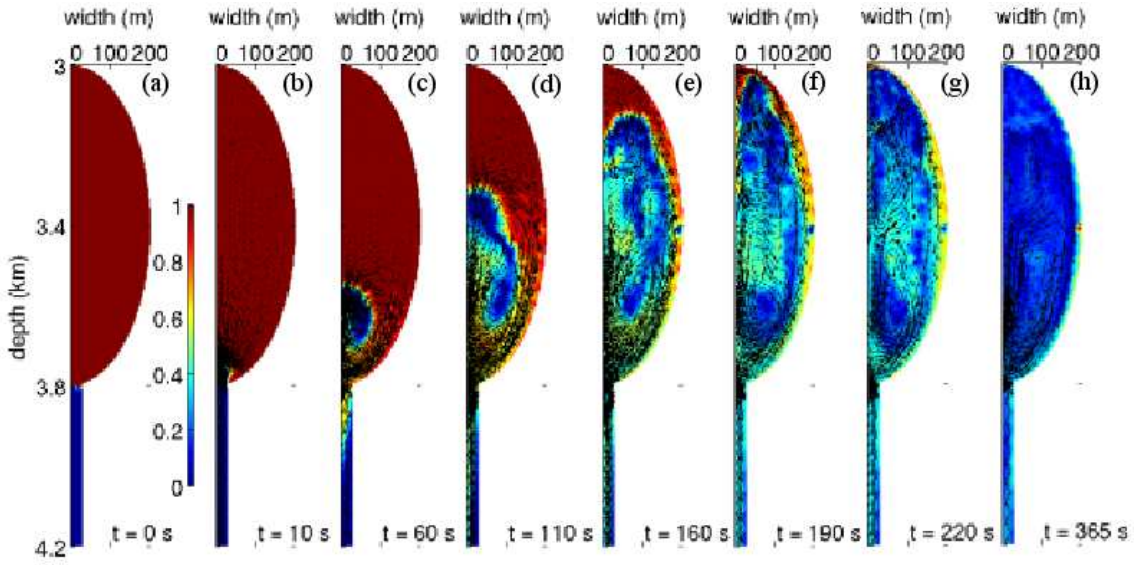

Figure 10.29: Evolution of magma composition for simulation CF-4. Each panel shows phonolite fraction within magma chamber and the first 400 m of dyke at different times.

10.30(a)) is mainly upwards; afterwards, it becomes mainly downwards when the phonolite starts to exit from the chamber. The period of flow oscillations is about 70 s, with peak values of mass flow rate per unit length of $3.75 \cdot 10^5$ kg/m $\cdot$ s, slightly greater than that computed for case CF-3. The mass flow through the dyke base shows the same trend with maximum of $6 \cdot 10^5$ kg/m $\cdot$ s. As for the previous simulations, the chamber mass (fig. 10.30(b)) is initially increased by the injected trachyte, and then it gradually decreases because of the replacement of phonolite by trachyte.

As for case CF-3, the pressure within chamber and along the system walls increases of maximum 30-40 MPa, twice the applied overpressure (fig. 10.31,left). The overpressure oscillates with a period of about 70 s and tends to a value of 20 MPa, equal to the driving pressure. The filtered pressure (fig 10.31, right) shows a trend similar to that of case CF-3 in figure 10.25. As for simulation CF-3, the initial large pressure increase causes volatiles dissolution accompanied by density increase (fig. 10.32(b) and (c)). The following pressure decrease and mixing between volatile-rich trachyte and phonolite produces volatiles exsolution

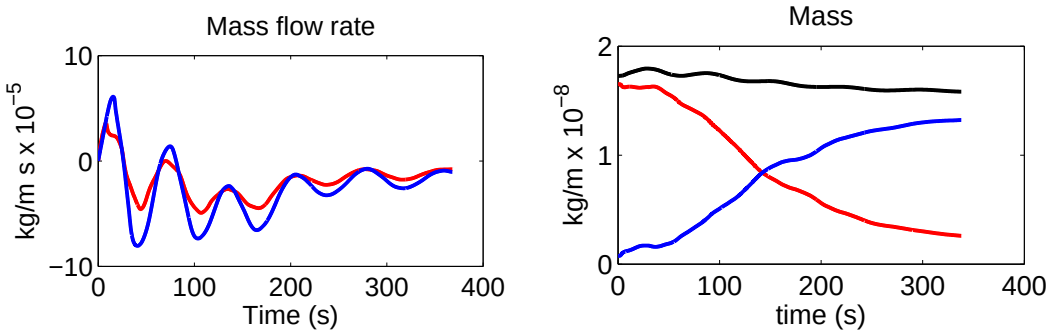

(a) (b)

Figure 10.30: Mass flow rate and mass change with time for simulation CF-4.(a) Mass flow rate computed at dyke base (blue) and chamber inlet (red); (b) mass of mixture (black), trachytic (blue) and phonolitic (red) component in the chamber.

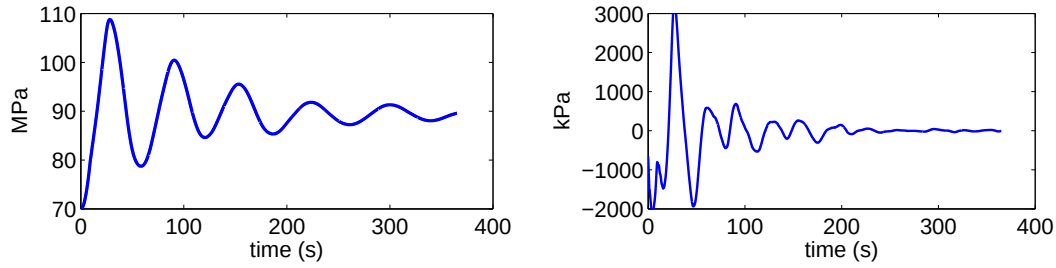

(a) chamber top, depth = 3 km

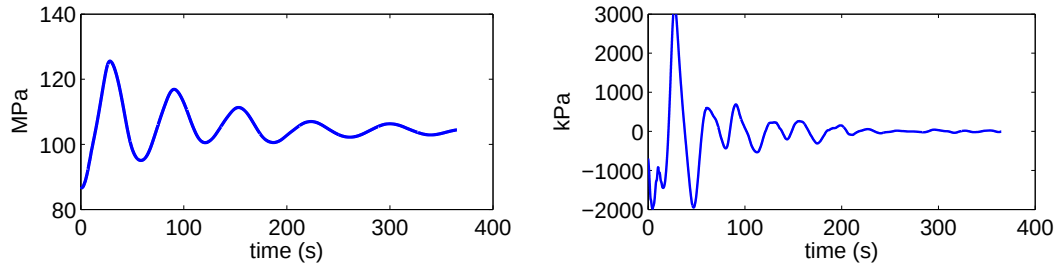

(b) chamber inlet, depth = 3.8 km

Figure 10.31: Pressure variation and filtered oscillations computed at (a) chamber top and (b) chamber inlet for simulation CF-4. Filtered pressure has been obtained with a band-pass filter with cut-off frequencies of 0.025 and 10 Hz (corresponding to a period of 40 and 0.1 s respectively). The right plots have y limits that cut the maximum oscillation but enable to observe the other oscillations

and density decrease of the new entered mass and in all the chamber.

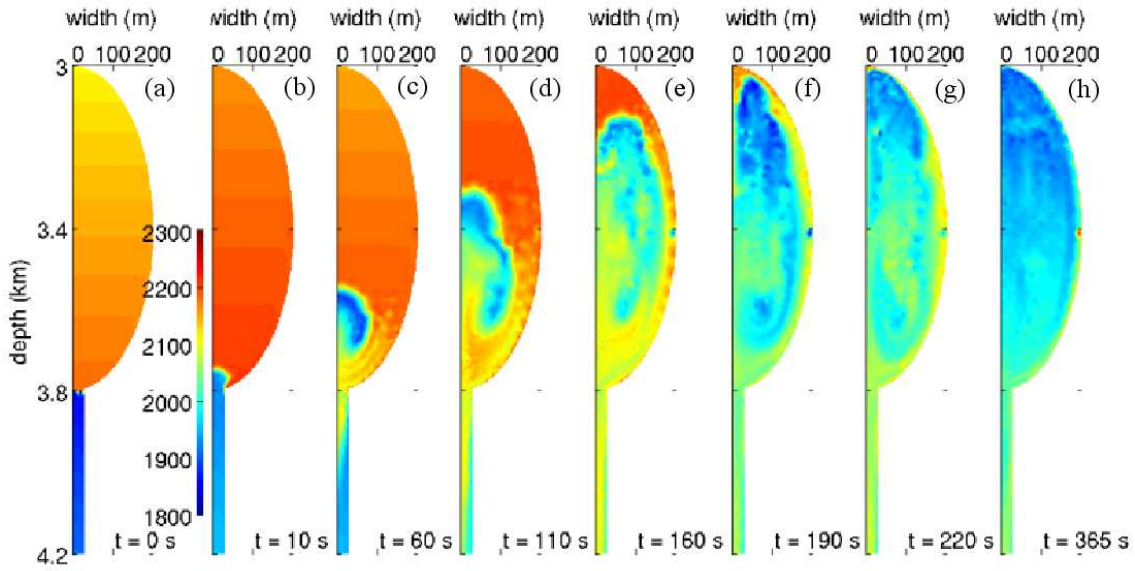

Figure 10.32: Evolution of (a) density (kg/m^3) and (b) gas phase fraction (volume %) for simulation CF-4. Each panel shows results within magma chamber and the first 400 m of dyke at different times.

Figures 10.33 and 10.34 show that the calculated gravity anomaly is very similar to that obtained for the previous CF-3 case.

Simulations CF-5

Results for simulation with volatile-poor trachyte (3 wt% total H_2O and 0.6 wt% total CO_2), 1 MPa of driving pressure and horizontal chamber (CF-5), are shown in figures 10.35 - 10.38. The conditions of this simulation are the same as for reference case CF-1, except for the lower volatile content of the trachyte, which is the same as for phonolite with the addition of 0.1 wt% CO_2 . Comparison between cases CF-5 and CF-1 allows therefore an evaluation of the role of different CO_2 concentrations in inducing convection and mixing dynamics within the magma chamber.

The lower buoyancy due to lower volatile content of the trachytic magma and smaller density difference between trachyte and phonolite cause the plume to take more time to develop, and results in much lower mass of trachyte entering the chamber. After about 180 s (fig. 10.35(a)), the trachyte starts to enter the chamber;

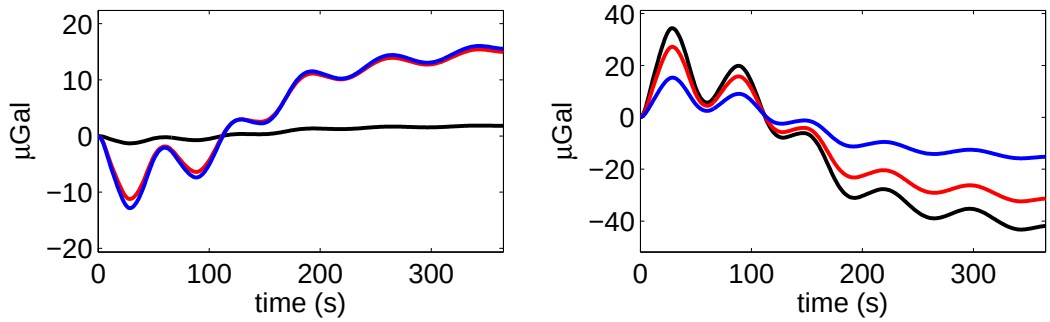

(a) Δg_x (b) Δg_z

Figure 10.33: Horizontal (a) and vertical (b) component of free-air corrected gravity changes vs. time for simulation CF-4. Profiles have been calculated for three distances from the chamber axis on the earth surface: 140 m (black), 1500 m (red), 3200 m (blue)

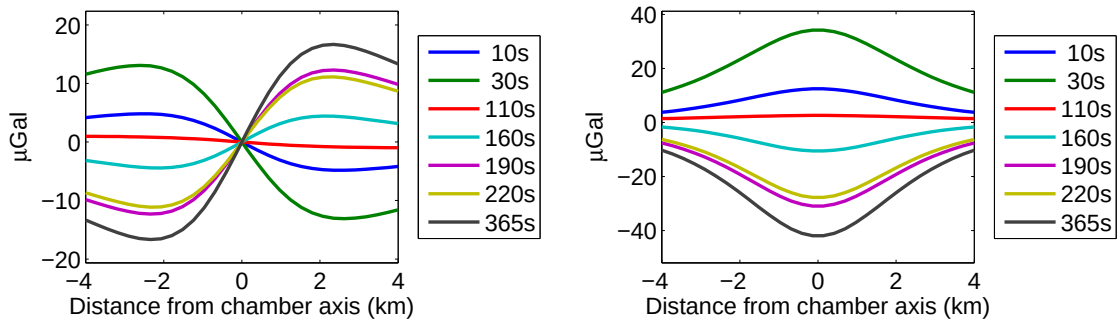

(a) Δg_x (b) Δg_z

Figure 10.34: Horizontal (a) and vertical (b) component of free-air corrected gravity changes with respect to distance from the chamber axis at fixed times, computed for simulation CF-4.

it rises along the chamber axis reaching the roof after 370 s (fig. 10.35(d)) and then spreading laterally (fig. 10.35(e) and (f)). At the meantime, batches of phonolite go down in the dyke (fig. 10.36). Because of the small density contrast, convection is not very efficient, with maximum velocity of 8-9 m/s; well-developed vortexes are not observed to form. After 1400 s, the chamber composition is still mainly phonolitic, with a fraction of trachyte less than 30% (fig. 10.35(g)).

Figure 10.37 shows that the mass flow rate per unit length through the chamber inlet is small, with maximum value of $2 \cdot 10^4$ kg/m $\cdot$ s, 10 times or more less than in previous cases. Contrary to the above simulations, the mass flow rate oscillates

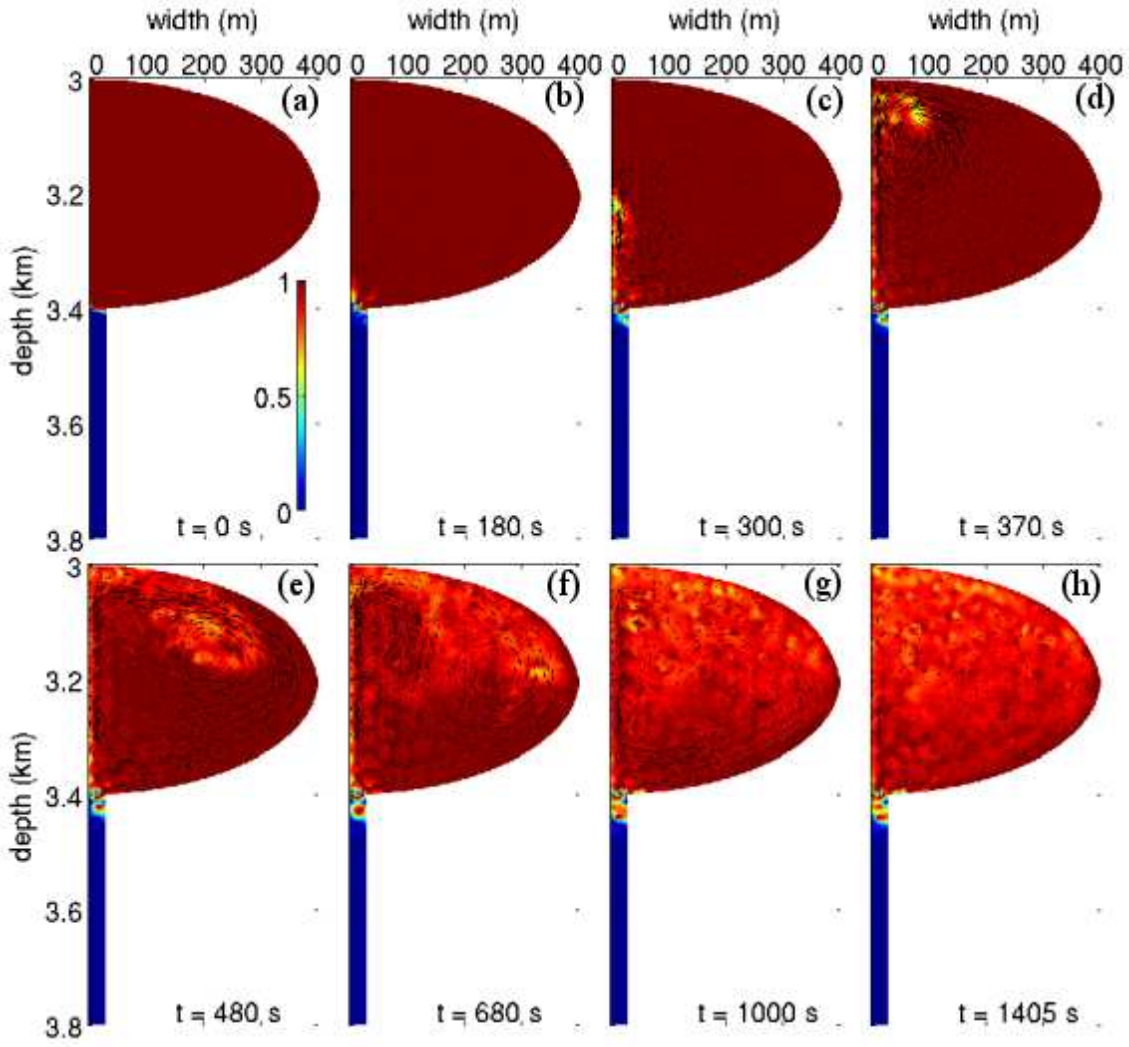

Figure 10.35: Evolution of magma composition for simulation CF-5. Each panel shows phonolite fraction within magma chamber and the first 400 m of dyke at different times.

around zero for about 500 s, smoothing down to zero at larger times. The period of oscillation is of 75 s. This behaviour corresponds to an intermittent plume (fig. 10.35); for the same reason, the downward motion of phonolite is not continuous producing pockets of phonolite-rich magma within the trachyte (fig. 10.35, (e) to (h)). The mass flow through the dyke base is also small, with a peak in flow rate per unit length of $2 \cdot 10^4$ kg/m s . A consequence of this small mass exchange between dyke and chamber is that the gravity changes are very small, with maximum vertical anomaly of $\pm 2\,\mu$Gal (figs. 10.38, 10.39). Such values are

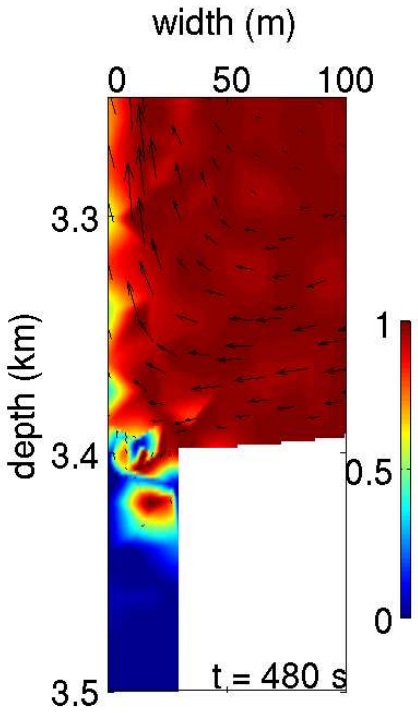

Figure 10.36: Magma composition (reported as phonolite fraction) at 480 s, for simulation CF-5. Zoom of the region near the chamber inlet.

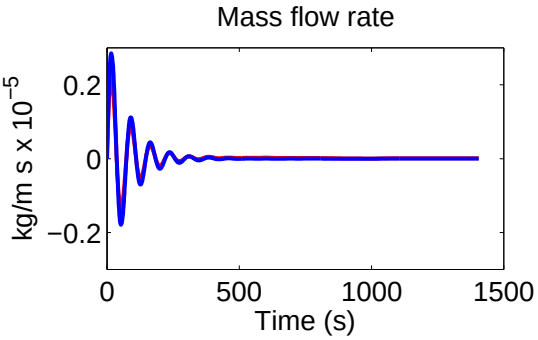

Figure 10.37: Mass flow rate at dyke base (blue) and chamber inlet (red) for simulation CF-5.

below the detection limit of monitoring techniques.

Figure 10.40 shows that even if the dynamics are not very efficient, pressure oscillations occur with peak increase of pressure of 1.5 MPa; pressure tends to stabilise to an overpressure of 1 MPa, equal to the driving pressure.

With respect to the previous cases, CF-5 is remarkable since it shows that a

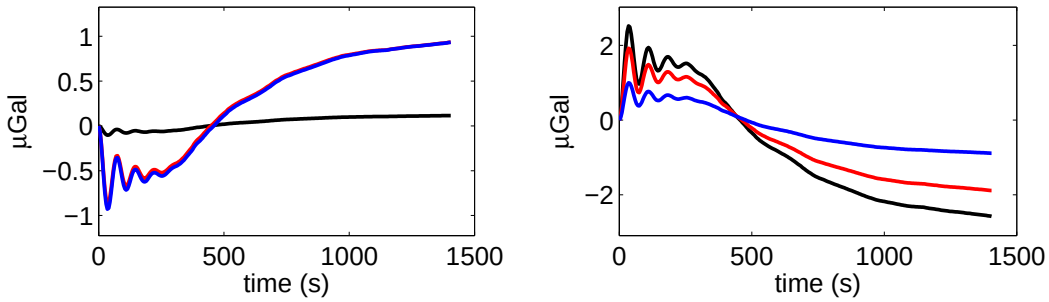

(a) Δg_x (b) Δg_z

Figure 10.38: Horizontal (a) and vertical (b) component of free-air corrected gravity changes vs. time for simulation CF-5. Profiles have been calculated for three distances from the chamber axis on the earth surface: 140 m (black), 1500 m (red), 3200 m (blue)

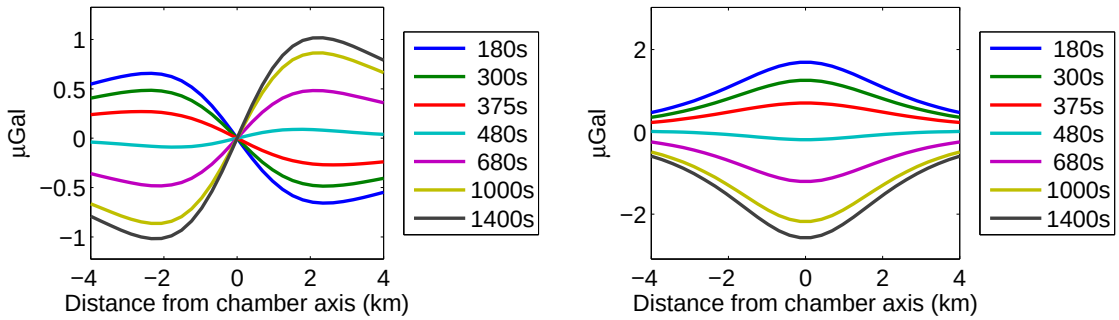

(a) Δg_x (b) Δg_z

Figure 10.39: Horizontal (a) and vertical (b) component of free-air corrected gravity changes with respect to distance from the chamber axis at fixed times, computed for simulation CF-5.

small density contrast induced by small difference in volatile content results in much lower mass of magma injected into the chamber ($3 \cdot 10^7$ vs $1.5 \cdot 10^8$ kg/m) and much larger time scale of magma convection and mixing (tens of minutes vs. minutes).

Simulations CF-6

The results for simulation CF-6, where the gravitationally stable condition is investigated, are shown in figures 10.41-10.45. Even if an overpressure of 1 MPa is applied to the dyke base, the positive density contrast impedes the

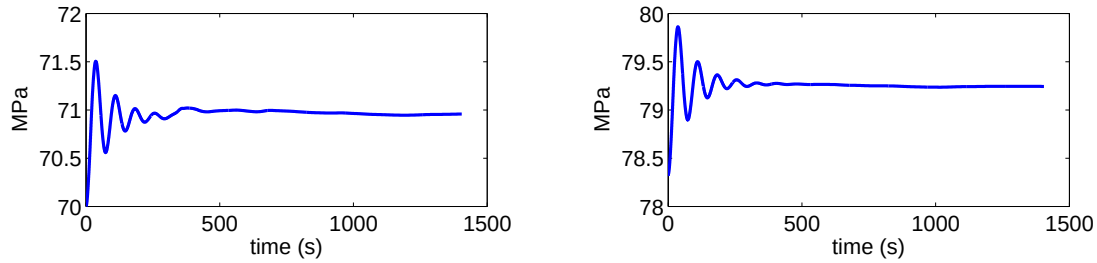

(a) chamber top, depth = 3 km (b) chamber inlet, depth = 3.4 km

Figure 10.40: Pressure changes computed at (a) chamber top and (b) chamber inlet for simulation CF-5.

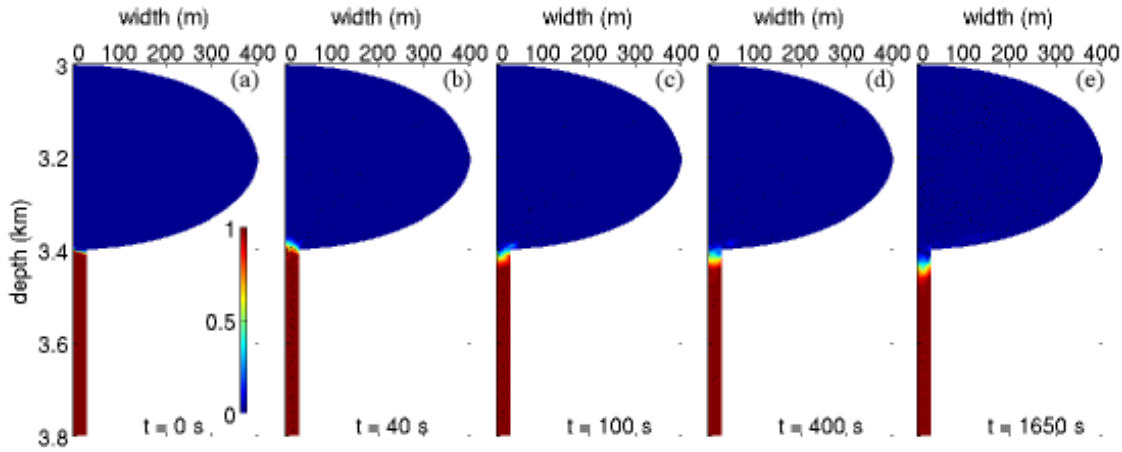

Figure 10.41: Evolution of magma composition for simulation CF-6. Each panel shows results within magma chamber and the first 400 m of dyke at different times.

injection of phonolite into the trachytic magma chamber (fig. 10.41) and mixing and convection are not triggered. The maximum computed velocities are 1 m/s and 2 m/s within chamber and dyke respectively. Figure 10.42 shows that mass flow through the chamber inlet and dyke base is small, up to $3.5 \cdot 10^4$ kg/m $\cdot$ s; this flow is not related to a plume formation but only to small oscillations of the magmas interface (fig. 10.41), with period of about 90 s. Pressure changes are similar to those for the previous CF-5 case (fig. 10.43): oscillations with a period of 90 s and a peak overpressure of 1.5 MPa. After about 600 s, the pressure tends to stabilise to an overpressure of 1 MPa, equal to the driving pressure. Figures 10.44 and 10.45 show that the small mass displacement induces a small gravity change,

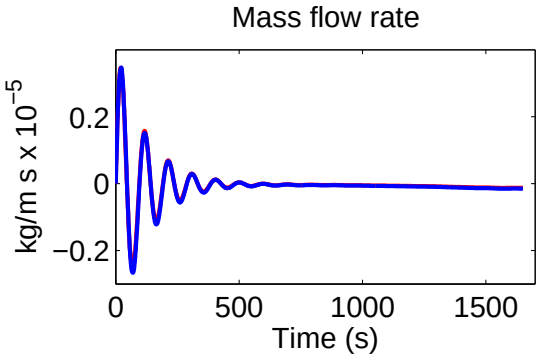

Figure 10.42: Mass flow rate at dyke base (blue) and chamber inlet (red) for simulation CF-6.

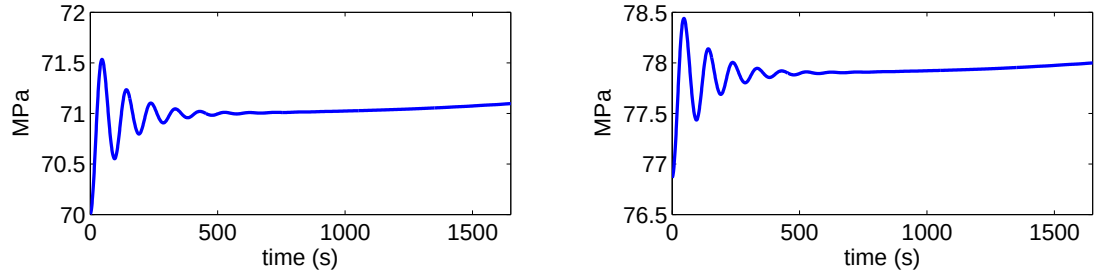

(a) chamber top, depth = 3 km

(b) chamber inlet, depth = 3.4 km

Figure 10.43: Pressure changes computed at (a) chamber top and (b) chamber inlet for simulation CF-6.

not detectable from monitoring instruments. Unlike the previous simulations, the vertical anomaly is positive because of pressurisation and density increase within the chamber.

10.3 Discussion

The present simulation results illustrate a number of processes characterising the dynamics of recharge of shallow magma chambers. which were never shown before. Some of them are not immediately intuitive, like the relatively small time scales (minutes to tens of minutes) associated with plume rise, magma convection and mixing, or like the negative gravity residuals associated with the arrival of deep magma at shallow depth. These results were obtained by taking into account the main forces acting on the simulated system, and represented by pressure

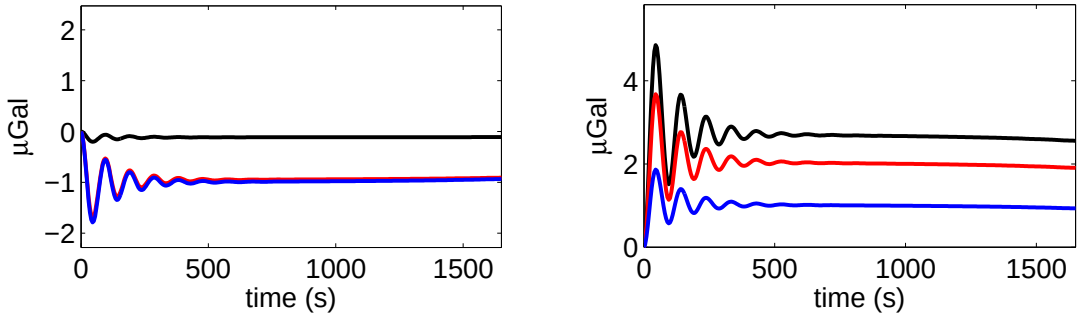

(a) Δg_x (b) Δg_z

Figure 10.44: Horizontal (a) and vertical (b) component of free-air corrected gravity changes vs. time for simulation CF-5. Profiles have been calculated for three distances from the chamber axis on the earth surface: 140 m (black), 1500 m (red), 3200 m (blue).

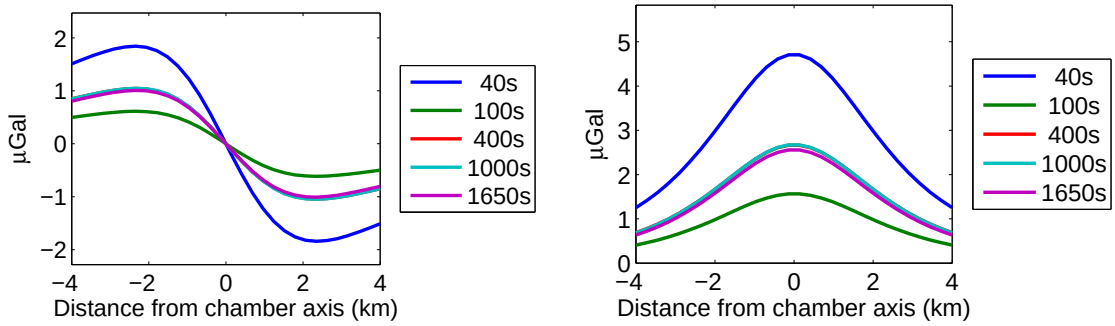

(a) Δg_x (b) Δg_z

Figure 10.45: Horizontal (a) and vertical (b) component of free-air corrected gravity changes with respect to distance from the chamber axis at fixed times, computed for simulation CF-6.

force, gravity/buoyancy force, inertial force, and friction force. It is the complex interplay between all of these forces, combined with the system definition for each simulation, which determines the time-space evolution of the system. In order to take into account realistic conditions of magma dynamics, multicomponent gas-liquid equilibrium, liquid magma density and viscosity are modelled as a function of composition in terms of major oxides, and the effects of gas bubbles are accounted for. Magmatic properties also vary in space and time, according to the local conditions. Magma compressibility is fully accounted for, allowing consideration of any possible gas volume fraction and density change, and leading

to confident calculation of the magma flow dynamics over the entire spectrum of the considered conditions.

The major limits of the present analysis are represented by the assumption of Newtonian rheology, the assumed isothermal flow conditions, the homogeneous flow assumption implying no separation between liquid and gas phases, the neglect of crystallization, and the 2D approximation. These limits require a brief discussion in order t evaluate their relevance for the obtained results.

Newtonian rheology

Liquid magma behaves as a Newtonian liquid, unless the rate of strain becomes so large to approach the critical rate for magma rupture (Dingwell and Webb, 1989). This condition leads to magma fragmentation in volcanic conduits, where the rate of strain can be of order 10 s^{-1} (Papale, 1999). Calculated rates of strain in the present simulations are several orders of magnitude lower, ensuring that liquid Newtonian rheology can be confidently assumed. Non-Newtonian pseudo-plastic (shear thinning) behaviour can occur at significantly lower rates of strain in liquid-crystal mixtures when the solid fraction exceeds 30 vol% (Caricchi et al., 2007). Crystals have been neglected in the present simulations. However, volcanic products at Campi Flegrei typically show low crystal contents around 10 vol% or less, suggesting that crystal-induced non-Newtonian rheology was unimportant. Finally, bubble suspensions may display shear-thinning behaviour when the capillary number $\mathrm{Ca} = \frac{\mu \mathrm{d_B} \dot{\gamma}}{\sigma} \approx 1$ (Llewellin and Manga, 2005), where μ is liquid viscosity, $\mathrm{d_B}$ is the undeformed bubble diameter, $\dot{\gamma}$ is rate of strain, and σ is surface tension at the gas-liquid interface. In the range of conditions of our simulations, non-Newtonian rheology requires $d_B > 200$ μm. However, the maximum 20 % gas volumes in the simulations, together with an assumed bubble number density of $10^{15} \mathrm{m}^{-3}$ (Cashman et al., 2000), results in an average bubble diameter < 10 μm, well below the size required for significant bubble deformation and appearance of shear thinning.

Isothermal flow

The repsent simulations consider the existence of a magma chamber connected with a deep feeding region. In such a system, the magma is assumed to have resided for sufficiently long time at shallow level, so that a well-develop temperature profile already exists in the rocks immediately surrounding the chamber. In such a case, significant cooling is not expected to occur over the short time-scales

(minutes) of the present simulations. Temperature changes may originate if the two phonolitic and trachytic magmas involved in the convection dynamics have originally a different temperature. A temperature of about 950 °C is estimated for the trachytic magma entering the shallow phonolitic chamber prior to the 4100 BP Agnano-Monte Spina eruption (Rutherford and coll., 2004). Unfortunately, the temperature of the phonolitic magma for that eruption is not know. Magma temperature estimates for a number of Campi Flegrei eruptions show values between 900 and 1000 °C in 80 % of cases (Sbrana, INGV-DPC Project V3_2 Campi Flegrei: Final report). Thus, it is likely that if there was a temperature difference between the two magma types, this was less than 5% . Taking the same temperature for the two magma types is therefore not expected to be a major assumption.

Homogeneous flow

The numerical code GALES employed for the present simulations treats the magmatic mixture as an homogeneous "pseudofluid", that is, a hypothetical one-phase fluid with properties accounting for the presence of different phases, like the silicate liquid and the gas bubbles (or crystals). This is a classical approach in fluid dynamics, which is justified as long as the true phases can be assumed to be characterized by the same velocity pattern. In the present case of gas bubble suspension in a melt, the balance between buoyancy and friction force on suspended gas bubbles determines whether the homogeneous assumption is justified or not. Such a balance is conveniently expressed by the Archimedes number referred to gas bubbles $\mathrm{Ar_B} = \dfrac{\mathrm{g d_B} \rho^L \left(\rho^L - \rho^G\right)}{\mu^2}$ (similar to Ar for the flow already introduced in section 10.2), where g is gravity acceleration, $\mathrm{d_B}$ is bubble diameter, ρ^L and ρ^G are liquid and gas density, respectively, and μ is liquid viscosity. However, even in cases where buoyancy dominates over friction, the homogeneous assumption can be still justified if inertia dominates over buoyancy, forcing the dispersed gas bubbles to follow the general flow pattern rather than separating from it.

In the range of conditions determined from the present simulations, the largest values or Ar are of order 10^{-14}, signifying that the gas bubbles and the liquid are fully coupled and that homogeneous flow is a well justified assumption.

Neglect of crystallization

Although small or negligible temperature changes may occur over the sim-

ulated tome scales of magma ascent and convection, crystallization to a certain extent is expected to occur as a consequence of supersaturation induced by H_2O exsolution and associated rise of liquidus surface, as well as of fugacity changes due to compositional changes upon magma mixing. Crystal nucleation and crystal-liquid reactions would cause a number of changes in fluid properties due to changes in liquid composition, crystal concentration, and concentration of volatiles with respect to the liquid. The effects of such changes on magma flow dynamics are highly non-linear, and can result in significant (Neri et al., 2003). Although crystal concentration in Campi Flegrei volcanic products of the last epoch of activity are in general confined to < 10-20 vol% with typical scarce or no microlites, there is evidence of crystal-liquid reactions and re-equilibration consequent to trachytic magma injection into the shallow phonolitic magma chamber of the 4100 BP Agnano-Monte Spina eruption (Rutherford and coll., 2004). As a consequence, a more sophisticated investigation accounting for liquid-crystal reactions is required in future more advanced modelling of magma chamber processes.

2D approximation

The present simulations assume cartesian 2D coordinates, implying that the third not-considered dimension must be much longer than the two dimensions over which the computation is done. The computational plane is therefore representative of the conditions on every plane perpendicular to the longest dimension, provided that such a plane is located sufficiently far from the neglected system borders. Such an assumption limits the investigation to a restricted type of magma chamber geometries for which one dimension is much larger than the remaining two. Accordingly, gravity changes computed in the previous section assume a third not-simulated chamber axis one order on magnitude larger than those which constitute the computational domain. The present 2D assumption is therefore not adequate for, e.g., spherical magma chamber, or for chamber fed by a cylindrical conduit rather than by a dyke. For the geometries considered in the present simulations, the present 2D assumption is adequate as long as side effects close to the edge of the not-simulated chamber and dyke axis can be neglected.

After having pointed out the advantages and limits of the present investigation, the results of the numerical simulations can be better understood and

discussed.

Time scale of magma convection and mixing

The first relevant point emerging from the present results is represented by the relatively short time scale of magma convection and mixing, of the order of minutes to a few tens of minutes in the considered cases. As said above, unfortunately, numerical simulations made with a 10 times narrower feeding dyke (case CF-7-CF-9 in table 10.3) were affected by bad numerical convergence and too large numerical residuals, therefore, they are not useful for this study. However, a rough indication on the time scale can be extracted. Although poorly confident, those simulations point to time scales of the order of a few to some tens of minutes for magma convection and mixing in the magma chamber. There is no independent evaluation of such time scales for real case at Campi Flegrei or for other volcanoes in the world, which is an important limit in that it does not allow comparison with other observations or results. There are however some indirect indications that concur to suggest relatively short time scales for such processes. One of such indications comes from the Agnano-Monte Spina eruption. As already reported above, experimental liquid-solid equilibrium studies (Rutherford and coll. (2004), Rutherford from INGV-DPC Project V3_2 Campi Flegrei: Final report) suggest that a shallow chamber hosting magma with phonolitic composition, which was invaded by deep CO_2 -rich trachytic magma on a time-scale of 1 day before the eruption. The erupted composition is however mostly trachytic, without any evidence of the two compositions involved in the mixing process at the scale of chemical analyses. This suggests that mixing was very efficient on a time scale less than 1 day. This suggestion is consistent with our results. As already explained, mixing is referred to in the numerical simulations only as a macroscopic process on a spatial scale comparable with that of computational node spacing (3 to 30 m). Such a macroscopic mixing is found to occur efficiently on the time scale of minutes to tens of minutes depending on the simulation conditions. It is therefore well possible, based on our results, that chemical mixing enhanced by such an efficient mechanical mixing takes only a matter of hours to homogenise the liquid composition. It can be noted that the disappearance of the phonolitic magmatic and-member in the chamber after convection and mixing in favour of < 80 wt% trachyte occupying most of the volume (cases CF-1-CF-4) is perfectly consistent with the mainly trachytic composition for the Agnano-Monte

Spina eruption and chamber processes as revealed by experimental petrology.

Magma dynamics

The present numerical results show that all examined cases, where an upward positive density gradient is assumed, buoyancy plays a dominant role in the processes. This is well shown by the substantial similarity of the simulated dynamics in cases CF-1 to CF-3, where the applied overpressure is varied from 0 to 20 MPa. On the contrary, when case CF-1 is repeated by taking the same overpressure and largely reducing the density contrast between the two magma types (case CF-5), much less efficient convection dynamics emerge.

Once the buoyant plume has accelerated upon further decompression and expansion during rise towards the chamber top, inertia becomes also important. This is revealed by the oscillatory motion of the gas-rich magma on top of the chamber, whereby clockwise vortex rotation induced by inertia alternates to counterclockwise rotation induced by buoyancy which tries to move the low density magma towards the top.

The repsent numerical simulations reveal the existence of pressure oscillations with periods of 1-2 minutes. Such total pressure oscillations have an amplitude initially 2-5 times larger than the applied overpressure, then they smooth down to a residual overpressure equal to the applied one. Even the case with no applied overpressure (CF-2) shows pressure oscillations and a peak in overpressure as large as 4 MPa. Pressure oscillations with much lower amplitude of the order of several tens to several hundreds KPa and periods of order 1-10 s also occur.

The peak in overpressure occurs in correspondence of plume rise towards chamber top. The excess in overpressure with respect to that applied from below is due to further volatile exsolution and expansion of the plume as it rises towards low pressure regions. Such an expansion indices compression of the ambient fluid, forcing part of the resident magma to flow out of the chamber and into the feeding dyke. The present results suggest therefore that wall rock rupture due to chamber overpressure is more likely to occur at an early stage of new magma injection into a pre-existing chamber.

As long as convection develops, the system re-equilibrates to the new imposed pressure through pressure oscillations, whereby magma compression due to further plume rise and expansion is dynamically counteracted by magma flow out of the chamber. This process results in oscillations of fluid flow velocity within

the feeding dyke, with periods of positive (upward) flow alternating to periods of negative flow. The trends in high-frequency pressure oscillations are much more difficult to be interpreted in terms of simple processes occurring within the simulated system. Such relatively rapid pressure changes depend in fact on a number of processes including vortex formation and frequency of rotation, pressure wave development and transport within the fluid system, wave reflections, and wave interference. It is worth noting that the GALES code is capable to solve compressible flow dynamics including transonic flow and shock waves. It is therefore an ideal tool to predict the patterns of transport and interference of pressure disturbances within a dynamic fluid system. This characteristic of the fluid flow code is particularly relevant in the present work, where pressure/stress transients produced at the fluid-rock boundary are employed to predict the expected patterns of ground deformation over a wide frequency spectrum (see the following chapter 11.

Mass and gravity changes

Oscillations similar to those found in total pressure are also produced by the numerical simulations for mass flow rate at chamber inlet, and for gravity on the Earth's surface. The discussion in the above subsection clarifies what is the relationship between pressure and mass flow-rate - hence gravity - oscillations: they are due to a dynamic balance between additional overpressure induced by plume rise and expansion pushing magma downwards, and applied dyke overpressure pushing magma upwards. The net result of this balance is a progressive replacement of dense resident phonolitic magma by light incoming trachytic magma, and total mass decrease in the magma chamber. The final displacement of light magma towards a region closer to the Earth's surface, and parallel displacement of dense magma far from it, results in a net decrease of the local gravity acceleration. Such a decrease occurs through oscillations, with a possible initial positive peak reflecting the initial stage of new magma injection into the chamber. Such a decrease in the local acceleration of gravity (or negative gravity residual) represents a somewhat counterintuitive result: the arrival of new magma into a shallow chamber is not accompanied by an increase, rather, a decrease of total mass stored at shallow level. Obviously, if the new magma pushed into the chamber is not buoyant with respect to the residentmagma, then the net effect would not be decrease, but increase in total mass due to compression by over-

pressure, thus positive gravity residual. However, it is discussed in section 7.1 that the thermodynamics of multicomponent gas-liquid reactions are such that a shallow degassing magma invariably decrease its total CO_2 /total H_2O ratio, with respect to the same magma degassing at deeper levels. Due to large effect of CO_2 in reducing the H_2O saturation content, a deeper magma commonly tends to be less dense, at equal pressure conditions, than a shallower magma. When the two magmas come into contact, the deep, CO_2 -enriched magma is therefore buoyant. It is argued here that such a process may be general, and represent one fundamental mean of triggering convection and mixing in volcanic systems. If so, negative gravity residuals may be expected in association with the arrival of new magma batches in shallow magma chambers.

The negative gravity residual found from the numerical simulations in association with the arrival at shallow level of new magma, markedly contrasts with a conclusion from Gottsmann et al. (2003), who identify such a magma arrival with an invariably positive residual. On the contrary, they associate a negative gravity residual with "void formation" and "eruption unlikely". Their conclusion derives from not taking into account the internal chamber dynamics, whereby complex convection processes may result in progressive replacement at shallow level of dense degassed by light volatile-rich magma. In any case, more in-depth evaluation requires the execution of numerical simulations in a broader range of possible conditions, as well as the development of more sophisticated modelling with non-fixed chamber walls.

Chapter 11

Simulations of rock deformation

11.1 Initial and boundary conditions

The rock system for the 2D numerical simulations performed here has been defined assuming that the chamber-dyke system is located at the site of the Agnano-Monte Spina eruption, in the north-east sector of the Neapolitan Yellow Tuff caldera (fig. 11.1). The horizontal direction of the 2D model is oriented east-west.

The P- and S-wave velocities were derived from the 3D velocity model of

Figure 11.1: View of the Campi Flegrei caldera. The green arrow indicates the Agnano plan.

the Campi Flegrei system (Zollo et al., INGV-DPC Project V3_2 Campi Flegrei: Final report, Judenherc and Zollo (2004); Battaglia et al. (2007); Dello Iacono et al. (2006); Vassallo and Zollo (2007)), in cooperation with Aldo Zollo and co-workers. The rock density was obtained from the compressional velocities according to the equation of Gardner et al. (1974):

$$\rho = 0.23 v_p^{1/4} \tag{11.1}$$

In order to verify the influence of rock properties on the calculated deformation patterns, four different velocity/density structures of increasing complexity was defined. The first model (named HOMO) considers an homogeneous medium with v_p = 3000 m/s, v_s = 1875 m/s (or constant v_p/v_s = 1.6) and ρ = 1700 kg/m^3 according to equation (11.1). The second model (1D-MODEL) assumes that rock properties vary with depth: the v_p vertical profile shown in figure 11.2 is an average profile computed by Zollo and co-workers; the v_p value ranges from 1500 m/s to 6500 m/s with a rapid increase at the passage from the volcanoclastics filling the caldera to the pre-caldera rock layers; constant v_p/v_s = 1.6 is assumed. The next two models assume that rock properties change both vertically and horizontally according to the results achieved by Zollo et al. (INGV-DPC Project V3_2 Campi Flegrei: Final report).

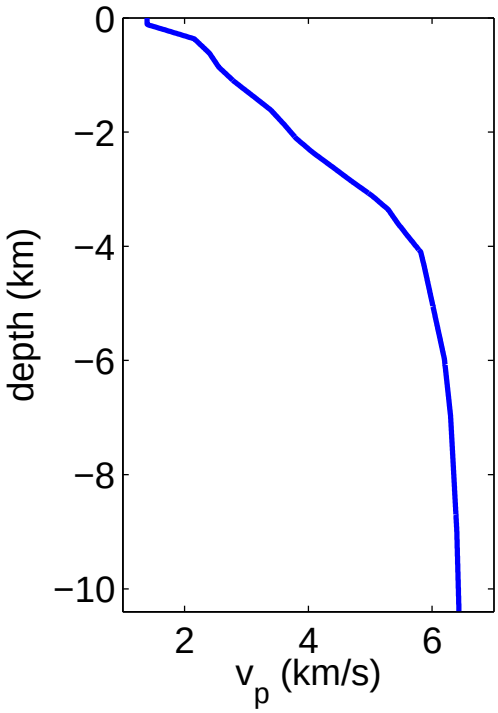

Figure 11.2: v_p vertical profile assumed for the model 1D-MODEL

In particular, the v_p 2D profile has been inferred from the v_p 3D model (Judenherc and Zollo, 2004; Vassallo and Zollo, 2007) selecting a band 50 km long and 15 km wide centered on the site of the Agnano-Monte Spina eruption (figure 11.3). Afterwards, v_p values in this band have been averaged along the third (north-south) direction. The adopted v_p section is shown in figure 11.4 (top panel). This third rock model (2D-MODEL) assumes a constant v_p/v_s = 1.6. The last, and most complex model (VPVS-MODEL) considers a v_p/v_s ratio varying with depth

Figure 11.3: View of the Campi Flegrei area where the green arrow indicate the Agnano Monte-Spina eruption site. The yellow band highlights the area considered to average the v_p values

(fig 11.5). The assumed v_p/v_s profile is an average obtained from those computed by Vanorio et al. (2005). Since density is a function of only v_p according to our assumption (eq. (11.1)), the last two models show same v_p and density, and different v_s model (figs. 11.4-11.6). The main differences between the v_s models are shown in the central part of the section, corresponding to the caldera area.

To complete the rock system definition, a topographic profile has been defined. The considered topography is very simplified with respect to the real one, representing only the caldera borders (fig. 11.7). This simplified profile allows the main topographic features of the caldera to be accounted for since evaluating the deformation patterns associated with the simulated dynamics.

In order to avoid spure reflections, absorbing layers were placed at the lateral and bottom boundaries of the rock domain. Several simulations have been carried out to calibrate the domain size and the space-time differentiation step. To avoid the influence of the absorbing boundaries, the domain size has been extended 50 km and 10 km along the horizontal and vertical direction, respectively. The grid spacing and the time step have been fixed to 10 m and $1.5 \cdot 10^{-4}$ s, respectively, in order to satisfy the model stability conditions reported in eq. (3.13).

The simulation of the rock elastic response to the fluid-dynamic processes has

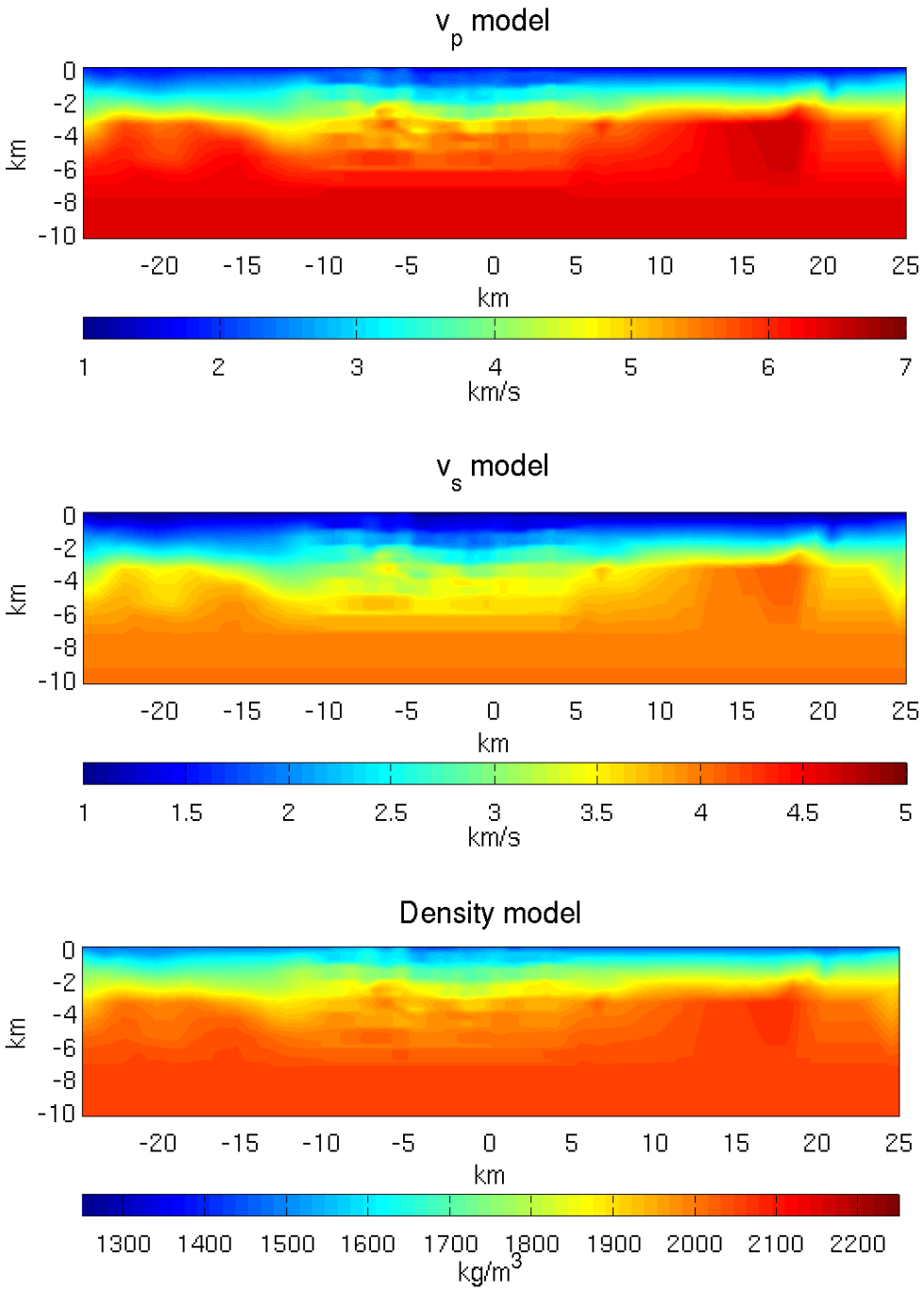

Figure 11.4: Velocities of p- and s-wave, v_p, v_s and density model for the 2D-MODEL.

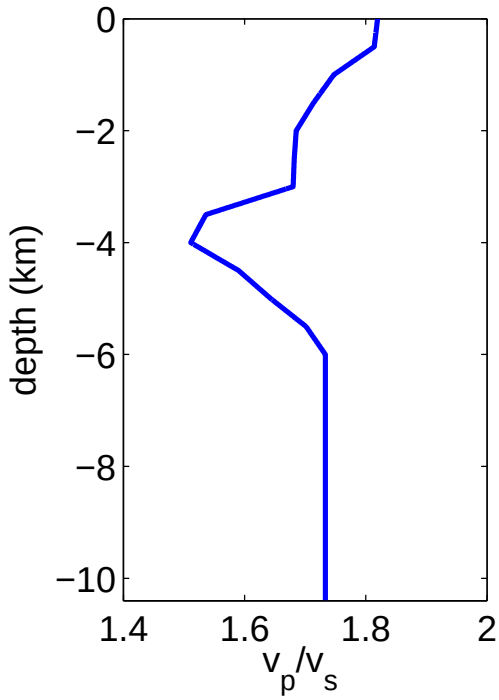

Figure 11.5: Velocities of p- and s-wave, v_p/v_s profile assumed in the model VPVS-MODEL, obtained from Vanorio et al. (2005).

been extended to several combination of magma dynamics processes and velocity structures. The simulated cases are reported in table 11.1. Simulations from ROCK-1 to ROCK-5 have been performed using stresses deriving from simulation CF-1 (volatile-rich magmas and driving pressure of 1MPa; see table 10.3). These calculations account for rock models and topography of increasing complexity, in order to study the effects of these factors on the resulting deformation and seismic signals. Simulation ROCK-6 is based on the results from CF-3 (see table 10.3), which is equal to CF-1 except for the initial overpressure. The comparison between this simulation and ROCK-3 shows the effect of different driving pressures on the recorded deformation and seismic signals. Simulation ROCK-7 considers as source the dynamics induced in the vertical chamber by an overpressure of 20 MPa (simulation CF-4; see table 10.3). Comparison between ROCK-6 and ROCK-7 points out the influence of chamber orientation on the rocks dynamics. Unfortunately, this simulations suffered from numerical problems that have been solved only at a late stage of this work. For this reason, results for this simulations are not illustrated here.

The sources for rock deformation simulations have been obtained reprocessing the results of the magma dynamics simulations as explained in section 3.3. Disregarding the duration of the fluid-dynamics simulations, the files used as seismic

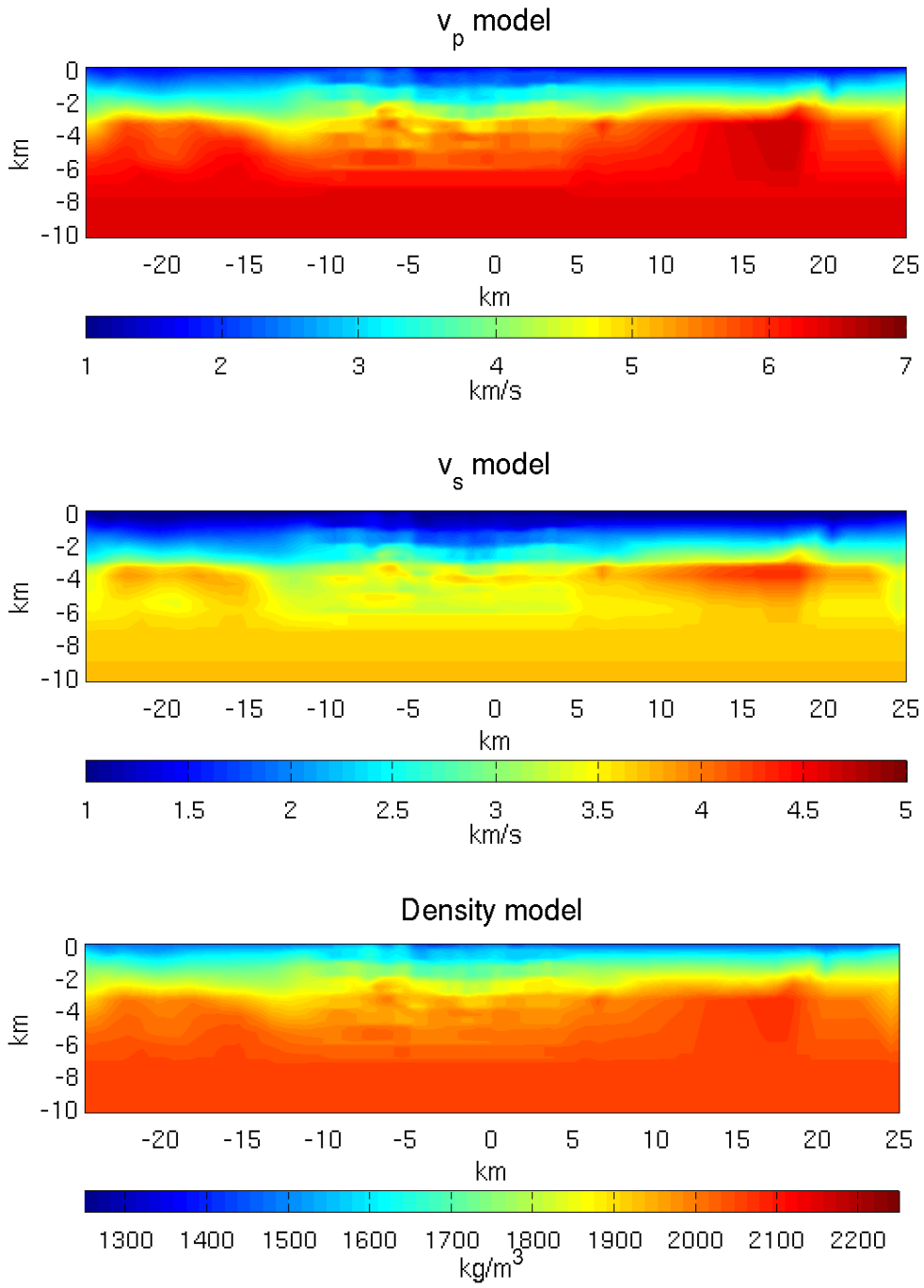

Figure 11.6: Velocities of p- and s-wave, v_p, v_s and density model for the model VPVS-MODEL.

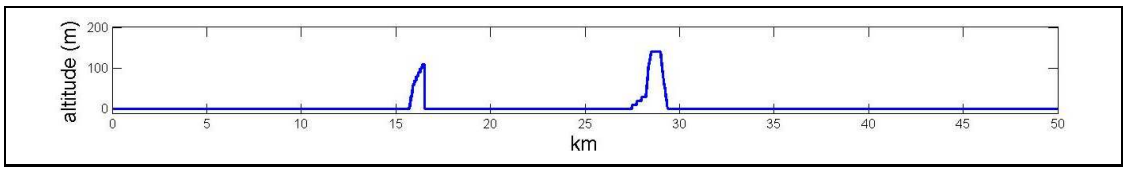

Figure 11.7: Assumed simple topographic profile representing the caldera borders. The vertical scale is exaggerated.

	source	rock model	topography
ROCK-1	CF-1	HOMO	flat
ROCK-2	CF-1	1D-MODEL	flat
ROCK-3	CF-1	2D-MODEL	flat
ROCK-4	CF-1	VPVS-MODEL	flat
ROCK-5	CF-1	VPVS-MODEL	TOPO
ROCK-6	CF-3	VPVS-MODEL	flat
ROCK-7	CF-4	VPVS-MODEL	flat

Table 11.1: Simulations performed with `ELM`. For each case, fluid simulation assumed as source, rock model and topography are indicate. The model abbreviations are explained in section 11.1. TOPO refers to the topography profile of figure 11.7

source reproduce only the first 285 s of the computed fluid-dynamics. This time limitations has been necessary in order to limit the size of source files, that cause computational problem if too large.

11.2 Results

Because of the small time step ($1.5 \cdot 10^{-3}$ s) and large computational domain (50 x 10 km; 5000 x 1040 nodes) snapshots of the velocity and displacement fields over he whole domain have been saved every 2500 computational time step (corresponding to 3.5 s). Deformation and seismic signal have been computed in correspondence of hypothetical recording stations placed along the domain surface from the chamber axis to 7 km eastwards, with an interval of 500 m (blue circles in fig. 11.8). For the simulation with topography (ROCK-5) the seismic signal has been recorded also at synthetic stations located west of the chamber,

with spacing of 1 km and extending to 7 km from the chamber axis (green circles in fig. 11.8), with the purpose of studying the possible effect of the topographic reliefs on the seismic signal. It is worth noting again that results computed in the first kilometers from the lateral boundaries are not reliable because of the boundary effects. The synthetic seismic signals have been band-pass filtered with cut-off

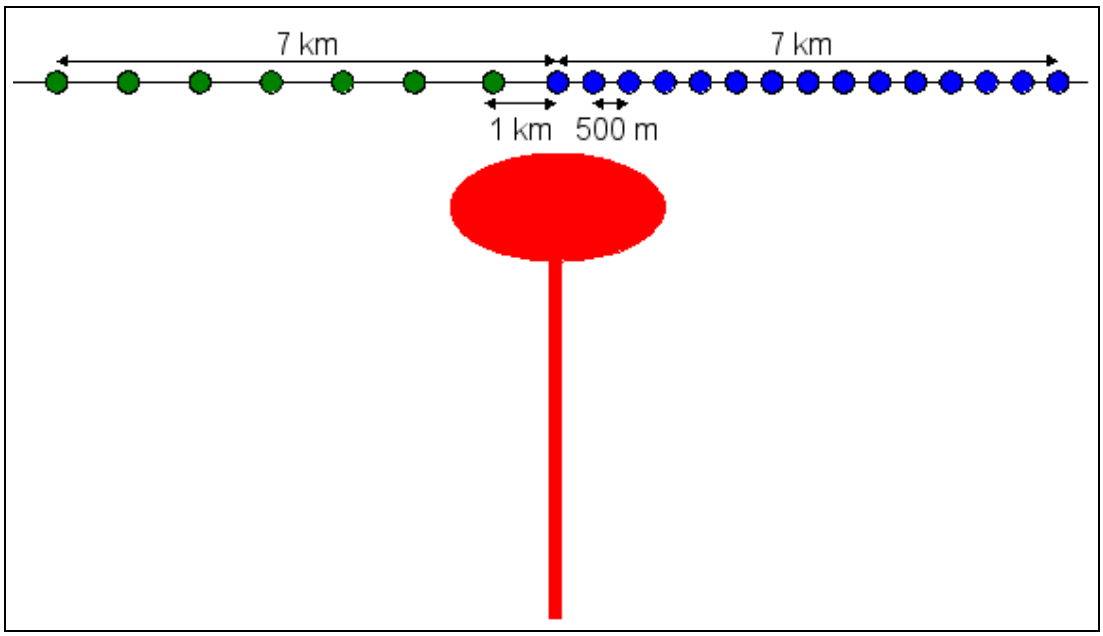

Figure 11.8: Position of the synthetic receivers (circles) with respect to the magma chamber. The blue circles indicate the stations considered in all of the simulations, while the green ones those considered only in simulation ROCK-5. The magma chamber and dyke sizes are exaggerated

frequency of 0.025 and 10 Hz (corresponding to periods of 40 ans 0.1 s) in order to highlight possible high-frequency oscillations and to avoid the numerical noise. Notwithstanding the small time step used in the elasto-dynamics simulations ($1.5 \cdot 10^{-3}$ s), we used a cut-off frequency of 10 Hz to ensure removal of numerical noise and consistency with the filter adopted for the stress time histories (see section 3.3).

Movies showing the simulated dynamics for all of the cases can be found in the cd attached to this thesis.

Simulation ROCK-1

Results for simulation with CF-1 as magmatic source, homogeneous rock properties (fig. 9.1) and flat topography are shown in figures 11.9-11.14. The computed vertical and radial rock displacement in the whole domain is plotted in figure 11.9 for different times. For all the figures, the vertical and horizontal displacements are assumed positive upward and eastward, respectively. Figures 11.10 displays the time evolution of the vertical (left) and radial (right) deformation at the Earth's surface. Figure 11.11 shows the time behaviour of the vertical and radial displacements calculated at some synthetic stations. Figures 11.12-11.14 show the full-band synthetic seismic signal computed at 3 stations located above the chamber axis, and 3 and 6 km away, and the band-pass filtered signals with the corresponding spectrograms.

Both vertical and horizontal deformation (figs. 11.9, 11.11) display oscillations which mimic those of fluid-dynamics in the magmatic system (see, i.e. figures 10.9(a), 10.12, 10.14). The deformation pattern is symmetrical with respect to the chamber axis reflecting the axial symmetry of the magmatic source and the homogeneity of the rock model. As expected, the largest values of vertical and horizontal deformations occur in correspondence of the magma chamber, in the middle of the simulation domain (fig. 11.9, panels (d)-(i)). The vertical component is mainly positive. During about the first 150 s, the region just below the magma chamber shows a negative (downwards) vertical displacement since the computed source forces are downwards, and, hence, induce a downwards deformation (fig. 11.9(a),panels (a)-(d)); afterwards, also this region shows a positive deformation due to the balance between the negative deformation due to the source forces and the positive vertical deformation induced by the horizontal one (fig. 11.9(a)e-f). The maximum value achieved by the vertical displacement is about 20-22 mm and occur after about 210 s above the magma chamber. The horizontal deformation ranges from 0 to about 10 mm and shows the largest values just below the magma chamber. The different deformation pattern observed below and above the chamber (fig. 11.9(b), in particular panels d and f) is an effect of the presence of the dyke which contributes to the horizontal deformation below the chamber.

The vertical displacement profiles observed at the surface (fig. 11.10) show the typical bell shape centered over the chamber axis which vanishes some 15

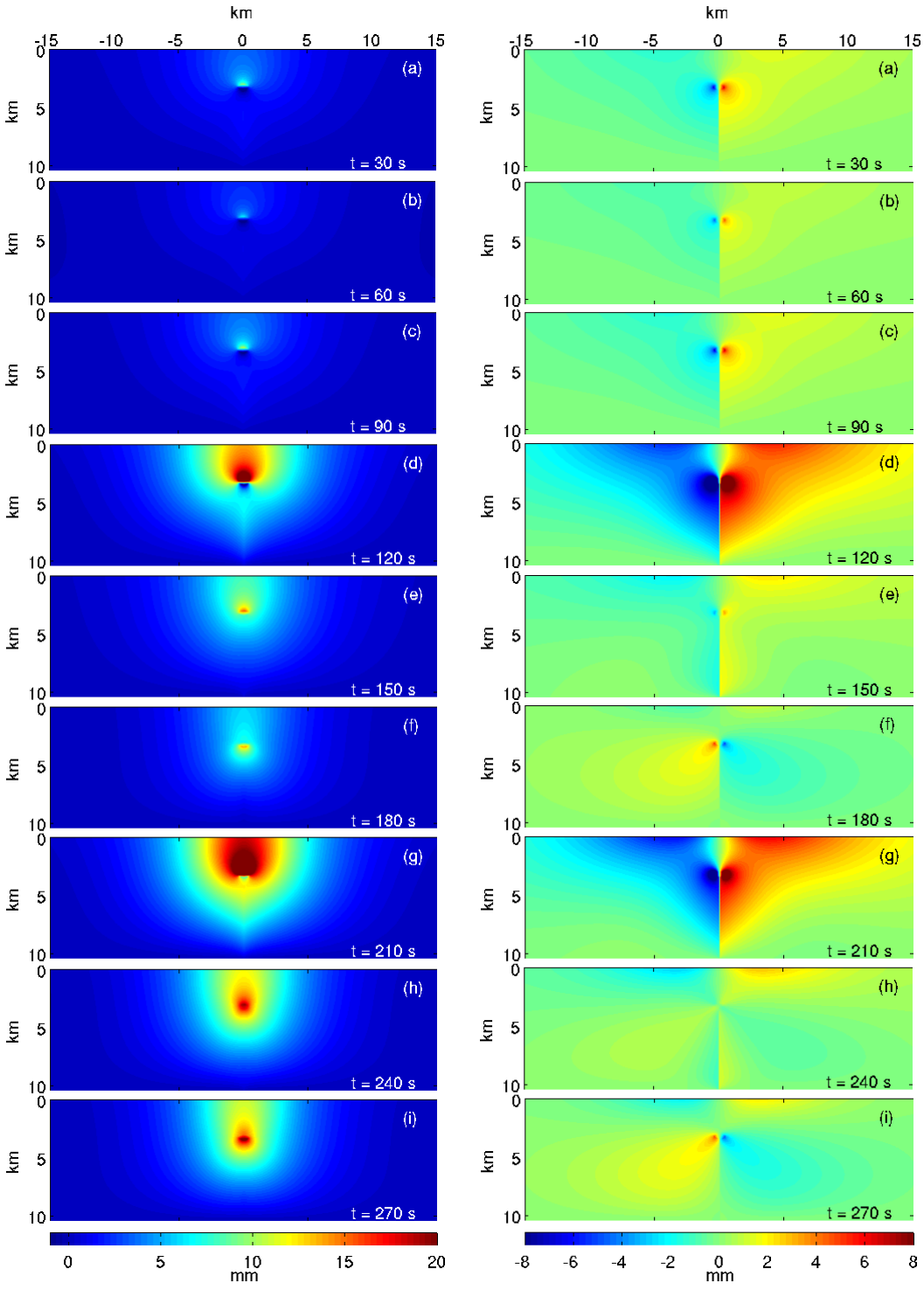

(a) vertical displacement

(b) horizontal displacement

Figure 11.9: Snapshots of the (a) vertical and (b) horizontal deformation computed at different times for simulation ROCK-1.

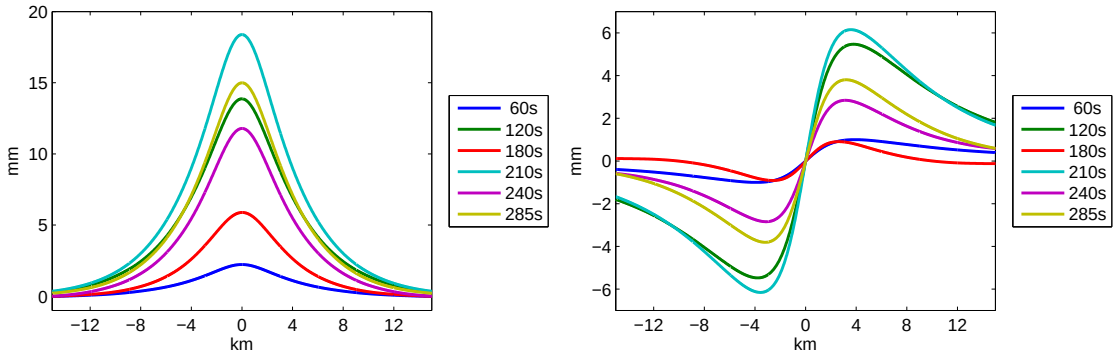

(a) Vertical displacement

(b) Horizontal displacement

Figure 11.10: Profiles of (a) vertical and (b) horizontal displacement in function of the distance from the chamber axis computed at different times for simulation ROCK-1.

km away from the axis. The maximum displacement occurs after about 210 s with value of 18 mm. At the end of the simulation time, the residual vertical deformation shows a maximum value of about 15 mm.

The profiles of the horizontal deformation (11.10(b)) take the classical shape with two lobes which are symmetrical with respect to the chamber axis where the deformation vanishes. All the profiles show the maximum displacement at about 3 km away from the chamber axis except at 180 s when the peak values occur 2 km away from the axis. The largest displacement is 6 mm and it is achieved after 210 s, as for the vertical deformation. The deformation profiles show non-zero values along the whole domain surface except at 180 s; moving toward the domain boundaries the deformation decreases; 15 km away from the chamber axis it shows values of 2 mm for profile taken at 120 and 210 s and < 1 mm for the remaining profiles. At the end of the simulation time, the vertical deformation shows a maximum value of about 4 mm.

The displacement signals computed at the synthetic stations show an increasing trend due to the static deformation; this behaviour is better highlighted by the vertical component (left plots in fig. 11.11). As illustrated before, the amplitude of the vertical signal decreases going away from the chamber axis; the station located 6 km away from the axis (left in fig. 11.11(d)) shows a deformation 3-4 times smaller than that computed above the chamber axis (left in fig. 11.11(a)). The horizontal component of the deformation computed above the chamber axis

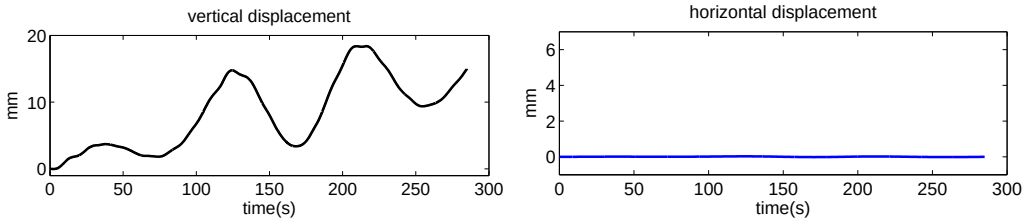

(a) station along the chamber axis

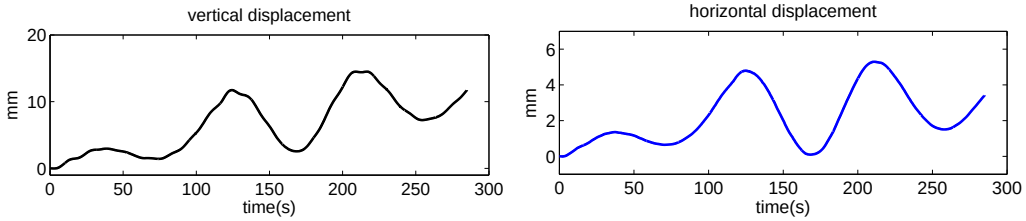

(b) station 2 km away from chamber axis

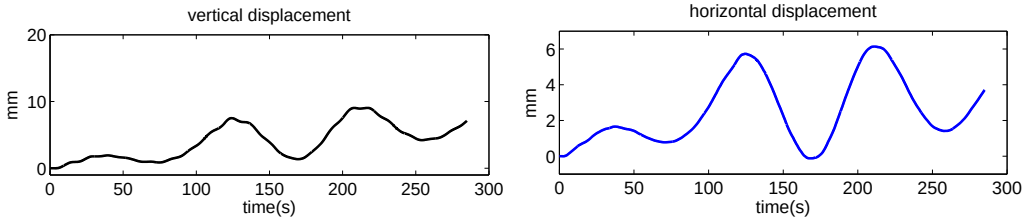

(c) station 4 km away from chamber axis

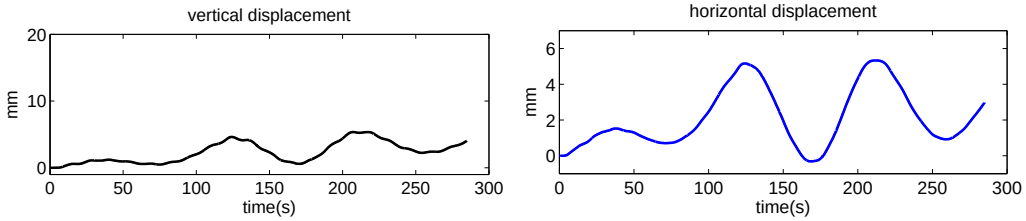

(d) station 6 km away from chamber axis

Figure 11.11: Vertical (left) and horizontal (right) displacement computed for simulation ROCK-1 at the synthetic station located (a) along, (b) 2, (c) 4, (d) 6 km away the chamber axis.

is obviously zero.

Both vertical and horizontal components of seismic signal (figs. 11.12(a), 11.13(a), 11.14(a)) display a main period of oscillation of about 100 s (corresponding to frequency of 0.01 Hz), that is well-rendered in the corresponding amplitude spectrograms (figs. 11.12(b), 11.13(b), 11.14(b)). The spectrograms of both the component of seismic signal show a further characteristic period of oscillation of 15 s (corresponding to a frequency of 0.07 Hz), even though this oscillation is more evident in the vertical signal than in the horizontal one. The filtered seismic signals (figs. 11.12(c), 11.13(c), 11.14(c)) confirm the presence of the oscillations with frequency of 0.07 Hz and highlights smaller oscillations with frequency 0.5-1 Hz, corresponding to a period of 1-3 s; this higher frequency is well identifiable in the horizontal component while is almost absent in the vertical one.

Simulation ROCK-2

Results for simulation in which the 1D-MODEL model has been adopted (ROCK-2) are shown in figures 11.15 - 11.19. The displacement field (fig. 11.15) is symmetrical with respect to the chamber axis, reflecting the symmetry of the rock model. As for the previous simulation, the displacement shows oscillations that mimic those observed for the magma dynamics. The adopted stratified rock properties model induces a smaller displacement with respect to that computed with the homogeneous model (figs. 11.15 and 11.9). The rocks surrounding the magmatic system have an higher wave velocities with respect to the homogeneous ones, then they deform less. The vertical variation of the rock properties causes also a displacement more concentrated near the chamber axis and with a different shape.

The larger vertical displacement occurs after 210 s (left panel in fig. 11.15(g)) even if the displacement computed after 120 s is very similar; the maximum values, > 10 mm, occur above the magma chamber. On the contrary, the horizontal component shows the larger values after 120s even if they are only slightly greater than those computed at 210s. The maximum horizontal displacement is > 5 mm and occurs near the sides of the chamber. The displacement signals calculated on the ground surface (fig. 11.16) highlight the similarity of the displacement amplitude obtained at 120 and 210 s. The increasing trend observed for the homogeneous case (fig. 11.11) is much less evident.

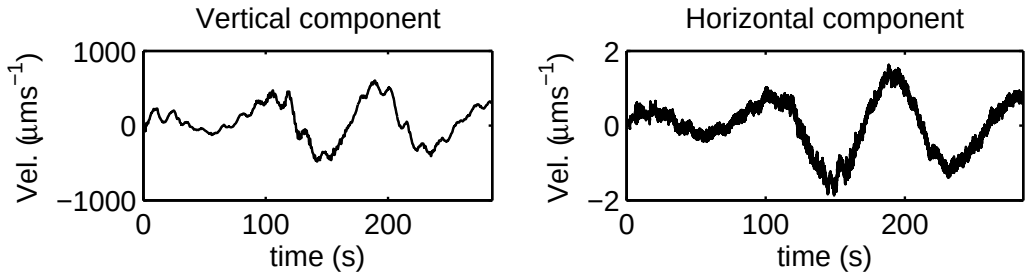

(a) full band seismic signal

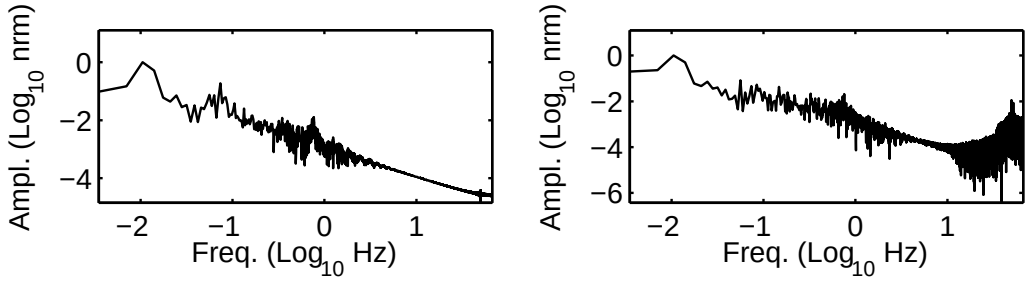

(b) Normalized amplitude spectrum of the full band signal

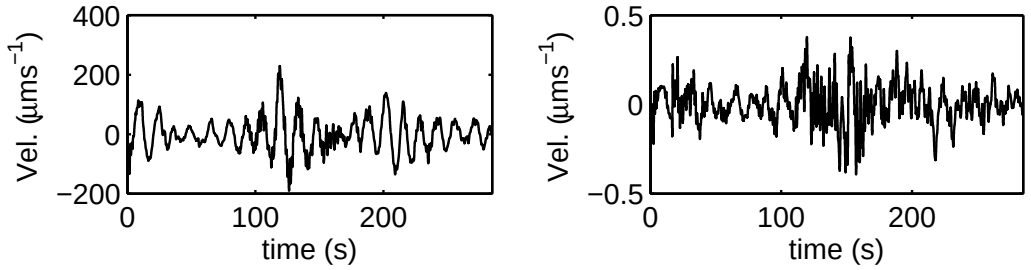

(c) filtered seismic signal

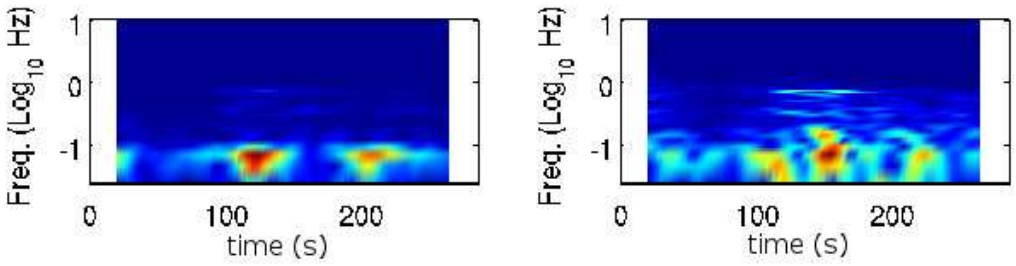

(d) spectrogram of the filtered signal

Figure 11.12: Vertical (left) and horizontal (right) components and corresponding spectrograms of (a) full-band and (c) filtered seismic signal computed at the station located in correspondence of the chamber axis for simulation ROCK-1. The applied filter is a band-pass filter with cut-off frequencies of 0.025 and 10 Hz.

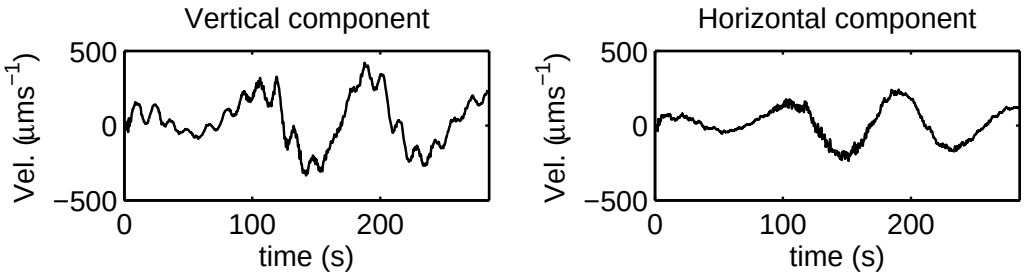

(a) full band seismic signal

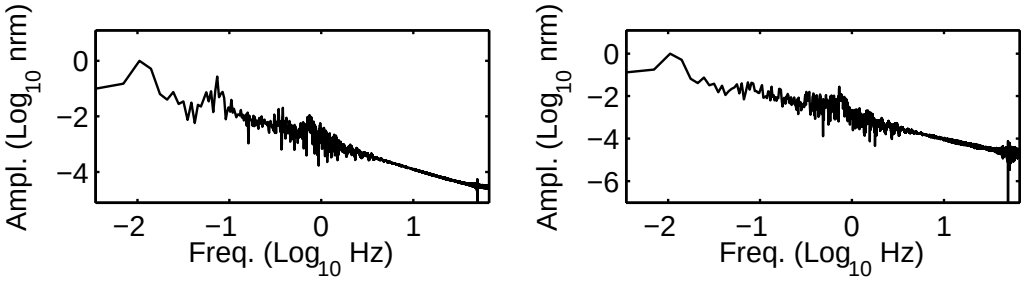

(b) Normalized amplitude spectrum of the full band signal

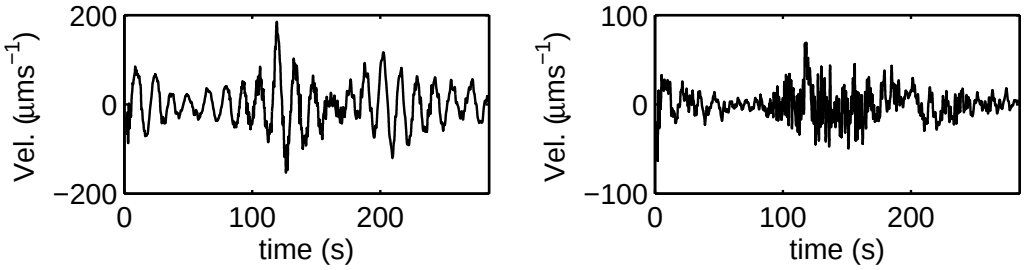

(c) filtered seismic signal

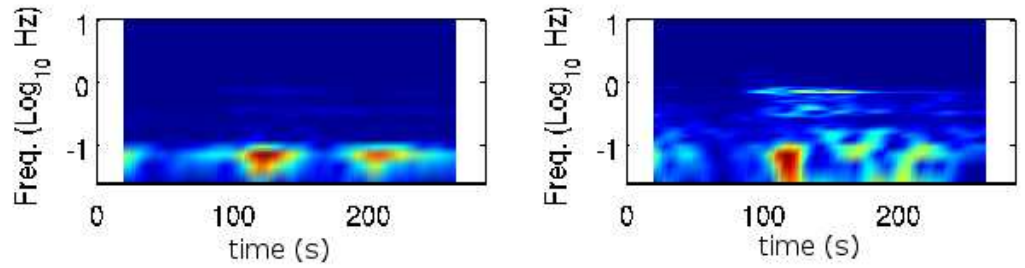

(d) spectrogram of the filtered signal

Figure 11.13: Vertical (left) and horizontal (right) components and corresponding spectrograms of (a) full-band and (c) filtered seismic signal computed at the station located 3 km away from the chamber axis for simulation ROCK-1. The applied filter is a band-pass filter with cut-off frequencies of 0.025 and 10 Hz.

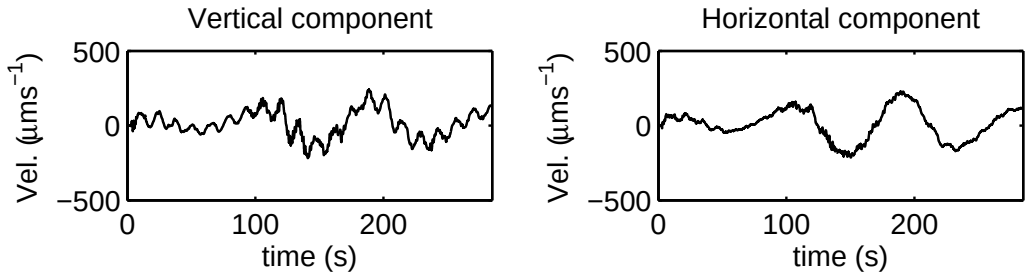

(a) full band seismic signal

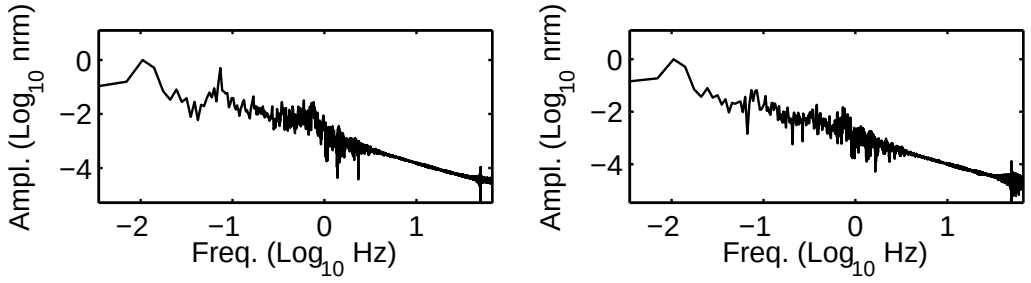

(b) Normalized amplitude spectrum of the full band signal

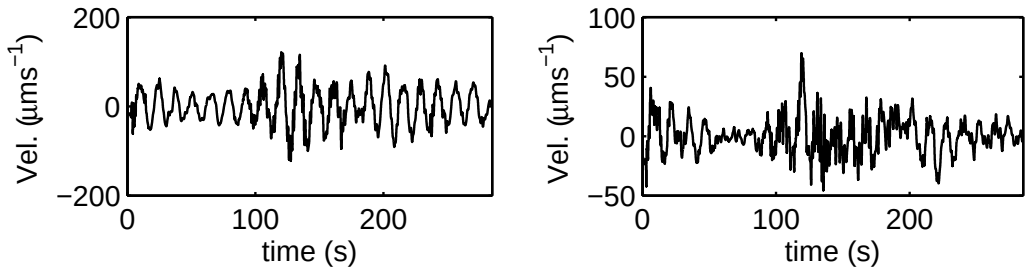

(c) filtered seismic signal

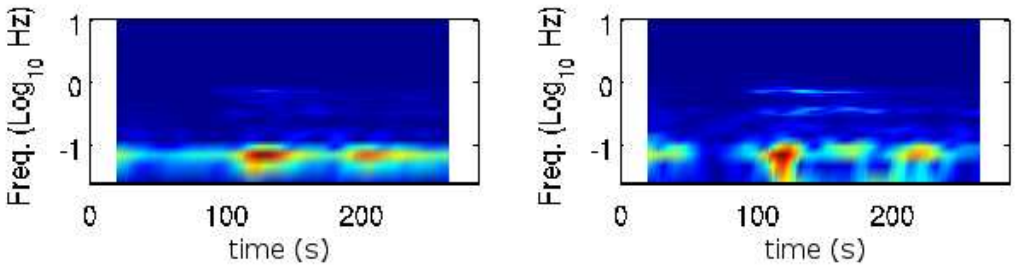

(d) spectrogram of the filtered signal

Figure 11.14: Vertical (left) and horizontal (right) components and corresponding spectrograms of (a) full-band and (c) filtered seismic signal computed at the station located 6 km away from the chamber axis for simulation ROCK-1. The applied filter is a band-pass filter with cut-off frequencies of 0.025 and 10 Hz.

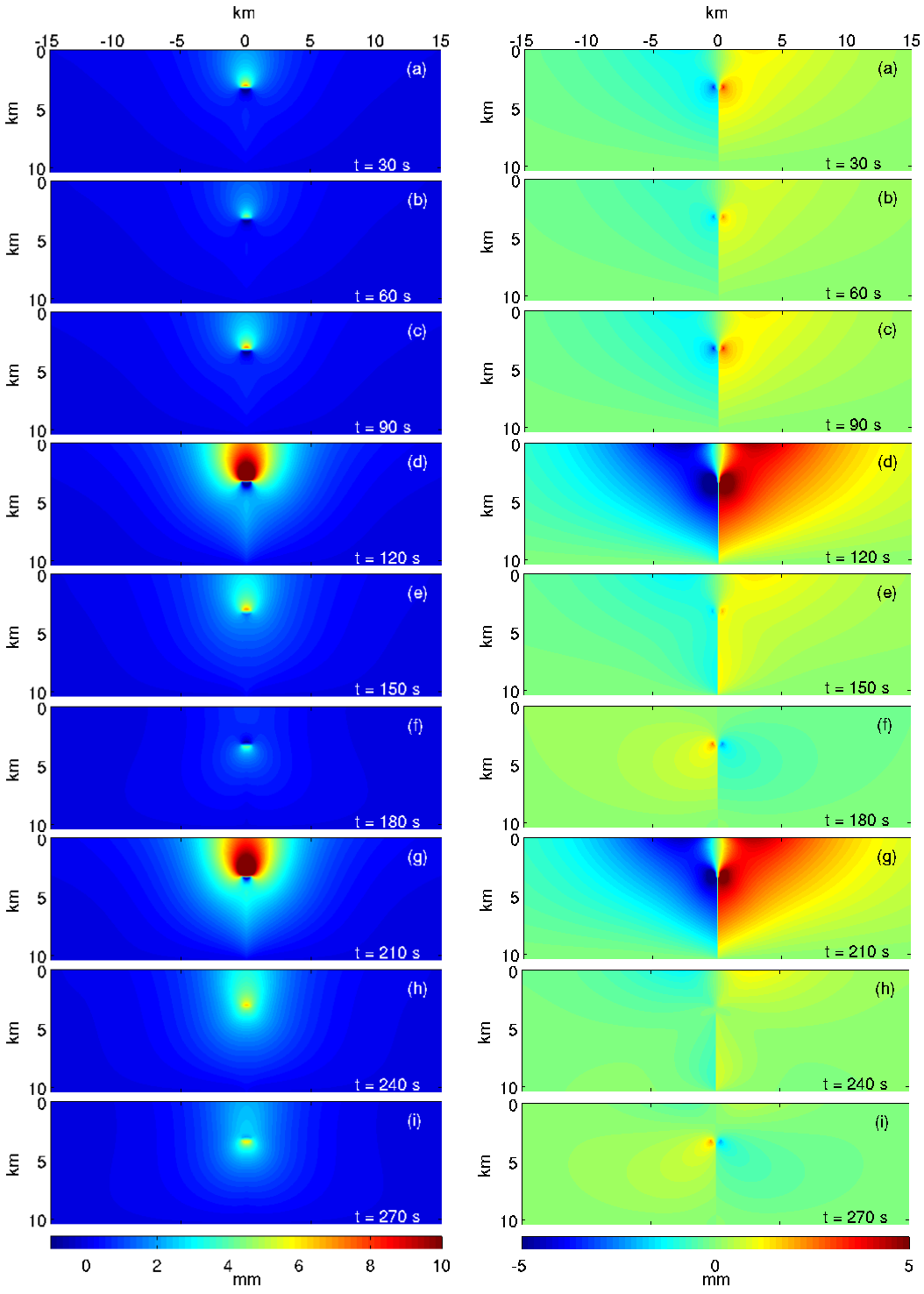

(a) vertical displacement (b) horizontal displacement

Figure 11.15: Snapshots of the (a) vertical and (b) horizontal displacement computed at different times for simulation ROCK-2.

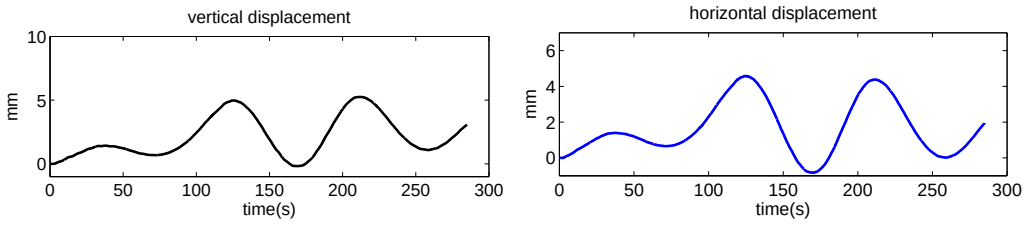

(a) station 2 km away from chamber axis

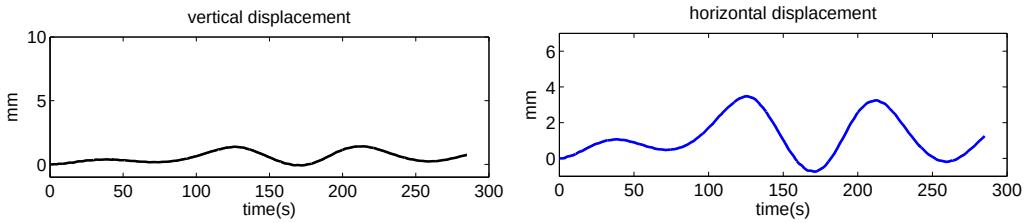

(b) station 6 km away from chamber axis

Figure 11.16: Vertical (left) and horizontal (right) displacement computed for simulation ROCK-2 at synthetic station located (a) 2 and (b) 6 km away from the chamber axis.

Figure 11.17 shows the evolution of displacement profile with time. As for the previous case, the vertical component (fig. 11.17(a)) displays the typical bell shape symmetrical with respect to the chamber axis that vanishes about at distances greater then 15 km. The maximum displacement of 8 mm is achieved after 210 s; as observed before, the displacement computed at 120 s is only slightly smaller than the maximum one, with a peak value of 7.5 mm. As for case ROCK-1, the two lobes of the horizontal component of the displacement are symmetrical with maximum about 3 km away from the chamber axis. The largest horizontal displacement is achieved at 120 and 210 s, with a maximum value of 4.5 mm.

Figures 11.18 and 11.19 display the full band and filtered seismic signal computed for two synthetic station located 3 and 6 km away from the chamber axis. Both stations signal shows big oscillations with period of about 100 s (figs. 11.18(a), 11.19(a)). The full-band spectrograms point out further characteristic frequency of 0.15 and 0.75-1 Hz, corresponding to period of about 7 and 1 s (figs. 11.18(b), 11.19(b)). The filtered signals confirm these oscillations: the 0.15 Hz oscillation is well identifiable in the vertical component (fig. 11.18(c) and 11.19(c), left) while the 0.75-1 Hz oscillations get across in the horizontal component. The spectrograms of the filtered signals detect also oscillations with frequency of 0.35 Hz,

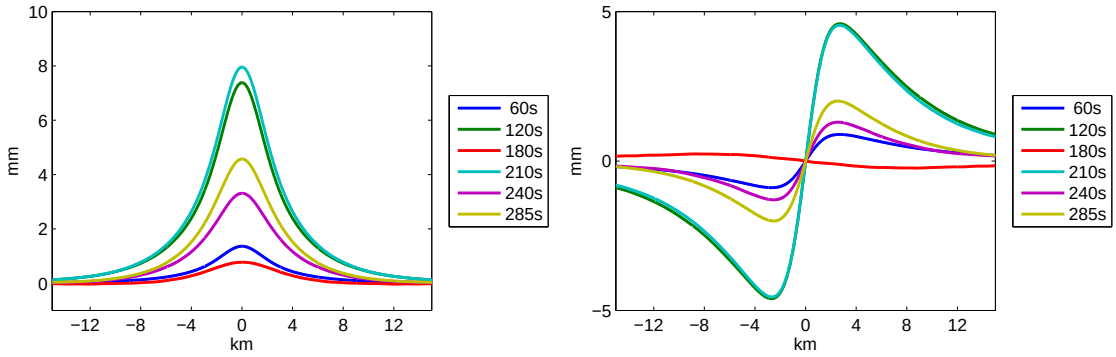

(a) Vertical displacement

(b) Horizontal displacement

Figure 11.17: Profiles of (a) vertical and (b) horizontal displacement in function of the distance from the chamber axis computed at different times for simulation ROCK-2.

corresponding to a period of about 3 s. It is worth noting that frequencies of 3 and 7 s are not identified in the seismic signals computed with the homogeneous model.

Simulation ROCK-3

Results for simulation ROCK-3 in which the 2D rock model (2D-MODEL) is adopted are shown in figures 11.20 - 11.23. The displacement pattern is similar to that of the previous simulation both in amplitude and shape. The latter is only slightly modified by the asymmetry of the rock properties model (fig. 11.20). The displacement recorded at the synthetic stations confirm the similarity with the previous case (figs. 11.21).

The profiles of the vertical and horizontal component of displacement (fig. 11.22) display the classical bell and two lobes shapes, respectively. The maximum vertical displacement occurs at 210s with values of 8.5 mm (fig. 11.22(a)), greater than the peak value obtained with the 1D-MODEL but smaller than that of the homogeneous case. As for the previous case, the horizontal component reaches the maximum values at 120 and 210 s; in the right part of simulated domain the peak value is slightly greater than in the left part with values around 4.5 mm; this value is slightly greater than that computed for the 1D-MODEL case but smaller than that for the homogeneous case. The vertical component decreases nearly to

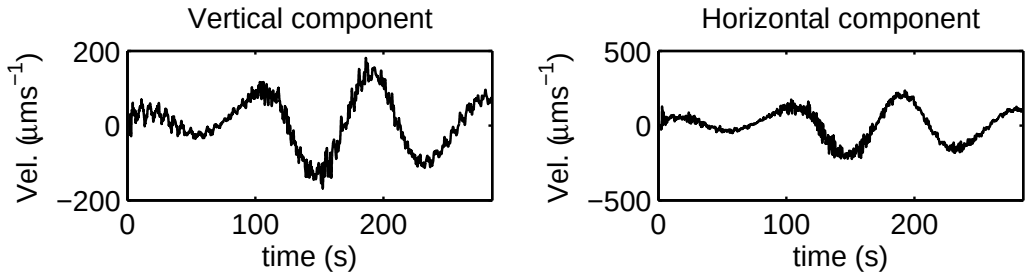

(a) full band seismic signal

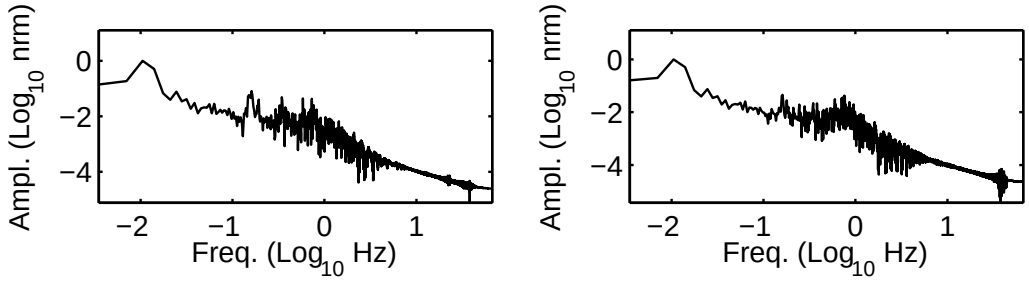

(b) Normalized amplitude spectrum of the full band signal

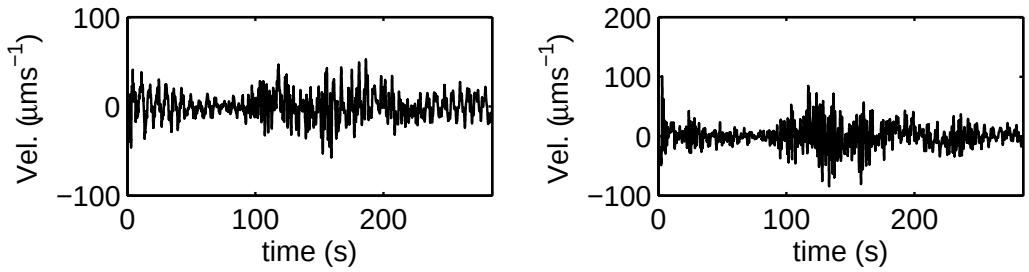

(c) filtered seismic signal

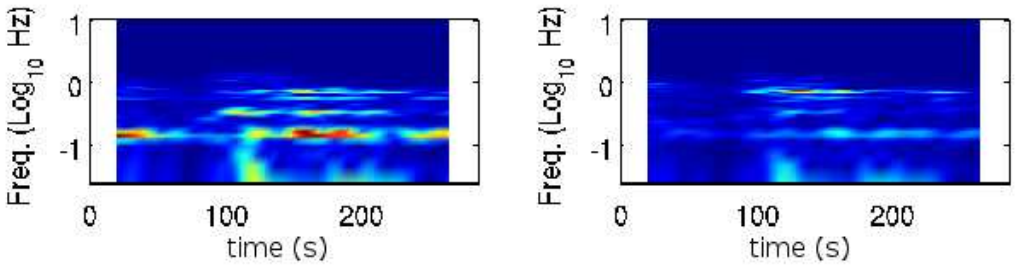

(d) spectrogram of the filtered signal

Figure 11.18: Vertical (left) and horizontal (right) components and corresponding spectrograms of (a) full-band and (c) filtered seismic signal computed at the station located 3 km away from the chamber axis for simulation ROCK-2. The applied filter is a band-pass filter with cut-off frequencies of 0.025 and 10 Hz.

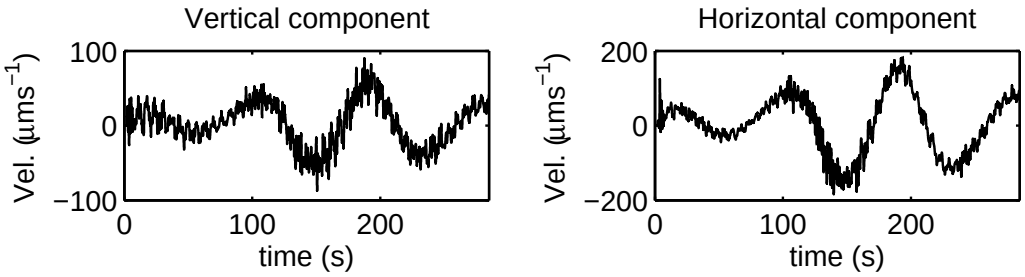

(a) full band seismic signal

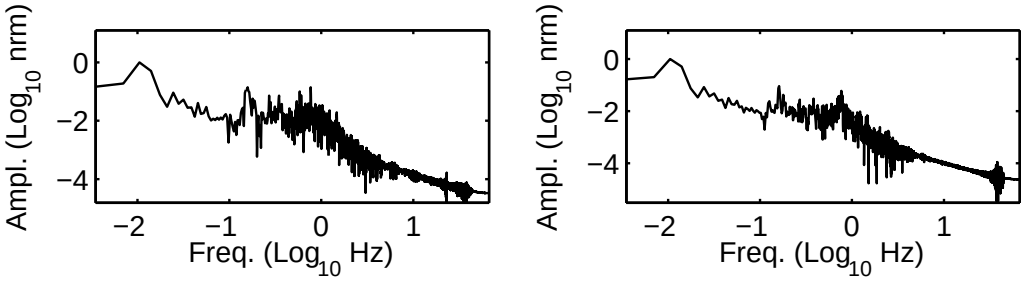

(b) Normalized amplitude spectrum of the full band signal

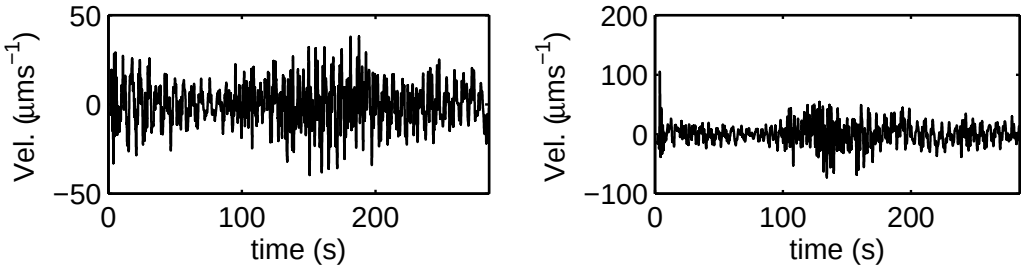

(c) filtered seismic signal

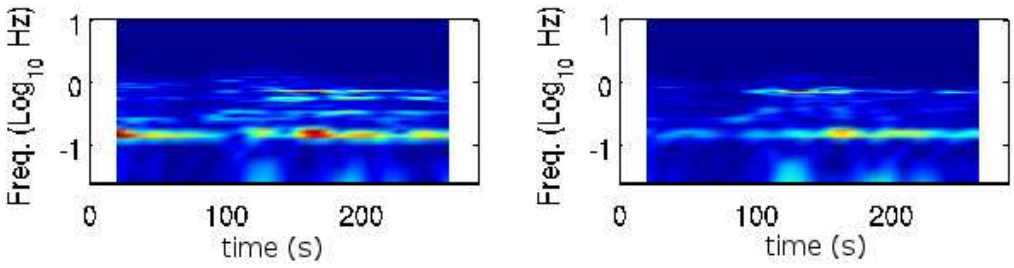

(d) spectrogram of the filtered signal

Figure 11.19: Vertical (left) and horizontal (right) components and corresponding spectrograms of (a) full-band and (c) filtered seismic signal computed at the station located 6 km away from the chamber axis for simulation ROCK-2. The applied filter is a band-pass filter with cut-off frequencies of 0.025 and 10 Hz.

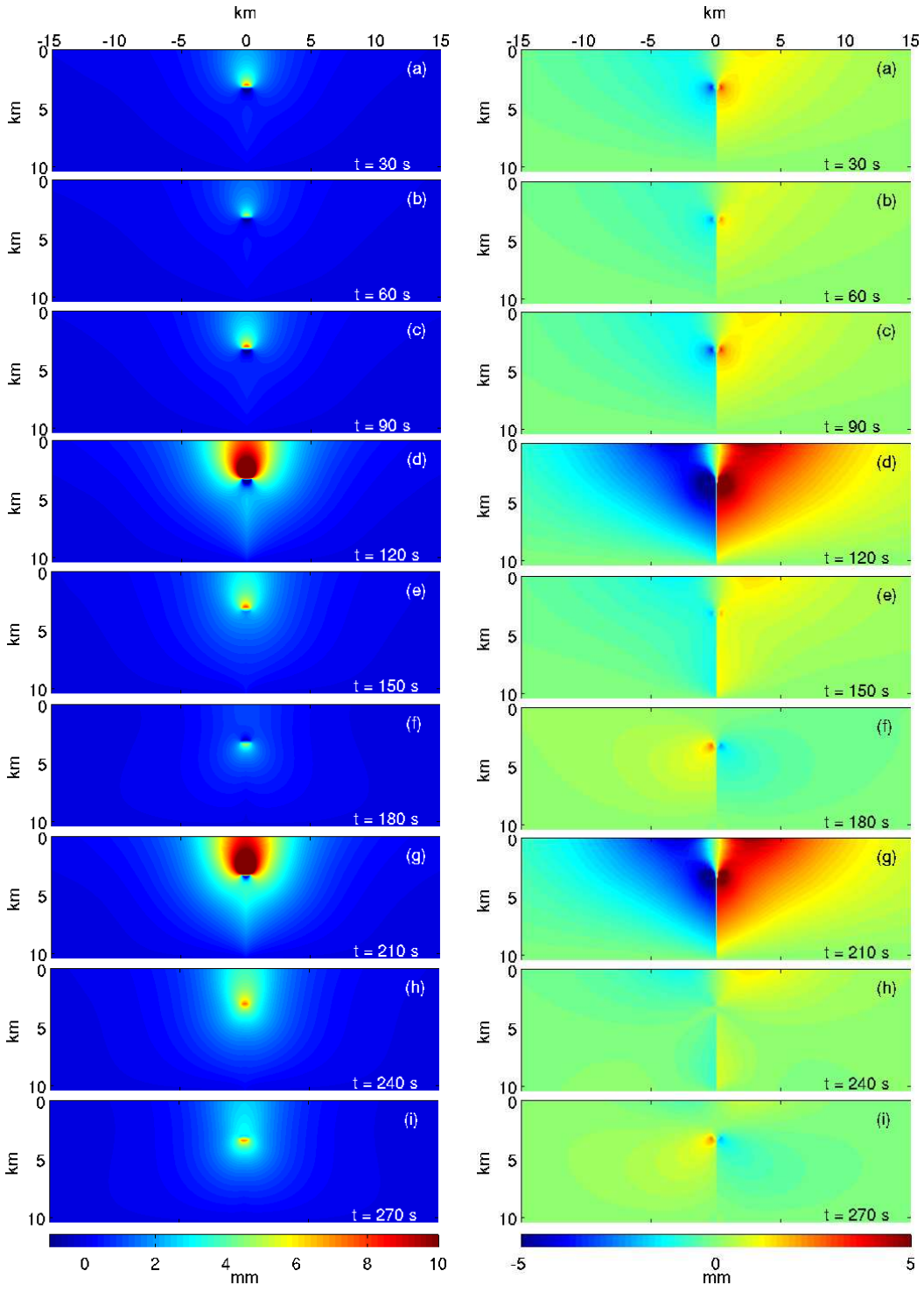

(a) vertical displacement (b) horizontal displacement

Figure 11.20: Snapshots of the (a) vertical and (b) horizontal displacement computed at different times for simulation ROCK-3.

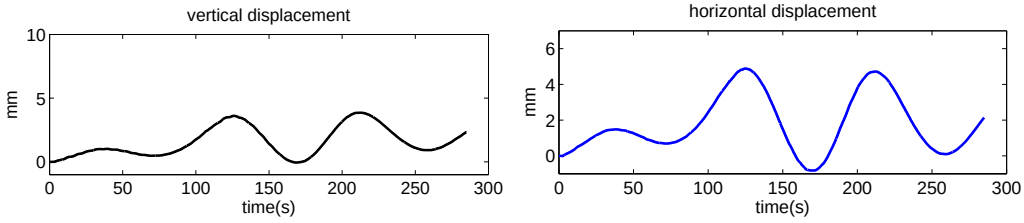

(a) station 3 km away from the chamber axis

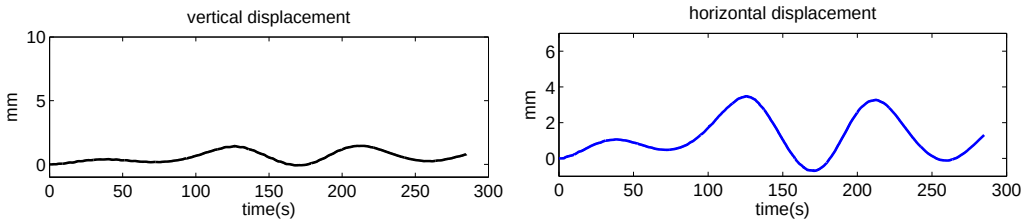

(b) station 6 km away from chamber axis

Figure 11.21: Vertical (left) and horizontal (right) displacement computed for simulation ROCK-3 at synthetic station located (a) 3 and (b) 6 km away from the chamber axis.

zero about 15 km away from the chamber axis while the horizontal displacement is not null along the whole profile even if it is very small toward the domain boundaries. As for the previous cases, the synthetic seismic signal exhibits a main oscillation with frequency of 0.01 Hz, corresponding to a period of 100 s. The filtered signals highlight also oscillations with frequency of 0.15, 0.35 and 0.75 Hz, corresponding to 6-7, 3 and 1-2 s; as shown by spectrograms of the filtered signal (fig. 11.23(d)), the oscillation with frequency of 0.35 Hz is more evident in the horizontal component than in the vertical one.

The small difference between simulations ROCK-2 and ROCK-3 can be explained comparing 1D-MODEL and 2D-MODEL; the magma chamber, in fact, is located within rocks with slightly different properties with respect to the 1D-MODEL model and from left to right of this model.

Simulation ROCK-4

Results for simulation that assumes the rock model with varying v_p/v_s ratio with depth (VPVS-MODEL) are shown in figures 11.24-11.27. The displacement pattern is very similar to that computed for the previous case; the vertical and

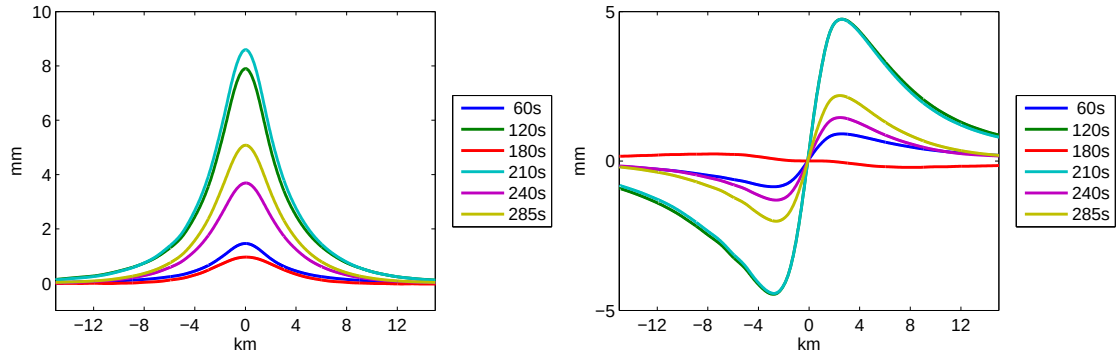

(a) Vertical displacement

(b) Horizontal displacement

Figure 11.22: Profiles of (a) vertical and (b) horizontal displacement in function of the distance from the chamber axis computed at different times for simulation ROCK-3.

horizontal displacements show oscillations that correspond to the oscillations of source dynamics, with maximum displacement after 210s (fig. 11.24). As for the previous case, the displacement recorded at the synthetic stations (fig. 11.25) confirms the oscillating trend and do not show the increasing global trend well-rendered in the homogeneous simulation. The vertical component of displacement (fig 11.26(a)) achieves a peak value of 9 mm and runs out at about 15 km away from the chamber axis. The horizontal component highlights the asymmetry of the displacement field (fig. 11.26(b)); in fact, the maximum displacement shows a peak value of about 5.5 and 5 mm on right and left half of domain, respectively; it drops to less than 0.5 mm on domain boundary. As for the previous case, the displacement profiles obtained at 120 and 210 s are comparable and show the greatest displacement. The displacement computed for this simulation is slightly greater than that of the previous two simulations except for the homogeneous case (ROCK-1).

Both vertical and horizontal component of the seismic signals (fig. 11.27) display the low-frequency oscillations of period 100 s. A further characteristic frequency of 0.15 Hz (corresponding to a period of 7 s) is well-rendered in the vertical component (left in fig. 11.27(a)) while it is masked by an higher frequency oscillation in the horizontal one. The full-band spectrograms (fig. 11.27(b)) confirm the presence of this frequency in both the signal components. The filtered signals and the associated spectrograms highlight the oscillation with frequency

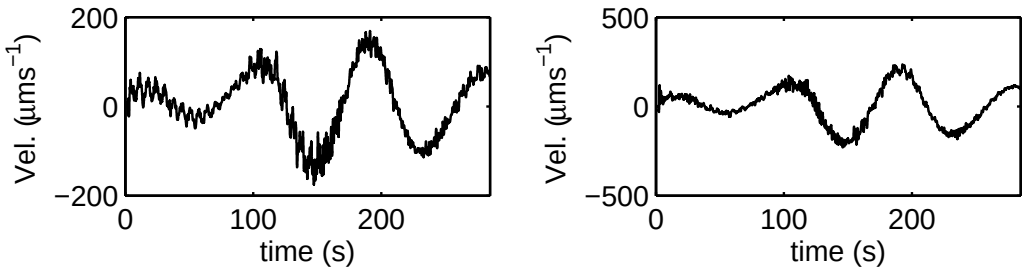

(a) full band seismic signal

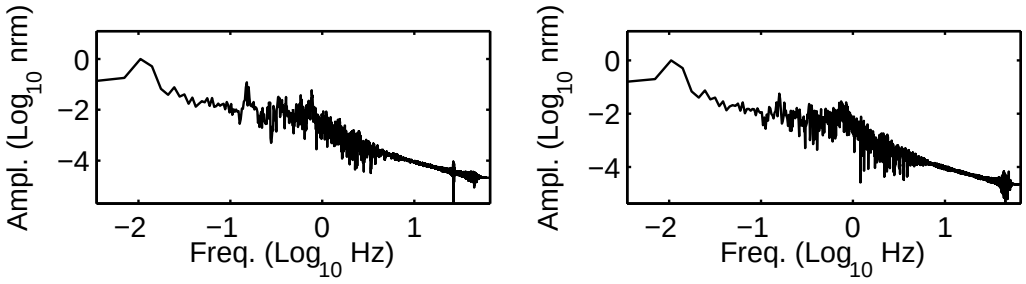

(b) Normalized amplitude spectrum of the full band signal

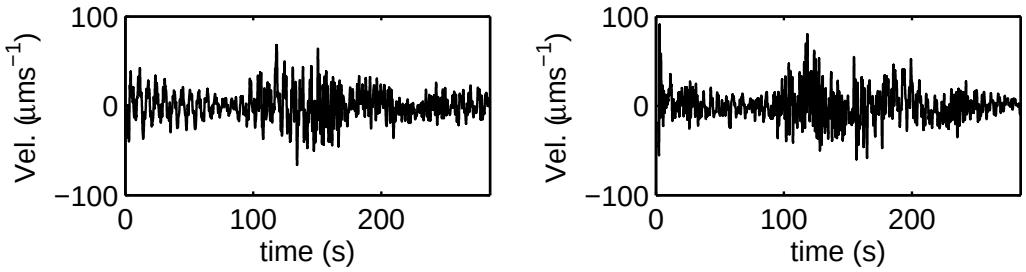

(c) filtered seismic signal

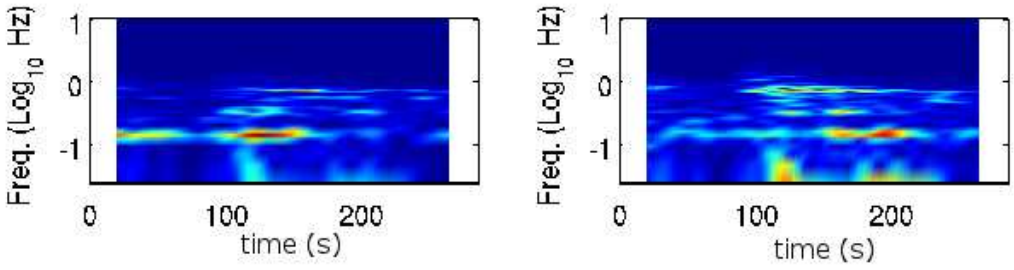

(d) spectrogram of the filtered signal

Figure 11.23: Vertical (left) and horizontal (right) components and corresponding spectrograms of (a) full-band and (c) filtered seismic signal computed at the station located 3 km away from the chamber axis for simulation ROCK-3. The applied filter is a band-pass filter with cut-off frequencies of 0.025 and 10 Hz.

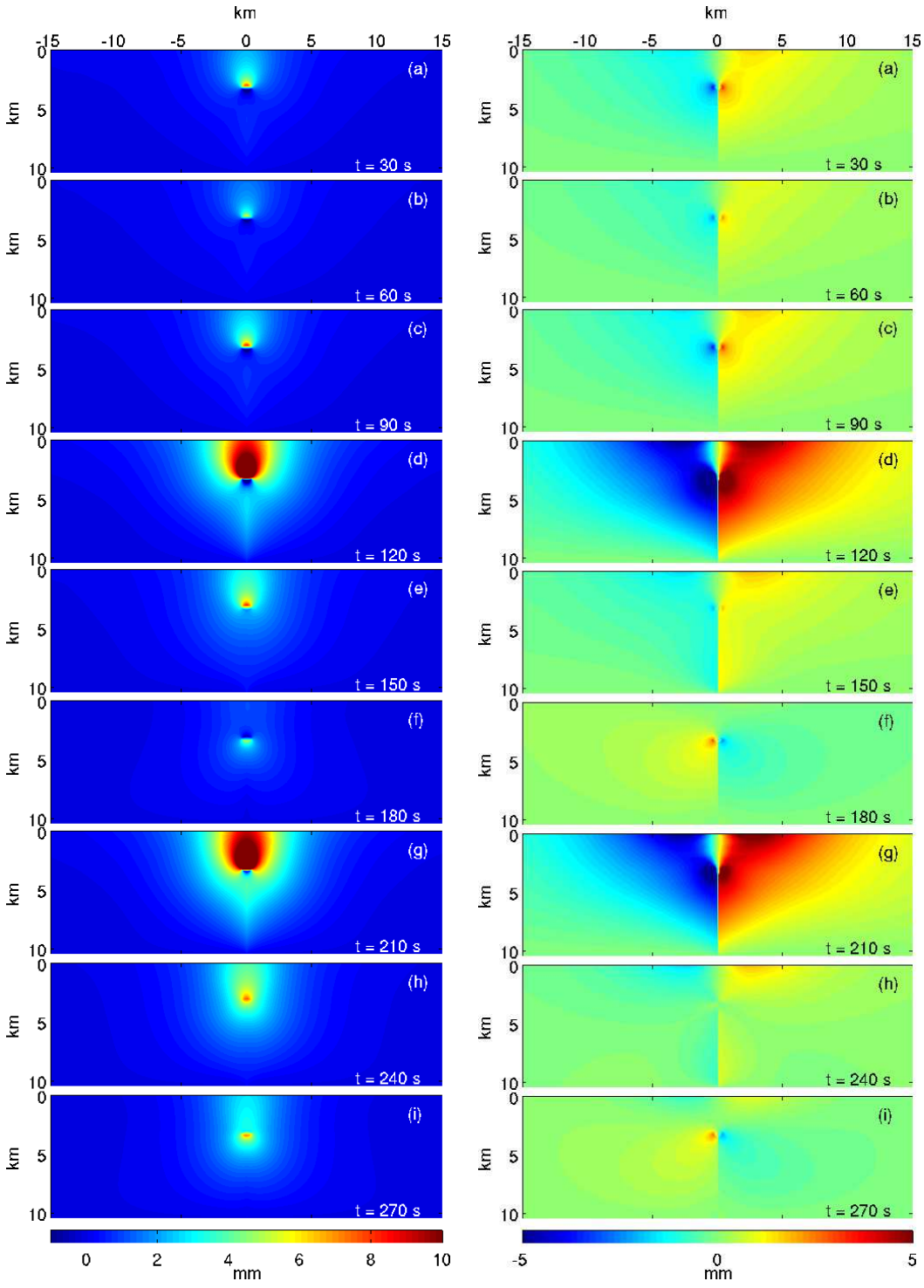

(a) vertical displacement (b) horizontal displacement

Figure 11.24: Snapshots of the (a) vertical and (b) horizontal displacement computed at different times for simulation ROCK-4.

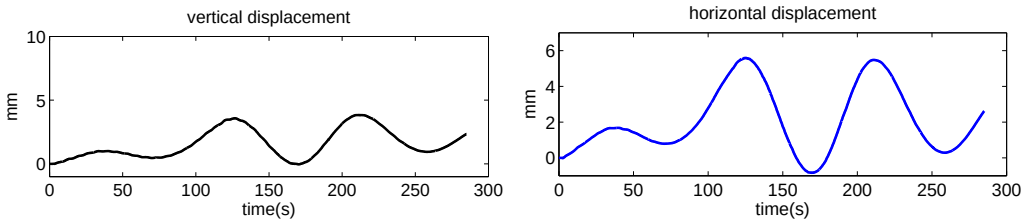

Figure 11.25: Vertical (left) and horizontal (right) displacement computed for simulation ROCK-4 at synthetic station located 3 away from the chamber axis.

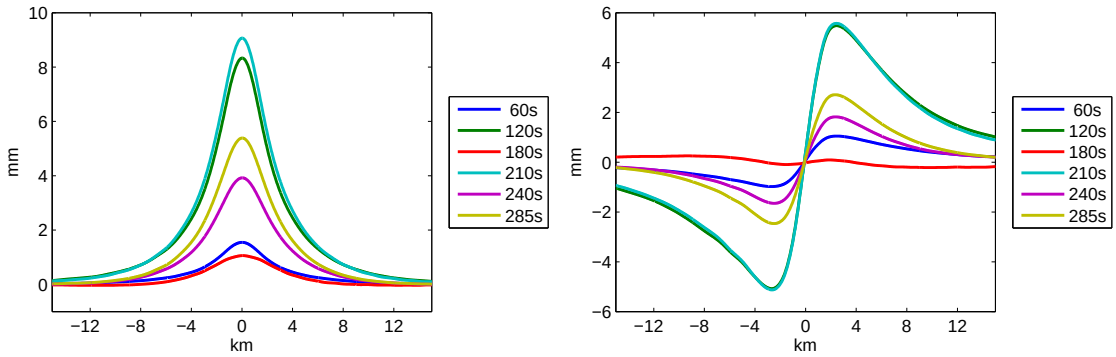

(a) Vertical displacement

(b) Horizontal displacement

Figure 11.26: Profiles of (a) vertical and (b) horizontal displacement in function of the distance from the chamber axis computed at different times for simulation ROCK-4.

of 0.15 and 0.75 Hz (corresponding to a period of 1-2 s). Differently from simulations ROCK-2 and ROCK-3, oscillations with frequency of 0.35 Hz (or period of about 3 s) are not evident.

Simulation ROCK-5

Figures 11.28 - 11.32 display results for simulation with rock properties model equal to the previous case (VPVS-MODEL) and the topographic profile (TOPO) instead of the flat surface (ROCK-5). The displacement patterns (fig. 11.28) are very similar to that computed for the previous simulation confirming that topography roughnesses have a scale length which is small once compared to the dominant wavelengths of the signals, therefore not inducing remarkable changes in the displacement field. As illustrated in figure 11.29, both vertical and hor-

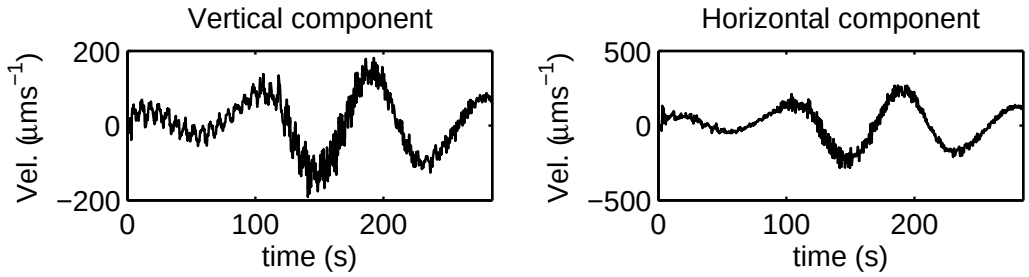

(a) full band seismic signal

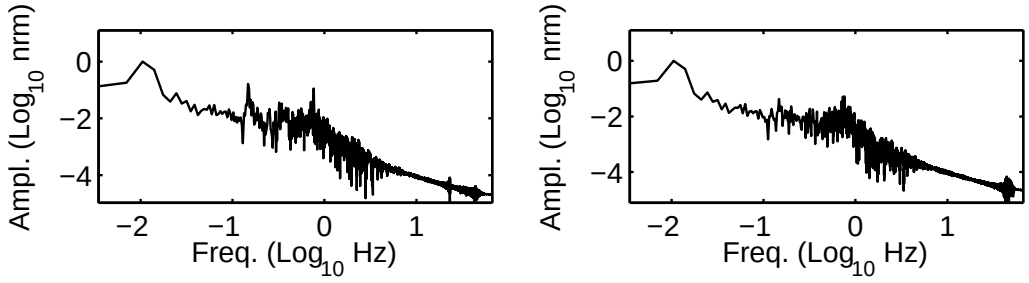

(b) Normalized amplitude spectrum of the full band signal

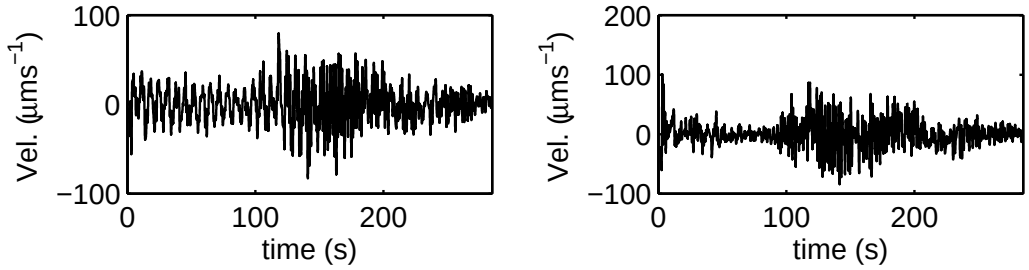

(c) filtered seismic signal

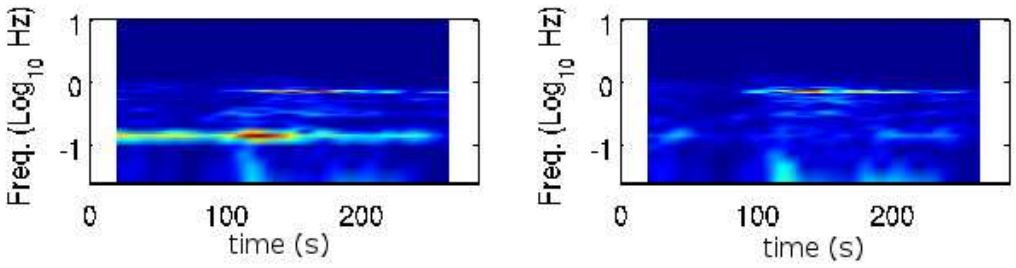

(d) spectrogram of the filtered signal

Figure 11.27: Vertical (left) and horizontal (right) components and corresponding spectrograms of (a) full-band and (c) filtered seismic signal computed at the station located 3 km away from the chamber axis for simulation ROCK-4. The applied filter is a band-pass filter with cut-off frequencies of 0.025 and 10 Hz.

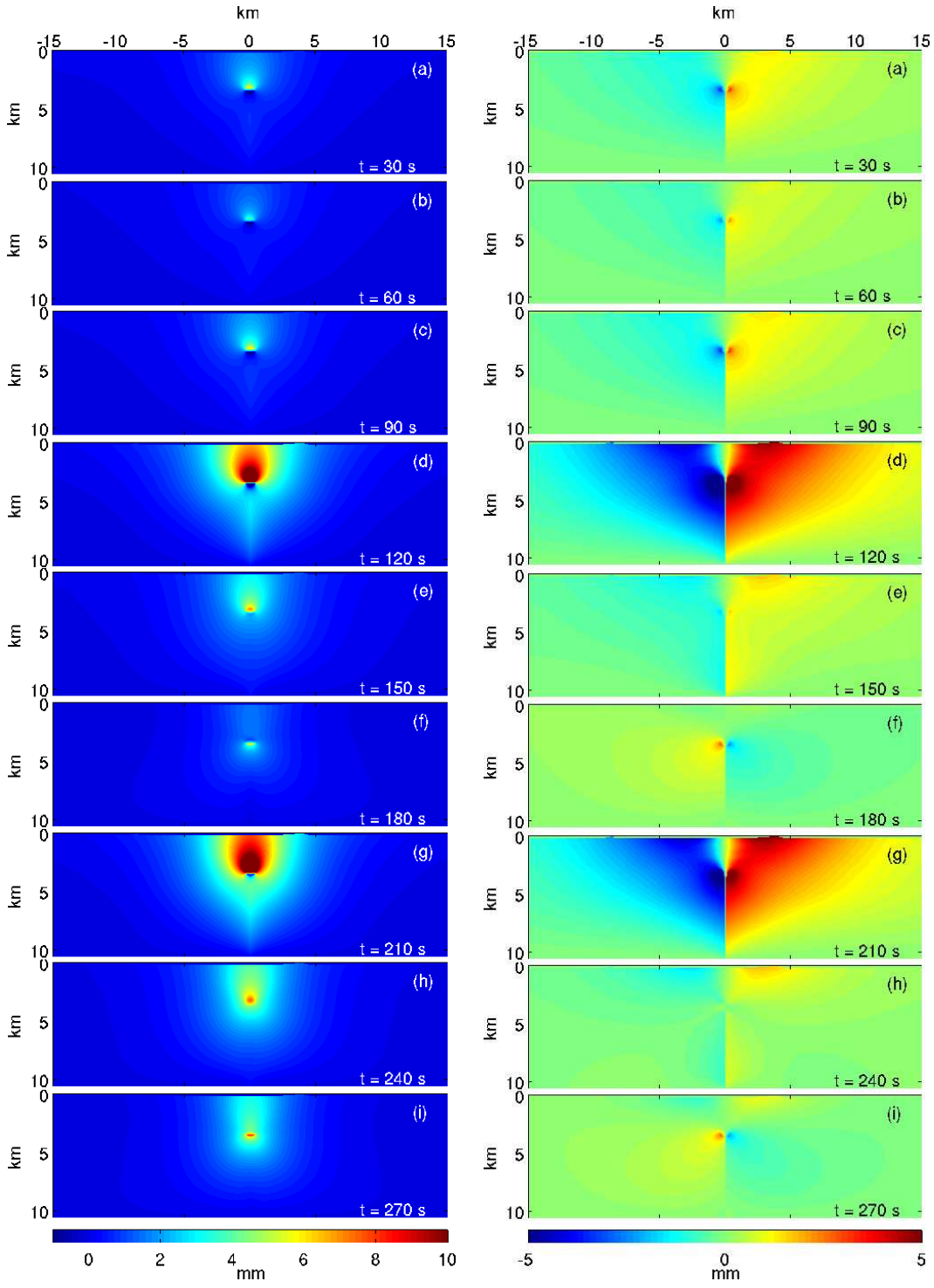

(a) vertical displacement (b) horizontal displacement

Figure 11.28: Snapshots of the (a) vertical and (b) horizontal displacement computed at different times for simulation ROCK-5.

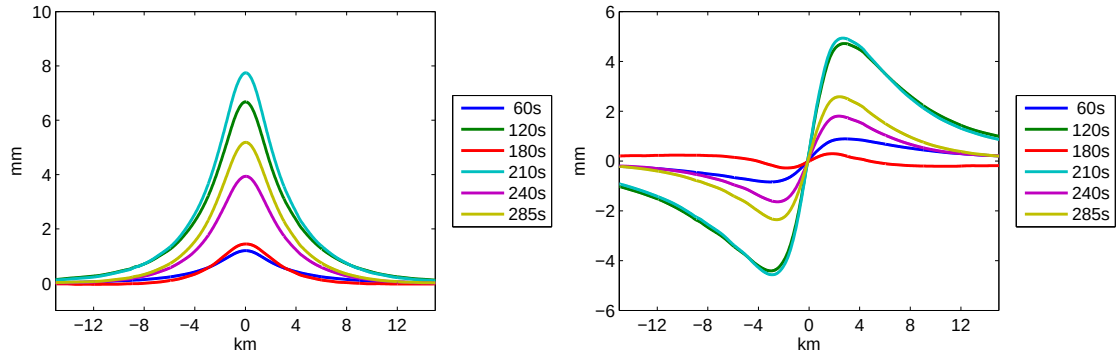

(a) Vertical displacement

(b) Horizontal displacement

Figure 11.29: Profiles of (a) vertical and (b) horizontal displacement in function of the distance from the chamber axis computed at different times for simulation ROCK-5.

izontal component of displacement are slightly lower, as a consequence of the presence of the topographic relieves. The maximum vertical displacement is 8 mm, while the horizontal one is 4.5 and 5 mm to the left and right side of domain, respectively. The shape of the vertical component (fig. 11.29(a)) is not affected by the topography, while the horizontal component (fig. 11.29(b)) shows a small slope variation in correspondence of the eastern relief. Figure 11.30 shows the displacement and velocity field in the region extending from the chamber axis to the eastern topographic relief down to depth of 1 km, and computed at 210 s for this simulation and the previous one (ROCK-4). The effects of the topography are more evident in the snapshot of the velocity fields (figs. 11.30(c), 11.30(d)), whose amplitude and spatial pattern markedly change once accounting for topographic reliefs.

As for the previous cases, the seismic signals (figs. 11.31 and 11.32) are dominated by oscillations with period of about 100 s. Further oscillations with frequency of 0.15 Hz are shown by both the full-band and the filtered signals. The spectrograms of the latter highlight also oscillations with frequency of 0.75 Hz (corresponding to a period of 1-2 s).

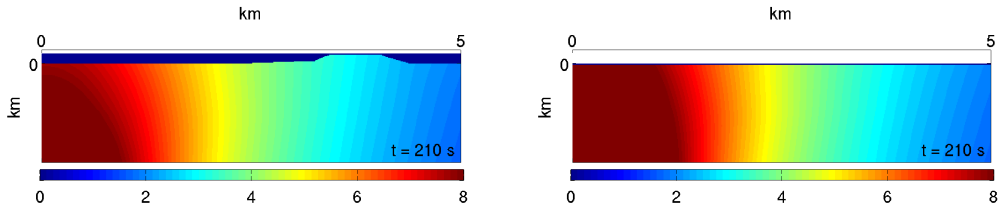

(a) Vertical component of displacement

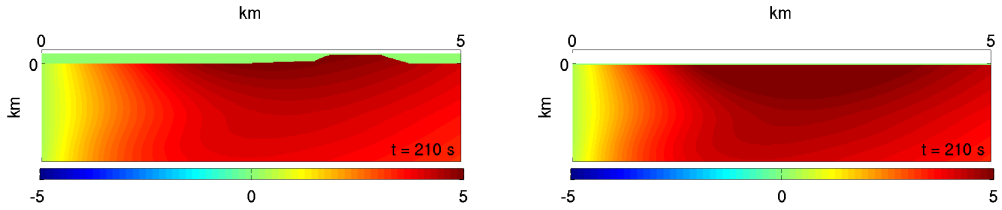

(b) Horizontal component of displacement

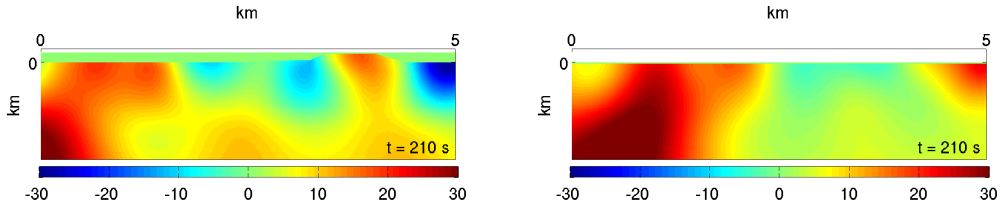

(c) Vertical component of velocity

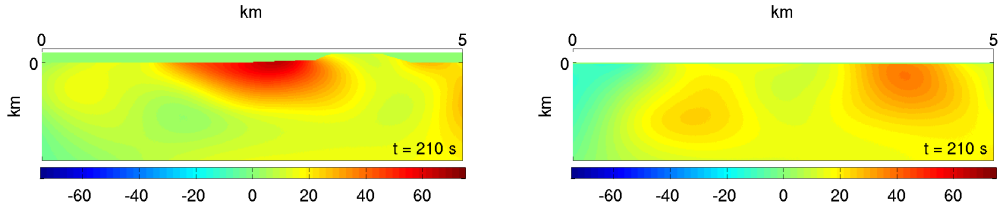

(d) Horizontal component of velocity

Figure 11.30: Snapshots of (a) vertical and (b) horizontal component of displacement and (c) vertical and (d) horizontal component of velocity in the region near the relief on the right part of domain (see fig. 11.7), for simulations ROCK-5 (left) and ROCK-4 (right) at 210 s.

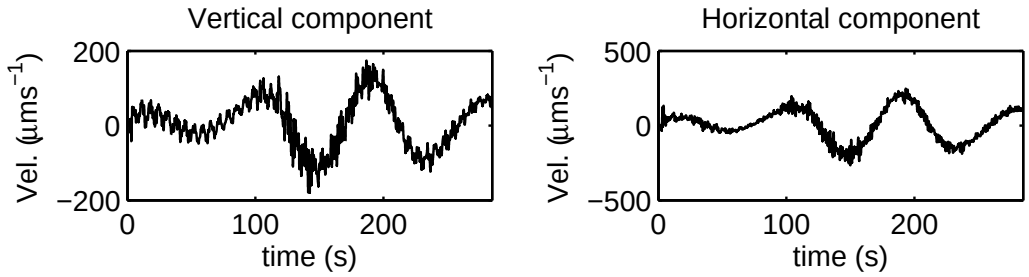

(a) full band seismic signal

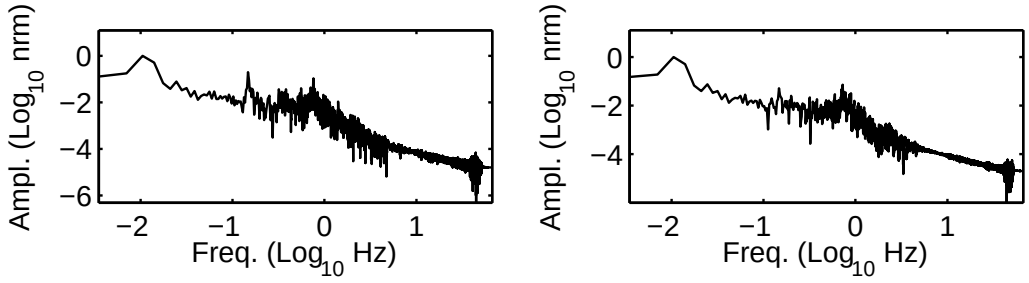

(b) Normalized amplitude spectrum of the full band signal

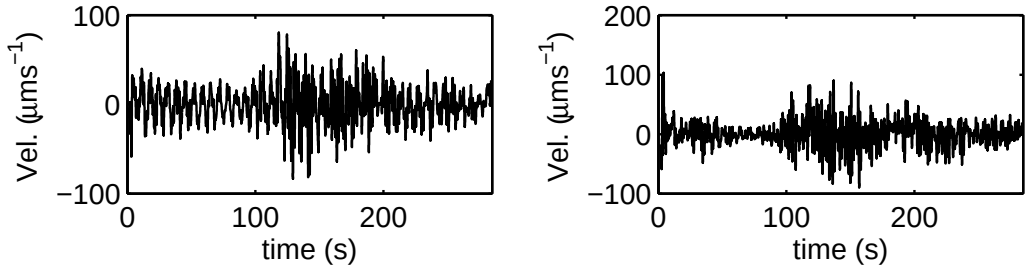

(c) filtered seismic signal

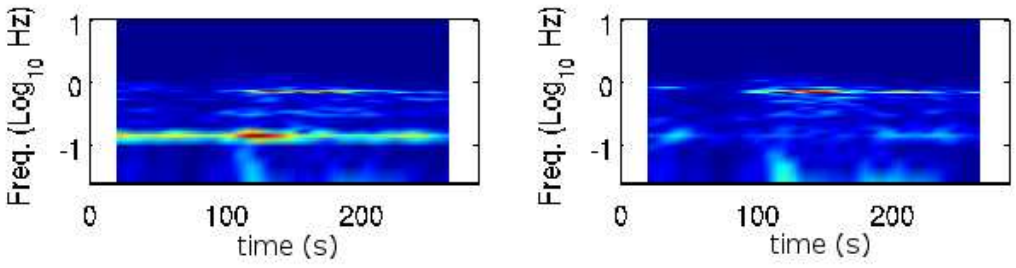

(d) spectrogram of the filtered signal

Figure 11.31: Vertical (left) and horizontal (right) components and corresponding spectrograms of (a) full-band and (c) filtered seismic signal computed at the station located 3 km away from the chamber axis for simulation ROCK-5. The applied filter is a band-pass filter with cut-off frequencies of 0.025 and 10 Hz.

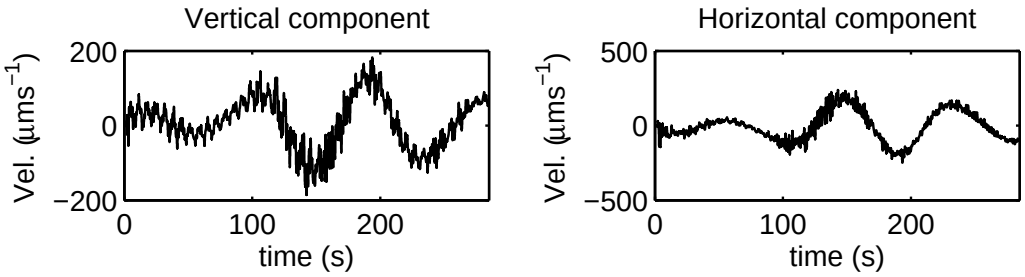

(a) full band seismic signal

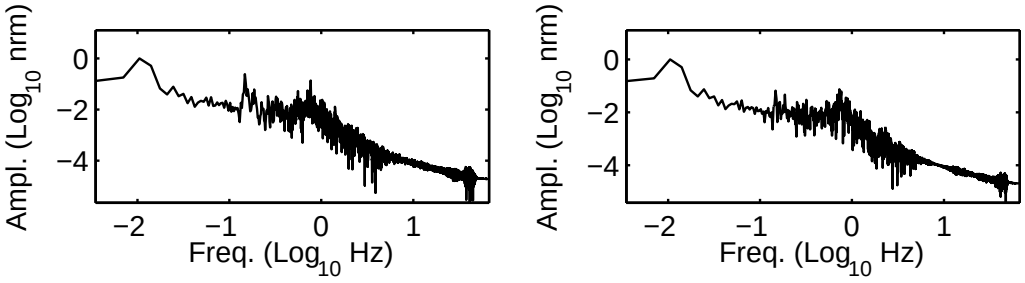

(b) Normalized amplitude spectrum of the full band signal

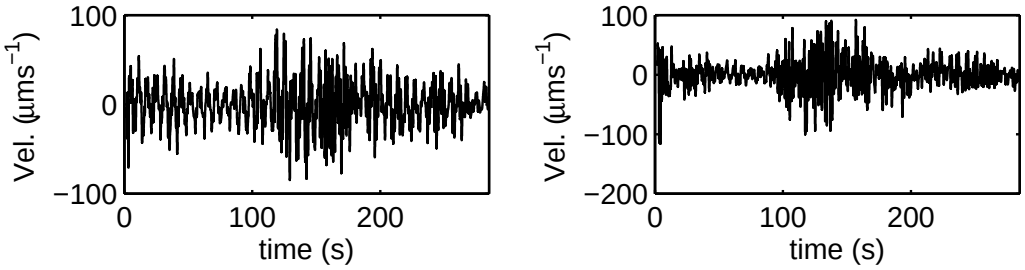

(c) filtered seismic signal

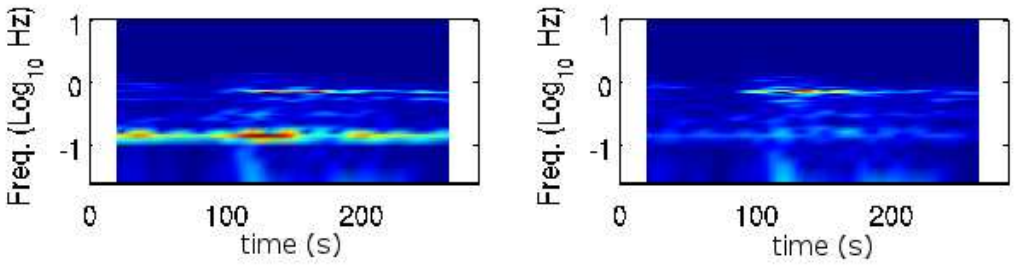

(d) spectrogram of the filtered signal

Figure 11.32: Vertical (left) and horizontal (right) components and corresponding spectrograms of (a) full-band and (c) filtered seismic signal computed at the station located 3 km westwards from the chamber axis for simulation ROCK-5. The applied filter is a band-pass filter with cut-off frequencies of 0.025 and 10 Hz.

Simulation ROCK-6

Results for the simulation ROCK-6, that assumes the fluid-dynamics simulation CF-3 as magmatic source and the VPVS-MODEL rock model are shown in figures 11.33-11.35. The comparison between this simulation and ROCK-4 allows studying the effect on the displacement and seismic signal of the overpressure triggering mixing and convection; in fact, the simulation CF-3 is equal to CF-1 except for the higher driving pressure (20 MPa instead of 1 MPa). Both vertical and horizontal displacements show oscillations that mimic those computed for the magmatic source (fig. 11.33). The displacement patterns are similar to those observed for case ROCK-4 even though the maximum displacement is achieved after 30 s, instead of 210 s; this behaviour is consistent with the source oscillations that show the maximum values at 30 and 210 s for CF-3 and CF-1 respectively. Figure 11.34 confirms that the shape of displacement is similar to that computed for case ROCK-4 (fig. 11.26): the vertical component of displacement is centered above the chamber and vanishes at about 15 km away from the chamber axis (fig. 11.34(a)); the horizontal one shows maximum values about 3 km away from the chamber axis (fig. 11.34(b)). As expected, the displacement amplitude is larger than that calculated for ROCK-4. The vertical component reaches a peak value of 60 mm, about 6 times the vertical maximum calculated for case ROCK-4; the horizontal component shows maximum values of about 45 mm, an order of magnitude greater than that observed for ROCK-4.

The full-band seismic signals (fig. 11.35(a)) shows a main frequency of oscillation of 0.015 Hz (corresponding to a 70 s period). The spectrograms (fig. 11.35(b)) point out a further characteristic frequency of 0.05 Hz (corresponding to a 15 s period). The filtered seismic signals (fig. 11.35(c), 11.35(d)) highlight an high-frequency oscillation with period of 6-7 s (or frequency of 0.15 Hz), well-rendered in the vertical component (left plot). With respect to the seismic signals computed for case ROCK-4, these signals do not show the 0.75 Hz oscillations and a 0.05 Hz oscillation appears.

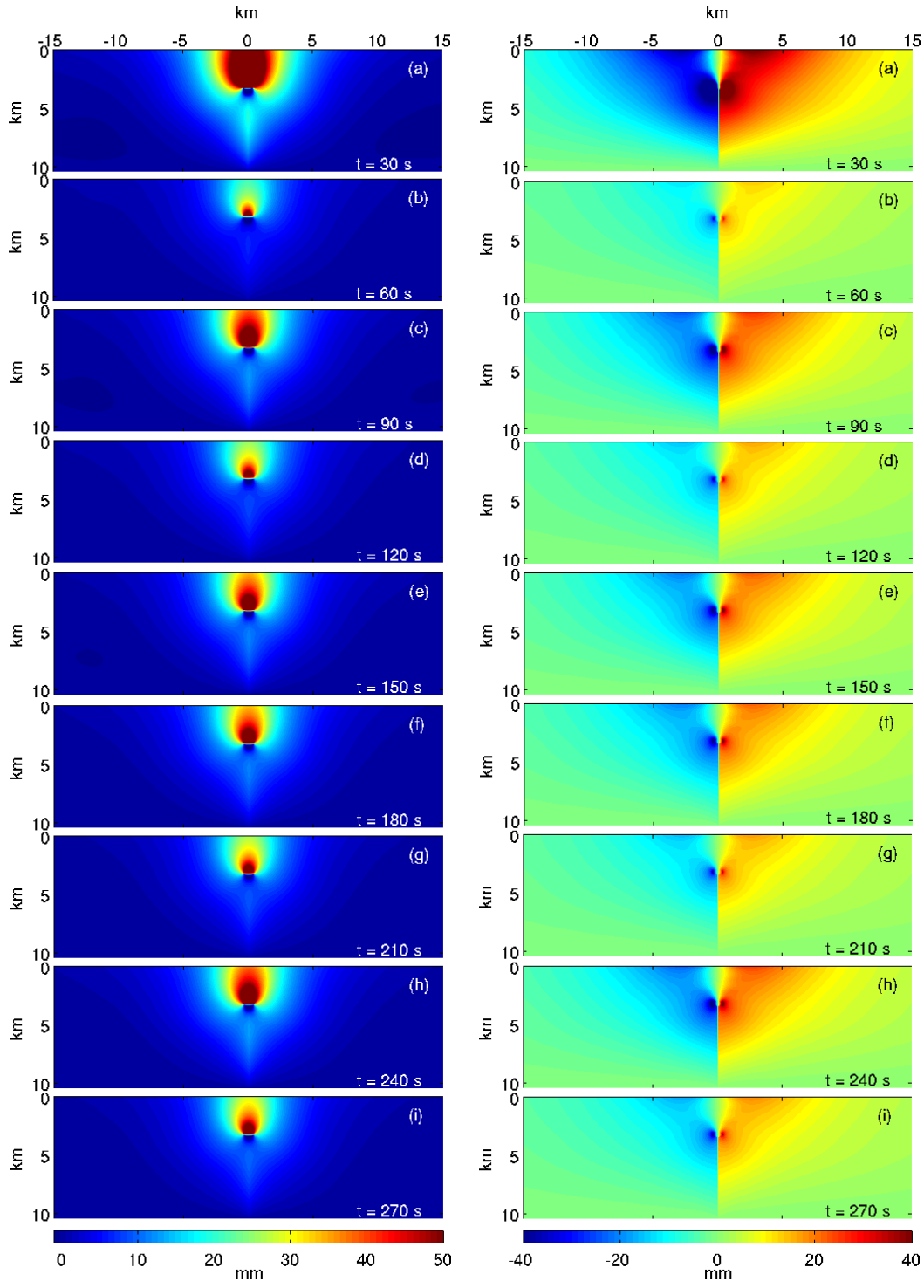

(a) vertical displacement (b) horizontal displacement

Figure 11.33: Snapshots of the (a) vertical and (b) horizontal displacement computed at different times for simulation ROCK-6.

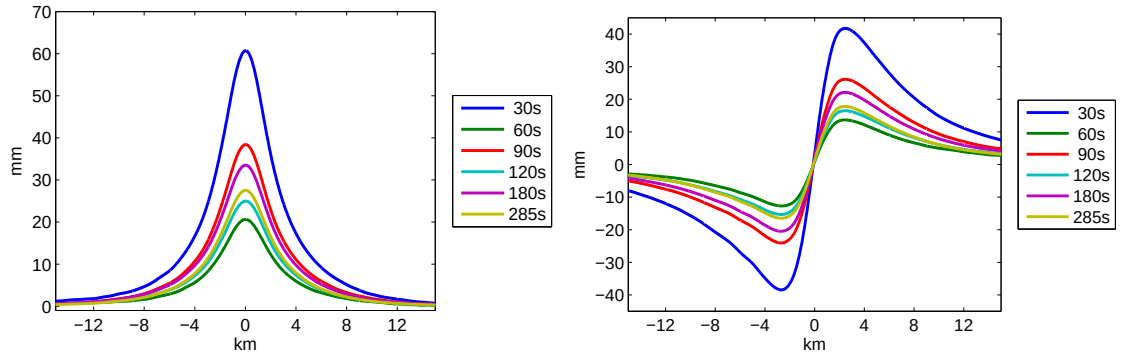

(a) Vertical displacement (b) Horizontal displacement

Figure 11.34: Profiles of (a) vertical and (b) horizontal displacement in function of the distance from the chamber axis computed at different times for simulation ROCK-6.

11.3 Discussion

The results from the present simulations illustrate the deformation field and seismic signals associated with the dynamics of mixing and convection induced by recharge of shallow magma chambers at Campi Flegrei. The above results are obtained through a 1-way coupling between two numerical codes that simulate the fluid-dynamics within the magmatic system (`GALES`), and the propagation of displacement and seismic waves through the surrounding rock system (`ELM`). The coupling has been achieved taking the time-space distribution of stress along the walls of the magmatic system computed through the fluid-dynamics code, and using it as the source for the elasto-dynamics simulations (see section 3.3). The Earth's surface has been accounted for using a free-surface boundary conditions. Models of the rock properties have been defined in collaboration with A. Zollo and co-workers, on the basis of the results obtained by seismic tomographies carried out at Campi Flegrei (see chapter 9).

The major limits of the present study are represented by the assumption of elastic behaviour of rocks neglecting wave attenuation, the 2D approximation, the 1-way coupling between the fluid and rock dynamics, and the assumption in rock dynamics simulations that the magma behaves as an elastic solid with homogeneous v_p, v_s and ρ. As for the simulations of fluid dynamics, a brief discussion of the above limits is required in order to evaluate their relevance for

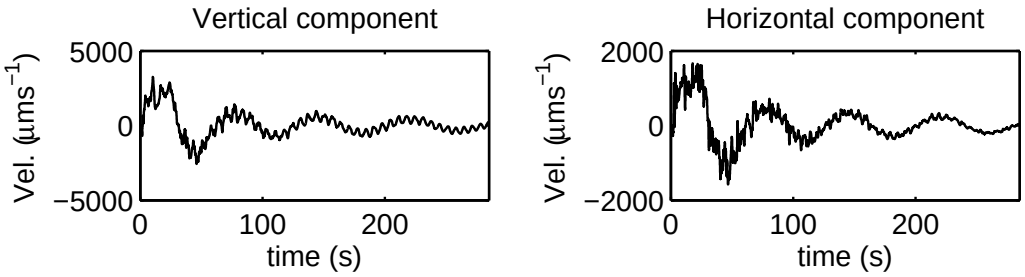

(a) full band seismic signal

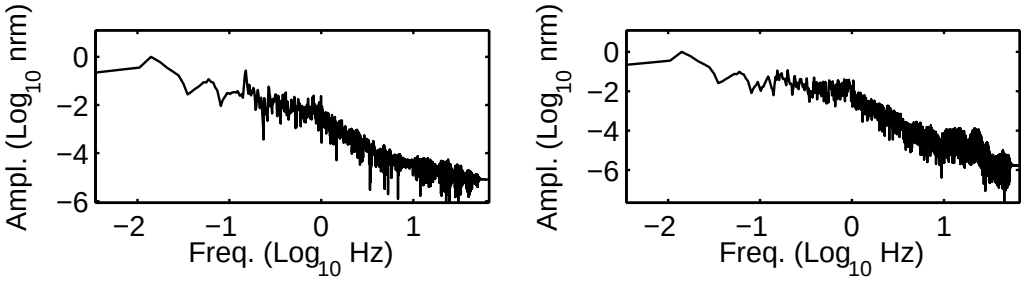

(b) Normalized amplitude spectrum of the full band signal

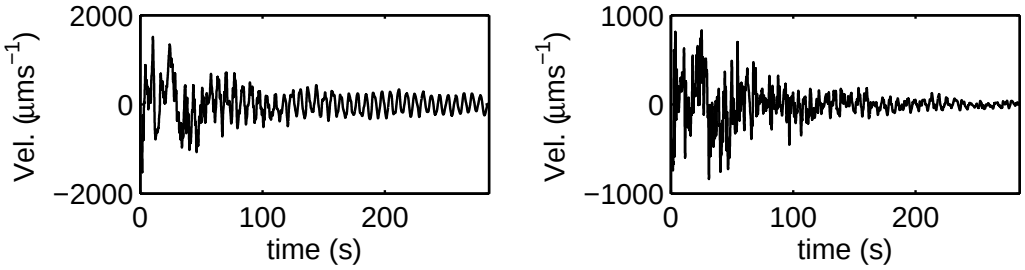

(c) filtered seismic signal

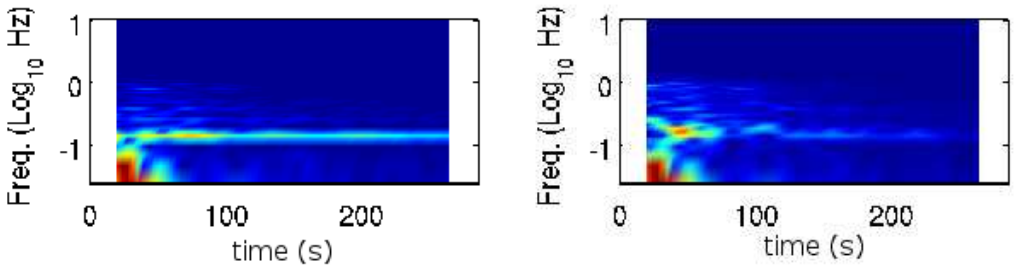

(d) spectrogram of the filtered signal

Figure 11.35: Vertical (left) and horizontal (right) components and corresponding spectrograms of (a) full-band and (c) filtered seismic signal computed at the station located 1 km westwards from the chamber axis for simulation ROCK-6. The applied filter is a band-pass filter with cut-off frequencies of 0.025 and 10 Hz.

the obtained results.

Elastic behaviour of rock

Earth's rocks show elastic or viscoelastic behaviour depending on temperature, confining stress, tectonic setting, and time-scale of the deformation. Elastic materials strain instantaneously when stretched and just as quickly return to their original state once the stress is removed. Viscoelastic materials show elastic and viscous characteristics when subject to stress, and exhibit time-dependent strain. Wave attenuation due to anelasticity of the medium scales with frequency, and is negligible for distance range shorter than the dominant wavelength. Therefore, in this investigation, the assumption of purely elastic behaviour of rock is well justified, at least for the longest-amplitude signals at periods ~ 70 s ($\lambda \sim 200$ km). This can be further understood by considering Maxwell's theory of viscoelastic bodies. A viscoelastic body (fluid or solid) subject to a rate of strain behaves elastically when the strain rate is greater than the inverse of the structural relaxation time of the body itself, or the time required to the body to re-arrange its structural setting to the new stress condition. This is expressed by the following inequality:

$$\text{elastic behaviour}: \qquad \dot{\gamma} > \frac{1}{\tau_s} = \frac{G_\infty}{\mu}$$

where $\dot{\gamma}$ is the rate of strain, τ_s is the structural relaxation time, G_∞ is the elastic modulus, and μ is viscosity. G_∞ takes a value of order 10 GPa, both for cool and molten rocks (Webb and Dingwell, 1990; Tang, 1997), while μ for bulk rocks is of order of 10^{17-19} Pa s (Qi et al., 2007). Therefore, elastic behaviour of rocks occurs when $\dot{\gamma} > 10^{-7}\, s^{-1}$. In mechanically excited rocks, the rate of strain scales with the frequency of rock oscillation f. Therefore

$$\text{elastic behaviour}: \qquad f > 10^{-7}\,\text{Hz}\,, \; or \text{T} < 10^{7}\text{s}$$

where T is the period of oscillation. Since the largest period of rock oscillation from the present simulation are of order of 10^2 s, it follows that the elastic rock assumption is largely justified.

2D approximation

The present simulations assume cartesian 2D coordinates implying that forces and wave propagation in the third direction are neglected. In order to compute the source forces, the numerical code assumes the third dimension of magmatic

system equal to 1 m. This assumption is in contrast with the 2D approximation considered in the fluid-dynamics simulations (see sec. 10.3) that assumes a third not-considered dimension much longer than the other two. The present approximation is, therefore, an important assumption that affects the amplitude of computed ground displacement and seismic signal, and which may have resulted in overestimation of ground motion.

To overcome this limit, future investigations will consider the simulations of rock deformation performed in a 3D domain assuming a magmatic system extending 2 km along the third axis, still neglecting forces on the not-considered chamber boundaries according to the 2D assumption in the fluid dynamics simulations.

1-way coupling

As pointed out above (see sec. 3.3), the 1-way coupling approximation is a significant simplification since rock and fluid dynamics influence each other. Moreover, changes in the volume of the magmatic system due to the stresses along its walls were neglected in the fluid-dynamics simulations. An a-posteriore analysis shows that the region of rock bordering the magmatic system is subject to a displacement of order mm to a few cm. This scale length is 2-3 orders of magnitude smaller than the resolution of the fluid-dynamics mesh, thus we can conclude that the volumetric deformation of the magma chamber is a second-order effect not expected to influence significantly the overall magma dynamics. This implies that the 1-way coupling approximation is justified for the large wavelength displacement found from the simulations. On the contrary, the high frequency oscillations related to the frequency of vibration of the fluid system can be affected by this assumption. Neglecting the dynamic coupling between the fluid and the hosting rocks, in fact, prevents on assessment of interface waves which have been previously described as a source mechanism of volcanic signals (Chouet, 1986). As a consequence, the computed seismic signals have to be considered as a first approximation of the real signals expected to originate from the considered system. A more comprehensive approach needs a fully two-way coupled fluid-rock model that is presently under development at INGV-Pisa.

Elastic properties of magma

The fluid-filled magma chamber and dyke are modelled as an elastic solid with homogeneous v_p, v_s and ρ. This assumption does not account for the space variation of magma properties, the dissipation mechanisms within the

fluid, and the impedance contrast of the fluid-rock interface. However, since the wavelength of the computed quasi-static displacement is large with respect to the size of the magmatic system, the presence of this liquid region is expected to produce secondary effects on the shape and amplitude of the displacement. The above approximation becomes more relevant for high-frequency oscillations, as we do not account for wave scattering, reflection and conversion at the fluid-rock boundaries. Therefore, as observed above, the present investigation should be considered as a first attempt to link pre-eruptive magma dynamics to measurable high-frequency geophysical signals.

Taking in mind these limitations , the results of the numerical simulations can be better discussed and understood.

Long-period displacement

The computed long-period ground displacement associated with the simulated magma mixing and convection dynamics shows oscillations which mimic those of total pressure observed in the magmatic system (fig. 10.12). For all of the considered cases, the vertical and horizontal displacements take the classical shape of a bell and two lobes, respectively. Figure 11.36 summarises the results corresponding to the reference case CF-1 in table 10.3, and highlighting the effects of the assumed rock model on the displacement field. The first relevant result is that the assumption of homogeneous rock properties causes an overestimation of the ground displacement, especially for the vertical component. Moreover, as illustrated by the normalised profiles (figs. 11.36(b) and (d)), the homogeneous rock model induces a less confined vertical and horizontal displacement, with the maximum value in the horizontal component being achieved further from the chamber axis with respect to the heterogeneous models. The increasing complexity of the non-homogeneous models (from ROCK-2 to ROCK-4) affects only slightly the displacement profiles: with increasing complexity of the rock model, the amplitude of the displacement increases, and its profile becomes slightly narrower although the differences are below the detection limit of current instruments. The effect of a variable v_p/v_s ratio (cases ROCK-3 vs. ROCK-4) seems to modify the displacement more than the increased heterogeneity of rock properties (cases ROCK-2 vs. ROCK-3). The inclusion of the topographic profile, induces

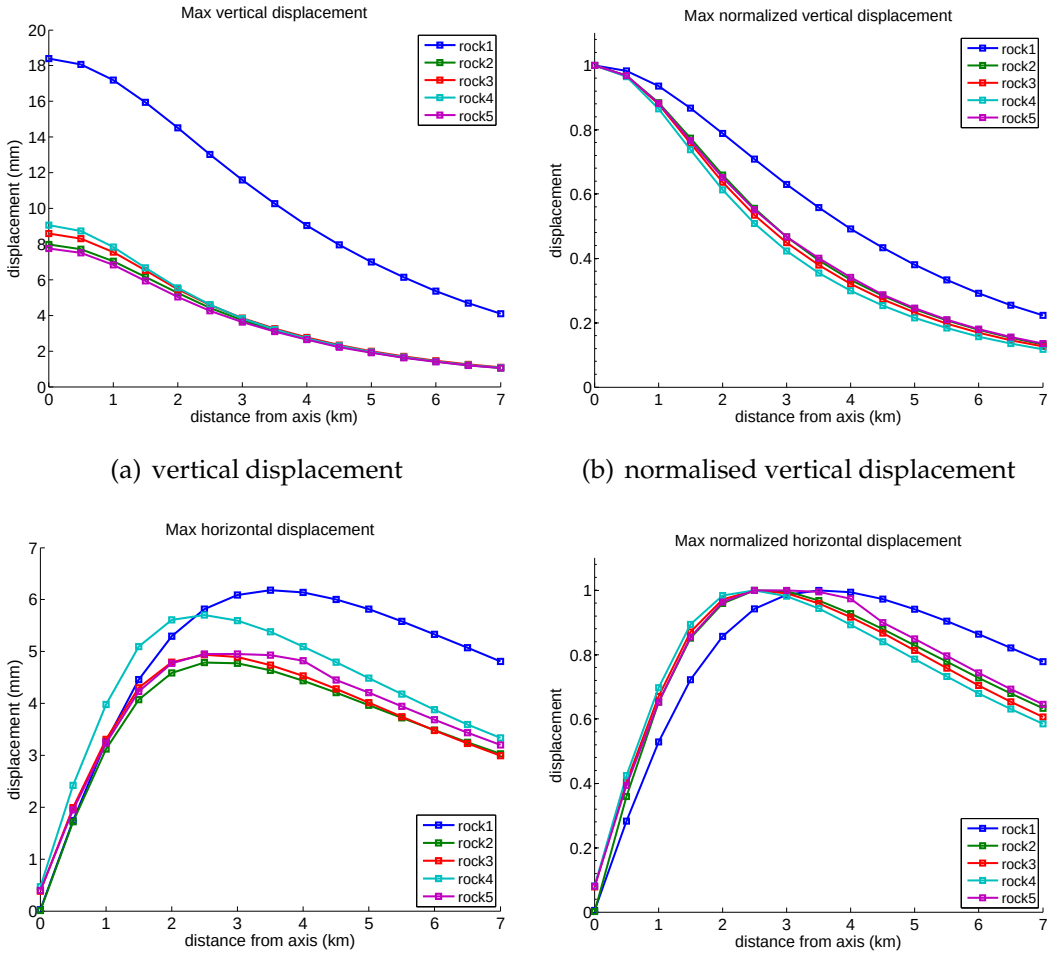

(a) vertical displacement

(b) normalised vertical displacement

(c) horizontal displacement

(d) normalised horizontal displacement

Figure 11.36: Profiles of maximum (a-b) vertical and (c-d) horizontal displacement computed for all of the simulations. Panels (b) and (d) show the profiles normalised to the maximum vertical and horizontal displacement.

a displacement smaller than that computed for the flat profile (cases ROCK-4 vs ROCK-5). The horizontal profile of displacement shows however a well-visible slope variation in correspondence of the topographic relief.

Comparison of cases ROCK-4 and ROCK-6 shows that the fluid-dynamics associated with a larger initial overpressure produce a displacement which, although being larger (figs. 11.26, 11.34), maintains the same profile (fig. 11.37).

Figure 11.38 shows that the shape of the computed displacement profile when rock heterogeneity is accounted for, agrees well with that observed at Campi Flegrei . On the contrary, homogeneous rock model produce a wider displacement

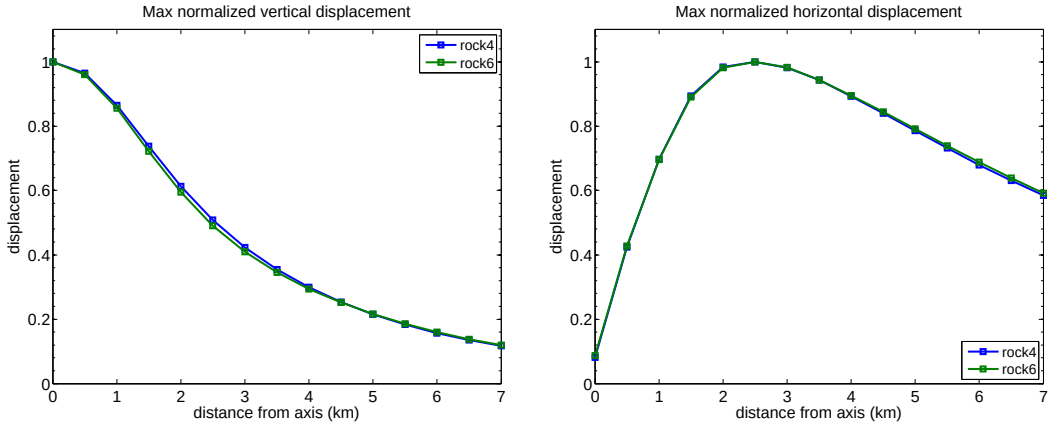

(a) horizontal displacement (b) normalised horizontal displacement

Figure 11.37: Profiles of normalised maximum (a) vertical and (b) horizontal displacement for simulations ROCK-4 and ROCK-6. The values are normalised with respect to the maximum vertical and horizontal displacement, respectively.

which does not fit the observations.

Seismic signals

Irrespective of the rock model adopted, the computed synthetic seismograms show a main characteristic period of 70-100 s, depending on the specific magma dynamics simulation considered. Removing this low frequency oscillation and the numerical noise from the seismic signal, further high frequency oscillations emerge. The periods of the relevant oscillations are 6-7 and 1-2 s when rock heterogeneity is accounted for, and cases with relatively low, reasonable magma overpressure are considered. High-overpressure case does not show the 1-2 s period, revealing instead oscillations at 15 s.

The above frequencies fall within the typical frequency bands observed in volcanic areas where signals, depending on their characteristic period, are classified as Ultra-Long-Period (ULP; $T > 10$ s), Very-Long-Period (VLP; $1 < T < 10$ s), and Long-Period (LP; $0.1 < T < 1$ s) (Chouet, 1996). These signals are generally interpreted in terms of the elastic response of the medium to mass transport processes, and/or forced oscillation of fluid-filled reservoir in response to transient pressurisation. This study demonstrates that first-order magmatic processes, such as convection and mixing in a magma chamber, can generate such signals, thus opening new perspective towards their quantitative interpretation.

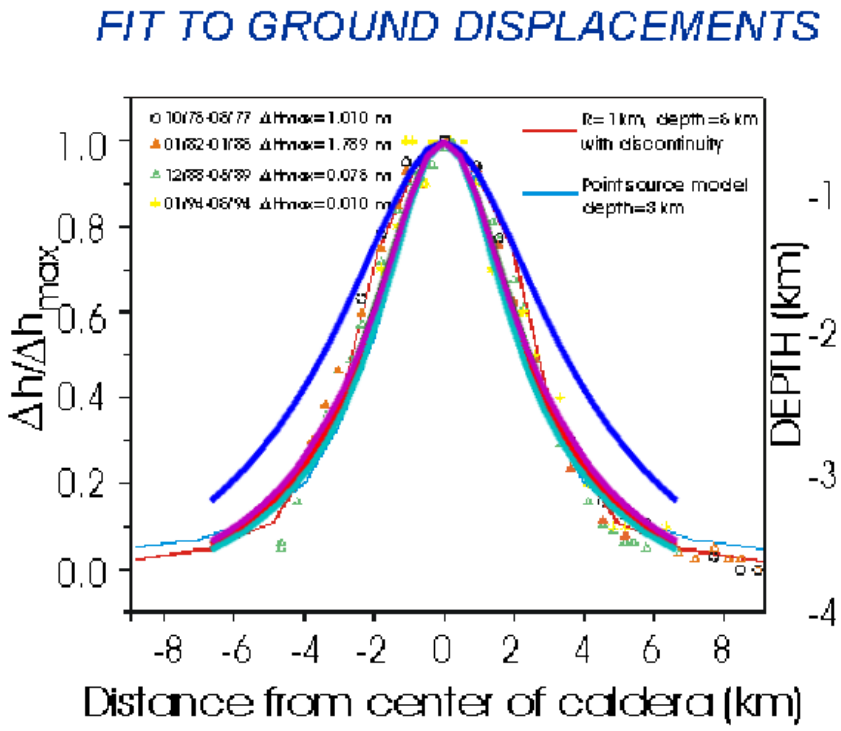

Figure 11.38: Comparison between ground displacement profiles observed at Campi Flegrei , that computed in this study, and those calculated by De Natale et al. (1997) for a point source embedded in homogeneous and heterogeneous models. The superimposed colored line show the ground displacement computed in this study for heterogeneous (cyan, red, magenta lines) and homogeneous (blue line) rocks.

Chapter 12

Implications for the unrest dynamics at Campi Flegrei, and conclusions

This work of thesis has implications which are relevant for the interpretation of the dynamics observed at Campi Flegrei, and for the evaluation of the short-term hazard. These implications are discussed in the following.

In previous chapters it has been shown that small-volume magma chambers were repeatedly emplaced at shallow level during the past history of Campi Flegrei. Such shallow magmatic bodies appear to have been connected to deeper regions of magma supply, and to have fed eruption, often shortly following phases of new magma arrival inside the chamber. There is not knowledge of such shallow magmatic bodies today present at Campi Flegrei . On the other hand, present days techniques to survey and image the underground of Campi Flegrei do not have the required resolution. What we know is that there is a relatively deep magmatic body at about 7.5 km depth, and that increased fumarolic activity accompanying and following bradyseismic crises at Campi Flegrei mostly involves fluids of magmatic origin. We also know that the present unrest at Campi Flegrei lasting from the fifties, constitutes an element of enormous concern for such an intensely urbanised area. Apart from a possible ground uplift event at the passage between the VIII and IX century, the only known unrest of similar relevance during last 2 ka preceded the 1538 eruption of Monte Nuovo inside the caldera. Obviously, by analogy with the reconstructed dynamics of past eruptions, the existence of a small shallow magmatic body would represent a factor of increased hazard at Campi Flegrei . The hazard would be the highest if an event of new magma entrance

in that shallow magmatic body occurs. The present work of thesis investigates the magma dynamics and the associated geophysical signals related to such an extremely hazardous event, that cannot be ruled out as one major factor involved in the decades-long and still ongoing unrest at Campi Flegrei . This chapter takes the bulk of results obtained through the magma dynamics and rock dynamics simulations described and discussed above, and attempt to place them into a global perspective relevant for the short-term volcanic hazard at Campi Flegrei .

The present work shows that the arrival of new gas-rich magma in a hypothetical shallow magma chamber at Campi Flegrei is capable to produce changes in the gravity field and ground motions patterns that can be relieved by a geophysical monitoring network. Such gravity, ground deformation and seismic signals occur over a short time and over a range of frequencies that are recognised, or increasingly be recognised, at many active volcanic areas in the world. The simulated dynamics show the displacement of a large amount of magmatic gases, mainly constituted by CO_2, towards the top regions of the magma chamber. It can be expected therefore that due to diffusion trough porous and partially fractured rocks at the roof of the magma chamber, a CO_2-rich magmatic gas phase enters the rock system and migrates towards the surface, interacting with the large hydrothermal system of Campi Flegrei . Such a process would be responsible of a transfer to shallow levels of energy in the from of enthalpy transported with the fluid, progressively displacing towards the surface the source of overpressure responsible for additional ground deformation. Since the amplitude of ground deformation due to an overpressurised source decays with the square of the distance, ground deformation due to overpressurisation of the hydrothermal system is expected to be responsible for most of the observed ground motion during bradyseismic crises at Campi Flegrei , as already recognised (Gaeta et al., 1998; Chiodini et al., 2001).

The general picture emerging, if a shallow magma chamber would be today present at Campi Flegrei , is that the initial phases of a bradyseismic crisis may reflect convected dynamics occurring inside the chamber itself, while most of the crisis, including highest amplitude ground deformation, reflects instead the delayed response of the shallow hydrothermal system upon ingression of CO_2-rich fluid of deep magmatic origin. The present simulation results, together with

observations of the unrest dynamics and previous investigations (Chiodini et al., 2001, 2003; De Natale et al., 1991, 2001; Gottsmann et al., 2003; Todesco et al., 2004; Bruno et al., 2007; Saccorotti et al., 2007; Troise et al., 2007), allow to draw a consistent set of expected signals for the possible initial "magmatic" phase, and the subsequent "hydrothermal" phase of the unrest.

Initial "magmatic" phase:

- Ground deformation: order of 1 cm.
- Seismic signal: three main periods, the dominant one is a ULP signal at 50-100 s, accompanied by VLP at 5-10 s, and LP/tremor at 1-2 s.
- Vertical gravity change: negative, order of tens of μgals, or below the detection limit if the new magma entering the chamber has a very small (0.1 wt%) difference in volatile content with respect to resident magma.

Following phase of hydrothermal system respose:

- Ground deformation: order of several cm to m.
- Seismic signal: VT (or high frequency volcano-tectonic earthquakes) due to overpressurisation and fracturing of rocks hosting the hydrothermal system; LP from fluid flow and resonance in fluid filled cracks.
- Vertical gravity change: either positive or negative, depending on the balance between new gas input, density contrast between new and resident fluids, and superimposition with residual gravity change due to internal magma chamber dynamics.
- Gas output: CO_2/H_2O increase, increase of total gas flux, increase of the magmatic component in the fumaroles.

The above picture has one relevant implication for the short-term volcanic hazard, which is that the most hazardous phase of the unrest, possibly leading to an eruption, is confined at the beginning of a new bradyseismic crisis, with most of the crisis corresponding instead to the slow process of gas and energy discharge from the system when the true hazard has been surpassed. Such a view is consistent with the only recent example in a caldera setting, represented by that of Rabaul volcano, Papua New Guinea, in 1994 (hvo.wr.usgs.gov/volcanowatch/1994/94_09_23.html; users.bandnet.com/bjensen/volcano/swpacific/newbritan rabaul.html). In that

case, intense ground deformation and seismic activity intermittently occurred during the eighties and beginning of nineties. A new explosive eruption occurred on September 19, 1994, following a period of relative quiet in the caldera activity, and preceded by only one day of new intense seismic activity.

Obviously, between the phase of new magma arrival and associated signals, and the onset of a new eruption, the magma needs to migrate towards the surface, breaking the rocks and producing increasingly intense signals registered by the monitoring network. However, the length of this pre-eruptive magma ascent phase is not necessarily long, and not easy to predict. The above cited case of Rabaul suggests an order of one day for magma ascent and beginning of the eruption, although it must be stressed that the monitoring network at the time of the eruption is not even comparable with that installed at Campi Flegrei . A 1-day delay between new magma input into a shallow chamber and eruption of magma is also suggested for the Plinian phases of the 4100 BP Agnano-Monte Spina eruption at Campi Flegrei , based on observed liquid-solid reactions in the volcanic products (see chapter 9), but it must be noted that such a phase did not occur at the beginning of the eruption. At least 10 days of extremely frequent earthquakes, following about two months of less frequent earthquakes felt by the population, preceded the A.D. 1538 eruption of Monte Nuovo at Campi Flegrei (Guidoboni from INGV-DPC Project V3_2 Campi Flegrei: Final report). As a conclusion, a range of time-delay is possible between magma arrival at shallow level, and eruption onset. Recognising events of new magma ingression into a shallow chamber at Campi Flegrei - if such a chamber exists today - would represent a mean of getting aware of a potential danger, and establish an early warning in the area. The present work represents a first comprehensive approach along this line of investigation, and a first attempt to characterise the dynamics and the geophysical signals associated to the presence of a periodically refilled shallow magma chamber at Campi Flegrei . More sophisticated, hence more confident investigation, requires a better definition of possible system conditions at Campi Flegrei , the development of a fully coupled approach to simulate the magma and rock dynamics, which is being implemented at the Istituto Nazionale di Geofisica e Vulcanologia in Pisa, and inclusion into the analysis of the coupled dynamics of the hydrothermal system at Campi Flegrei .

Appendixes

Appendix A

Mixture model

The physical model adopts an ideal mixture of n components in liquid or gaseous state. The partial specific (per unit mass) Gibbs free energy of component k in phase π, component k, and mixture are (Gerasimov et al., 1974):

$$g_k^\pi = g_k^{\pi,0}(p,T) + R_k T \ln \xi_k^\pi \tag{A.1}$$

$$g_k = \sum_\pi \eta_k^\pi g_k^\pi \tag{A.2}$$

$$g = \sum_k y_k g_k = \sum_{k,\pi} y_k^\pi g_k^\pi \tag{A.3}$$

where $g_k^{\pi,0}$ is the specific Gibbs free energy in the standard state, ξ_k^π is mole fraction of component k in phase π with respect to phase π, and $\eta_k^\pi = y_k^\pi / y_k$ is the weight fraction of component k in phase π with respect to component k. In the assumption of ideal mixture, ξ_k^π and η_k^π depend only on pressure and temperature. Either ξ_k^π or η_k^π are given by the relations for chemical equilibrium, and can be derived the ones from the others through a linear relationship. Equation (A.1) is used for both liquid and gaseous mixtures.

The partial derivatives entering the $\boldsymbol{V}_{,\Upsilon}$ matrix of the discontinuity capturing term are derived from (eq. A.1):

$$\left.\frac{\partial g_k^\pi}{\partial p}\right|_{T,\xi} = \frac{1}{\rho_k^\pi} \tag{A.4}$$

$$\left.\frac{\partial (g_k^\pi / T)}{\partial T}\right|_{p,\xi} = -\frac{h_k^\pi}{T^2} \tag{A.5}$$

$$\left.\frac{\partial g_k^\pi}{\partial \xi_h^\pi}\right|_{p,T,\xi_\cdot^\pi[h,\mathbf{n}]} = \frac{R_k T}{\xi_k^\pi}\delta_{kh} \tag{A.6}$$

where notation $\xi_\cdot^\pi[h,\mathbf{n}]$ means that all ξs but ξ_h^π and ξ_n^π are constant. Specific internal energy and enthalpy of component k in phase π, component k and mixture are:

$$e_k^\pi = c_{vk}^\pi T \tag{A.7}$$

$$h_k^\pi = c_{pk}^\pi T = e_k^\pi + \frac{p}{\rho_k^\pi} \tag{A.8}$$

$$e_k = \sum_\pi \eta_k^\pi e_k^\pi \tag{A.9}$$

$$h_k = \sum_\pi \eta_k^\pi h_k^\pi \tag{A.10}$$

$$e = \sum_k y_k e_k = \sum_{k,\pi} y_k^\pi e_k^\pi \tag{A.11}$$

$$h = \sum_k y_k h_k = \sum_{k,\pi} y_k^\pi h_k^\pi = e + \frac{p}{\rho} \tag{A.12}$$

where ρ_k^π, c_{vk}^π, c_{pk}^π are density and specific heat coefficients at constant volume and pressure of component k in phase π. The equation of state $\rho_k^\pi = \rho_k^\pi(p,T)$ may have a general form.

The ideal solution mixture implies the following thermodynamic relations (Modell and Reid, 1983):

$$\frac{1}{\rho} = \sum_{k,\pi} \frac{y_k^\pi}{\rho_k^\pi} = \sum_k \frac{y_k}{\rho_k} \tag{A.13}$$

$$\left.\frac{\partial(1/\rho)}{\partial y_k}\right|_{p,T,y_\cdot[k,\mathbf{n}]} = \frac{1}{\rho_k} - \frac{1}{\rho_n} \tag{A.14}$$

$$\left.\frac{\partial e}{\partial y_k}\right|_{p,T,y_\cdot[k,\mathbf{n}]} = e_k - e_n \tag{A.15}$$

where notation $y_\cdot[k,\mathbf{n}]$ means that all ys but y_k and y_n are constant. The total specific energy of the mixture in (3.3) is $e_t = e + \dfrac{|\boldsymbol{u}|^2}{2}$.

Diffusion is modelled with the linear fluxes of mass, momentum and heat (Bird et al., 1960):

$$\tau_{ij} = \mu\left(u_{i,j} + u_{j,i}\right) + \lambda u_{k,k}\delta_{ij} \tag{A.16}$$

$$q_i = -\kappa T_{,i} \tag{A.17}$$

$$J_i^k = -\rho\mathscr{D}_k\left(y_{k,i} - y_k\mathscr{M}\sum_{h=1}^{n}\frac{y_{h,i}}{\mathscr{M}_h}\right) + \rho y_k\sum_{h=1}^{n}\mathscr{D}_h\left(y_{h,i} - y_h\sum_{p=1}^{n}\frac{y_{p,i}}{\mathscr{M}_p}\right) \tag{A.18}$$

where $\lambda = \mu_b - \frac{2}{3}\mu$, with the assumption of neglecting the bulk viscosity μ_b (Chalot and Hughes, 1994).

The thermal diffusion coefficient κ is calculated as:

$$\kappa = \sum_{k,\pi} x_k^\pi \kappa_k^\pi \tag{A.19}$$

where κ_k^π is the thermal diffusion coefficient of component k in phase π, and x_k^π is the molar fraction of component k in phase π in the mixture. The mass fluxes J_i^ks are written in the approximated form by Curtiss and Hirschfelder (Hirschfelder et al., 1969; Bird et al., 1960) using an effective diffusion coefficient of component k in the mixture $\mathscr{D}_k$, modelled as a function of the molar fractions of the components in the phases. The addition of a correction flux (Giovangigli, 1999) is needed to satisfy mass conservation, so that fluxes verify:

$$\sum_{k=1}^{n} J_i^k = 0. \tag{A.20}$$

The mixture molar mass $\mathscr{M}$ is:

$$\frac{1}{\mathscr{M}} = \sum_k \frac{y_k}{\mathscr{M}_k} = \sum_{k,\pi}\frac{y_k^\pi}{\mathscr{M}_k} \tag{A.21}$$

The sound velocity in the mixture is calculated as (Wallis, 1979):

$$c = \left(\sum_{k,\pi}\frac{\alpha_k^\pi}{\rho_k^\pi c_k^\pi}\rho\right)^{-\frac{1}{2}}$$

where α_k^π and c_k^π are volume fraction and sound velocity of component k in phase π in the mixture.

Appendix B

Numerical formulation of GALES

The system of equations (3.1-3.3) is written in terms of the vector of conservation variables $\boldsymbol{U}$ using compact notation Hauke and Hughes (1998):

$$\boldsymbol{U}_{,t} + \boldsymbol{F}_{i,i}^{\text{adv}} = \boldsymbol{F}_{i,i}^{\text{diff}} + \boldsymbol{\mathscr{F}} \tag{B.1}$$

$$\boldsymbol{U} = \rho \begin{pmatrix} y_1 \\ \vdots \\ y_n \\ u_1 \\ u_2 \\ u_3 \\ e_t \end{pmatrix} \tag{B.2}$$

where $\boldsymbol{F}_i^{\text{adv}}$ and $\boldsymbol{F}_i^{\text{diff}}$ are the advective and diffusive flux vectors in the ith direction, and $\boldsymbol{\mathscr{F}}$ is the source vector.

In order to solve the incompressible limit, the conservation variables $\boldsymbol{U}$ are replaced by the pressure primitive variables $\boldsymbol{Y}$ which are employed as unknowns:

$$\mathbf{Y} = \begin{pmatrix} y_1 \\ \vdots \\ y_{n-1} \\ p \\ u_1 \\ u_2 \\ u_3 \\ T \end{pmatrix} \tag{B.3}$$

The $n-1$ independent mass fractions of components y_k, pressure p and temperature T represent the $n+1$ thermodynamic quantities necessary to completely describe the compressible mixture of n components at chemical equilibrium. The pressure primitive variables $(p, \boldsymbol{u}, T)$ for simple fluid compressible-incompressible flows proved to be a reliable choice in terms of accuracy, convergence, computational costs and robustness of the related numerical algorithm Hauke and Hughes (1998). Extention to the $\boldsymbol{Y}$ vector (B.3) involves inclusion of the mass fraction of components, and makes the calculation of physical properties and boundary conditions easier.

The system of equations (B.1) is rewritten in terms of primitive variables in quasi-linear form Hauke and Hughes (1998):

$$\boldsymbol{U}_{,\boldsymbol{Y}}\boldsymbol{Y}_{,t} + \boldsymbol{F}^{\mathrm{adv}}_{i,\boldsymbol{Y}}\boldsymbol{Y}_{,i} = (\boldsymbol{K}_{ij}\boldsymbol{Y}_{,j})_{,i} - \boldsymbol{S}\boldsymbol{Y} \tag{B.4}$$

where $\boldsymbol{U}_{,\boldsymbol{Y}}$, $\boldsymbol{F}^{\mathrm{adv}}_{i,\boldsymbol{Y}}$ are the matrices of partial derivatives of $\boldsymbol{U}$ and $\boldsymbol{F}^{\mathrm{adv}}_{i}$ with respect to $\boldsymbol{Y}$. The linearization requires that the diffusive flux and source vector are expressed as $\boldsymbol{F}^{\mathrm{diff}}_{i} = \boldsymbol{K}_{ij}\boldsymbol{Y}_{,j}$ where $\boldsymbol{K}_{ij}$ are the diffusivity matrices, and $\mathscr{F} = -\boldsymbol{S}\boldsymbol{Y}$ where $\boldsymbol{S}$ is the source matrix (Shakib et al., 1991).

A similar multicomponent formulation has been introduced in Chalot et al. (1990), where a vibrational energy term, neglected here, is also considered. The analysis in Chalot et al. (1990) takes into account only entropy variables and compressible mixtures of ideal or perfect gases. The multicomponent formulation in this work, based on pressure primitive variables, allows the solution of compressible as well as incompressible flows of gas, liquid, and gas-liquid mixtures with general EOS. The tight similarity between the method of this work and those in Hauke and Hughes (1998) and Chalot et al. (1990) allows to develop all the necessary stabilisation terms, while keeping the advantages of the numerical method for single fluid flow.

Bibliography

Aki, K. and Richardson, P. G. (1980). *Quantitative seismology*. Freeman, San Francisco.

Allen, M. and Tildesley, D. J. (1987). *Computer Simulations of Liquids*. Oxford University Press, New York.

Arbabi, S. and Sahimi, M. (1988). Elastic properties of three-dimensional percolation networks with stretching and bond-bending forces. *Phys. Rev. B*, 38(10):7173–7176.

Avallone, A., Zollo, A., Briole, P., Delacourt, C., and Beauducel, F. (1999). Subsidenc of Campi Flegrei (Italy) detected by sar interferometry. *Geophys. Res. Lett.*, 26:2303–2306.

Barberi, F., Carapezza, M., Innocenti, F., Luongo, G., and Santacroce, R. (1989). The problem of volcanic unrest: the Phlegrean Fields case history. In *Atti Conv. Lincei*, volume 80, pages 387–405.

Barberi, F., Corrado, G., Innocenti, F., and Luongo, G. (1984). Phlegrean Fields 1982-1984: Brief chronicle of a volcano emergency in a densely populated area. *Bull. Volcanol.*, 78(2):175–185.

Barberi, F., Innocenti, F., Lirer, L., Munno, R., Pescatore, T., and Santacroce, R. (1978). The Campanian Ignimbrite: a major prehistoric eruption in the Neapolitan area (Italy). *Bull. Volcanol.*, 41:1–22.

Battaglia, J., Zollo, A., Virieux, J., and Dello Iacono, D. (2007). Merging active and passive data sets in travel-time toography:the case study of Campi Flegrei Caldera (Southern Italy). *Geophys. Prosp.* submitted.

Bergantz, G. W. (2000). On the dynamics of magma mixing by reintrusion: implications for pluton assembly process. *J. Struct. Geology*, 22(9):1297–1309.

Berrino, G., Corrado, G., Luongo, G., and Toro, B. (1984). Ground deformation and gravity changes accompanying the 1982 Pozzuoli uplift. *Bull. Volcanol.*, 47:187–200.

Bird, R. B., Stewart, W. E., and Lightfoot, E. N. (1960). *Transport phenomena*. Wiley.

Blake, S. (1981). Volcanism and dynamics of open magma chambers. *Nature*, 289:783–785.

Bonafede, M. and Mazzanti, M. (1998). Modelling gravity variations consistent with ground deformation in the Campi Flegrei caldera (Italy). *J. Volcanol. Geotherm. Res.*, 81:137–157.

Bouchon, M. (1981). A simple method to calculate the green's function for elastic layered media. *Bull. Seismol. Soc. Am.*, 71:959–971.

Bower, S. and Woods, A. W. (1997). Control of magma volatile content and chamber depth on the mass erupted during explosive volcanic eruptions. *J. Geophys. Res.*, 102:10,263–10,290.

Brooks, A. N. and Hughes, T. J. R. (1982). Streamline Upwind Petrov-Galerkin formulations for convection dominated flows with particular emphasis on the incompressible Navier-Stokes equations. *Comput. Methods Appl. Mech. Engrg.*, 33:199–259.

Bruno, P., Ricciardi, G., Petrillo, Z., Di Fiore, V., Troiano, A., and Chiodini, G. (2007). Geophysical and hydrogeological experiments from a shallow hydrothermal system at Solfatara Volcano, Campi Flegrei, Italy: Response to caldera unrest. *J. Geophys. Res.*, 112(B06201).

Burnham, C. W. and Davis, N. F. (1974). The role of H_2O in silicate melts. II, thermodynamic and phase relations in the system $NaAlSi_3O_8$-H_2O to 10 kilobars, 700 °C-1100 °C. *Amer. J. Sci.*, 274:902–940.

Caputo, M. (1979). Two-thousand years of geodetic and geophysical observations in the Phlegrean Fields near Naples. *J. R. Astron. Soc.*, 56:316–328.

Caricchi, L., Burlini, L., Ulmer, P., Vassalli, M., and Papale, P. (2007). Non-newtonian rheology of crystal-bearing magmas and implications for magma ascent dynamics. *Earth Pl. Sci. Lett.*, 264:402–419.

Cashman, K. V., Sturtevant, B., Papale, P., and Navon, O. (2000). *Encyclopedia of Volcanoes*, chapter Magmatic fragmentation. Academic Press.

Chalot, F. and Hughes, T. (1994). A consistent equilibrium chemistry algorithm for hypersonic flows. *Comput. Methods Appl. Mech. Engrg.*, 112:25–40.

Chalot, F., Hughes, T. J. R., and Shakib, F. (1990). Symmetrization of conservation laws with entropy for high-temperature hypersonic computations. *Comput. Syst. Engrg.*, 1:495–521.

Chau, K. T. and Wong, R. H. C. (1996). Uniaxial compressive strength and point load strength of rocks. *Int. J. Rock Mech. Min. Sci.*, 33(2):183–188.

Chiodini, G., Frondini, F., Cardellini, C., Granieri, D., Marini, L., and Ventura, G. (2001). CO_2 degassing and energy release at Solfatara Volcano, Campi Flegrei, Italy. *J. Geophys. Res.*, 106:16213–16221.

Chiodini, G., Todesco, M., Caliro, S., Del Gaudio, C., Macedonio, G., and Russo, M. (2003). Magma degassing as a trigger of bradyseismic events: The case of Phlegrean Fields (Italy). *Geophys. Res. Lett.*, 30:1434–1437.

Chouet, B. (1982). Free surface displacements in the near field of a tensile crack expanding in three dimensions. *J. Geophys. Res.*, 86:3868–3872.

Chouet, B. (1986). Dynamics of a fluid-driven crack in three dimensions by the finite difference method. *J. Geophys. Res.*, 91:13967–13992.

Chouet, B. (1987). Representation of an extended seismic source in a propagator-based formalism. *Bull. Seismol. Soc. Am.*, 77:14–27.

Chouet, B. (1996). *Monitoring and mitigation of volcano hazards*, chapter New methods and future trends in seismological volcano monitoring, pages 23–97. Springer-Verlag, New York.

Civetta, L., Orsi, G., Pappalardo, L., Fisher, R. V., Heiken, G., and Ort, M. (1997). Geochemical zoning, mingling, eruptive dynamics and depositional processes

- the Campanian Ignimbrite, Campi Flegrei caldera, Italy. *J. Volcanol. Geotherm. Res.*, 75:183–219.

Coombs, M. L., Eichelberger, J. C., and Rutherford, M. J. (2000). Magma storage and mixing conditions for the 1953-1974 eruptions in South-west Trident volcano, Katmai National Park, Alaska. *Contrib. Mineral. Petrol.*, 140:99–118.

Courtillot, V. (1990). A volcanic eruption. *Scientific American*, October.

de Lorenzo, S., Gasparini, P., Mongelli, F., and Zollo, A. (2001a). Thermal state of Campi Flegrei caldera inferred from seismic attenuation tomography. *J. Geodynamics*, 32:467–486.

de Lorenzo, S., Zollo, A., and Mongelli, F. (2001b). Source parameters and three-dimensional attenuation structure from the inversion of microearthquake pulse width data: Qp imaging and inferences on the thermal state of the Campi Flegrei caldera (Southern Italy). *J. Geophys. Res.*, 206:16265–16286.

De Natale, G., Petrazzuoli, S., and Pingue, F. (1997). The effect of collapse structures on ground deformations in calderas. *Geophys. Res. Lett.*, 24(13):1555–1558.

De Natale, G. and Pingue, F. (1993). Ground deformations in collapsed caldera structures. *J. Volcanol Geotherm. Res.*, 57:19–38.

De Natale, G., Pingue, F., Allard, P., and Zollo, A. (1991). Geophysical and geochemical modelling of the Campi Flegrei caldera. *J. Volcanol Geotherm. Res.*, 48:199–222.

De Natale, G., Troise, C., and Pingue, F. (2001). A mechanical fluid-dynamical model for ground movements at Campi Flegrei caldera. *J. Geodynamics*, 32:487–517.

de Vita, S., Orsi, G., Civetta, L., Carandente, A., D'Antonio, M., Di Cesare, T., Di Vito, M., Fisher, R. V., Isaia, R., Marotta, E., Ort, M., Pappalardo, L., Piochi, M., and Southon, J. (1999). The Agnano-Monte Spina eruption (4.1 ka) in the resurgent, nested Campi Flegrei caldera (Italy). *J. Volcanol. Geotherm. Res.*, 91:269–301.

De Vivo, B., Rolandi, G., Gans, P. B., Calvert, A., Bohrson, W. A., Spera, F. J., and Belkin, A. E. (2001). New constrains on the pyroclastic eruption history of the Campanian volcanic plain (italy). *Mineral. Petrol.*, 73:47–65.

Decker, R. and Decker, B. (1991). *Mountains of fire*. Cambridge University Press, Cambridge.

Deino, A. L., Orsi, G., de Vita, S., and Piochi, M. (2004). The Astroni volcano: the only example of closely spaced eruptions in the same vent area during the recent history of the Campi Flegrei caldera (Italy). *J. Volcanol. Geotherm. Res.*, 133:157–170.

Dellino, P., Isaia, R., La Volpe, L., and Orsi, G. (2001). Statistical analysis of textural data from complex pyroclastic sequences: implication for fragmentation processes of the Agnano-Monte Spina eruption (4.1 ka), Phlegraean Fields, southern Italy. *Bull. of Volcanol.*, 63(7):443–461.

Dellino, P., Isaia, R., La Volpe, L., and Orsi, G. (2004). Interaction between particles trasported by fallout and surge in the deposits of Agnano-Monte Spina eruption (Campi Flegrei, Southern Italy). *J. Volcanol. Geotherm. Res.*, 133:193–210.

Dello Iacono, D., Zollo, A., Vassallo, M., Vanorio, T., and Judenherc, S. (2006). Seismic images and rock properties of the very shallow structure of Campi Flegrei caldera (Southern Italy). *Bull. of Volcanol.* submitted.

Di Vito, M., Isaia, R., Orsi, G., Southon, J., de Vita, S., D'Antonio, M., Pappalardo, L., and Piochi, M. (1999). Volcanic and deformation history of the Campi Flegrei caldera in the past 12 ka. *J. Volcanol. Geotherm. Res.*, 91:221–246.

Di Vito, M., Lirer, L., Mastrolorenzo, G., and Rolandi, G. (1987). The Monte Nuovo eruption (Campi Flegrei, Italy). *Bull. Volcanol.*, 49:608–615.

Dingwell, D. B. and Webb, S. L. (1989). Structural relaxation in silicate melts and non-newtonian melt rheology in geological processes. *Phys. Chem. Miner.*, 16:508–516.

Dobran, F. (2001). *Volcanic processes: mechanisms in material transport*. Kluwer Academic/Plenum Publishers, New York.

Donea, J. (1984). A Taylor-Galerkin method for convective transport problems. *Int. J. Numer. Methods Engrg.*, 20:101–120.

D'Oriano, C., Poggianti, E., Bertagnini, A., Cioni, R., Landi, P., Polacci, M., and Rosi, M. (2005). Changes in the eruptive style during the A.D. 1538 Monte Nuovo eruption (Phlegrean Fields, Italy): the role of syn-eruptive crystallization. *Bull Vilcanol.*, 67:601–621.

Douglas, J. and Russel, T. (1982). Numerical methods for convection dominated diffusion problems based on combining the method of characteristics with finite element or finite differences procedures. *SIAM J. Numer. Anal.*, 18:871–885.

Dunkin, J. W. (1965). Computation of modal solutions in layered, elastic media at high frequencies. *Bull. Seismol. Soc. Am.*, 55:335–358.

Dvorak, J. J. and Gasparini, P. (1991). History of earthquakes and vertical movement in Campi Flegrei caldera, Southern Italy: comparison of precursory events to the a.d. 1538 eruption of Monte Nuovo and activity since 1968. *J. Volcanol. Geotherm. Res.*, 48:77–92.

Fedele, F., Giaccio, B., Isaia, R., and Orsi, G. (2002). Ecosystem impact of the Campanian Ignimbrite eruption in Late Pleistocene Europe. *Quat. Research*, 57:420–424.

Finetti, I. and Morelli, C. (1974). Esplorazione sismica a riflessione dei Golfi di Napoli e Pozzuoli. *Boll. Geof. Teor. Appl.*, 16(62/63):175–222.

Fisher, R., Heiken, G., and Hullen, J. (1997). *Volcanoes, crucibles of change*. Princeton University Press, Princeton, NJ.

Fisher, R., Orsi, G., Ort, M., and Heiken, G. (1993). Mobility of large-volume pyroclastic flow-emplacement of the Campanian Ignimbrite, Italy. *J. Volcanol. Geotherm. Res.*, 56:205–220.

Folch, A., Codina, R., and Martí, J. (2001). Numerical modeling of magma withdrawal during explosive caldera-forming eruptions. *J. Geophys. Res.*, 106(B8):16,163–16,176.

Folch, A., Martí, J., Codina, R., and Vazquez, M. (1998). A numerical model for temporal variations during explosive central vents eruptions. *J. Geophys. Res.*, 103(B9):20,883–20,899.

Folch, A., Vazquez, M., Codina, R., and Martí, J. (1999). A fractional-step finite-element method for the Navier-Stokes equations applied to magma-chamber withdrawal. *Comput. Geosci.*, 25(3):263–275.

Franca, L. and Frey, S. L. (1992). Stabilized finite element methods: II. The incompressible Navier-Stokes equations. *Comput. Methods Appl. Mech. Engrg.*, 89:141–219.

Gaeta, F., De Natale, G., Peluso, F., Mastrolorenzo, G., Castagnolo, D., Troise, C., Pingue, F., Mita, D., and Rossano, S. (1998). Genesis and evolution of unrest episodes at campi flegrei caldera: the role of thermal fluid-dynamical processes in the geothermal system. *J. Geophys. Res.*, 103:20921–20933.

Gamma, E., Helm, R., Johnson, R., and Vlissides, J. (1994). *Design Patterns: Elements of Reusable Object-Oriented Software*. Addison-wesley professional computing series, EDITION = 1^{st},. ADDISON-WESLEY.

Gardner, G., Gardner, L., and Gregory, A. (1974). Formation velocity and density - the diagnostic basis for stratigraphic traps. *Geophysics*, 39:770–780.

Gerasimov, Y. A., Dreving, V., Eremiv, E., Kiselev, A., Lebedev, V., Panchenkov, G., and Shlygin, A. (1974). *Physical Chemistry*. Number 1. MIR, Moscow.

Ghiorso, M. (1994). Algorithms for the estimation of phase stability in heterogeneous thermodynamic systems. *Geochim. Cosmochim. Acta*, 58:5489–5501.

Ghiorso, M., Carmichael, I., Rivers, M., and Sack, R. (1983). The Gibbs free energy of mixing of natural silicate liquids; an expanded regular solution approximation for the calculation of magmatic intensive variables. *Controb. Mineral. Petrol.*, 84:107–145.

Giordano, D. and Dingwell, D. B. (2003). Viscosity of hydrous Etna Basalt; implications for Plinian-style basaltic eruptions. *Bull. VOlcanol.*, 65(1):8–14.

Giordano, D., Dingwell, D. B., and Romano, C. (2000). The geology and geophysics of Tenerife. *J. volcanol. geotherm. res.*, 103(1-4):239–245.

Giovangigli, V. (1999). *Multicomponent Flow Modeling*. Birkhäuser, Boston.

Gottsmann, J., Berrino, B., Rymer, H., and Williams-Jones, G. (2003). Hazard assessment during caldera unrest at the Campi Flegrei, Italy: A contribution from gravity-height gradients. *Earth Planet. Sci. Lett.*, 211(3-4):295–309.

Hauke, G. and Hughes, T. J. R. (1998). A comparative study of different sets of variables for solving compressible and incompressible flows. *Comput. Methods Appl. Mech. Engrg.*, 153:1–44.

Hecht, F. (1998). *BAMG Bidimensional Anisotropic Mesh Generator*. INRIA, Roquencourt, 75153 Le Chenay CEDEX, France.

Hess, K. U. and Dingwell, D. B. (1996). Viscosities of hydrous leucogranitic melts: a non-arrhenian model. *Am. Mineral.*, 81:1297–1300.

Hirschfelder, J. O., Curtiss, C. F., and Bird, R. B. (1969). *Molecolar Theory of Gases and Liquids*. Wiley, New York.

Holloway, J. R. and Blanck, J. G. (1994). Application of experimental results to C-O-H species in natural melts. In Carroll, M. R. and Holloway, J. R., editors, *Volatiles in magma*, volume 30 of *Rev. Mineral.*, pages 187–230, Washington D. C. Mineral. Soc. of Am.

Hughes, T. J. R., Franca, L. P., and Hulbert, G. (1989). A new finite element formulation for computational fluid dynamics: VIII. The Galerkin/least-squares method for advective-diffusive equations. *Comput. Methods Appl. Mech. Engrg.*, 73:173–189.

Ishii, M. (1977). One-dimensional drift-flux model and constitutive equations for relative motion between phases in various two-phase flow regimes. Technical report, Argonne Natl. Lab., Argonne, Illinois. ANL-77-47.

Ishii, M. and Zuber, N. (1979). Drag coefficient and relative velocity in bubbly, droplet or particulate flows. *AiChE J.*, 25:843–855.

Johnson, C., Navert, U., and Pitänkar, J. (1984). Finite element methods for linear hyperbolic problems. *Comput. Methods Appl. Mech. Engrg.*, 45:285–312.

Judenherc, S. and Zollo, A. (2004). The Bay of Naples (southern Italy): Constraints on the volcanic structures inferred from a dense seismic survey. *J. Geophys. Res.*, 109(B10312).

Julian, B. R. (1994). Volcanic tremor: Nonlinear excitation by fluid flow. *J. Geophys. Res.*, 99(B6):11859–11877.

Kennett, L. N. and Kerry, N. J. (1979). Seismic waves in a stratified half-space. *Geophys. J. R. Astron. Soc.*, 57:557–583.

Kerrick, D. and Jacobs, G. (1981). A modified redlick-kwong equation for H_2O , CO_2 and H_2O -CO_2 mixtures at elevated pressures and temperatures. *Am. J. Sci.*, 281:735–767.

Kuritani, T. (2004). Magmatic differentiation examined with a numerical model considering multicomponent thermodynamic and momentum, energy and species trasport. *Lithos*, 74(3-4):117–130.

Ladd, A. J. C. and Kinney, J. H. (1997). Elastic constants of cellular structures. *Physica A*, 240:349–360.

Landau, L. D. and Lifshiftz, E. M. (1986). *Theory of elasticity*. Pergamon Press, Oxford.

Lange, R. A. (1994). The effect of H_2O, CO_2 e F on the density and viscosity of silicate melts. *Rev. Mineral.*, 30:331–369.

Lirer, L., Rolandi, G., Di Vito, M., and Mastrolorenzo, G. (1987). L'eruzione del Monte Nuovo (1538) nei Campi Flegrei. *Boll. Soc. Geol. It.*, 106:447–460.

Llewellin, E. and Manga, M. (2005). Bubble suspension rheology and implications for conduit flow. *J. Volcanol. Geotherm. Res.*, 143:205–217.

Longo, A., Vassalli, M., Papale, P., and Barsanti, M. (2006). Numerical simulation of convection and mixing in magma chamber replenished with CO_2-rich magma. *Geophys. Res. Lett.*, 33.

Malvern, L. (1969). *Introduction to the Mechanics of a Continuous Medium*. Prentice-Hall, Inc., Englewood Cliffs, New Jersey.

Marsh, B. D. (1981). On the cristallinity, probability of occurence and rheology of lava and magma. *Contrib. Mineral. Petrol.*, 78:85–98.

Mashima, H. (2004). Time scale of magma mixing between basalt and dacite estimated for the Saga-Futagoya volcanic rocks in northwest Kyushu, southwest Japan. *J. Volcanol. Geotherm. Res.*, 131(3-4):333–349.

Misiti, V., Freda, C., Taddeucci, J., Romano, C., Scarlato, P., Longo, A., Papale, P., and Poe, B. T. (2006). The effect of H_2O on the viscosity of K-trachytic melts at magmatic temperatures. *Chem. Geol.*

Mittal, S. and Tezduyar, T. (1998). A unified finite element formulation for compressible and incompressible flows using augmented conservation variables. *Comput. Methods Appl. Mech. Engrg.*, 161:229–243.

Moczo, P., Kristek, J., Gallis, M., Pazak, P., and Balazovjech, M. (2007). The finite-difference and finite-element modeling of seismic wave propagation and earthquake motion. *Acta physica slovaca*, 57(2):177–406.

Modell, M. and Reid, R. C. (1983). *Thermodynamic and its applications*. International Series in the Physical and Chemical Engineering Sciences. Prentice Hall, Englewood Cliffs, 2^{nd} edition.

Monette, L. and Anderson, M. (1994). Elastic and fracture properties of the two-dimensional triangular and square lattices. *Modelling Simul. Mater. Sci Eng.*, 2:53–66.

Muller, G. (1985). The reflectivity method: a tutorial. *J. Geophys.*, 58:153–174.

Neri, A., Esposti Ongaro, T., Macedonio, G., and Gidaspow, D. (2003). Multiparticle simulation of collapsing volcanic columns and pyroclastic flows. *J. Geophys. Res.*, 108(B4).

Neuberg, J., Luckett, R., Baptie, B., and Olsen, K. (2000). Models of tremor and low-frequency earthquake swarms on Montserrat. *J. Volcanol. Geotherm. Res.*, 101:83–104.

Nishimura, T. and Chouet, B. (2003). A numerical simulation of magma motion, crustal deformation, and seismic radiation associated with volcanic eruptions. *Geophys. J. Int.*, 153:99–718.

O'Brien, G. (2008). Discrete visco-elastic lattice methods for seismic wave propagation. *Geophys. Res. Lett.*, 35(L02302).

O'Brien, G. and Bean, C. J. (2004a). A 3D discrete numerical elastic lattice method for seismic wave propagation in heterogeneous media with topography. *Geophys. Res. Lett*, 31(14).

O'Brien, G. and Bean, C. J. (2004b). A discrete numerical method for modeling volcanic earthquake source mechanisms. *J. Geophys. Res.*, 109(B09301).

Oldenburg, C. M., Spera, F. J., Yuen, D. A., and Sewell, G. (1989). Dynamic mixing in magma bodies: Theory, simulations and implications. *J. Geophys. Res.*, 94(B7):9215–9236.

O'Neill, M. E. and Hill, D. P. (1979). Causal absorption: its effect on synthetic seismograms computed by the reflectivity method. *Bull. Seismol. Soc. Am.*, 69:17–25.

Orsi, G., Civetta, L., D'Antonio, M., Di Girolamo, P., and Piochi, M. (1995). Step-filling and development of a three-layers magma chamber: the Neapolitan Yellow Tuff case history. *J. Volcanol. Geotherm. Res.*, 67:291–312.

Orsi, G., Civetta, L., Del Gaudio, C., de Vita, S., Di Vito, M., Isaia, R., Petrazzuoli, S., Ricciardi, G., and Ricco, C. (1999). Short-Term ground deformations and seismicity in the nested Campi Flegrei Caldera (Italy): an example of active block resurgence in a densely populated area. *J. Volcanol. Geotherm. Res.*, 91:415–451.

Orsi, G., D'Antonio, M., de Vita, S., and Gallo, G. (1992). The Neapolitan Yellow Tuff, a large-magnitude trachytic phreatomagmatic eruption: eruptive dynamics, magma withdrawal and caldera collapse. *J. Volcanol. Geotherm. Res.*, 53:275–287.

Orsi, G., de Vita, S., and Di Vito, M. (1996). The restless, resurgent Campi Flegrei nested caldera (Italy): costraints on its evolution and configuration. *J. Volcanol. Geotherm. Res.*, 74:179–214.

Orsi, G., Di Vito, M. A., and Isaia, R. (2004). Volcanic hazard assessment at the Campi Flegrei Caldera. *Bull. of Volcanol.*, 66:514–530.

Orsi, G., Gallo, G., and Zanchi, A. (1991). Simple shear block resurgence in caldera depressions. A model from Pantelleria and Ischia. *J. Volcanol. Geotherm. Res.*, 47:1–11.

Pallister, J. S., Hoblitt, R. P., and Reyes, A. G. (1992). A basalt trigger for the 1991 eruptions of Pinatubo volcano? *Nature*, 356:426–428.

Papale, P. (1999). Modeling of the solubility of a two-component H_2O + CO_2 fluid in silicate liquids. *Am. Mineral.*, 84:477–492.

Papale, P. (2005). Determination of total H_2O and CO_2 budgets in evolving magmas from melt inclusion data. *J. Geophys. Res.*, 110.

Papale, P. and Civetta, L. (2007). *INGV-DPC Project V3_2 Campi Flegrei: Final report*.

Papale, P. and Dobran, F. (1994). Magma flow along the volcanic conduit during the plinian and pyroclastic flow phases of the May 18,1980 Mt. St. Helens eruption. *J. Geophys. Res.*, 99:4355–4373.

Papale, P., Moretti, R., and Barbato, D. (2006). The compositional dependence of the saturation surface of H_2O +CO_2 fluids in silicate melts. *Chem. Geol.*, 229(1-3):78–95.

Pappalardo, L., Civetta, L., de Vita, S., Di Vito, M. A., Orsi, G., Carandente, A., and Fisher, R. V. (2002). Timing of magma extraction during the Campanian Ignimbrite eruption (Campi Flegrei caldera). *J. Volcanol. Geotherm. Res.*, 114:479–497.

Parascandola, A. (1947). *I fenomeni bradisismici del Serapeo di Pozzuoli*. Genovesi, Napoli.

Phillips, J. and Woods, A. (2002). Suppression of large-scale magma mixing by melt-volatile separation.

Pirroneau, O. and Tezduyar, T. (1982). On the transport-diffusion algorithm and its applications to the Navier-Stokes equations. *Numer. Math.*, 38:309–332.

Press, W., Teukolsky, S., Vetterling, W., and Flannery, B. (1992). *Numerical Recipes in C++: The Art of Scientific Computing*. Cambridge Univ. Press, 2^{nd} edition.

Qi, C., Wang, M., Qian, Q., and Chen, J. (2007). Structural hierarchy and mechanical properties of rocks. Part 1. Structural hierarchy and viscosity. *Phys. Mesomech.*, 10:47–56.

Quareni, F., Yuen, D. A., Sewell, G., and Christensen, U. R. (1985). High Rayleigh number convection with strongly variable viscosity: A comparison between mean field and two-dimensional solutions. *J. Geophys. Res.*, 90(B14):12,633–12,644.

Rampino, M., Sanders, J., Newman, W., and Königsson, L. (1987). *Climate History, periodicity and predictability*. Van Nostrandt Reinhold, NY.

Reid, R. C., Prausnitz, J., and Sherwood, T. (1977). *The properties of gases and liquids*. International Series in the Physical and Chemical Engineering Sciences. McGraw Hill, New York, 3^{rd} edition.

Roche, O. and Druitt, T. H. (2001). Onset of caldera collapse during ignimbrite eruption. *Earth Planet. Sci. Lett.*, 19(3-4):191–202.

Romano, C., Giordano, D., Papale, P., Mincione, V., and Dingwell, D. B. (2003). The dry and hydrous viscosities of alkaline melts from Vesuvius and Phlegrean Fields. *Chem. Geol.*, 202(1-2):23–38.

Rosi, M., Vezzosi, L., Aleotti, P., and De Cenzi, M. (1996). Interaction between caldera collapse and eruptiove dynamics during the Campanian Ignimbrite eruption, Phlegrean Fields, Italy. *Bull. Volcanol.*, 57:541–554.

Rutherford, M. J. and coll. (2004). Experimental and analytical investigation of pre-eruption conditions in Phlegrean Field trachyte magmas: Significance for modeling eruption dynamics. GNV Internal report.

Saccorotti, G., Petrosino, S., Bianco, F., Castellano, M., Galluzzo, D., Rocca, M. L., Del Pezzo, E., Zaccarelli, L., and Cusano, P. (2007). Seismicity associated with the 2004−2006 renewed ground uplift at Campi Flegrei Caldera, Italy. *Phys. Eart. Plan. Interiors*, 165:14–24.

Sandia National Laboratories (2007). *TRILINOS*. http://trilinos.sandia.gov/.

Scarpati, C., Cole, P., and Perrotta, A. (1993). The Neapolitan Yellow Tuff - A large volume multiphase eruption from Campi Flegrei, Southern Italy. *Bull. Volcanol.*, 55:343–356.

Shakib, F., Hughes, T. J., and Johan, Z. (1991). A new finite element formulation for computational fluid dynamics: X. The compressible Euler and Navier-Stokes equations. *Comput. Methods Appl. Mech. Engrg.*, 89:141–219.

Shakib, F., Hughes, T. J. R., and Johan, Z. (1989). A multi-element group preconditioned GMRES algorithm for nonsymmetric systems arising in finite element analysis. *Comput. Methods Appl. Mech. Engrg.*, 75:415–456.

Sigurdsson, H., Carey, S., Cornell, W., and Pescatore, T. (1985). The eruption of vesuvius in ad 79. *Natl. Geogr. Res.*, 1:332–387.

Simakin, A. and Botcharnikov, R. (2001). Degassing of stratified magma by compositional convection. *J. Volcanol. Geophys. Res.*, 105:207–214.

Snyder, D. (1997). The mixing and mingling of magmas. *Endeavour*, 21(1):19–22.

Snyder, D. (2000). Thermal effects of the intrusion of basaltic magma into a more silicic magma chamber and implications for eruption triggering. *Earth Planet. Sci. Lett.*, 175:257–273.

Sparks, S. R. J., Sigurdsson, H., and Wilson, L. (1977). Magma mixing: A mechanism for triggering acid explosive eruptions. *Nature*, 267:315–318.

Spera, F. J., Oldenburg, C. M., Christensen, U. R., and Todesco, M. (1995). Simulation of convection in the system $KAlSi_2O6$-$CaMgSi_2O_6$: Implications for compositionally zoned magma bodies. *Am. Mineral.*, 80:1188–1207.

Spera, F. J., Yuen, D. A., Greer, J. C., and Sewell, G. (1986). Dynamics of magma withdrawal from stratified magma chambers. *Geology*, 14:723–726.

Tait, S., Jaupart, C., and Vergniolle, S. (1989). Pressure, gas content and eruption periodicity of a shallow crystallizing magma chamber. *Earth Planet. Sci. Lett.*, 92:107–123.

Tang, C. (1997). Numerical simulation of progressive rock failure and associated seismicity. *Int. J. Rock Mech. Min. Sci.*, 34:249–261.

Tezduyar, T. and Hughes, T. J. R. (1983). Finite element formulations for convection dominated flows with particular emphasis on the compressible Euler equations. In *Proceedings of the AIAA 21st Aerospace Sciences Meeting*.

Todesco, M., Rutqvist, J., Chiodini, G., Pruess, K., and Oldenburg, C. (2004). Modeling of recent volcanic episodes at Phlegran Fields (Italy): geochemical variations and ground deformation. *Geothermics*, 33:531–547.

Toomey, A. and Bean, C. (2000). Numerical simulation of seismic waves using a discrete particle scheme. *Geophys. J. Int.*, 141:595–604.

Touzani, R. (2004). *OFELI An Object Finite Element Library Version 1.3.0*. Laboratoire de Mathématiques, Université Blaise Pascal Clermont-Ferrand II. http://www.ofeli.net.

Trial, A. F., Spera, F. J., Greer, J., and Yuen, D. A. (1992). Simulations of magma withdrawal from composizionally zoned bodies. *J. Geophys. Res.*, 97(B5):6713–6733.

Troise, C., De Natale, G., Pingue, F., Obrizzo, F., Martino, P. D., Tammaro, U., and Boschi, E. (2007). Renewed ground uplift at campi flegrei caldera (italy): New insight on magmatic processes and forecast. *Geophys. Res. Lett.*, 34(L03301).

Vanorio, T., Virieux, J., Capuano, P., and Russo, G. (2005). Three-dimensional seismic tomography from P wave and S wave microearthquake travel times and rock physics characterization of the Campi Flegrei Caldera. *J. Geophys. Res.*, 110(B03201).

Vassallo, M. and Zollo, A. (2007). Depth and morphology of reflectors from the non-linear inversion of arrival-time and waveform semblance data. Part I: methods and applications to synthetic data. *Geophys. Prosp.* in press.

Venetzky, D. Y. and Rutherford, M. J. (1997). Preeruption conditions and timing of dacite-andesite magma mixing in the 2.2 ka eruption at Mount Rainier. *J. Geophys. Res.*, 102(B9):20,069–20,086.

Wallis, G. B. (1979). *One-dimensional two-phase flow*. McGraw Hill, New York, 2nd edition.

Webb, S. and Dingwell, D. (1990). Non-Newotnian rheology of igneous melts at high stresses and strain rates: experimental results for rhyolite, andesite, basalt, and nepholinite. *J. Geophys. Res.*, 95:15695–15701.

Wohletz, K., Orsi, G., and de Vita, S. (1995). Thermal evolution of the Phlegrean magmatic system. *J. Volcanol. Geotherm. Res.*, 91:381–414.

Yanagi, T., Okada, H., and Ohta, K. (1992). *Unzen volcano: the 1990-1992 eruption*. Nishinippon & Kyushu press, Fukuoka.

Zhang, Z. X. (2002). An empirical relation between mode I fracture toughness and the tensile strength of rock. *Int. J. Rock Mech. Min. Sci.*, 3:401–406.

Zienkiewicz, O. C. and Codina, R. (1995). A general algorithm for compressible and incompressible flows - Part I. The split, characteristic-based scheme. *Int. J. Numer. Methods Fluids*, 20:869–885.

Zienkiewicz, O. C., Morgan, K., and Satya Sai, B. (1995). A general algorithm for compressible and incompressible flows - Part II. Tests on the explicit form. *Int. J. Numer. Methods Fluids*, 20:887–913.

Zollo, A., Judenherc, S., Auger, E., D'Auria, L., Virieux, J., Capuano, P., Chiarabba, C., de Franco, R., Makris, J., Michelini, A., and Musacchio, G. (2003). Evidence of the buried rim of Campi Flegrei caldera from 3-D active seismic imaging. *Gephys. Res. Lett.*, 30(19).